High-order Calderón Preconditioning of Integral Equations for the Analysis of Scattering from PEC and Homogeneous Penetrable Objects

by

Felipe Valdés Valenzuela

A dissertation submitted in partial fulfillment
of the requirements for the degree of
Doctor of Philosophy
(Electrical Engineering)
in The University of Michigan
2012

Doctoral Committee:

    Professor Eric Michielssen, Co-Chair
    Associate Professor Francesco P. Andriulli, Telecom-Bretagne, Co-Chair
    Professor Mahta Moghaddam
    Professor Kamal Sarabandi
    Associate Professor Anthony Grbic
    Associate Professor Divakar Viswanath

A mis padres, Claudio y Malva

ACKNOWLEDGEMENTS

First and foremost I would like to thank my parents. If it was not for their love, support, sacrifices, and the great interest that they put in my education, I would not have been able to accomplish what I did. It is for all of this that I dedicate this dissertation to them. Being the youngest in may family, my syblings have always supported and protected me; this achievement also belongs to them. I would also like to thank Andrea Villablanca and her family for their support, especially at the beginning of this journey.

Among the people who contributed to my academic success at the University of Michigan, my greatest appreciation surely belongs to my advisor, Professor Eric Michielssen. I am grateful of the opportunity that he gave me to come to the University of Michigan and work with him. He has always encouraged, guided, and supported me to do better work during these years. I have certainly learned a lot from him. I also would like to thank the members of my dissertation committee Professors Kamal Sarabandi, Mahta Moghaddam, Anthony Grbic, Divakar Viswanath, and Francesco Andriulli for their precious time reading this dissertation and providing me with comments and suggestions.

There are many people who contributed to my academic success throughout the past two decades of formal education that I received. Some of them have been more inspiting than others, but I am grateful to all of them from my first grade teacher to my Ph.D. advisor.

I have been extremely fortunate to get the chance to work with wonderful colleagues in my research group. In particular I would like to thank Onur Bakir, Abdulkadir Yucel, Luis Gomez, Hakan Bagci, Xi Lin, and specially Francesco Andriulli, for their help and the knowledge they shared with me.

During the past five and a half years at the University of Michigan, I have enjoyed the friendship of many great people. I would like to thank all of my good friends: Hatim Bukhari, Laura Fink, Francesca Simone, Laura Constain, Rodirgo Parra, Mark Kravitz, Alberto Faraggi, Julia Fahlke, Veronica Menaldi,

TABLE OF CONTENTS

LIST OF FIGURES

x

LIST OF TABLES

CHAPTER I

Introduction

1.1   Motivation

Boundary integral equations (BIE) have remained a popular choice among code developers and practitioners for analyzing time-harmonic and transient electromagnetic interaction with perfect electrically conducting (PEC) as well as homogeneous penetrable objects [1]. Opposite to Finite Differences or Finite Element methods in which equations are solved for the electric and magnetic fields everywhere in the propagation domain, BIEs are solved for the trace of those fields on the surface of a scatterer. These traces are referred here as equivalent currents. Numerical solution of a BIE requires the discretization of the scatterer's surface, generally in terms of a mesh of planar or curvilinear triangles and/or quadrangles. On this discrete surface, spatial dependence of the equivalent current distribution(s) is accounted by N_S vector basis functions. In time-domain (TD) BIEs, the temporal dependence of the currents is represented by means of N_T scalar basis functions, which yields a total of $N_S N_T$ real coefficients to be determined. In frequency-domain BIEs, time dependence is accounted by a complex coefficient scaling each vector basis function, which yields a total of $2N_S$ real (or N_S complex) coefficients to be determined.

Irrespective of the time regime, discretization of a BIE leads to a linear system of equations in the current's expansion coefficients. The computational cost of iteratively solving this system is directly proportional to cost of multiplying the system matrix with a trial solution vector, and to the number of iterations N_{iter} required for convergence to a prescribed residual error. There exist many "fast methods" that reduce the complexity of a matrix-vector multiplication, some of these being suitable for frequency-domain [2]-[5], and other for time-domain [6],[7]. Often N_{iter} scales with the condition number of the system matrix, with small condition numbers guaranteeing fast convergence. Unfortunately, the standard formulations used for PEC and homogeneous penetrable objects are plagued with spectral problems which

render in system matrices whose condition number grows rapidly as the mesh discretization density increases [8], the frequency approaches zero or is close to a resonance. As a result, the cost of solving the BIE for realistic structures is often prohibitively high. The work presented here deals with techniques for preconditioning the system so that the condition number of the system matrix is reduced, and henceforth N_{iter}.

1.2   Overview of Previous Work

Among all BIEs proposed for the analysis of scattering from PEC structures, the Electric Field Integral Equation (EFIE) plays a predominant role. An alternative to the EFIE is the Magnetic Field Integral Equation (MFIE), which can also be linearly combined with the EFIE to form a Combined Field Integral Equation (CFIE). The same operators encountered in the EFIE and MFIE pertinent to the analysis of scattering from PEC structures can also be used to derive BIEs suitable homogeneous penetrable objects.

1.2.1   Calderón Preconditioning of the EFIE for Scattering from PEC Objects

Techniques for preconditioning the EFIE based on Calderón identities have become quite popular in recent years [9]-[14]. In essence, these techniques exploit the self-regularizing property of the EFIE operator, viz. the fact that the square of the EFIE operator is a compact perturbation of the identity, to produce well-conditioned system matrices even when the mesh includes sub wavelength geometric features. Unfortunately, only a few such preconditioners developed to date are easily integrated into existing codes. The Calderón Multiplicative Preconditioner (CMP) technique proposed in [11] is one of them. In particular, CMP has been successfully used as a preconditioning technique for the EFIE in frequency-domain [11],[15] as well as for the time-domain EFIE (TDEFIE) [12]. In this work, they are referred as CMP-EFIE and CMP-TDEFIE, respectively. In close connection to the CMP, a modified TDEFIE that is immune to DC instabilities has been presented in [13]. This equation is obtained by leveraging the time domain Calderón identities in conjunction with a careful rearrangement of temporal derivatives appearing in the TDEFIE operator. This rearrangement is referred here as "Dottrick-TDEFIE".

The CMP uses two separate discretizations of the EFIE operator, one in terms of standard Rao-Wilton-Glisson (RWG) basis functions [16], and the other in terms of Buffa-Christiansen (BC) basis functions [17].

The former are div-conforming, while the latter are div- and quasi curl-conforming, i.e. they are geometrically nearly orthogonal to the RWG functions. The effectiveness of the RWG-BC combination in the construction of the CMP stems from the fact that the RWG and BC functions are linked by a well-conditioned Gram matrix and guarantee the annihilation of the square of the discretized hypersingular component of the EFIE operator. Chen and Wilton proposed basis functions similar to the BC ones in the context of analyzing scattering from penetrable objects [18]. Both the BC and Chen-Wilton basis functions are of zeroth-order and designed for use in conjunction with RWG basis functions.

In the last decade, EFIE solvers that use high-order representations of the surface and/or the current density have become increasingly popular. A high-fidelity representation of the surface can be achieved using a high-order parametric mapping from a reference cell to the scatterer surface, usually in the form of curvilinear patches (as opposed to flat ones). Among the many high-order basis functions for representing surface current densities, those proposed by Graglia-Wilton-Peterson ($GWP(p)$), which comprise of products of scalar polynomials (complete up to order p) and RWG basis functions, are very popular [19]. For a given solution accuracy, high-order EFIE solvers have been shown to be more CPU and memory efficient than their zeroth-order counterparts [20]. That said, they still suffer from ill conditioning when applied to structures with sub wavelength geometric features. To allow for a high-order CMP, a high-order extension of the BC functions is called for. Jan et al. [23] already presented an extension of the BC basis functions on curvilinear triangular patches; unfortunately their method does not extend to high-order current representations.

1.2.2   *Single Source Equations for Scattering from Homogeneous Penetrable Objects*

The literature abounds with integral equation techniques for analyzing scattering from homogeneous penetrable objects. Dual source techniques, such as those presented by Poggio and Miller [1] and Müller [24], solve a coupled pair of electric, magnetic, or combined field integral equations in electric and/or magnetic surface current unknowns. These formulations have been studied and used extensively for almost four decades and are the de facto standard. Single source techniques, which solve one integral equation for an electric *or* magnetic surface current density, were proposed by Marx [25] and Glisson [26]. Appealing as these methods may be, they never gained a foothold among code developers and practitioners. The reasons

are two-fold: (i) Marx' and Glisson's equations are of the first kind and involve hypersingular operators; hence they lead to ill-conditioned matrices when discretized and are susceptible to dense-mesh [27] and low-frequency [28] breakdown. (ii) They exhibit resonances; that is, their solution is not unique at a set of discrete frequencies that is increasingly dense as the electrical size of the scatterer increases. A handful of papers present single source integral equations that improve on those in [25][26]. For example, Colliander and Ylä-Oijala [29] presented a second kind single source equation that does not suffer from dense-mesh breakdown; unfortunately their equation remains susceptible to resonances and hence problematic when applied to the analysis of electrically large scatterers. Also, Yeung proposed a combined field single source equation [30] that is resonance-free (at least for the first few resonances of a spherical cavity). Unfortunately, his equation contains a hypersingular electric field integral operator that renders the entire equation hypersingular and susceptible to dense-mesh breakdown. Finally, Mautz [31] presented a resonant free single source equation by introducing an electric current and its rotated counterpart in Glisson's original formulation [26]. However, this integral equation is not easily discretized using basis functions of the mixed order type, since these can be either div- or curl-conforming, but not both.

Numerical discretization of single source equations is by no means a simple task as they contain double operator products, which are not encountered on standard formulations for PEC or homogeneous penetrable objects. Not surprisingly, to date, no time-domain single source formulation for penetrable objects has been reported in the literature.

1.3   Advancements proposed by this work

In the past four years, CMP and BC basis functions have received a lot of attention inside the Computational Electromagnetics (CEM) community. As promising as these techniques are, up to date, they suffer from the main limitation that BC basis functions are of zeroth-order in nature. In consequence:

- The numerical implementations of the CMP reported up to date are limited to zeroth-order surface representations and current expansions.

- High-order discretization of the time-domain CMP-TDEFIE and Dottrick-TDEFIE have never been reported to date.

Single source equations on the other side have not received much attention. This may be explained by the fact that standard discretization schemes do not fit for this type of equations. For this reason:

- Single source equations for analyzing scattering from homogeneous penetrable objects that are free from dense-mesh and low-frequency breakdowns also free from internal resonances have never been presented up to date in the literature.

- Time-domain single source equations for analyzing scattering from homogeneous penetrable objects have never been presented to date.

This work presents the following contributions:

- A true high-order BC extension, viz. a set of high-order div- and quasi curl-conforming (DQCC(p)) functions that, when used in conjunction with the GWP(p) functions, exhibits the aforementioned properties of the BC-RWG pair.

- A high-order numerical implementation of the CMP, both in frequency- and time-domain. This is accomplished using $\mathrm{GWP}(p)$ and the $\mathrm{DQCC}(p)$ basis functions presented here.

- A high-order numerical implementation of the Dottrick-TDEFIE.

- A discretization technique for double or triple operator products, which is achieved by multiplying system matrices arising from the discretization of the various (standalone) operators involved, carefully choosing basis and testing functions. This technique has enabled the proper discretization of a single source equation for penetrable objects, which is free from dense-mesh and low frequency breakdowns, as well as free from resonances.

- A high-order numerical implementation of time domain single source equations for analyzing scattering from homogeneous penetrable objects.

1.4   Document Overview

This document can be outlined as follows. Chapter I describes (in very general terms) the numerical solution of BIEs, provides historic background and previous work that investigates BIEs and lists their main limitations, some of which are addressed in this work. Chapter II introduces a set of high-order div- and quasi curl-conforming ($\mathrm{DQCC}(p)$) basis functions. For illustration purposes, this set of functions is

presented in the context of CMP-EFIE for PEC objects in frequency-domain. The proposed basis functions are constructed as orthogonal projections of the range of the EFIE operator onto div-conforming $GWP(p)$ s defined on a barycentrically refined mesh. Chapter III presents a single source equation for analyzing scattering from homogeneous penetrable objects in frequency-domain. The proposed equation is free from resonances, and free from dense-mesh and low-frequency breakdowns. This equation contains double and triple operator products, the discretization of which is achieved by multiplying system matrices arising from the discretization of the various (standalone) operators involved using carefully chosen basis and testing functions. Specifically, $GWP(p)$ functions are used alongside the $DQCC(p)$ functions presented in Chapter II to stably discretize electric and magnetic field operator products. Chapters IV and V extend the work presented in Chapters II and III to a time-domain framework. In particular, Chapter IV presents a high-order CMP-TDEFIE) as well as a high-order Dottrick-TDEFIE pertinent to the analysis of scattering from PEC objects. Both time-domain implementations are achieved using $GWP(p)$ and $DQCC(p)$ basis functions. In Chapter V, time-domain single source EFIE and MFIE are presented and appropriately discretized to achieve an accurate and stable time-domain scheme. As in the frequency-domain case, the equations presented here contain double operator products, discretization of which is achieved by multiplying system matrices arising from the discretization of the various (standalone) operators involved, using carefully chosen basis and testing functions. To this end, the $DQCC(p)$ basis functions presented in Chapter II are used alongside $GWP(p)$ basis functions. Conclusions and future work are outlined in Chapter VI.

CHAPTER II

High-order Div- and Quasi Curl-Conforming Basis Functions

This chapter presents a new set of high-order div- and quasi curl-conforming ($\text{DQCC}(p)$) basis functions. For illustration purposes, this set of functions is presented in the context of CMP-EFIE for PEC objects in frequency-domain. Section 2.1 presents the general framework for analyzing scattering from PEC objects with the EFIE and CMP-EFIE, in frequency-domain. Section 2.2 describes the BC basis functions. The construction of the $\text{DQCC}(p)$ basis functions is detailed in Section 2.3. Details in the computational implementation of these functions and numerical results are shown in Sections 2.4 and 2.5, respectively.

2.1   Introduction: Calderon Multiplicative Preconditioner

2.1.1   Non-preconditioned EFIE solver

Consider a closed, simply connected PEC surface S residing in a homogeneous medium with permittivity ϵ and permeability μ. The (scaled) current density $\boldsymbol{J}$ on S induced by the incident time-harmonic electric field $\boldsymbol{E}^{inc}$ satisfies the EFIE [21]

$$\mathcal{T}[\boldsymbol{J}] = -\hat{\boldsymbol{n}}_r \times \boldsymbol{E}^{inc} \tag{6.1}$$

where

$$\mathcal{T}[\boldsymbol{J}] = \mathcal{T}_s[\boldsymbol{J}] + \mathcal{T}_h[\boldsymbol{J}] \tag{6.2}$$

with

$$\mathcal{T}_s[\boldsymbol{J}] = \frac{ik}{4\pi} \hat{\boldsymbol{n}}_r \times \int_S \frac{e^{ik|\boldsymbol{r}-\boldsymbol{r'}|}}{|\boldsymbol{r}-\boldsymbol{r'}|} \boldsymbol{J}(\boldsymbol{r'}) ds' \tag{6.3}$$

and

$$T_h[\boldsymbol{J}] = \frac{-i}{4\pi k}\hat{\boldsymbol{n}}_r \times \int_S \nabla' \frac{e^{ik|r-r'|}}{|r-r'|} \nabla'_S \boldsymbol{J}(r')\,ds' \qquad (6.4)$$

Here, $k = \omega\sqrt{\epsilon\mu}$ and $\hat{\boldsymbol{n}}_r$ is the outward pointing unit vector normal to S at $\boldsymbol{r}$; ω is the angular frequency. A time dependence $e^{-i\omega t}$ ($i = \sqrt{-1}$) is assumed and suppressed. The subscripts "s" and "h" stand for "singular" (vector potential) and "hyper-singular" (scalar potential), respectively. To numerically solve (6.1), S is approximated by a mesh S_δ of planar or curvilinear triangles with minimum edge size δ, and $\boldsymbol{J}$ is expressed as

$$\boldsymbol{J}(r) \approx \sum_{j=1}^{N} I_j \boldsymbol{f}_j(r) \qquad (6.5)$$

where I_j, $j = 1,\ldots,N$ are expansion coefficients of $\boldsymbol{J}$ in terms of a set of the div-conforming basis functions $F = \{\boldsymbol{f}_j(r), j = 1,\ldots,N\}$.

Throughout this section it is assumed that F is the set of pth-order interpolatory Graglia-Wilton-Peterson functions, i.e. $F = \text{GWP}(p)$ [19]. These functions interpolate at $p+1$ and $p(p+1)$ nodes along each of the N_E edges and on each of the N_P patches in S_δ, respectively. The total number of GWP(p) functions therefore is $N = (p+1)N_E + p(p+1)N_P$; note that $\text{RWG} = \text{GWP}(0)$ [19]. GWP(p) functions that interpolate at a node internal to a patch or on an edge henceforth will be referred to as patch and edge functions, respectively. For later use we note the Euler identity for a simply connected surface

$$N_V - N_E + N_P = 2 \qquad (6.6)$$

where N_V is the number of vertices in S_δ.

Substitution of expansion (6.5) into (6.1), and testing the resulting equation with curl-conforming functions in $nF = \{\hat{\boldsymbol{n}}_r \times \boldsymbol{f}_i(r), i = 1,\ldots,N \mid \boldsymbol{f}_i(r) \in F\}$ yields the $N \times N$ linear system of equations

8

$$\mathbf{T}_F \, \mathbf{I} = \mathbf{V}_F \qquad\qquad (6.7)$$

where

$$(\mathbf{T}_F)_{i,j} = \left\langle \hat{\boldsymbol{n}}_r \times \boldsymbol{f}_i, \mathcal{T}[\boldsymbol{f}_j] \right\rangle \qquad\qquad (6.8)$$

$$(\mathbf{I})_j = I_j \qquad\qquad (6.9)$$

and

$$(\mathbf{V}_F)_i = -\left\langle \hat{\boldsymbol{n}}_r \times \boldsymbol{f}_i, \hat{\boldsymbol{n}}_r \times \boldsymbol{E}^{inc} \right\rangle \qquad\qquad (6.10)$$

Here $\langle \boldsymbol{a}, \boldsymbol{b} \rangle = \int_{S_\delta} \boldsymbol{a}(\boldsymbol{r}) \, \boldsymbol{b}(\boldsymbol{r}) \, ds$ denotes the inner product between to vector functions $\boldsymbol{a}$ and $\boldsymbol{b}$ on S_δ.

When analyzing electromagnetic phenomena involving electrically large and/or complex structures, i.e., when N is large, (6.7) cannot be solved directly and iterative solvers are called for. The computational cost of solving (6.7) iteratively is proportional to the cost of multiplying the impedance matrix $\mathbf{T}_F$ by a trial solution vector and the number of iterations N_{iter} required to reach a desired residual error; N_{iter} typically is proportional to $\mathbf{T}_F$'s condition number, viz. the ratio of $\mathbf{T}_F$'s largest and smallest singular values. Unfortunately, the singular values of the operator $\mathcal{T}$ comprise two branches, one accumulating at zero, and the other at infinity [8]. Thus the condition number of $\mathbf{T}_F$ grows without bound as $\boldsymbol{J}$ is increasingly well-approximated, i.e. as $\delta \to 0$ and/or $p \to \infty$. When this happens the number of iterations required for convergence often is prohibitively high.

2.1.2 Calderón preconditioned EFIE solver

A well-conditioned EFIE can be obtained by leveraging $\mathcal{T}$'s self-regularizing property expressed by the Calderón identity [8][11][12].

$$\mathcal{T}^2[\boldsymbol{J}] = -\frac{\boldsymbol{J}}{4} + \mathcal{K}^2[\boldsymbol{J}] \qquad\qquad (6.11)$$

with

$$\mathcal{K}[\boldsymbol{J}](\boldsymbol{r}) = \frac{\hat{\boldsymbol{n}}_r}{4\pi} \times \int_S \nabla' \frac{e^{ik|\boldsymbol{r}-\boldsymbol{r}'|}}{|\boldsymbol{r}-\boldsymbol{r}'|} \times \boldsymbol{J}(\boldsymbol{r}') ds' \tag{6.12}$$

The operator $\mathcal{K}$ is compact on smooth surfaces: its singular values accumulate at zero and the same

holds true for $\mathcal{K}^2$ [8][33]. It follows that the operator $-1/4 + \mathcal{K}^2$ has a bounded spectrum with singular

values accumulating at $-1/4$. Eqn. (6.11) implies that the Calderón-preconditioned EFIE

$$\mathcal{T}^2[\boldsymbol{J}] = -\mathcal{T}[\hat{\boldsymbol{n}}_r \times \boldsymbol{E}^{inc}] \tag{6.13}$$

may be amenable to stable discretization regardless of the mesh density or basis function order.

Unfortunately, the discretization of $\mathcal{T}^2[\boldsymbol{J}] = \mathcal{T}\left[\mathcal{T}[\boldsymbol{J}]\right]$ is by no means trivial. The literature abounds

with techniques for discretizing

$$\mathcal{T}^2[\boldsymbol{J}] = \mathcal{T}_s^2[\boldsymbol{J}] + \mathcal{T}_s\mathcal{T}_h[\boldsymbol{J}] + \mathcal{T}_h\mathcal{T}_s[\boldsymbol{J}] + \mathcal{T}_h^2[\boldsymbol{J}] \tag{6.14}$$

that separately handle the first three terms in the above expansion, explicitly leaving out the fourth as

$\mathcal{T}_h^2 \equiv 0$ [9][10]. However, the implementation of these techniques into existing codes is quite intrusive.

The CMP proposed in [11] does not suffer from this drawback. The CMP approximates $\mathcal{T}^2[\boldsymbol{J}]$ as the

product of two impedance matrices $\mathbf{T}_{\tilde{F}}$ and $\mathbf{T}_F$ with $\tilde{F} = \left\{ \tilde{\boldsymbol{f}}_j(\boldsymbol{r}), j = 1,\dots,N \right\}$, separated by a Gram matrix

that accounts for the possible lack of (bi-)orthogonality between the functions in $\tilde{F}$ and nF. In other

words, the CMP-EFIE matrix equation reads

$$\mathbf{T}^{CMP} \mathbf{I} = \mathbf{V}^{CMP} \tag{6.15}$$

where

$$\mathbf{T}^{CMP} = \mathbf{T}_{\tilde{F}} \, \mathbf{G}_{nF;\tilde{F}}^{-1} \, \mathbf{T}_F \tag{6.16}$$

$$\mathbf{V}^{CMP} = \left(\mathbf{T}_{\tilde{F}} \, \mathbf{G}_{nF;\tilde{F}}^{-1} \right) \mathbf{V}_F \tag{6.17}$$

and

$$(\mathbf{G}_{nF;\tilde{F}})_{i,j} = \left\langle \hat{\boldsymbol{n}}_r \times \boldsymbol{f}_i, \tilde{\boldsymbol{f}}_j \right\rangle \tag{6.18}$$

is the matrix of overlap integrals of functions in $\tilde{F}$ and nF. Eqn. (6.15) does not require the decomposition of matrix elements in $\mathbf{T}_{\tilde{F}}$ and $\mathbf{T}_F$ into their singular (vector potential) and hypersingular (scalar potential) components, simplifying its implementation. That said, (6.16) only will be well-conditioned if

C1. the functions in $\tilde{F}$ and F are div-conforming;

C2. the matrix $\mathbf{G}_{nF;\tilde{F}}$ is well-conditioned; this ensures the rapid iterative solution of $\mathbf{G}_{nF;\tilde{F}}\mathbf{y} = (\mathbf{T}_F\mathbf{x})$ for trial solution vectors $\mathbf{x}$ while solving (6.15); this requirement precludes the choice $\tilde{F} = F = \mathrm{GWP}(p)$ as such leads to a singular Gram matrix;

C3. the sets $\tilde{F}$ and F ensure the cancellation of $\mathcal{T}_h^2[\boldsymbol{J}]$ upon discretization, i.e.

$$\mathbf{T}_{h,\tilde{F}}\, \mathbf{G}_{nF;\tilde{F}}^{-1}\, \mathbf{T}_{h,F} = 0 \tag{6.19}$$

where

$$(\mathbf{T}_{h,F})_{i,j} = \left\langle \hat{\boldsymbol{n}}_r \times \boldsymbol{f}_i, \mathcal{T}_h[\boldsymbol{f}_j] \right\rangle \tag{6.20}$$

If (6.19) is not satisfied, the desirable spectral properties of $\mathcal{T}^2$ will not be inherited by $\mathbf{T}_{\tilde{F}}\, \mathbf{G}_{nF;\tilde{F}}^{-1}\, \mathbf{T}_F$.

The above criteria are satisfied by the sets $F = \mathrm{RWG}$ and $\tilde{F} = \mathrm{BC}$, the set of (zeroth-order) div- and quasi curl-conforming Buffa-Christiansen basis functions, used by *all* CMP implementations reported to date [11]-[13][15][21]-[23].

2.2   Zeroth-order Quasi Curl-conforming Basis Functions

This section reviews the construction of the BC basis functions and their main properties [11][12]. Just as $F = \mathrm{RWG}$, the set $\tilde{F} = \mathrm{BC}$ contains $N = N_E$ basis functions. Contrary to the current of the RWG function $\boldsymbol{f}_n$, which crosses edge n (Fig. II.1(a)), that of the BC function $\tilde{\boldsymbol{f}}_n$ flows along edge n (Fig. II.1(c)). Consider the *barycentrically refined mesh* $\overline{S}_\delta$, obtained by adding the three medians to each

triangle of the original mesh S_δ. Each BC basis function is a linear combination of div-conforming RWGs defined on $\overline{S}_\delta$ [11][12]. Even though BC functions are strictly div-conforming, they also are quasi curl-conforming in that they resemble curl-conforming RWGs in nF (Fig. II.1(b)). This renders the Gram matrix in (6.19) (with $F = \text{RWG}$ and $\tilde{F} = \text{BC}$) well-conditioned. That is, the sets $F = \text{RWG}$ and $\tilde{F} = \text{BC}$ fulfill conditions C1 and C2 above. To show that these sets also satisfy condition C3, consider the space $\text{Span}\left(F^{sol}\right) \subset \text{Span}\left(F\right)$ spanned by "div-conforming solenoidal RWG" functions

$$F^{sol} = \left\{ \boldsymbol{f}_j^{sol}(\boldsymbol{r}), j = 1,\ldots,N^{sol} \right\} \tag{6.21}$$

with $N^{sol} = N_V - 1$; the $\boldsymbol{f}_j^{sol}$ are charge-free and could, for example, be "loop" functions describing current flowing around all but one of the vertices in S_δ (Fig. II.2(a)) [23-24]. The set F^{sol} can be complemented by a set F^{nonsol} such that $\text{Span}\left(F\right) = \text{Span}\left(F^{sol}\right) \oplus \text{Span}\left(F^{nonsol}\right)$. The set F^{nonsol} contains "div-conforming non-solenoidal RWG" functions

$$F^{nonsol} = \left\{ \boldsymbol{f}_j^{nonsol}(\boldsymbol{r}), j = 1,\ldots,N^{nonsol} \right\} \tag{6.22}$$

with $N^{nonsol} = N - (N_V - 1) = N_P - 1$; the $\boldsymbol{f}_j^{nonsol}$ all produce charge and could, for example, be "star" functions describing current flowing out of all but one patch in S_δ (Fig. II.2(b)) [34][35]. Similarly, consider the space $\text{Span}\left(\tilde{F}^{sol}\right) \subset \text{Span}\left(\tilde{F}\right)$ spanned by "div-conforming solenoidal BC" functions

$$\tilde{F}^{sol} = \left\{ \tilde{\boldsymbol{f}}_j^{sol}(\boldsymbol{r}), j = 1,\ldots,\tilde{N}^{sol} = N^{nonsol} \right\} \tag{6.23}$$

The dimensionality of $\text{Span}\left(\tilde{F}^{sol}\right)$ equals that of $\text{Span}\left(F^{nonsol}\right)$; indeed, it can be verified that an appropriate linear combination of the BC functions associated with the three edges of a patch in S_δ describes a divergence-free current circulating the patch (Fig. II.2(c)) [12]. The set $\tilde{F}^{sol}$ can be complemented by a set $\tilde{F}^{nonsol}$ such that $\text{Span}\left(\tilde{F}\right) = \text{Span}\left(\tilde{F}^{sol}\right) \oplus \text{Span}\left(\tilde{F}^{nonsol}\right)$. The set $\tilde{F}^{nonsol}$ contains "div-conforming non-solenoidal BC" functions (Fig. II.2(d))

$$\tilde{F}^{nonsol} = \left\{ \tilde{f}_j^{nonsol}(r), j = 1, \ldots, \tilde{N}^{nonsol} = N^{sol} \right\} \tag{6.24}$$

Again, the dimensionality of $\mathrm{Span}\left(\tilde{F}^{nonsol}\right)$ equals that of $\mathrm{Span}\left(F^{sol}\right)$ [12].

Next, assume that the matrices $\mathbf{T}_{h,F}$, $\mathbf{T}_{h,\tilde{F}}$, and $\mathbf{G}_{nF;\tilde{F}}$, are not constructed using the sets $F = \mathrm{RWG}$ and $\tilde{F} = \mathrm{BC}$, but instead from $F^{sol} \cup F^{nonsol}$ and $\tilde{F}^{nonsol} \cup \tilde{F}^{sol}$ with functions in the left and right subset labeled 1 through $N_V - 1$ and N_V through N, respectively; note the reverse order of the "*sol*" and "*nonsol*" superscripts for functions in $F = \mathrm{RWG}$ and $\tilde{F} = \mathrm{BC}$. It is clear from (6.4) and (6.20) that the entries $(\mathbf{T}_{h,F})_{i,j}$ and $(\mathbf{T}_{h,\tilde{F}})_{i,j}$ vanish when the source function is solenoidal or the test function is irrotational, which implies

$$\mathbf{T}_{h,F} = \begin{pmatrix} \mathbf{0} & \mathbf{0} \\ \mathbf{0} & \mathbf{T}_{h,F^{nonsol}} \end{pmatrix}, \text{ and } \mathbf{T}_{h,\tilde{F}} = \begin{pmatrix} \mathbf{T}_{h,\tilde{F}^{nonsol}} & \mathbf{0} \\ \mathbf{0} & \mathbf{0} \end{pmatrix} \tag{6.25}$$

The blocks in these matrices have dimensions

$$\begin{pmatrix} (N_V - 1) \times (N_V - 1) & (N_V - 1) \times (N_P - 1) \\ (N_P - 1) \times (N_V - 1) & (N_P - 1) \times (N_P - 1) \end{pmatrix} \tag{6.26}$$

Since an irrotational function can be written as the surface gradient of a scalar function ϕ, and a solenoidal function can be written as the surface curl of a scalar function ψ, the inner product of two such functions can be expressed as

$$\int_S \left(\nabla_S \phi(r)\right)\left(\hat{\boldsymbol{n}}_r \times \nabla_S \psi(r)\right) ds \tag{6.27}$$

which can be transformed by partial integration into

$$\int_S \phi(r) \nabla_S \left(\hat{n}_r \times \nabla_S \psi(r)\right) ds = 0 \tag{6.28}$$

Therefore, the Gram matrix $\mathbf{G}_{nF;\tilde{F}}$ has the form

$$\mathbf{G}_{nF;\tilde{F}} = \begin{pmatrix} \mathbf{B} & \mathbf{0} \\ \mathbf{C} & \mathbf{D} \end{pmatrix} \qquad\qquad (6.29)$$

and so does its inverse

$$\mathbf{G}_{nF;\tilde{F}}^{-1} = \begin{pmatrix} \mathbf{B'} & \mathbf{0} \\ \mathbf{C'} & \mathbf{D'} \end{pmatrix} \qquad\qquad (6.30)$$

From (6.25) and (6.30), it is clear that $\mathbf{T}_{h,\tilde{F}}\,\mathbf{G}_{nF;\tilde{F}}^{-1}\,\mathbf{T}_{h,F} = \mathbf{0}$. The fact that the dimension of the solenoidal

subspace of the RWG basis functions equals that of the non-solenoidal subspace of the BC basis functions

(and vice-versa), is essential for the CMP technique to work, as it ensures the cancellation of $\mathcal{T}_h^2[\boldsymbol{J}]$ upon

discretization.
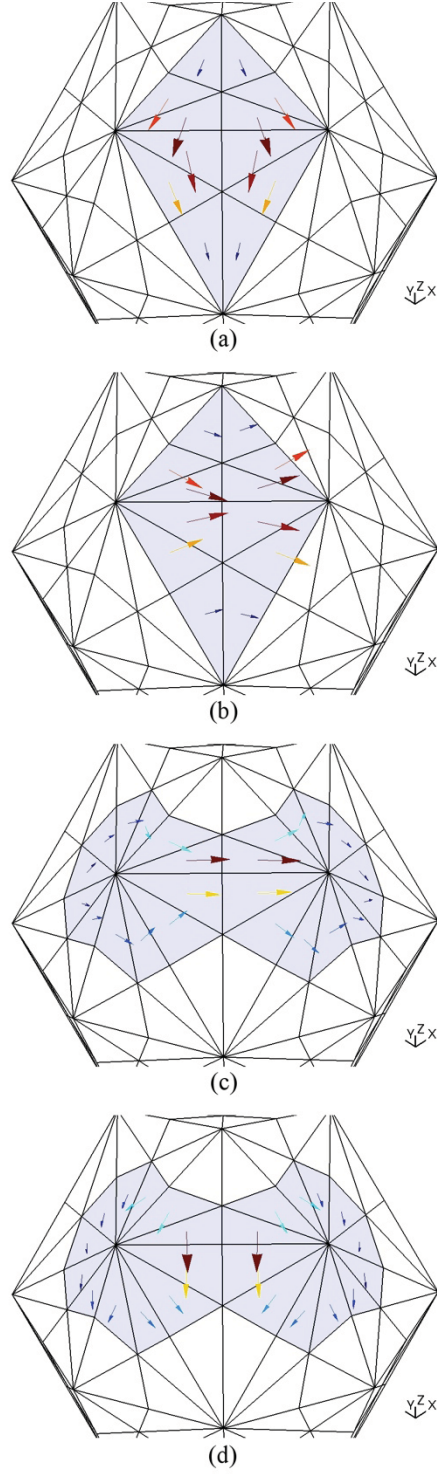
Fig. II.1. RWG and BC functions defined for edge n in S_δ. Functions are plotted on top of $\overline{S}_\delta$. (a) Div-conforming RWG, $\boldsymbol{f}_n$. (b) Curl-conforming RWG, $\hat{\boldsymbol{n}}_r \times \boldsymbol{f}_n$. (c) Div-conforming BC, $\tilde{\boldsymbol{f}}_n$. (d) Curl-conforming BC, $\hat{\boldsymbol{n}}_r \times \tilde{\boldsymbol{f}}_n$.
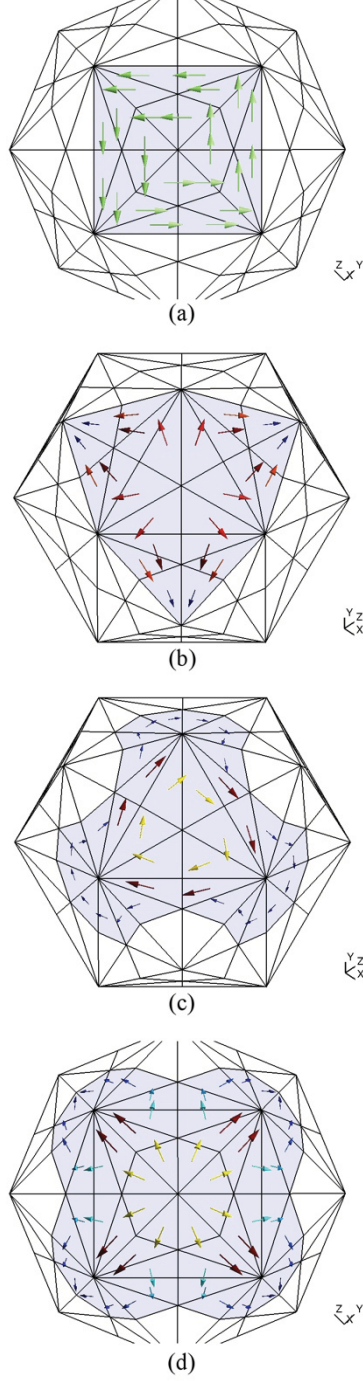
Fig. II.2. Div-conforming RWG and BC solenoidal and non-solenoidal functions defined in S_δ. Note that functions are plotted on top of $\overline{S}_\delta$. (a) Div-conforming RWG solenoidal function $\boldsymbol{f}_n^{sol}$, describing current flowing around vertex n in S_δ. (b) Div-conforming RWG non-solenoidal function $\boldsymbol{f}_n^{nonsol}$, describing current flowing out of patch n in S_δ. (c) Div-conforming BC solenoidal function $\tilde{\boldsymbol{f}}_n^{sol}$, describing current flowing around patch n in S_δ. (d) Div-conforming BC non-solenoidal function $\tilde{\boldsymbol{f}}_n^{nonsol}$, describing current flowing out of vertex n in S_δ.

2.3 High-order Quasi Curl-Conforming Basis Functions

In this section, the construction of the basis functions in $\tilde{F} = \text{DQCC}(p)$ is discussed in detail. Of equal importance is the set of $\text{GWP}(p)$ basis functions, for that reason, a more detailed notation for these functions is established here. For each patch $P \in S_{\Delta s}$ there are $p(p+1)$ GWP functions that interpolate at a node strictly inside P. These functions are grouped in the set

$$F_P = \left\{ \boldsymbol{f}_n \in \text{GWP} : \text{Sup}(\boldsymbol{f}_n) \subseteq P \right\} \tag{6.31}$$

Here $\text{Sup}(\boldsymbol{f}_n)$ denotes the support of $\boldsymbol{f}_n$, i.e. the region in $S_{\Delta s}$ in which $\boldsymbol{f}_n(\boldsymbol{r}) \neq 0$. Similarly, for each edge $E \in S_{\Delta s}$ (shared by patches $P_E^+, P_E^- \in S_{\Delta s}$) there are $p+1$ functions that interpolate at a node along E and they are grouped in the set

$$F_E = \left\{ \boldsymbol{f}_n \in \text{GWP} : \left(\text{Sup}(\boldsymbol{f}_n) \subset P_E^+ \cup P_E^- \right) \left(\boldsymbol{f}_n \notin F_{P_E^+} \wedge \boldsymbol{f}_n \notin F_{P_E^-} \right) \right\} \tag{6.32}$$

Of course,

$$\text{GWP} = \bigcup_{P=1}^{N_P} F_P \cup \bigcup_{E=1}^{N_E} F_E \tag{6.33}$$

That being said, consider the following basis for $\text{Span}(\text{GWP})$:

$$F = \text{RWG} \cup F_{ho}^{sol} \cup F_{ho}^{nonsol} \tag{6.34}$$

where $F_{ho} = F_{ho}^{sol} \cup F_{ho}^{nonsol}$ is the set that complements that of RWG such that $\text{Span}(F) = \text{Span}(\text{GWP}) = \text{Span}(\text{RWG}) \oplus \text{Span}(F_{ho})$. The sets

$$F_{ho}^{sol} = \left\{ \boldsymbol{f}_{ho,j}^{sol}, j = 1, \ldots, N_{ho}^{sol} \right\} \tag{6.35}$$

and

$$F_{ho}^{nonsol} = \left\{ \boldsymbol{f}_{ho,j}^{nonsol}, j = 1, \ldots, N_{ho}^{nonsol} \right\} \tag{6.36}$$

17

span the solenoidal and non-solenoidal subspaces of $\text{Span}\left(F_{ho}\right)$, respectively. The change of basis matrix that transforms coordinates in F into coordinates in GWP is denoted by $\mathbf{H}_F$.

The set $\tilde{F} = \text{DQCC}(p)$ is the union of three subsets, namely

$$\tilde{F} = \text{BC} \cup \tilde{F}_{ho}^{nonsol} \cup \tilde{F}_{ho}^{sol} \tag{6.37}$$

where $\tilde{F}_{ho} = \tilde{F}_{ho}^{nonsol} \cup \tilde{F}_{ho}^{sol}$ is the set that complements BC such that $\text{Span}(\tilde{F}) = \text{Span}(\text{BC}) \oplus \text{Span}(\tilde{F}_{ho})$ [36]. The sets

$$\tilde{F}_{ho}^{nonsol} = \left\{ \tilde{f}_{ho,j}^{nonsol}, j = 1,\ldots,\tilde{N}_{ho}^{nonsol} \right\} \tag{6.38}$$

and

$$\tilde{F}_{ho}^{sol} = \left\{ \tilde{f}_{ho,j}^{sol}, j = 1,\ldots,\tilde{N}_{ho}^{sol} \right\} \tag{6.39}$$

span the non-solenoidal and solenoidal subspaces of $\text{Span}(\tilde{F}_{ho})$ respectively.

Throughout this section, notation introduced previously for spaces and sets applicable to F will be reused and extended for all spaces and functions derived from the barycentrically refined mesh $\bar{S}_{\Delta s}$ by adding bars on top of symbols. That is,

$$\bar{F} = \overline{\text{RWG}} \cup \bar{F}_{ho} = \overline{\text{RWG}} \cup \bar{F}_{ho}^{sol} \cup \bar{F}_{ho}^{nonsol} \tag{6.40}$$

where the sets

$$\bar{F}_{ho}^{sol} = \left\{ \bar{f}_{ho,j}^{sol}, j = 1,\ldots,\bar{N}_{ho}^{sol} \right\} \tag{6.41}$$

and

$$\bar{F}_{ho}^{nonsol} = \left\{ \bar{f}_{ho,j}^{sol}, j = 1,\ldots,\bar{N}_{ho}^{nonsol} \right\} \tag{6.42}$$

span the solenoidal and non-solenoidal subspaces of $\text{Span}\left(\bar{F}_{ho}\right)$, respectively; $\overline{\text{GWP}(p)} = \overline{\text{GWP}}$ and $\overline{\text{RWG}}$ denote $\text{GWP}(p)$ and RWG basis functions defined on $\bar{S}_{\Delta s}$; etc.

To ensure that sets F_{ho} and $\tilde{F}_{ho}$ satisfy conditions C1 through C3, functions in $\tilde{F}_{ho}^{sol}$ and $\tilde{F}_{ho}^{nonsol}$ are constructed with the following properties:

P1. they are linear combinations of div-conforming functions in $\bar{F}_{ho}^{sol}$ and $\bar{F}_{ho}^{nonsol}$ respectively, making div-conforming,

P2. they "resemble" the functions in nF_{ho}^{nonsol} and nF_{ho}^{sol} respectively, rendering the Gram matrix $\mathbf{G}_{nF;\tilde{F}}$ well-conditioned,

P3. their cardinality is matched to that of F_{ho}^{nonsol} and F_{ho}^{sol} respectively, i.e., $\tilde{N}_{ho}^{sol} = N_{ho}^{nonsol}$ and

$\tilde{N}_{ho}^{nonsol} = N_{ho}^{sol}$, thereby guaranteeing the cancellation $\dot{\mathbf{T}}_{h,\tilde{F}}^{(0)} \mathbf{G}_{nF;\tilde{F}}^{-1} \dot{\mathbf{T}}_{h,F}^{(0)} = \mathbf{0}$.

In the remainder of this section the three points listed above are addressed. Section 2.3.1 details the Helmholtz decomposition of the spaces F_{ho} and $\bar{F}_{ho}$, into F_{ho}^{sol} and F_{ho}^{nonsol}, and $\bar{F}_{ho}^{sol}$ and $\bar{F}_{ho}^{nonsol}$, respectively. Using these decompositions the sets $\tilde{F}_{ho}^{sol}$ and $\tilde{F}_{ho}^{nonsol}$ are built in Section 2.3.2.

2.3.1   Helmholtz decomposition of F_{ho} and $\bar{F}_{ho}$

As described in [37], the set F_{ho}^{sol} can be sought as the union of patch- and edge-based solenoidal functions, i.e.

$$F_{ho}^{sol} = \bigcup_{P=1}^{N_P} F_{ho,P}^{sol} \cup \bigcup_{E=1}^{N_E} F_{ho,E}^{sol} \tag{6.43}$$

where $F_{ho,P}^{sol} = \left\{ \boldsymbol{f}_{ho,j_P(k)}^{sol}, k=1,\ldots,N_{ho,P}^{sol} \right\}$, with $N_{ho,P}^{sol} = p(p-1)/2$, is the set of solenoidal functions with support inside patch $P \in S_{\Delta s}$ (Fig.II.3(a)), and $F_{ho,E}^{sol} = \left\{ \boldsymbol{f}_{ho,j_E(k)}^{sol}, k=N_{ho,E}^{sol} \right\}$, with $N_{ho,E}^{sol} = p$, is the set of solenoidal functions with support inside $P_E^+ \cup P_E^-$, the two patches that share edge $E \in S_{\Delta s}$ (Fig.II.3(c)). Here, $j_P(k)$ and $j_E(k)$ are integer mappings that transform the function's local index k in $F_{ho,P}^{sol}$ or $F_{ho,E}^{sol}$ into its global index in F_{ho}^{sol}. Similar integer mappings from local-to-global indexing are used throughout the remainder of this chapter.

Likewise, the set F_{ho}^{nonsol} can be sought as the union of patch-based non-solenoidal functions,

$$F_{ho}^{nonsol} = \bigcup_{P=1}^{N_P} F_{ho,P}^{nonsol} \tag{6.44}$$

where $F_{ho,P}^{nonsol} = \left\{ \boldsymbol{f}_{ho,j_P(k)}^{nonsol}, k=1,\ldots,N_{ho,P}^{nonsol} \right\}$, with $N_{ho,P}^{nonsol} = [(p+1)(p+2)-2]/2$, is the set of non-solenoidal functions with support inside patch $P \in S_{\Delta s}$ (Fig.II.3(b)).

Patch solenoidal and non-solenoidal functions in P can be obtained by performing a singular value decomposition (SVD) to the matrix that maps all patch-based functions $\boldsymbol{f}_{j_P(i)} \in F_P$, $i=1,\ldots,p(p+1)$, onto their charges (divergence) at points in P. Edge solenoidal functions can be obtained by performing a SVD to the matrix that maps all edge-based functions $\boldsymbol{f}_{j_E(i)} \in F_E$, $i=1,\ldots,p+1$, and all $2N_{ho,P}^{nonsol}$ patch-based non-solenoidal functions in $F_{ho,P_E^+}^{nonsol} \cup F_{ho,P_E^-}^{nonsol}$ onto their charges at points in $P_E^+ \cup P_E^-$. As described in [36], patch- and edge-based functions can be orthogonalized. A *partial local orthogonalization* can be performed as follows:

1. For each edge in S_δ, orthogonalize the solenoidal functions associated with it.

2. For each patch in S_δ, separately orthogonalize the solenoidal and non-solenoidal functions.

After this partial orthogonalization has been performed, all functions in F_{ho}^{nonsol} are orthogonal to one another; but not necessarily orthogonal to any or all functions in F_{ho}^{sol}. Furthermore, among the functions in F_{ho}^{sol}, only those that are patch-based are orthogonal to one another, but not necessarily orthogonal to any or all of the edge solenoidal functions.

A *full local orthogonalization* can also be performed. The difference with respect to the previous one being that now patch-based solenoidal and non-solenoidal functions are orthogonalized altogether. Hence all functions in F_{ho}^{nonsol} are orthogonal to one another, and also orthogonal to all patch based functions, but not necessarily to any or all edge based functions in F_{ho}^{sol}.

To summarize, the set F_{ho}^{sol} contains $N_{ho,P}^{sol}N_P$ patch-based functions and $N_{ho,E}^{sol}N_E$ edge-based functions. Likewise, F_{ho}^{nonsol} contains $N_{ho,P}^{nonsol}N_P$ patch-based functions. The cardinalities of F_{ho}^{sol} and F_{ho}^{nonsol} are therefore

$$N_{ho}^{sol} = N_{ho,P}^{sol}N_P + N_{ho,E}^{sol}N_E \qquad (6.45)$$

and

$$N_{ho}^{nonsol} = N_{ho,P}^{nonsol}N_P \qquad (6.46)$$

Of course $N_{ho}^{sol} + N_{ho}^{nonsol} = pN_E + p(p+1)N_P = N_S - N_E$.

For future use, we define the matrix $\mathbf{L}_P$ (of size $p(p+1) \times N_{ho,P}^{sol}$) that expresses functions in $F_{ho,P}^{sol}$ as linear combinations of functions in F_P, i.e. its k-th column contains the coefficients of $f_{ho,j_P(k)}^{sol}$ in terms of the functions $f_{j_P(i)} \in F_P$, $i=1,\ldots,p(p+1)$. Similarly, the matrix $\mathbf{S}_P$ (of size $p(p+1) \times N_{ho,P}^{nonsol}$) expresses functions in $F_{ho,P}^{nonsol}$ as linear combinations of functions in F_P. The matrix $\mathbf{L}_E$ (of size $(2p+1)(p+1) \times N_{ho,E}^{sol}$) expresses functions in $F_{ho,E}^{sol}$ as linear combinations of functions in $F_E \cup F_{P_E^+} \cup F_{P_E^-}$.

Next, consider the barycentrically refined mesh $\bar{S}_{\Delta s}$. For each patch $\bar{P} \in \bar{S}_{\Delta s}$ and for each edge $\bar{E} \in \bar{S}_{\Delta s}$ sets $\bar{F}_{ho,\bar{P}}^{sol}$, $\bar{F}_{ho,\bar{P}}^{nonsol}$, and $\bar{F}_{ho,\bar{E}}^{sol}$ can be obtained in the same way as described above for $S_{\Delta s}$. The union of all solenoidal sets equals $\bar{F}_{ho}^{sol}$, with cardinality

$$\bar{N}_{ho}^{sol} = 3p(p+1)N_P + 2pN_E \qquad (6.47)$$

Similarly, the union of all non-solenoidal sets equals $\bar{F}_{ho}^{nonsol}$, with cardinality

$$\bar{N}_{ho}^{nonsol} = 3\big[(p+2)(p+1)-2\big]N_P \qquad (6.48)$$

Sets $\bar{F}_{ho,\bar{P}}^{sol}$, $\bar{F}_{ho,\bar{P}}^{nonsol}$, and $\bar{F}_{ho,\bar{E}}^{sol}$, for all $\bar{P},\bar{E} \in \bar{S}_{\Delta s}$, can be conveniently grouped according to elements in $S_{\Delta s}$. As depicted in Fig.II.4(a), for each patch $P \in S_{\Delta s}$ there are six barycentric patches $\bar{P}_j(P) \in \bar{S}_{\Delta s}$,

21

$j = 1,\ldots,6$, twelve barycentric edges $\overline{E}_j(P) \in \overline{S}_{\Delta s}$, $j = 1,\ldots,12$, and seven barycentric vertices $\overline{V}_j(P) \in \overline{S}_{\Delta s}$, $j = 0,\ldots,6$. Note that only edges one through six, and vertex zero, lay *inside* P; all other edges and vertices lie *in the boundary* of P. Also, for each edge $E \in S_{\Delta s}$ there are two barycentric edges $\overline{E}_j(E) \in \overline{S}_{\Delta s}$, $j = 1,2$.

All barycentric non-solenoidal functions associated to patch $P \in S_{\Delta s}$ are grouped in the set

$$\overline{F}_{ho,P}^{nonsol} = \bigcup_{j=1}^{6} \overline{F}_{ho,\overline{P}_j(P)}^{nonsol}$$
$$= \left\{ \overline{\boldsymbol{f}}_{ho,\overline{J}_P(k)}^{nonsol}, k = 1,\ldots,\overline{N}_{ho,P}^{nonsol} \right\} \tag{6.49}$$

with

$$\overline{N}_{ho,P}^{nonsol} = 3[(p+1)(p+2)-2] \tag{6.50}$$

Every function in $\overline{F}_{ho,P}^{nonsol}$ is a linear combination of functions in the set

$$\overline{F}_P = \bigcup_{j=1}^{6} \overline{F}_{\overline{P}_j(P)} \cup \overline{F}_{\overline{E}_j(P)} \tag{6.51}$$

of cardinality $\#\overline{F}_P = 6(p+1)^2$.

Similarly, barycentric non-solenoidal functions associated to edge $E \in S_{\Delta s}$ are grouped in the set

$$\overline{F}_{ho,E}^{nonsol} = \overline{F}_{ho,P_E^+}^{nonsol} \cup \overline{F}_{ho,P_E^-}^{nonsol}$$
$$= \left\{ \overline{\boldsymbol{f}}_{ho,\overline{J}_E(k)}^{nonsol}, k = 1,\ldots,\overline{N}_{ho,E}^{nonsol} \right\} \tag{6.52}$$

with

$$\overline{N}_{ho,E}^{nonsol} = 6[(p+1)(p+2)-2] \tag{6.53}$$

Of course, functions in $\overline{F}_{ho,E}^{nonsol}$ are linear combinations of functions in $\overline{F}_{P_E^+} \cup \overline{F}_{P_E^-}$.

22

The grouping of barycentric solenoidal functions associated to patch $P \in S_{\Delta s}$ requires a few prior definitions. Consider the barycentric vertices $\bar{V}_j(P)$, $j = 1, \ldots, 6$, in the boundary of P. For each vertex $\bar{V}_j(P)$ there is a set $\bar{\Pi}(\bar{V}_j(P))$ of all barycentric patches, and a set $\bar{\Xi}(\bar{V}_j(P))$ of all barycentric edges, that have $\bar{V}_j(P)$ as a common vertex. The union of these sets for al vertices in P defines the *barycentric neighborhood* of P:

$$\bar{\Pi}(P) = \bigcup_{j=1}^{6} \bar{\Pi}(\bar{V}_j(P)) \tag{6.54}$$

and

$$\bar{\Xi}(P) = \bigcup_{j=1}^{6} \bar{\Xi}(\bar{V}_j(P)) \tag{6.55}$$

The cardinalities of these sets are denoted by $\#\bar{\Pi}(P)$ and $\#\bar{\Xi}(P)$ respectively, and they depend on how many patches share the vertices $\bar{V}_1(P)$, $\bar{V}_2(P)$, and $\bar{V}_3(P)$. In the example mesh of Fig.II.4(b), $\bar{V}_1(P)$ and $\bar{V}_2(P)$ are shared by 12 barycentric patches, $\bar{V}_3(P)$ is shared by 8. The set that groups all barycentric solenoidal functions with support in the barycentric *neighborhood* of P is defined as

$$\bar{F}_{ho,NP}^{sol} = \bigcup_{\bar{P} \in \bar{\Pi}(P)} \bar{F}_{ho,\bar{P}}^{sol} \cup \bigcup_{\bar{E} \in \bar{\Xi}(P)} \bar{F}_{ho,\bar{E}}^{sol}$$
$$= \left\{ \bar{f}_{ho,\bar{j}_{NP}(k)}^{sol}, k = 1, \ldots, \bar{N}_{ho,NP}^{sol} \right\} \tag{6.56}$$

with

$$\bar{N}_{ho,NP}^{sol} = \frac{p(p-1)}{2} \#\bar{\Pi}(P) + p \#\bar{\Xi}(P) \tag{6.57}$$

Every function in $\bar{F}_{ho,NP}^{sol}$ is a linear combination of functions in the set

$$\bar{F}_{NP} = \bigcup_{\bar{P} \in \bar{\Pi}(P)} \bar{F}_{\bar{P}} \cup \bigcup_{\bar{E} \in \bar{\Xi}(P)} \bar{F}_{\bar{E}} \tag{6.58}$$

of cardinality $\#\bar{F}_{NP} = p(p+1)\#\bar{\Pi}(P) + (p+1)\#\bar{\Xi}(P)$.

We now define the matrix $\overline{\mathbf{S}}_P$ (of size $\# \overline{F}_P \times \overline{N}_{ho,P}^{nonsol}$) that expresses all functions in $\overline{F}_{ho,P}^{nonsol}$ as linear combinations of functions in $\overline{F}_P$. Similarly, the matrix $\overline{\mathbf{S}}_E$ (of size $2 \# \overline{F}_P \times \overline{N}_{ho,E}^{nonsol}$) expresses functions in $\overline{F}_{ho,E}^{nonsol}$ as linear combinations of functions in $\overline{F}_{P_E^+} \cup \overline{F}_{P_E^-}$. The matrix $\overline{\mathbf{L}}_P$ (of size $\# \overline{F}_{NP} \times \overline{N}_{ho,NP}^{sol}$) expresses functions in $\overline{F}_{ho,NP}^{sol}$ as linear combinations of functions in $\overline{F}_{NP}$.
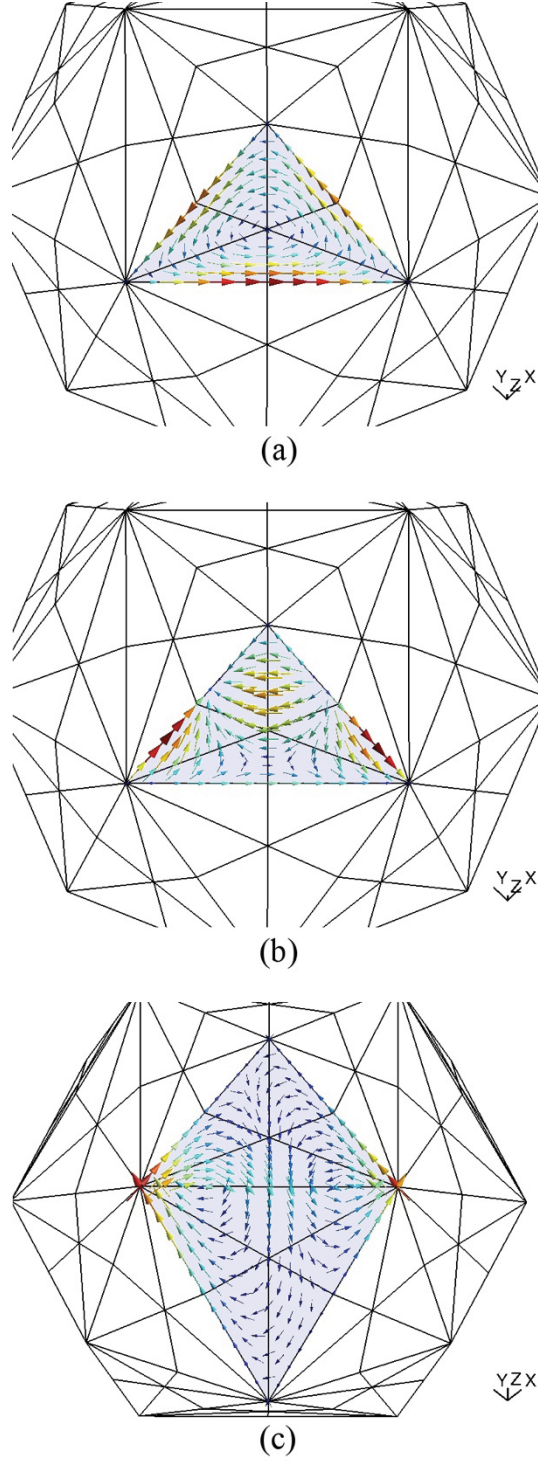
Fig.II.3. Div-conforming F_{ho} solenoidal and non-solenoidal functions defined in $S_{\Delta s}$. Note that functions are plotted on top of $\overline{S}_{\Delta s}$. (a) Div-conforming F_{ho} *patch solenoidal* function $\boldsymbol{f}_{ho,j}^{sol}$, its support (shaded area) is limited to a patch in $S_{\Delta s}$. (b) Div-conforming F_{ho} *patch non-solenoidal* function $\boldsymbol{f}_{ho,j}^{nonsol}$, its support (shaded area) is limited to a patch in $S_{\Delta s}$. (c) Div-conforming F_{ho} *edge solenoidal* function $\boldsymbol{f}_{ho,j}^{sol}$, its support (shaded area) include the two patches sharing the edge in $S_{\Delta s}$.
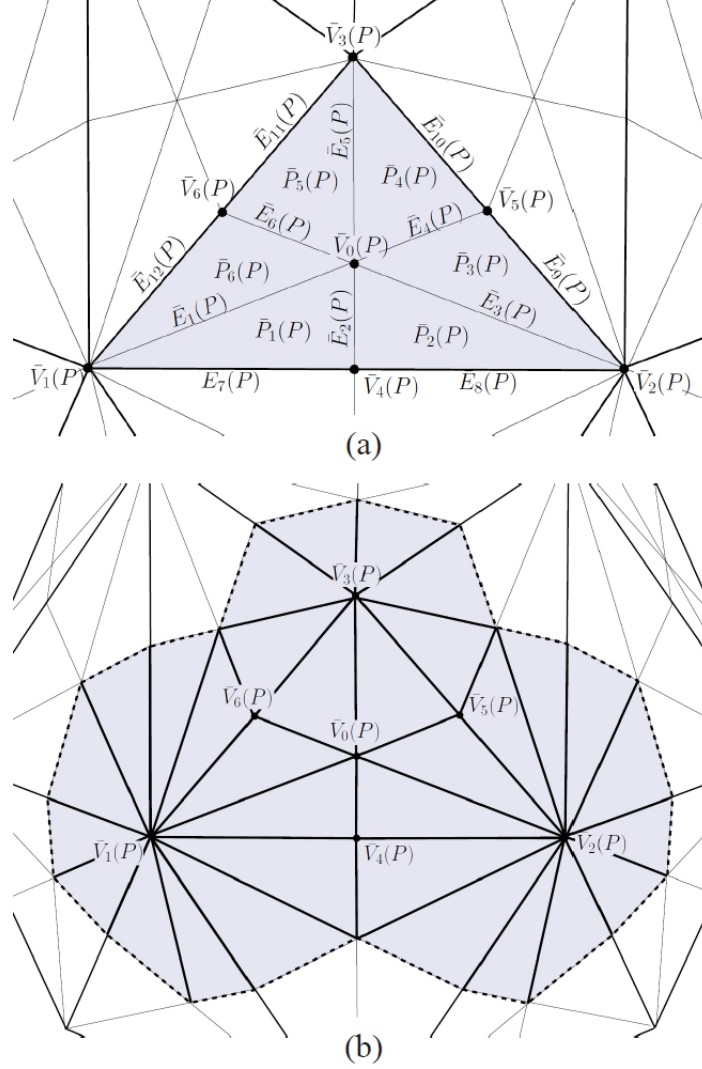
Fig.II.4. (a) Barycentric patches $\bar{P}_j(P), j = 1,\ldots,6$, edges $\bar{E}_j(P), j = 1,\ldots,12$, and vertices $\bar{V}_j(P), j = 0,\ldots,6$ in patch $P \in S_{\Delta s}$. (b) Barycentric neighborhood of patch $P \in S_{\Delta s}$. Every thick line is rooted on a barycentric vertex $\bar{V}_j(P)$ and represents an edge in $\bar{\Xi}(P)$. Patches in $\bar{\bar{\Pi}}(P)$ are shaded.

2.3.2 Helmholtz decomposition of $\tilde{F}_{ho}$

In this section we make use of the sets defined in (6.49), (6.52), and (6.56) to build functions in $\tilde{F}_{ho}^{sol}$ and $\tilde{F}_{ho}^{nonsol}$ that have the properties P1 through P3, described above.

26

For each patch-based solenoidal function $\boldsymbol{f}_{ho,j_P(i)}^{sol} \in F_{ho,P}^{sol}$ there is a corresponding div-conforming non-solenoidal function $\tilde{\boldsymbol{f}}_{ho,j_P(i)}^{nonsol}$ that "best approximates" the curl-conforming counterpart of the former, i.e. the function $\hat{\boldsymbol{n}}_r \times \boldsymbol{f}_{ho,j_P(i)}^{sol} \in nF_{ho,P}^{sol}$, with $i = 1,\ldots,N_{ho,P}^{sol}$. Here the term "best approximates" should be understood as $\tilde{\boldsymbol{f}}_{ho,j_P(i)}^{nonsol}$ being the orthogonal projection of $\hat{\boldsymbol{n}}_r \times \boldsymbol{f}_{ho,j_P(i)}^{sol}$ onto the space spanned by all functions in $\bar{F}_{ho,P}^{nonsol}$ [25], i.e.

$$\tilde{\boldsymbol{f}}_{ho,j_P(i)}^{nonsol}(\boldsymbol{r}) = \sum_{k=1}^{\bar{N}_{ho,P}^{nonsol}} p_{k,j_P(i)}^{nonsol} \bar{\boldsymbol{f}}_{ho,\bar{j}_P(k)}^{nonsol}(\boldsymbol{r}), \qquad \forall\, i = 1,\ldots,N_{ho,P}^{sol} \tag{6.59}$$

where the coefficient $p_{k,j_P(i)}^{nonsol}$ is the (k,i)-th entry of the matrix $\mathbf{P}_{ho,P}^{nonsol}$, obtained by

$$\mathbf{P}_{ho,P}^{nonsol} = \mathbf{G}_{\bar{F}_{ho,P}^{nonsol};\bar{F}_{ho,P}^{nonsol}}^{-1} \mathbf{G}_{\bar{F}_{ho,P}^{nonsol};nF_{ho,P}^{sol}} \tag{6.60}$$

The Gram matrices in (6.60) are defined for patch $P \in S_{\Delta s}$ and their entries are given by

$$(\mathbf{G}_{\bar{F}_{ho,P}^{nonsol};\bar{F}_{ho,P}^{nonsol}})_{m,n} = \left\langle \bar{\boldsymbol{f}}_{ho,\bar{j}_P(m)}^{nonsol}, \bar{\boldsymbol{f}}_{ho,\bar{j}_P(n)}^{nonsol} \right\rangle \tag{6.61}$$

with $m,n = 1,\ldots,\bar{N}_{ho,P}^{nonsol}$, and

$$(\mathbf{G}_{\bar{F}_{ho,P}^{nonsol};nF_{ho,P}^{sol}})_{m,n} = \left\langle \bar{\boldsymbol{f}}_{ho,\bar{j}_P(m)}^{nonsol}, \hat{\boldsymbol{n}}_r \times \boldsymbol{f}_{ho,j_P(n)}^{sol} \right\rangle \tag{6.62}$$

with $m = 1,\ldots,\bar{N}_{ho,P}^{nonsol}$ and $n = 1,\ldots,N_{ho,P}^{sol}$. For example, the function depicted in Fig. II.5(b) is the "best" non-solenoidal approximation of the function depicted in Fig. II.5(a), which is the curl-conforming counterpart of that depicted in Fig.II.3(a). Note that if the set $\bar{F}_{ho,P}^{nonsol}$ is orthonormal, then $\mathbf{G}_{\bar{F}_{ho,P}^{nonsol};\bar{F}_{ho,P}^{nonsol}}$ equals the identity matrix.

Similarly, for each edge-based solenoidal function $\boldsymbol{f}_{ho,j_E(i)}^{sol} \in F_{ho,E}^{sol}$ there is a corresponding div-conforming non-solenoidal function $\tilde{\boldsymbol{f}}_{ho,j_E(i)}^{nonsol}$ that is the orthogonal projection of $\hat{\boldsymbol{n}}_r \times \boldsymbol{f}_{ho,j_E(i)}^{sol}$ onto the space spanned by all functions in $\bar{F}_{ho,E}^{nonsol}$ [36], i.e.

$$\tilde{\boldsymbol{f}}_{ho,j_E(i)}^{nonsol}(\boldsymbol{r}) = \sum_{k=1}^{\bar{N}_{ho,E}^{nonsol}} p_{k,j_E(i)}^{nonsol} \bar{\boldsymbol{f}}_{ho,\bar{j}_E(k)}^{nonsol}(\boldsymbol{r}), \qquad \forall\, i = 1,\ldots, N_{ho,E}^{sol} \tag{6.63}$$

where the coefficient $p_{k,j_E(i)}^{nonsol}$ is the (k,i)-th entry of the matrix $\mathbf{P}_{ho,E}^{nonsol}$, obtained by

$$\mathbf{P}_{ho,E}^{nonsol} = \mathbf{G}_{\bar{F}_{ho,E}^{nonsol};\bar{F}_{ho,E}^{nonsol}}^{-1} \mathbf{G}_{\bar{F}_{ho,E}^{nonsol};nF_{ho,E}^{sol}} \tag{6.64}$$

The Gram matrices in (6.64) are defined for patches P_E^+ and P_E^-. Matrix $\mathbf{G}_{\bar{F}_{ho,E}^{nonsol};\bar{F}_{ho,E}^{nonsol}}$ is the block-diagonal

matrix

$$\mathbf{G}_{\bar{F}_{ho,E}^{nonsol};\bar{F}_{ho,E}^{nonsol}} = \begin{bmatrix} \mathbf{G}_{\bar{F}_{ho,P_E^+}^{nonsol};\bar{F}_{ho,P_E^+}^{nonsol}} & \mathbf{0} \\ \mathbf{0} & \mathbf{G}_{\bar{F}_{ho,P_E^-}^{nonsol};\bar{F}_{ho,P_E^-}^{nonsol}} \end{bmatrix} \tag{6.65}$$

and the entries of $\mathbf{G}_{\bar{F}_{ho,E}^{nonsol};nF_{ho,E}^{sol}}$ are given by

$$(\mathbf{G}_{\bar{F}_{ho,E}^{nonsol};nF_{ho,E}^{sol}})_{m,n} = \left\langle \bar{\boldsymbol{f}}_{ho,\bar{j}_E(m)}^{nonsol}, \hat{\boldsymbol{n}}_r \times \boldsymbol{f}_{ho,j_E(n)}^{sol} \right\rangle \tag{6.66}$$

with $m = 1,\ldots,\bar{N}_{ho,E}^{nonsol}$ and $n = 1,\ldots,N_{ho,E}^{sol}$. For example, the function depicted in Fig. II.5(d) is the "best"

non-solenoidal approximation of the function depicted in Fig. II.5(c), which is the curl-conforming

counterpart of that depicted in Fig.II.3(c). Again, if the set $\bar{F}_{ho,E}^{nonsol}$ is orthonormal, then $\mathbf{G}_{\bar{F}_{ho,E}^{nonsol};\bar{F}_{ho,E}^{nonsol}}$ equals

the identity matrix.

Finally, for each patch-based non-solenoidal function $\boldsymbol{f}_{ho,j_P(i)}^{nonsol} \in F_{ho,P}^{nonsol}$ there is a corresponding div-

conforming solenoidal function $\tilde{\boldsymbol{f}}_{ho,j_P(i)}^{sol}$ that is the orthogonal projection of $\hat{\boldsymbol{n}}_r \times \boldsymbol{f}_{ho,j_P(i)}^{nonsol} \in nF_{ho,P}^{nonsol}$ onto the

space spanned by all functions in $\bar{F}_{ho,NP}^{sol}$ [36][38], i.e.

$$\tilde{\boldsymbol{f}}_{ho,j_P(i)}^{sol}(\boldsymbol{r}) = \sum_{k=1}^{\bar{N}_{ho,NP}^{sol}} p_{k,j_P(i)}^{sol} \bar{\boldsymbol{f}}_{ho,\bar{j}_{NP}(k)}^{sol}(\boldsymbol{r}), \qquad \forall\, i = 1,\ldots, N_{ho,P}^{nonsol} \tag{6.67}$$

where the coefficient $p_{k,j_P(i)}^{sol}$ is the (k,i)-th entry of the matrix $\mathbf{P}_{ho,P}^{sol}$, obtained by

$$\mathbf{P}_{ho,P}^{sol} = \mathbf{G}_{\bar{F}_{ho,NP}^{sol};\bar{F}_{ho,NP}^{sol}}^{-1} \; \mathbf{G}_{\bar{F}_{ho,NP}^{sol};nF_{ho,P}^{nonsol}} \tag{6.68}$$

The Gram matrices in (6.68) are defined for patches in $\overline{\Pi}(P)$ and their entries are given by

$$(\mathbf{G}_{\bar{F}_{ho,NP}^{sol};\bar{F}_{ho,NP}^{sol}})_{m,n} = \left\langle \bar{\boldsymbol{f}}_{ho,\bar{\jmath}_{NP}(m)}^{sol}, \bar{\boldsymbol{f}}_{ho,\bar{\jmath}_{NP}(n)}^{sol} \right\rangle \tag{6.69}$$

with $m,n = 1,\ldots,\bar{N}_{NP}^{sol}$, and

$$(\mathbf{G}_{\bar{F}_{ho,NP}^{sol};nF_{ho,P}^{nonsol}})_{m,n} = \left\langle \bar{\boldsymbol{f}}_{ho,\bar{\jmath}_{NP}(m)}^{sol}, \hat{\boldsymbol{n}}_r \times \boldsymbol{f}_{ho,j_P(n)}^{nonsol} \right\rangle \tag{6.70}$$

with $m = 1,\ldots,\bar{N}_{P}^{sol}$ and $n = 1,\ldots,N_{ho,P}^{nonsol}$. For example, the function depicted in Fig. II.5(f) is the "best" solenoidal approximation of the function depicted in Fig. II.5(e), which is the curl-conforming counterpart of that depicted in Fig.II.3(b).

To summarize, the set $\tilde{F}_{ho}^{sol}$ is composed of $N_{ho,P}^{nonsol}$ functions $\tilde{\boldsymbol{f}}_{ho,j_P(i)}^{sol}$ per patch $P \in S_{\Delta s}$, which gives a total of

$$\tilde{N}_{ho}^{sol} = N_{ho,P}^{nonsol} N_P = N_{ho}^{nonsol} \tag{6.71}$$

Similarly, the set $\tilde{F}_{ho}^{nonsol}$ is composed of $N_{ho,P}^{sol}$ functions $\tilde{\boldsymbol{f}}_{ho,j_P(i)}^{nonsol}$ per patch $P \in S_{\Delta s}$ and $N_{ho,E}^{sol}$ functions $\tilde{\boldsymbol{f}}_{ho,j_E(i)}^{nonsol}$ per edge $E \in S_{\Delta s}$;

$$\tilde{N}_{ho}^{nonsol} = N_{ho,P}^{sol} N_P + N_{ho,E}^{sol} N_E = N_{ho}^{sol} \tag{6.72}$$
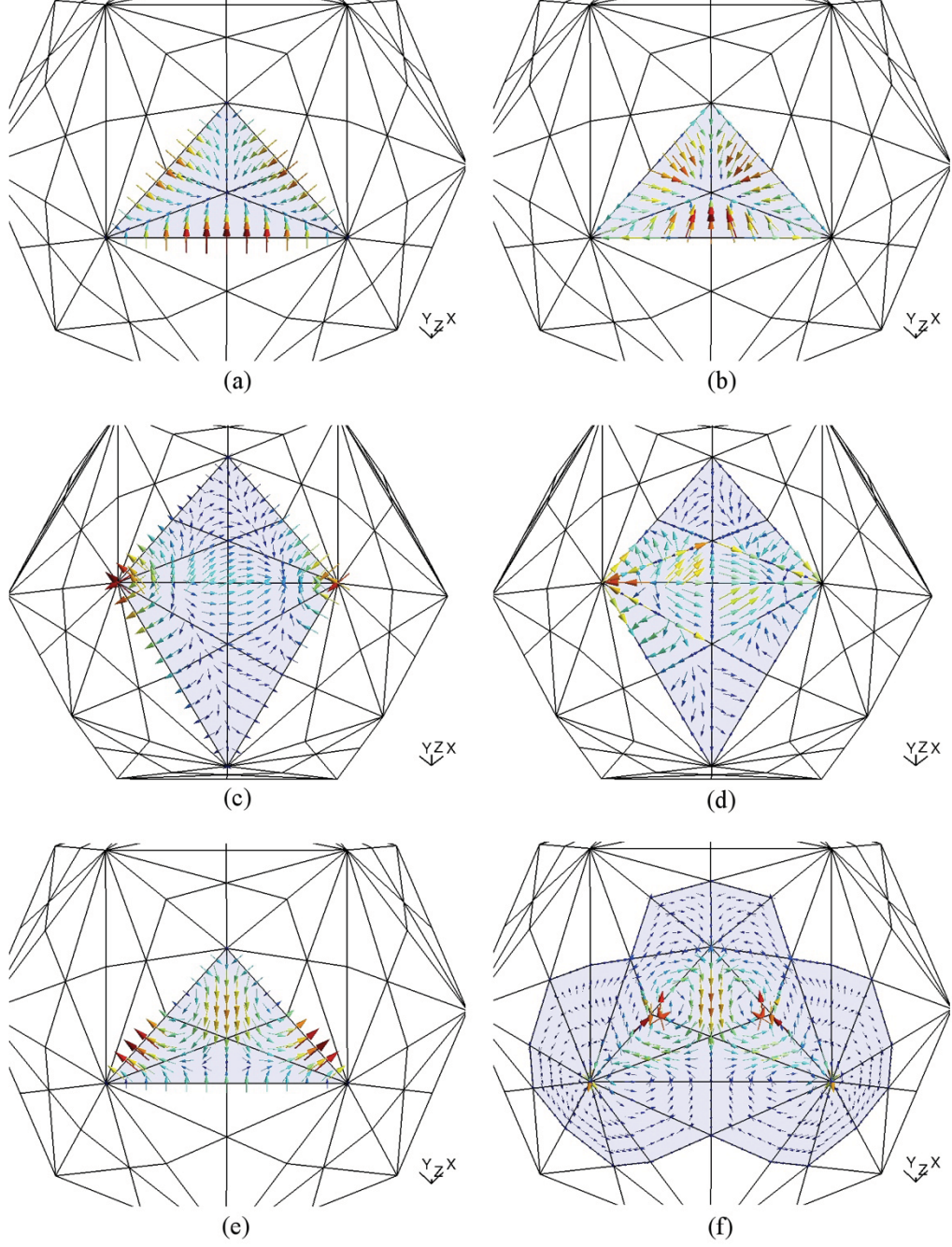
Fig. II.5. Div- and quasi curl-conforming functions in $\tilde{F}_{ho}$, approximating those in nF_{ho}. Note that functions are plotted on top of $\overline{S}_{\Delta s}$. (a) $\hat{\boldsymbol{n}}_r \times \boldsymbol{f}_{ho,j}^{sol}$, i.e. curl-conforming counterpart of the *patch solenoidal* function $\boldsymbol{f}_{ho,i}^{sol}$ depicted in Fig.II.3(a). (b) Div-conforming *patch non-solenoidal* function $\tilde{\boldsymbol{f}}_{ho,j}^{nonsol}$ approximating $\hat{\boldsymbol{n}}_r \times \boldsymbol{f}_{ho,j}^{sol}$. (c) $\hat{\boldsymbol{n}}_r \times \boldsymbol{f}_{ho,j}^{sol}$, i.e. curl-conforming counterpart of the *edge solenoidal* function $\boldsymbol{f}_{ho,i}^{sol}$ depicted in Fig.II.3(c). (d) Div-conforming *edge non-solenoidal* function $\tilde{\boldsymbol{f}}_{ho,j}^{nonsol}$ approximating $\hat{\boldsymbol{n}}_r \times \boldsymbol{f}_{ho,j}^{sol}$. (e) $\hat{\boldsymbol{n}}_r \times \boldsymbol{f}_{ho,j}^{nonsol}$, i.e. curl-conforming counterpart of the *patch non-solenoidal* function $\boldsymbol{f}_{ho,j}^{nonsol}$ depicted in Fig.II.3(b). (f) Div-conforming *patch solenoidal* function $\tilde{\boldsymbol{f}}_{ho,j}^{sol}$ approximating $\hat{\boldsymbol{n}}_r \times \boldsymbol{f}_{ho,j}^{nonsol}$.

30

2.4 Implementation of the High-Order CMP

This section provides details on the construction of the basis functions in $\tilde{F}$ and their use in a high-order implementation of the CMP-EFIE. First, explicit expressions for the matrices $\mathbf{P}_{ho}^{sol}$ and $\mathbf{P}_{ho}^{nonsol}$ are given in terms of Gram matrices and basis transformations. With these matrices, expressions for $\mathbf{T}_{\tilde{F}}$, $\mathbf{G}_{nF;\tilde{F}}$, and $\mathbf{T}_{F}$ are given. Finally, issues relating to computational cost are discussed.

The evaluation of $\mathbf{P}_{ho,P}^{nonsol}$ in (6.60) requires the computation of two Gram matrices: $\mathbf{G}_{\bar{F}_{ho,P}^{nonsol};\bar{F}_{ho,P}^{nonsol}}$ and $\mathbf{G}_{\bar{F}_{ho,P}^{nonsol};nF_{ho,P}^{sol}}$. Since each function in $\bar{F}_{ho,P}^{nonsol}$ is a linear combination of functions in $\bar{F}_{P}$, the Gram matrices $\mathbf{G}_{\bar{F}_{ho,P}^{nonsol};\bar{F}_{ho,P}^{nonsol}}$ in (6.61), and $\mathbf{G}_{\bar{F}_{ho,P}^{nonsol};nF_{ho,P}^{sol}}$ in (6.62) can be obtained respectively as

$$\mathbf{G}_{\bar{F}_{ho,P}^{nonsol};\bar{F}_{ho,P}^{nonsol}} = \bar{\mathbf{S}}_{P}^{\mathrm{T}} \mathbf{G}_{\bar{F}_{P};\bar{F}_{P}} \bar{\mathbf{S}}_{P} \tag{6.73}$$

and

$$\mathbf{G}_{\bar{F}_{ho,P}^{nonsol};nF_{ho,P}^{sol}} = \bar{\mathbf{S}}_{P}^{\mathrm{T}} \mathbf{G}_{\bar{F}_{P};n\bar{F}_{P}} \mathbf{R}_{P} \mathbf{L}_{P} \tag{6.74}$$

The matrix $\mathbf{R}_{P}$ (of size $12(p+1)^{2} \times p(p+1)$) expresses functions in F_{P} as linear combinations of functions in $\bar{F}_{P}$. Substitution of the above expressions into eqn. (6.60) yields

$$\mathbf{P}_{ho,P}^{nonsol} = \left(\bar{\mathbf{S}}_{P}^{\mathrm{T}} \mathbf{G}_{\bar{F}_{P};\bar{F}_{P}} \bar{\mathbf{S}}_{P}\right)^{-1} \left(\bar{\mathbf{S}}_{P}^{\mathrm{T}} \mathbf{G}_{\bar{F}_{P};n\bar{F}_{P}} \mathbf{R}_{P} \mathbf{L}_{P}\right). \tag{6.75}$$

Similarly, the evaluation of $\mathbf{P}_{ho,E}^{nonsol}$ can be performed using Gram matrices encompassing the appropriate $\overline{\mathrm{GWP}}$ basis functions, viz.

$$\mathbf{P}_{ho,E}^{nonsol} = \left(\bar{\mathbf{S}}_{E}^{\mathrm{T}} \mathbf{G}_{A;A} \bar{\mathbf{S}}_{E}\right)^{-1} \left(\bar{\mathbf{S}}_{E}^{\mathrm{T}} \mathbf{G}_{A;nB} \mathbf{R}_{E} \mathbf{L}_{E}\right), \tag{6.76}$$

with sets $A = \bar{F}_{P_{E}^{+}} \cup \bar{F}_{P_{E}^{-}}$ and $B = A \cup \bar{F}_{\bar{E}_{1}(E)} \cup \bar{F}_{\bar{E}_{2}(E)}$. The matrix $\mathbf{R}_{E}$ (of size $12(p+1)^{2} + 2(p+1) \times 2p(p+1) + (p+1)$) expresses functions in $F_{P_{E}^{+}} \cup F_{P_{E}^{-}} \cup F_{E}$ as linear combinations of

functions in B. Once again, the inverse matrices in (6.75) and (6.76) need not to be computed if $\bar{F}_{ho,\bar{P}}^{nonsol}$ is an orthonormal set $\forall \bar{P} \in \bar{S}_{\Delta s}$.

The evaluation of $\mathbf{P}_{ho,P}^{sol}$ in (6.68) requires the computation of two Gram matrices:

$$\mathbf{G}_{\bar{F}_{ho,NP}^{sol};\bar{F}_{ho,NP}^{sol}} = \bar{\mathbf{L}}_P^{\mathrm{T}} \mathbf{G}_{\bar{F}_{NP};\bar{F}_{NP}} \bar{\mathbf{L}}_P \tag{6.77}$$

and

$$\mathbf{G}_{\bar{F}_{ho,NP}^{sol};nF_{ho,P}^{nonsol}} = \bar{\mathbf{L}}_P^{\mathrm{T}} \mathbf{G}_{\bar{F}_{NP};n\bar{F}_P} \mathbf{R}_P \mathbf{S}_P. \tag{6.78}$$

Substitution of the above expression into (6.68) yields

$$\mathbf{P}_{ho,P}^{sol} = \left(\bar{\mathbf{L}}_P^{\mathrm{T}} \mathbf{G}_{\bar{F}_{NP};\bar{F}_{NP}} \bar{\mathbf{L}}_P \right)^{-1} \left(\bar{\mathbf{L}}_P^{\mathrm{T}} \mathbf{G}_{\bar{F}_{NP};n\bar{F}_P} \mathbf{R}_P \mathbf{S}_P \right). \tag{6.79}$$

In contrast to the basis functions presented in [36], the ones presented here are essentially patch-based. This means that the size of all matrices in (6.75), (6.76), and (6.79) scale only with p (and not with the size of $S_{\Delta s}$) and therefore the computation of the coefficient matrices $\mathbf{P}_{ho,P}^{nonsol}$, $\mathbf{P}_{ho,P}^{sol}$, $\forall P \in S_{\Delta s}$, and $\mathbf{P}_{ho,E}^{nonsol}$, $\forall E \in S_{\Delta s}$, can be performed in a pre-processing stage and its coefficients stored in memory.

The implementation of the high-order CMP-EFIE follows the same structure of the zeroth-order CMP (see [11]), which makes use of matrices $\mathbf{P}_{zo}$ and $\mathbf{R}_{zo}$, that express functions in BC and RWG as linear combinations of functions in $\overline{\text{RWG}}$, respectively. The matrix $\mathbf{P}_{zo}$ encountered in the zeroth-order CMP is extended here to $\mathbf{P}$ defined as

$$\mathbf{P} = \begin{pmatrix} \mathbf{P}_{zo} & \mathbf{0} & \mathbf{0} \\ \mathbf{0} & \mathbf{0} & \mathbf{P}_{ho}^{sol} \\ \mathbf{0} & \mathbf{P}_{ho}^{nonsol} & \mathbf{0} \end{pmatrix}, \tag{6.80}$$

where $\mathbf{P}_{ho}^{nonsol}$ is the (sparse) matrix that encompasses matrices $\mathbf{P}_{ho,P}^{nonsol}$, $P = 1,\ldots,N_P$, and $\mathbf{P}_{ho,E}^{nonsol}$, $E = 1,\ldots,N_E$, and $\mathbf{P}_{ho}^{sol}$ is the (sparse) matrix that encompasses matrices $\mathbf{P}_{ho,P}^{sol}$, $P = 1,\ldots,N_P$. Explicit

expressions for the entries of $\mathbf{P}_{zo}$ can be found in [17]. The matrix $\mathbf{R}_{zo}$ encountered in the zeroth-order CMP is replaced here by the matrix $\mathbf{R}$, which expresses functions in GWP(p) as linear combinations of functions in $\overline{\text{GWP}}$.

Using $\mathbf{P}$, matrix $\mathbf{T}_{\tilde{F}}$ in (6.16) can be evaluated as

$$\mathbf{T}_{\tilde{F}} = \mathbf{P}^{\mathrm{T}}\mathbf{H}_{\tilde{F}}^{\mathrm{T}}\mathbf{T}_{\overline{\text{GWP}}}\mathbf{H}_{\tilde{F}}\mathbf{P} \tag{6.81}$$

where $\mathbf{H}_{\tilde{F}}$ is the matrix that expresses functions in $\overline{F}$ as linear combinations of functions in $\overline{\text{GWP}}$.

Similarly, matrix $\mathbf{T}_{F}$ is evaluated as

$$\mathbf{T}_{F} = \mathbf{H}_{F}^{\mathrm{T}}\mathbf{T}_{\text{GWP}}\mathbf{H}_{F} \tag{6.82}$$

where $\mathbf{H}_{F}$ is the matrix that expresses functions in F as linear combinations of functions in GWP. The evaluation of $\mathbf{G}_{nF;\tilde{F}}$ in (6.18) can be recast into

$$\mathbf{G}_{nF;\tilde{F}} = \mathbf{H}_{F}^{\mathrm{T}}\mathbf{R}^{\mathrm{T}}\mathbf{G}_{n\overline{\text{GWP}};\overline{\text{GWP}}}\mathbf{H}_{\tilde{F}}\mathbf{P} . \tag{6.83}$$

The computational cost of solving (6.15) is that of multiplying the matrix $\mathbf{T}^{\text{CMP}}$ times the number of iterations required to reach a prescribed residual error. Evaluation of a vector times $\mathbf{T}^{\text{CMP}}$ involves multiplying first by $\mathbf{T}_{F}$ as in (6.82), then by the inverse of $\mathbf{G}_{nF;\tilde{F}}$ as in (6.83), and finally by $\mathbf{T}_{\tilde{F}}$ as in (6.81). As mentioned previously, the cost of multiplying $\mathbf{R}$ and $\mathbf{P}$ by a vector scales as $O(N)$. Thus, the cost of multiplying $\mathbf{G}_{nF;\tilde{F}}$ by a vector also scales as $O(N)$. Provided that $\mathbf{G}_{nF;\tilde{F}}$ is well-conditioned, and it is, then its inverse can be multiplied by a vector using just a few (i.e., $O(1)$) iterations of an iterative solver like the generalized minimal residual (GMRES) [39] or the transpose-free quasiminimal residual (TFQMR) [40]. Using the multilevel fast multipole method [2], the cost of multiplying $\mathbf{T}_{\overline{F}}$ by a vector scales as $C_{T} + O(N)$ where C_{T} is the cost of multiplying $\mathbf{T}_{F}$ by a vector. Indeed, even though the dimension of $\mathbf{T}_{\overline{F}}$ is greater that that of $\mathbf{T}_{F}$ by a factor of 6, the additional degrees of freedom introduced by the barycentric

mesh do not change the number of multipoles required for field expansion compared to that used when multiplying by $\mathbf{T}_F$. Therefore, the cost of multiplying $\mathbf{T}_{\bar{F}}$ increases only by an additive linear term. The fact that the number of iterations required for the high-order CMP-EFIE to converge is much smaller than that of the standard EFIE justifies the use of the former scheme.

2.5   Numerical Results

This section presents several examples that demonstrate the effectiveness of the DQCC(p) basis functions presented and its performance in the high-order CMP-EFIE. The results emphasize its main advantage: high-order accuracy in the solutions, without compromising the number of iterations needed for convergence. The results presented here are obtained using a parallel EFIE MoM solver, which uses the proposed high-order CMP or a standard diagonal preconditioner. This solver uses a TFQMR-based iterative method [40] to solve the EFIE MoM systems.

2.5.1   High-order accuracy

The first two examples demonstrate the convergence of the radar cross section (RCS) as the order of the basis functions in the high-order CMP-EFIE is increased. Each example comprises a smooth PEC object: a sphere of radius 1 m., and a star-shaped object whose surface is parameterized as $r(\theta,\phi) = 1.5 + \sin^2(2\theta)\cos^2(\phi)$ m., both illuminated by a 30 MHz., $\hat{x}$-polarized plane wave traveling in the $\hat{z}$ direction. Fig. II.6(a) (Fig. II.7(a)) shows the bistatic RCS of the PEC sphere (star-shaped object) when computed with basis functions of orders $p = 0,1,2,3$. Fig. II.6(b) (Fig. II.7(b)) shows the relative error of the computed RCS of the PEC sphere (star-shaped object) with respect to Mie series (4th-order) solution. In these examples, the geometric models consist of 32 patches for the sphere and 102 patches for the star-shaped object. Each patch is obtained by means of an exact mapping from a reference patch onto the surface of the object. The evaluation of basis functions on curvilinear patches requires the computation of a Jacobian function, which requires additional computation time when compared to flat patches [19]. The overhead introduced by the evaluation of the Jacobian is more than compensated however by the reduction in the number of patches required to accurately describe the sphere surface.

(a)

(b)
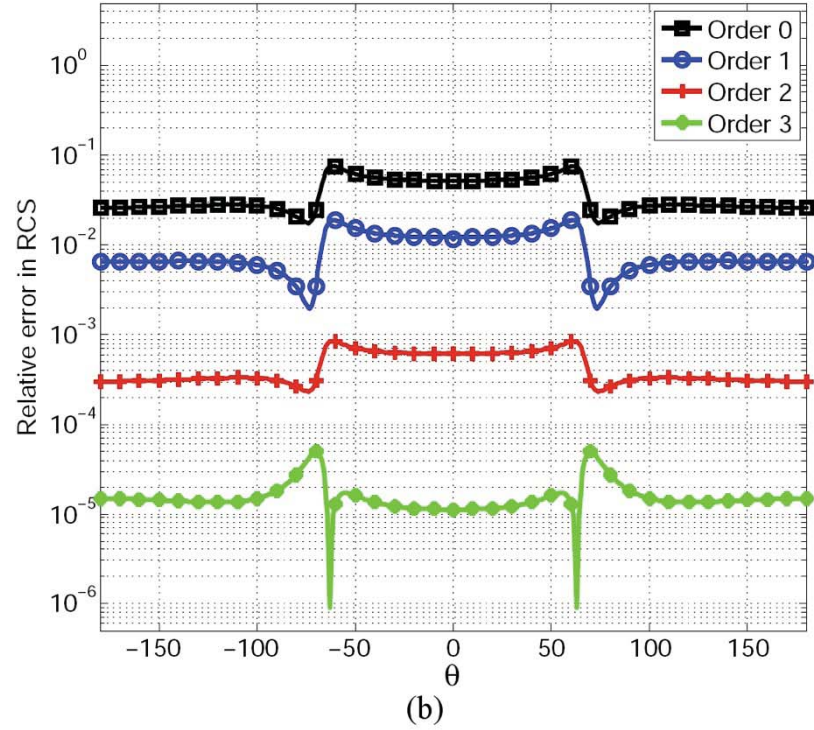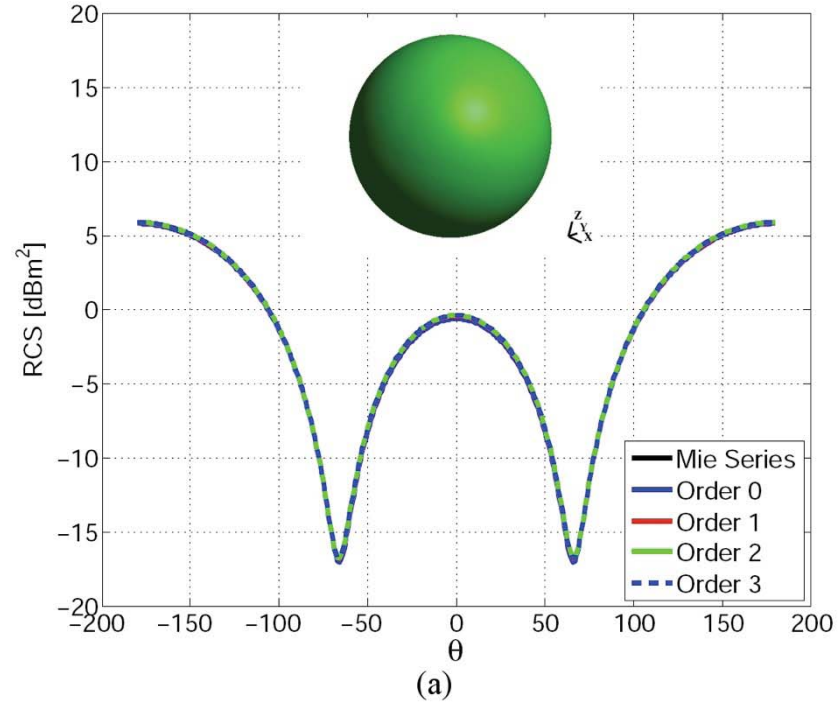
Fig. II.6. Bistatic RCS of a PEC sphere of radius 1 m. illuminated by a 30 MHz $\hat{x}$-polarized plane wave traveling in the $\hat{z}$ direction. The surface of the sphere is modeled with 32 curvilinear patches. The current density is modeled with basis functions of orders $p = 0,1,2,3$. The number of unknowns ranges from 48 ($p = 0$) to 576 ($p = 3$): (a) Bistatic RCS in the x-z plane. (b) Relative error in the RCS with respect to Mie series solution.
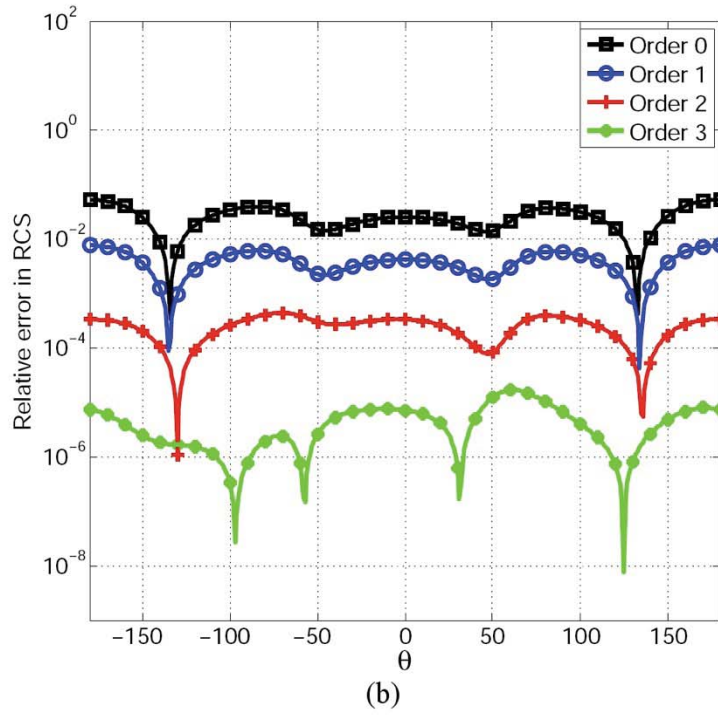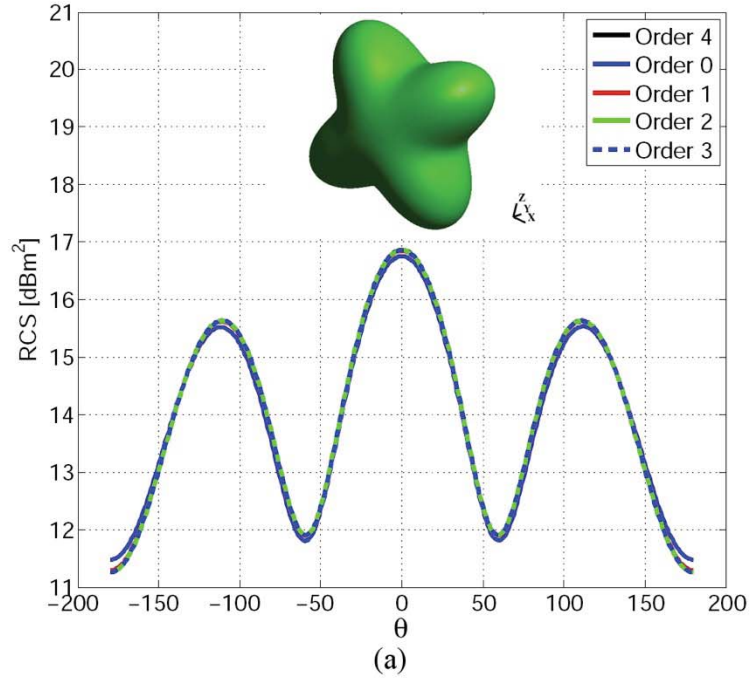
Fig. II.7. Bistatic RCS of a PEC star-shaped object illuminated by a 30 MHz $\hat{x}$-polarized plane wave traveling in the $\hat{z}$ direction. The surface of the object is modeled with 102 curvilinear patches. The current density is modeled with basis functions of orders $p = 0,1,2,3$. The number of unknowns ranges from 153 ($p = 0$) to 1836 ($p = 3$). (a) Bistatic RCS in the x-z plane. (b) Relative error in the RCS with respect to the solution obtained using basis functions of order $p = 4$.

2.5.2   Condition number

The following three examples illustrate the behavior of the condition numbers of the non-preconditioned EFIE and CMP-EFIE system matrices as the surface current expansion is increasingly well-approximated, i.e. as $\delta \to 0$ and/or $p \to \infty$. Table II.A shows the condition numbers of $\mathbf{G}_{nF;\tilde{F}}$, $\mathbf{T}_F$, and $\mathbf{T}^{\text{CMP}}$, obtained with several mesh discretizations of the PEC sphere of Fig. II.6(a) using basis functions of orders $p = 1, 2, 3, 4$. Similarly, Table II.B and Table II.C show the same data for the star-shaped object of Fig. II.7(a) and a PEC cube with side length of 1 m., respectively. These results show that for a fixed order p, the condition numbers of $\mathbf{G}_{nF;\tilde{F}}$ and $\mathbf{T}^{\text{CMP}}$ remain bounded as the mesh density is increased, whereas the condition number of $\mathbf{T}_F$ does not.

By virtue of the Calderón identity in (6.11), the operator $\mathcal{T}^2$ is spectrally equivalent to the identity operator. Hence the condition number of $\mathbf{T}^{\text{CMP}}$ depends on how well the sets F and $\tilde{F}$ can discretize the identity operator, i.e. the Gram matrix $\mathbf{G}_{nF;\tilde{F}}$. As mentioned in Section 2.3.1, the growth in the condition number of $\mathbf{G}_{nF;\tilde{F}}$ (and therefore of $\mathbf{T}^{\text{CMP}}$) with p is related to the way in which the functions in F_{ho}^{sol} and F_{ho}^{nonsol} are obtained. Table II.D shows the condition numbers of $\mathbf{G}_{nF;\tilde{F}}$ and $\mathbf{T}^{\text{CMP}}$ for three different ways of obtaining these sets, and for orders $p = 1, 2, 3, 4$. As expected, full local orthogonalization of the functions in F_{ho}^{sol} and F_{ho}^{sol} result in lower condition numbers for the matrices $\mathbf{G}_{nF;\tilde{F}}$ and $\mathbf{T}^{\text{CMP}}$ that are more stable with respect to p when compared to partial local orthogonalization. Also, as conjectured at the end of Section 2.3.1, a global orthogonalization of the functions in F_{ho}^{sol} and F_{ho}^{sol} yields $\mathbf{G}_{nF;\tilde{F}}$ and $\mathbf{T}^{\text{CMP}}$ matrices with condition numbers that are almost independent of p.

Table II.A.

Condition numbers of $\mathbf{G}_{nF;\tilde{F}}$, $\mathbf{T}_F$, and $\mathbf{T}^{\text{CMP}}$ for three different mesh discretizations of a PEC sphere

p	N_P	N	$\mathbf{G}_{nF;\tilde{F}}$	$\mathbf{T}_F$	$\mathbf{T}^{\text{CMP}}$
	32	160	11.77	335.87	21.18
1	102	510	13.4	2318.48	25.63
	224	1120	14.35	5542.08	32.95
	32	336	45.06	2942.35	63.31
2	102	1071	68.08	21298.59	98.67
	224	2352	59.97	47297.28	88.26
	32	576	62.59	25681.78	202.45
3	102	1836	72.94	189540.53	233.97
	224	4032	78.02	417912.93	265.26
	32	880	156.68	201766.16	571.16
4	102	2805	183.08	1604161.36	705.08
	224	6160	192.28	3394907.21	740.86

Table II.B.

Condition numbers of $\mathbf{G}_{nF;\tilde{F}}$, $\mathbf{T}_F$, and $\mathbf{T}^{\text{CMP}}$ for three different mesh discretizations of a PEC star-shaped object

p	N_P	N	$\mathbf{G}_{nF;\tilde{F}}$	$\mathbf{T}_F$	$\mathbf{T}^{\text{CMP}}$
	32	160	13.24	239.07	23.56
1	102	510	14.49	1167.83	26.5
	224	1120	14.06	4013.27	28.53
	32	336	51.38	2005.19	78.68
2	102	1071	91.44	11268.25	125.03
	224	2352	70.19	36240.98	109.66
	32	576	82.46	17867.56	262.67
3	102	1836	88.62	102686.45	279.92
	224	4032	83.03	325654.23	262.08
	32	880	179.14	145715.16	700.56
4	102	2805	226.84	905399.7	926.65
	224	6160	198.94	2689593.01	735.11

TABLE II.C.

Condition numbers of $\mathbf{G}_{nF;\tilde{F}}$, $\mathbf{T}_F$, and $\mathbf{T}^{\text{CMP}}$ for three different mesh
discretizations of a PEC cube

p	N_P	N	$\mathbf{G}_{nF;\tilde{F}}$	$\mathbf{T}_F$	$\mathbf{T}^{\text{CMP}}$
	24	120	14.94	658.14	26.63
1	154	770	12.41	6719.43	35.38
	240	1200	12.21	10411.1	42.66
	24	252	76.75	5266.6	118.11
2	154	1617	73.03	59766.95	115.66
	240	2520	59.98	97635.17	96.78
	24	432	69.48	50812.32	221.55
3	154	2772	69.5	582413.73	315.89
	240	4320	71.17	841216.68	338.87
	24	660	172.38	325648.19	674.44
4	154	4235	165.76	3910371	881.96
	240	6600	168.5	6382122.93	921.35

TABLE II.D.

Condition numbers of $\mathbf{G}_{nF;\tilde{F}}$, and $\mathbf{T}^{\text{CMP}}$ for three different
Helmholtz decomposition strategies

		Partial local orthogonalization		Full local orthogonalization		Full global orthogonalization	
p	N	$\mathbf{G}_{nF;\tilde{F}}$	$\mathbf{T}^{\text{CMP}}$	$\mathbf{G}_{nF;\tilde{F}}$	$\mathbf{T}^{\text{CMP}}$	$\mathbf{G}_{nF;\tilde{F}}$	$\mathbf{T}^{\text{CMP}}$
1	60	29.9	21.18	29.9	20.99	2.51	3.14
2	336	73.1	63.31	55.5	48.15	2.54	3.17
3	576	152.3	202.45	126.5	134.97	2.79	3.29
4	880	220.2	571.16	177.4	248.44	2.94	3.47

2.5.3   Speed of convergence

The examples in this section compare the speed of convergence of the diagonally-preconditioned EFIE and CMP-EFIE when solved iteratively. Fig. II.8(a-e) show the residual error versus iteration count achieved by a TFQMR solver during the iterative solution of the matrix systems obtained by discretizing the diagonally-preconditioned EFIE and HO-CMP with basis functions of orders $p = 1,2,3,4,5$. The

geometry is a PEC sphere of radius 1 m. Similarly, Fig. II.9(a-e) show the same data for a PEC cube with side length of 1 m. In both examples, the excitation is a 30 MHz., $\hat{x}$-polarized plane wave traveling in the $\hat{z}$ direction, and the prescribed accuracy (relative residual error) for the TFQMR solver is 10^{-5}. As dictated by the condition number of $\mathbf{T}^{\mathrm{CMP}}$, the number of iterations required for the CMP-EFIE to reach the prescribed accuracy does not grow as the discretization density is increased. In contrast, the diagonally-preconditioned EFIE requires an increasing number of iterations as the mesh becomes denser. Moreover, this behavior worsens as the order p of the basis functions is increased, severely penalizing the efficiency and accuracy of high-order basis functions.
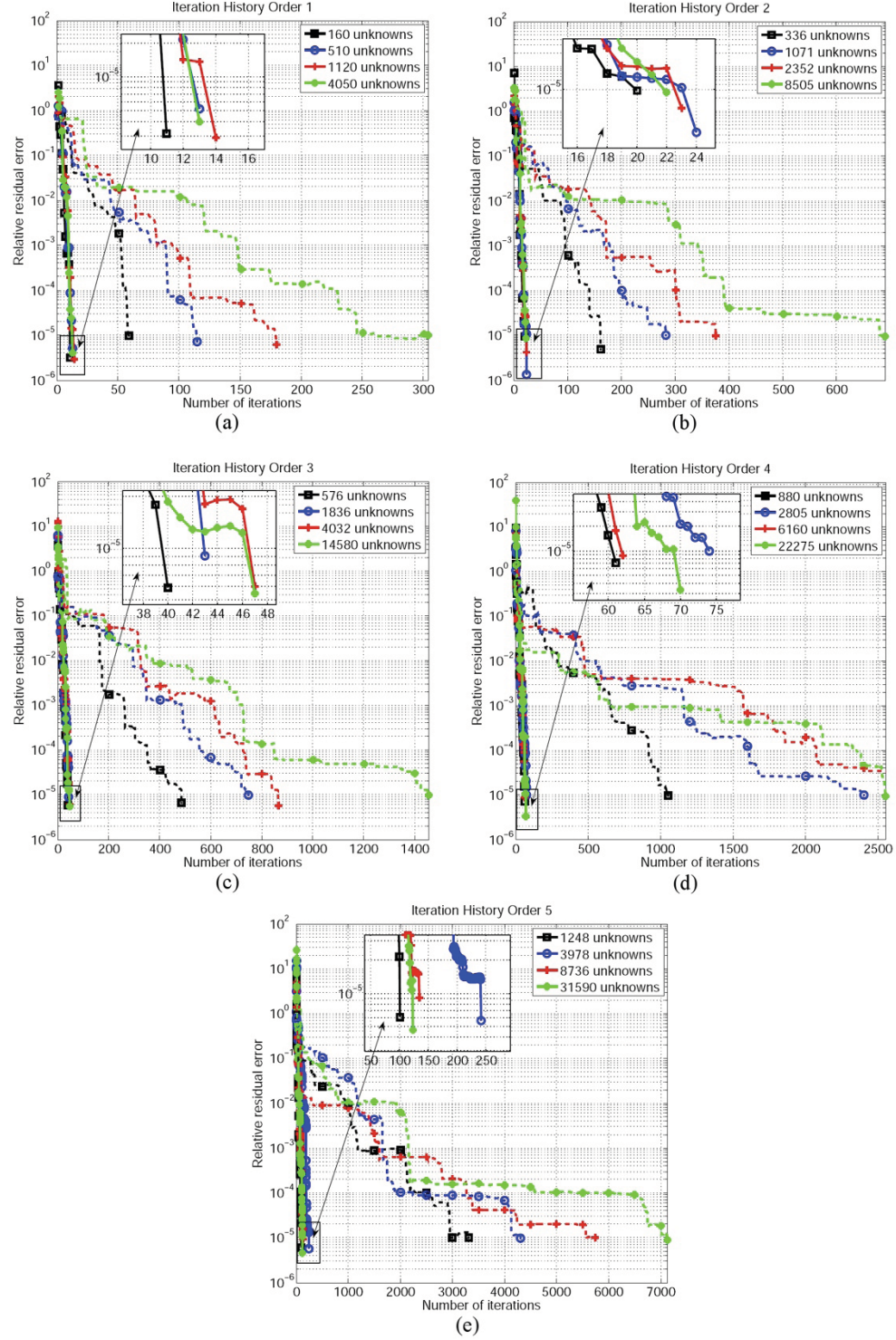
Fig. II.8. Residual history of diagonally-preconditioned EFIE (dashed lines) and CMP-EFIE (solid lines) for the case of a PEC sphere of radius 1 m., illuminated by a 30 MHz., $\hat{x}$-polarized plane wave traveling in the $\hat{z}$ direction. Four different discretizations are used, ranging from 32 to 810 curvilinear elements. Results are shown for several orders of the basis functions: (a) order 1; (b) order 2; (c) order 3; (d) order 4; (e) order 5.
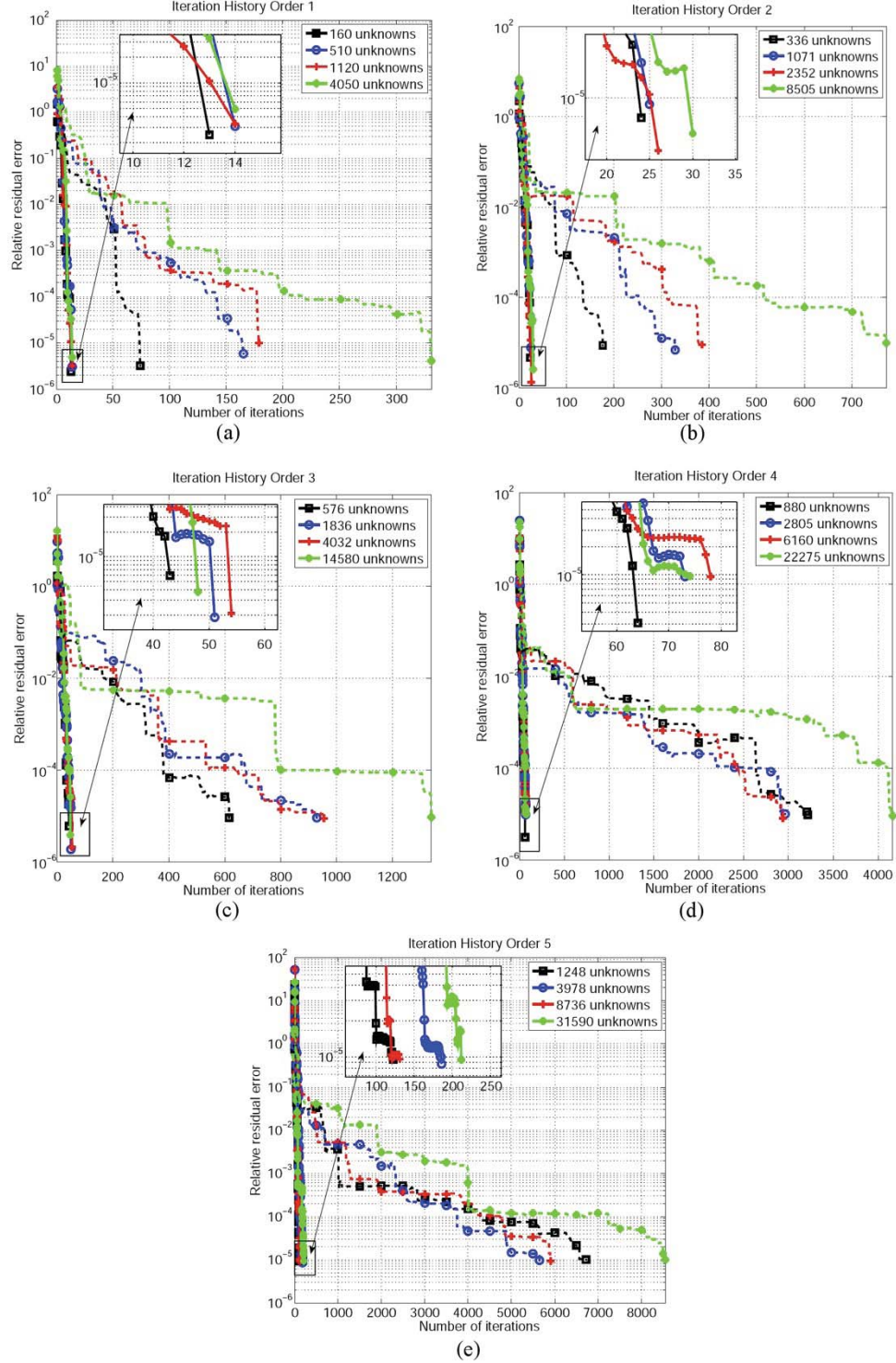
Fig. II.9. Residual history of diagonally-preconditioned EFIE (dashed lines) and CMP-EFIE (solid lines) for the case of a PEC cube of side 1 m., illuminated by a 30 MHz., $\hat{x}$-polarized plane wave traveling in the $\hat{z}$ direction. Four different discretizations are used, ranging from 24 to 918 elements. Results are shown for several orders of the basis functions: (a) order 1; (b) order 2; (c) order 3; (d) order 4; (e) order 5.

2.5.4   Monopole Antenna

Next, the diagonally-preconditioned EFIE and CMP-EFIE are used to analyze scattering from a printed monopole antenna similar to the one presented in [41]. The antenna geometry and mesh are shown in Fig. II.10(a). Note that the dielectric substrate has not been considered here. The antenna is fed with a voltage delta-gap. The divergence of the electric current, i.e. the (scaled) charge distribution on the surface of the antenna is plotted in Fig. II.10(b). The current distribution in this example was obtained using the HO-CMP, with basis functions of order $p = 1$ and a frequency of 3.55 GHz. The radiation pattern of the antenna is plotted in Fig. II.10(c) for two different frequencies: 3.55 and 5.5 GHz. Finally, Fig. II.10(d) shows the residual error versus iteration count achieved by a TFQMR solver during the iterative solution of the matrix systems stemming from the diagonally-preconditioned EFIE and HO-CMP with basis functions of orders $p = 0,1$.

2.5.5   Airbus A380

The last example involves a model of the Airbus A380 shown in Fig. II.11(a). The surface of the aircraft is discretized using second-order curvilinear patches, allowing the use of (relatively) large patches on smooth surfaces (wings and main body), and small patches near fine geometric features (engines and wing tips). The airplane is illuminated by a $\hat{\boldsymbol{y}}$-polarized plane wave traveling in the $\hat{\boldsymbol{x}}$ direction. Fig. II.11(b) shows the bistatic RCS obtained for four different frequencies, ranging from 1.5 to 30 MHz. Fig. II.11(c) and Fig. II.11(d) show the divergence of the current density induced on the surface of the aircraft, at frequencies of 6 MHz and 30 MHz, respectively. Note that at 30 MHz the high-order basis functions allow for the use of less than 5 patches per wavelength on the wings and main body of the aircraft. Finally, Fig. II.11(e) shows the residual error versus iteration count achieved by a TFQMR solver during the iterative solution of the matrix systems obtained by discretizing the diagonally-preconditioned EFIE and CMP-EFIE with basis functions of orders $p = 1,2,3$. In this case, the excitation frequency is 6 MHz. Similarly, Fig. II.11(f) shows the residual error versus iteration count achieved by a TFQMR solver for an excitation frequency of 30 MHz. Using basis functions of order $p = 0$, it took 30 minutes and 16852 iterations for the diagonally preconditioned EFIE to converge to a prescribed relative residual error of 10^{-4}.

For the CMP-EFIE it took 11 minutes and 485 iterations. Using basis functions of order $p=1$, the diagonally preconditioned EFIE could only reach a relative residual error of 1.8×10^{-3} after 8.6 hours and 100000 iterations. For the CMP-EFIE it took 1.2 hours and 383 iterations to reach the prescribed relative residual error of 10^{-4}.
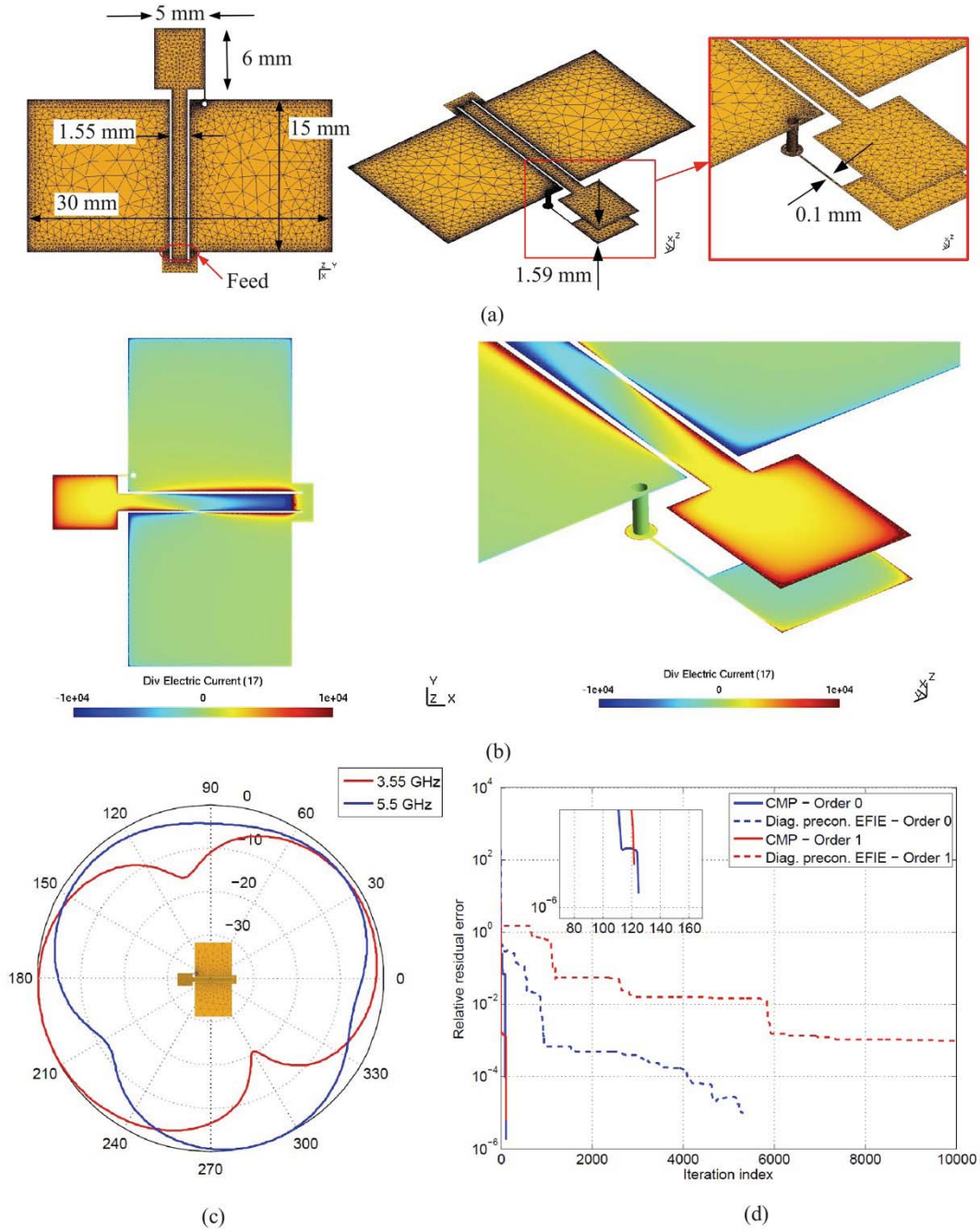
Fig. II.10. Monopole antenna excited with a voltage delta-gap. (a) Mesh and dimensions of the antenna. (b) Divergence of the current density induced on the antenna, for a frequency of 3.55 GHz. (c) Radiation pattern in the x-y plane for two different frequencies. (d) Residual history of diagonally-preconditioned EFIE (dashed lines) and CMP-EFIE (solid lines), for a frequency of 5.5 GHz for orders $p = 0,1$.
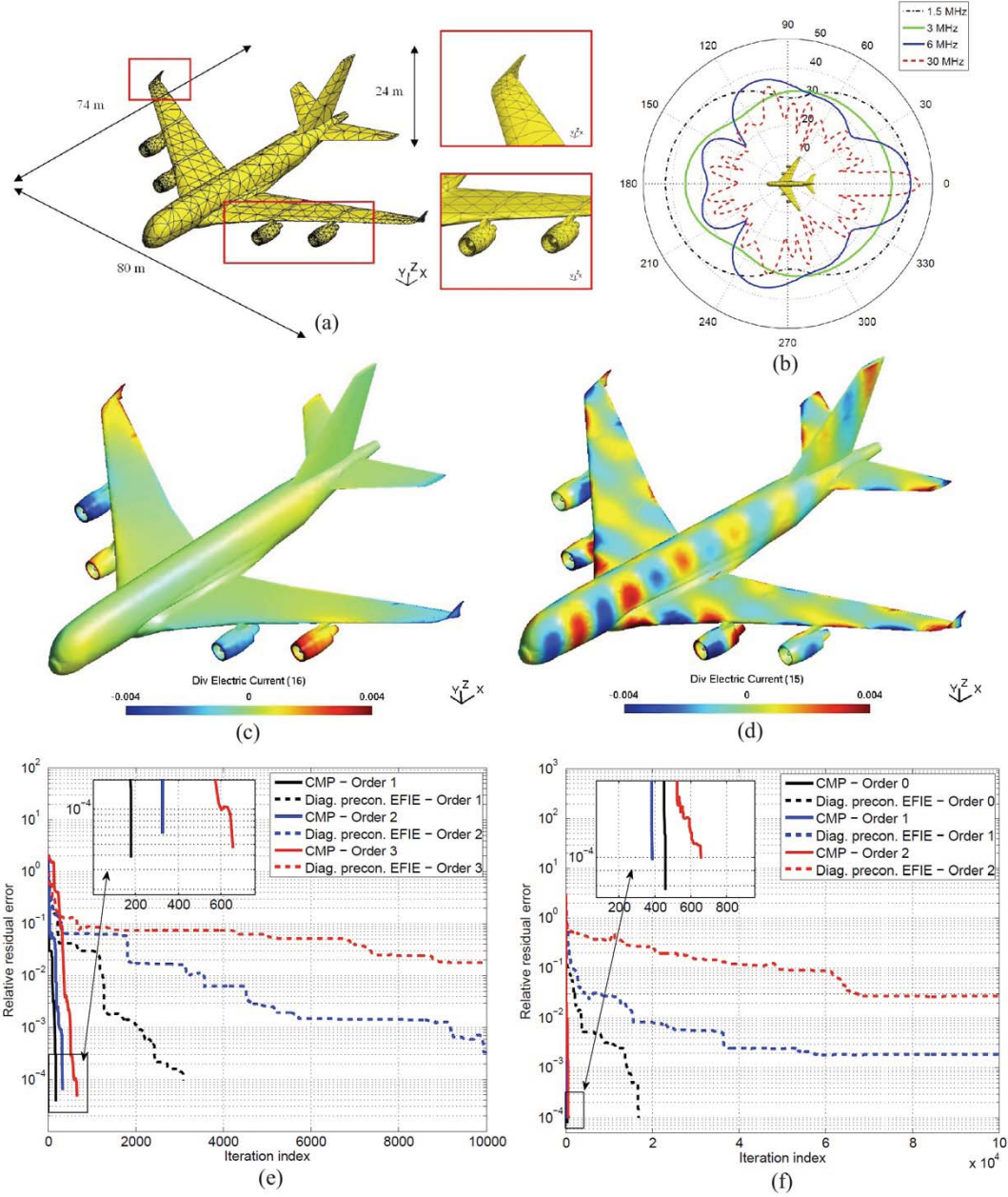
Fig. II.11. Airbus A380 model illuminated by $\hat{\mathbf{y}}$-polarized plane wave traveling in the $\hat{\mathbf{x}}$ direction. (a) Mesh and dimensions of the aircraft; second order curvilinear patches are used to discretize the surface. (b) Bistatic RCS in the x-y plane for four different frequencies. (c) Divergence of the current density induced on the aircraft, for a frequency of 6 MHz. (d) Divergence of the current density induced on the aircraft, for a frequency of 30 MHz. (e) Residual history of diagonally-preconditioned EFIE (dashed lines) and CMP-EFIE (solid lines), for a frequency of 6 MHz for orders $p = 1,2,3$. (f) Residual history of diagonally-preconditioned EFIE (dashed lines) and CMP-EFIE (solid lines), for a frequency of 30 MHz for orders $p = 0,1,2$.

46

CHAPTER III

Single Source Integral Equations for Analyzing Scattering from Homogeneous Penetrable Objects in Frequency Domain

3.1 **Formulation of Single Source Integral Equations**

Consider a homogeneous penetrable object with surface S and outward pointing unit normal vector $\hat{\boldsymbol{n}}_r$, which is immersed in a homogeneous background medium (Fig. III.1(a)). The object is illuminated by time-harmonic electric and magnetic fields $\{\boldsymbol{E}^{inc}, \boldsymbol{H}^{inc}\}$ produced by sources with angular frequency ω, residing external to S. The background and the object are denoted by $j = 1$ and $j = 2$, respectively. Let ϵ_j, μ_j, η_j and k_j denote the permittivity, permeability, impedance, and wave number of medium j, respectively. We wish to find the total electric and magnetic fields $\{\boldsymbol{E}_j, \boldsymbol{H}_j\}$ in regions $j = 1$ and 2. As in the previous chapter, a time dependence $e^{-i\omega t}$ ($i = \sqrt{-1}$) is assumed and suppressed.

The identity operator is denoted $\mathcal{I}$ and the single and double layer operators pertinent to medium j are defined as

$$\mathcal{T}_j[\boldsymbol{X}] = \mathcal{T}_j^s[\boldsymbol{X}] + \mathcal{T}_j^h[\boldsymbol{X}] \tag{7.1}$$

with

$$\mathcal{T}_j^s[\boldsymbol{X}] = \frac{ik_j}{4\pi}\hat{\boldsymbol{n}}_r \times \int_S \frac{e^{ik_j|\boldsymbol{r}-\boldsymbol{r}'|}}{|\boldsymbol{r}-\boldsymbol{r}'|}\boldsymbol{X}(\boldsymbol{r}')ds', \tag{7.2}$$

$$\mathcal{T}_j^h[\boldsymbol{X}] = \frac{-i}{4\pi k_j}\hat{\boldsymbol{n}}_r \times \int_S \nabla'\frac{e^{ik_j|\boldsymbol{r}-\boldsymbol{r}'|}}{|\boldsymbol{r}-\boldsymbol{r}'|}\nabla'_s \boldsymbol{X}(\boldsymbol{r}')ds', \tag{7.3}$$

and

$$\mathcal{K}_j[X] = \frac{\hat{\boldsymbol{n}}_r}{4\pi} \times \int_S \nabla' \frac{e^{ik_j|r-r'|}}{|\boldsymbol{r}-\boldsymbol{r}'|} \times X(\boldsymbol{r}')ds'. \tag{7.4}$$

To obtain integral equations in electric and magnetic source densities $\{\boldsymbol{J}_j, \boldsymbol{M}_j\}$ residing on S that permit the evaluation of $\{\boldsymbol{E}_j, \boldsymbol{H}_j\}$, two scenarios are considered [42]. In the externally equivalent scenario, $\{\boldsymbol{J}_1, \boldsymbol{M}_1\}$ radiate in a homogeneous medium with $\{\epsilon_1, \mu_1\}$ alongside the original sources and produce the fields $\{\boldsymbol{E}_1, \boldsymbol{H}_1\}$ outside S and (auxiliary) fields $\{\boldsymbol{E}_{in}, \boldsymbol{H}_{in}\}$ inside S (Fig. III.1(b)), i.e.

$$\eta_1 \hat{\boldsymbol{n}}_r \times \boldsymbol{H}_1 - \eta_1 \hat{\boldsymbol{n}}_r \times \boldsymbol{H}_{in} = \boldsymbol{J}_1, \tag{7.5}$$

$$\hat{\boldsymbol{n}}_r \times \boldsymbol{E}_1 - \hat{\boldsymbol{n}}_r \times \boldsymbol{E}_{in} = -\boldsymbol{M}_1, \tag{7.6}$$

or

$$\left(\frac{\mathcal{I}}{2} + \mathcal{K}_1\right)[\boldsymbol{J}_1] - \mathcal{T}_1[\boldsymbol{M}_1] = \eta_1 \hat{\boldsymbol{n}}_r \times \boldsymbol{H}^{inc} - \eta_1 \hat{\boldsymbol{n}}_r \times \boldsymbol{H}_{in}, \tag{7.7}$$

$$\left(\frac{\mathcal{I}}{2} + \mathcal{K}_1\right)[\boldsymbol{M}_1] + \mathcal{T}_1[\boldsymbol{J}_1] = -\hat{\boldsymbol{n}}_r \times \boldsymbol{E}^{inc} + \hat{\boldsymbol{n}}_r \times \boldsymbol{E}_{in}. \tag{7.8}$$

In the internally equivalent scenario, $\{\boldsymbol{J}_2, \boldsymbol{M}_2\}$ radiate in a homogeneous medium with $\{\epsilon_2, \mu_2\}$ and produce the fields $\{\boldsymbol{E}_2, \boldsymbol{H}_2\}$ inside S and (auxiliary) fields $\{\boldsymbol{E}_{out}, \boldsymbol{H}_{out}\}$ outside S (Fig. III.1(c)), i.e.

$$\eta_2 \hat{\boldsymbol{n}}_r \times \boldsymbol{H}_{out} - \eta_2 \hat{\boldsymbol{n}}_r \times \boldsymbol{H}_2 = \boldsymbol{J}_2, \tag{7.9}$$

$$\hat{\boldsymbol{n}}_r \times \boldsymbol{E}_{out} - \hat{\boldsymbol{n}}_r \times \boldsymbol{E}_2 = -\boldsymbol{M}_2, \tag{7.10}$$

or

$$\left(\frac{\mathcal{I}}{2} - \mathcal{K}_2\right)[\boldsymbol{J}_2] + \mathcal{T}_2[\boldsymbol{M}_2] = \eta_2 \hat{\boldsymbol{n}}_r \times \boldsymbol{H}_{out}, \tag{7.11}$$

$$\left(\frac{\mathcal{I}}{2} - \mathcal{K}_2\right)[\boldsymbol{M}_2] - \mathcal{T}_2[\boldsymbol{J}_2] = -\hat{\boldsymbol{n}}_r \times \boldsymbol{E}_{out}. \tag{7.12}$$

The auxiliary fields $\{E_{in}, H_{in}\}$ and $\{E_{out}, H_{out}\}$ can be chosen arbitrarily as long as they satisfy Maxwell's equations inside and outside S, respectively. In addition, the fields $\{E_{out}, H_{out}\}$ must satisfy the Silver-Müller radiation condition [24].

In the original problem of Fig. III.1(a), the tangential components of $\{E_j, H_j\}$ $j = 1, 2$, are continuous across S, i.e.

$$\hat{n}_r \times H_1 = \hat{n}_r \times H_2 , \tag{7.13}$$

$$\hat{n}_r \times E_1 = \hat{n}_r \times E_2 . \tag{7.14}$$

Combinations of (7.7), (7.8), (7.11), (7.12), (7.13), and (7.14) give rise to many formulations for reconstructing $\{E_j, H_j\}$, each of which corresponds to a different choice of the auxiliary fields $\{E_{in}, H_{in}\}$ and $\{E_{out}, H_{out}\}$. Dual source equations can be constructed by assuming $\{E_{in}, H_{in}\} = \{E_{out}, H_{out}\} = \{0, 0\}$, for which (7.7), (7.8), (7.11), and (7.12) become

$$\eta_1 \hat{n}_r \times H^{inc} + \mathcal{T}_1[M_1] + \left(\frac{\mathcal{I}}{2} - \mathcal{K}_1 \right)[J_1] = J_1 , \tag{7.15}$$

$$\hat{n}_r \times E^{inc} + \mathcal{T}_1[J_1] + \left(-\frac{\mathcal{I}}{2} + \mathcal{K}_1 \right)[M_1] = -M_1 , \tag{7.16}$$

$$-\mathcal{T}_2[M_2] + \left(\frac{\mathcal{I}}{2} + \mathcal{K}_2 \right)[J_2] = J_2 , \tag{7.17}$$

$$-\mathcal{T}_2[J_2] - \left(\frac{\mathcal{I}}{2} + \mathcal{K}_2 \right)[M_2] = -M_2 . \tag{7.18}$$

Note that for the above choice of the auxiliary fields, (7.5), (7.9), and (7.13) and (7.6), (7.10), and (7.14) imply that $J_2 = -\left(\eta_2 / \eta_1 \right) J_1$ and $M_2 = -M_1$, respectively. Inserting these relations into (7.15)-(7.18), and then combining (7.15) with (7.17), and (7.16) with (7.18) yields

$$-\left(\mathcal{K}_1 + \mathcal{K}_2 \right)[J_1] + \left(\mathcal{T}_1 + \frac{\eta_1}{\eta_2} \mathcal{T}_2 \right)[M_1] = -\eta_1 \hat{n}_r \times H^{inc} , \tag{7.19}$$

$$\left(\mathcal{T}_1 + \frac{\eta_2}{\eta_1}\mathcal{T}_2\right)[\boldsymbol{J}_1] + \left(\mathcal{K}_1 + \mathcal{K}_2\right)[\boldsymbol{M}_1] = -\hat{\boldsymbol{n}}_r \times \boldsymbol{E}^{inc}. \tag{7.20}$$

Eqns. (7.19)-(7.20) are the well-known dual source Poggio-Miller-Chang-Harrington-Wu-Tsai (PMCHWT) equations [1], and can be solved simultaneously for $\{\boldsymbol{J}_1, \boldsymbol{M}_1\}$. The dual source Müller equations can be derived in a similar fashion [24].

Single source equations can be obtained, for example, by choosing

$$\boldsymbol{E}_{in} = \boldsymbol{H}_{in} = \boldsymbol{0}, \quad (7.21)$$

and

$$\boldsymbol{E}_{out} = \boldsymbol{E}_2. \tag{7.22}$$

The latter condition, together with (7.10) implies that $\boldsymbol{M}_2 = \boldsymbol{0}$. Continuity of the tangential component of the electric and magnetic fields across S dictates that $\{\boldsymbol{J}_1, \boldsymbol{M}_1\}$ can be expressed in terms of $\boldsymbol{J}_2$ as

$$\boldsymbol{J}_1 = \eta_1 \hat{\boldsymbol{n}}_r \times \boldsymbol{H}_{out} - \frac{\eta_1}{\eta_2}\boldsymbol{J}_2, \tag{7.23}$$

$$\boldsymbol{M}_1 = -\hat{\boldsymbol{n}}_r \times \boldsymbol{E}_2. \tag{7.24}$$

Eqns. (7.7), (7.8), (7.11), and (7.12) become

$$\left(\frac{\mathcal{I}}{2} + \mathcal{K}_1\right)[\eta_1 \hat{\boldsymbol{n}}_r \times \boldsymbol{H}_{out} - \frac{\eta_1}{\eta_2}\boldsymbol{J}_2] + \mathcal{T}_1[\hat{\boldsymbol{n}}_r \times \boldsymbol{E}_2] = \eta_1 \hat{\boldsymbol{n}}_r \times \boldsymbol{H}^{inc}, \tag{7.25}$$

$$\left(\frac{\mathcal{I}}{2} + \mathcal{K}_1\right)[-\hat{\boldsymbol{n}}_r \times \boldsymbol{E}_2] + \mathcal{T}_1[\eta_1 \hat{\boldsymbol{n}}_r \times \boldsymbol{H}_{out} - \frac{\eta_1}{\eta_2}\boldsymbol{J}_2] = -\hat{\boldsymbol{n}}_r \times \boldsymbol{E}^{inc}, \tag{7.26}$$

$$\hat{\boldsymbol{n}}_r \times \boldsymbol{H}_{out} = \frac{1}{\eta_2}\left(\frac{\mathcal{I}}{2} - \mathcal{K}_2\right)[\boldsymbol{J}_2], \tag{7.27}$$

$$\hat{\boldsymbol{n}}_r \times \boldsymbol{E}_2 = \mathcal{T}_2[\boldsymbol{J}_2], \tag{7.28}$$

respectively.

Single source EFIE and MFIE can be obtained by inserting (7.27) and (7.28) into (7.26) and (7.25), respectively:

$$\frac{\eta_1}{\eta_2}\frac{\mathcal{T}_1}{2}[\boldsymbol{J}_2]+\frac{\eta_1}{\eta_2}\mathcal{T}_1\mathcal{K}_2[\boldsymbol{J}_2]+\mathcal{K}_1\mathcal{T}_2[\boldsymbol{J}_2]+\frac{\mathcal{T}_2}{2}[\boldsymbol{J}_2]=\hat{\boldsymbol{n}}_r\times\boldsymbol{E}^{inc} \tag{7.29}$$

$$\frac{\eta_1}{\eta_2}\left(\frac{\mathcal{K}_1}{2}+\mathcal{K}_1\mathcal{K}_2+\frac{\mathcal{K}_2}{2}+\frac{\mathcal{I}}{4}\right)[\boldsymbol{J}_2]-\mathcal{T}_1\mathcal{T}_2[\boldsymbol{J}_2]=-\eta_1\hat{\boldsymbol{n}}_r\times\boldsymbol{H}^{inc}\ . \tag{7.30}$$

Unlike dual source formulations, which require the simultaneous solution of two equations in two unknowns, either of the single source equations (7.29) or (7.30) can be solved independently.
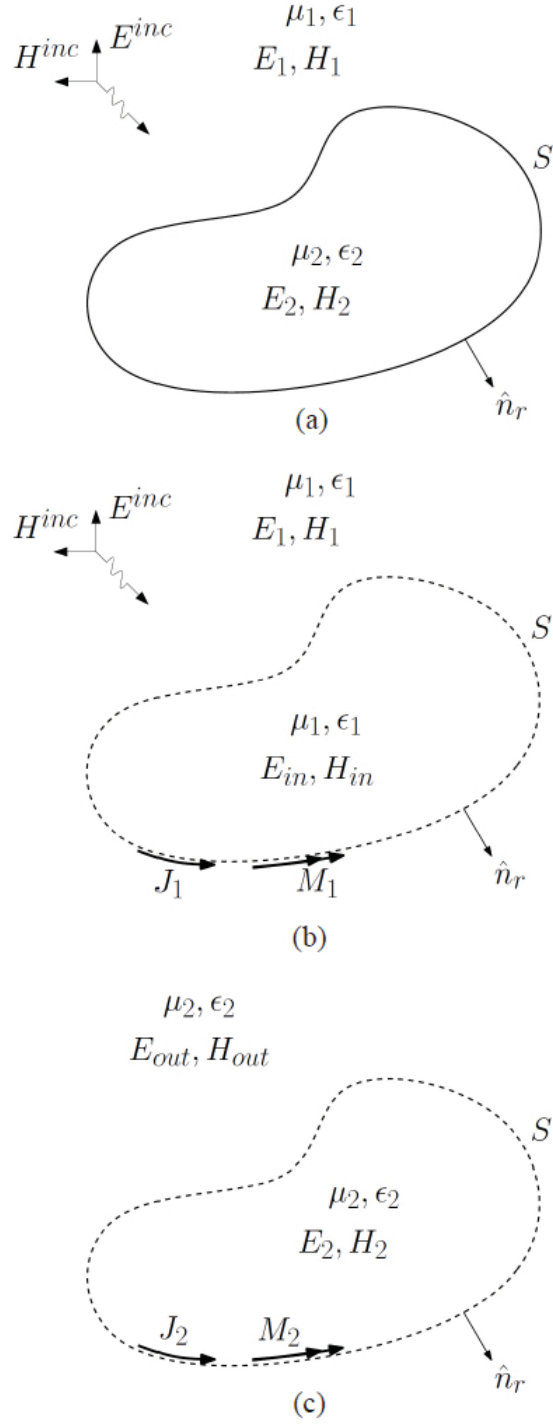
Fig. III.1 Generic penetrable 3-D scatterer. (a) Original problem. (b) Externally equivalent scenario. (c) Internally equivalent scenario.

3.2 Calderón Preconditioned Combined Field Integral Equation

The single source EFIE and MFIE operators in (7.29) and (7.30) are plagued by spectral problems. First, the EFIE suffers from dense-mesh breakdown. The operators $\mathcal{T}_j$ comprise a compact vector potential component $\mathcal{T}_j^s$ with spectrum accumulating at zero and a hypersingular scalar potential component $\mathcal{T}_j^h$ with unbounded spectrum [9][11][12][43]. In addition, the EFIE suffers from low-frequency breakdown. Indeed, because $\mathcal{T}_j^s$'s singular values scale as $O(\omega)$, $\mathcal{T}_j^h$'s as $O(1/\omega)$, and $\mathcal{K}_j$'s as $O(1)$, contributions to the system matrix stemming from $\mathcal{T}_j^h$ dominate those from $\mathcal{T}_j^s$ and $\mathcal{K}_j$ as $\omega \to 0$ [44]. Finally, the EFIE exhibits resonances, i.e., its solution is not unique at a set of frequencies that grows increasingly dense as the electrical size of the scatterer increases [45]. Discretization of the EFIE therefore yields a system matrix with condition number that grows without bound as: (i) the minimum edge length δ in the mesh S_δ that approximates S tends to zero, (ii) $\omega \to 0$, or (iii) ω approaches one of the object's resonant frequencies. Even though the MFIE does not suffer from the dense-mesh or low-frequency breakdown, it is susceptible to resonances and hence problematic when applied to the analysis of electrically large scatterers.

One may attempt to remove the resonances by using the equation $\text{CFIE} = \text{EFIE} + \alpha\, \text{MFIE}$. Unfortunately, this CFIE still suffers from dense-mesh breakdown [15]. The literature abounds with techniques that cure the unbounded nature of the spectrum of $\mathcal{T}_j$ by leveraging its self-regularizing property, expressed by the Calderón identity (6.11). To date, these techniques have been used mainly to construct regularized EFIEs pertinent to the analysis of scattering from perfect electrically conducting (PEC) bodies. Here, a single source Calderón-preconditioned electric field integral equation (CP-EFIE) pertinent to the analysis of scattering from penetrable bodies is obtained by using the localization technique presented in [46]. Specifically, localization is performed by operating with

$$\mathcal{T}_0[X] \equiv \frac{-k_1}{4\pi}\hat{\boldsymbol{n}}_r \times \int_S \frac{e^{-k_1|r-r'|}}{|\boldsymbol{r}-\boldsymbol{r'}|} X(\boldsymbol{r'})ds' - \frac{1}{4\pi k_1}\hat{\boldsymbol{n}}_r \times \int_S \nabla' \frac{e^{-k_1|r-r'|}}{|\boldsymbol{r}-\boldsymbol{r'}|} \nabla'_s\, X(\boldsymbol{r'})ds' \qquad (7.31)$$

on (7.29), yielding

$$\frac{\eta_1}{\eta_2}\left(\frac{\mathcal{T}_0\mathcal{T}_1}{2}+\mathcal{T}_0\mathcal{T}_1\mathcal{K}_2\right)[\boldsymbol{J}_2]+\left(\frac{\mathcal{T}_0\mathcal{T}_2}{2}+\mathcal{T}_0\mathcal{K}_1\mathcal{T}_2\right)[\boldsymbol{J}_2]=\mathcal{T}_0[\hat{\boldsymbol{n}}_r\times\boldsymbol{E}^{inc}]. \tag{7.32}$$

The CP-EFIE and MFIE can be combined to produce a resonance-free Calderón-preconditioned CFIE: CP-CFIE = CP-EFIE + α MFIE [41,48]. Note that the operator $\mathcal{T}_0$ is in essence $\mathcal{T}_1$, but with a purely imaginary wave number (provided that k_1 is real).

3.3 Low-frequency Breakdown

In this section, the CP-CFIE is shown to be immune to low-frequency breakdown and lead to stable solutions at very low frequencies. The singular values of the operators $\mathcal{K}_1$ and $\mathcal{K}_2$, and the operator product $\mathcal{K}_1\mathcal{K}_2$ in (7.30), scale as $O(1)$ as the frequency goes to zero. Operator products in (7.30) and (7.32) of the form $\mathcal{T}_i\mathcal{T}_j$ $(i,j=0,1,2)$ can be decomposed as

$$\begin{aligned}\mathcal{T}_i\mathcal{T}_j&=\left(\mathcal{T}_i^s+\mathcal{T}_i^h\right)\left(\mathcal{T}_j^s+\mathcal{T}_j^h\right)\\&=\mathcal{T}_i^s\mathcal{T}_j^s+\mathcal{T}_i^s\mathcal{T}_j^h+\mathcal{T}_i^h\mathcal{T}_j^s+\mathcal{T}_i^h\mathcal{T}_j^h.\end{aligned} \tag{7.33}$$

Since $\mathcal{T}_i^h\mathcal{T}_j^h$ in (7.33) is zero it follows that as $\omega\to 0$, the singular values of $\mathcal{T}_i\mathcal{T}_j$ scale as

$$O\left(\omega^2+\omega\frac{1}{\omega}+\frac{1}{\omega}\omega\right)=O(1). \tag{7.34}$$

Similarly, $\mathcal{T}_0\mathcal{T}_1\mathcal{K}_2$ in (7.32) can be decomposed into

$$\mathcal{T}_0\mathcal{T}_1\mathcal{K}_2=\left(\mathcal{T}_0^s\mathcal{T}_1^s+\mathcal{T}_0^s\mathcal{T}_1^h+\mathcal{T}_0^h\mathcal{T}_1^s\right)\mathcal{K}_2, \tag{7.35}$$

therefore its frequency dependence also scales as $O(1)$. The treatment of $\mathcal{T}_0\mathcal{K}_1\mathcal{T}_2$ in (7.32) requires some care; $\mathcal{T}_0^h\mathcal{K}_1\mathcal{T}_2^h$ is not zero and the Calderón identity $\mathcal{K}_j\mathcal{T}_i=-\mathcal{T}_i\mathcal{K}_j$ is only valid for $i=j$. However, $\mathcal{T}_0\mathcal{K}_1\mathcal{T}_2$ can be rewritten as

$$\mathcal{T}_0\mathcal{K}_1\mathcal{T}_2 = \left(\mathcal{T}_0 - \frac{k_1}{k_0}\mathcal{T}_1\right)\mathcal{K}_1\left(\mathcal{T}_2 - \frac{k_1}{k_2}\mathcal{T}_1\right) + \frac{k_1}{k_2}\mathcal{T}_0\mathcal{K}_1\mathcal{T}_1 + \frac{k_1}{k_0}\mathcal{T}_1\mathcal{K}_1\mathcal{T}_2 - \frac{k_1}{k_2}\frac{k_1}{k_0}\mathcal{T}_1\mathcal{K}_1\mathcal{T}_1$$

$$= \left(\mathcal{T}_0 - \frac{k_1}{k_0}\mathcal{T}_1\right)\mathcal{K}_1\left(\mathcal{T}_2 - \frac{k_1}{k_2}\mathcal{T}_1\right) - \frac{k_1}{k_2}\mathcal{T}_0\mathcal{T}_1\mathcal{K}_1 - \frac{k_1}{k_0}\mathcal{K}_1\mathcal{T}_1\mathcal{T}_2 + \frac{k_1}{k_2}\frac{k_1}{k_0}\mathcal{K}_1\mathcal{T}_1\mathcal{T}_1. \tag{7.36}$$

The previous arguments show that the singular values of the last three terms scale as $O(1)$, as $\omega \to 0$. Because the factors $\mathcal{T}_i - (k_j/k_i)\mathcal{T}_j$ scale with frequency as $O(\omega)$ [44], it follows that the singular values of the first term on the right hand side of (7.36) scale as $O(\omega^2)$. Therefore $\mathcal{T}_0\mathcal{K}_1\mathcal{T}_2$'s singular values scale as $O(1)$ as $\omega \to 0$. With this, all terms in the CP-CFIE operator are seen to scale as $O(1)$ with frequency and, hence, are balanced as $\omega \to 0$.

3.4 Resonance Frequencies and Dense-mesh Breakdown

In this section, the spectral properties of the single source CP-CFIE are investigated. It is argued that the CP-CFIE is resonance-free and immune to dense-mesh breakdown. Indeed, the operators $\mathcal{K}_1$ and $\mathcal{K}_2$, and the operator product $\mathcal{K}_1\mathcal{K}_2$ are compact. Moreover it is worth noticing that $\mathcal{T}_i\mathcal{T}_j$, in general, cannot be written as the sum of a compact operator plus an identity. Instead it can be written as the sum of a compact operator plus a regular operator whose spectrum is uniformly bounded from above and below, i.e. an operator that is spectrally equivalent to an identity. It is well-known that compact plus regular operators share all the relevant properties of second kind operators [47], thus $\mathcal{T}_i\mathcal{T}_j$ $(i,j=0,1,2)$ is well-behaved. These facts immediately show that the second term on the left hand side of the single source MFIE (7.30) and the terms inside the leftmost bracket on the left hand side of the CP-EFIE (7.32) are well behaved as $\delta \to 0$. To show that $\mathcal{T}_0\mathcal{K}_1\mathcal{T}_2$ is well behaved as $\delta \to 0$, reconsider (7.36). The last three terms on the right hand side of (7.36) are well-behaved by the above argument. The first term on the right hand side of (7.36) is compact because $\mathcal{T}_i - (k_j/k_i)\mathcal{T}_j$ $(i,j=0,1,2)$ has a weakly singular kernel [47].

In the following, we demonstrate that the proposed CP-CFIE is resonant free for a penetrable sphere; from this, as it is pointed out in [9], one can infer that the equation is resonant free also for structures that are a smooth deformation of a sphere (see also [48], Theorem 4.35). We will be using arguments similar to

those used in [9] to demonstrate the resonant-free nature of a CP-CFIE for analyzing scattering from PEC objects. In the process, we also readdress the limit of $\delta \to 0$.

A complete set of vector functions on the surface of a sphere of radius a is given by the vector spherical harmonics

$$\boldsymbol{X}_l^m(\theta,\phi) \equiv \frac{a}{i\sqrt{l(l+1)}} \hat{\boldsymbol{n}} \times \nabla Y_l^m(\theta,\phi) \tag{7.37}$$

$$\boldsymbol{U}_l^m(\theta,\phi) \equiv \hat{\boldsymbol{n}} \times \boldsymbol{X}_l^m(\theta,\phi), \tag{7.38}$$

where $Y_l^m(\theta,\phi)$ denotes the scalar spherical harmonic of degree l and order m.

Operating $\mathcal{T}_j$, $\left(\mathcal{K}_j + \mathcal{I}/2\right)$, and $\left(\mathcal{K}_j - \mathcal{I}/2\right)$ on $\boldsymbol{X}_l^m$ and $\boldsymbol{U}_l^m$ yields [33,51]

$$\mathcal{T}_j \begin{bmatrix} \boldsymbol{X}_l^m \\ \boldsymbol{U}_l^m \end{bmatrix} = \left\{ \begin{array}{c} -\mathbb{J}_l(k_j a)\mathbb{H}_l(k_j a)\boldsymbol{U}_l^m \\ \mathbb{J}_l'(k_j a)\mathbb{H}_l'(k_j a)\boldsymbol{X}_l^m \end{array} \right\}, \tag{7.39}$$

$$\left(\mathcal{K}_j + \frac{\mathcal{I}}{2}\right) \begin{bmatrix} \boldsymbol{X}_l^m \\ \boldsymbol{U}_l^m \end{bmatrix} = \left\{ \begin{array}{c} i\,\mathbb{J}_l'(k_j a)\mathbb{H}_l(k_j a)\boldsymbol{X}_l^m \\ -i\,\mathbb{J}_l(k_j a)\mathbb{H}_l'(k_j a)\boldsymbol{U}_l^m \end{array} \right\}, \tag{7.40}$$

$$\left(\mathcal{K}_j - \frac{\mathcal{I}}{2}\right) \begin{bmatrix} \boldsymbol{X}_l^m \\ \boldsymbol{U}_l^m \end{bmatrix} = \left\{ \begin{array}{c} i\,\mathbb{J}_l(k_j a)\mathbb{H}_l'(k_j a)\boldsymbol{X}_l^m \\ -i\,\mathbb{J}_l'(k_j a)\mathbb{H}_l(k_j a)\boldsymbol{U}_l^m \end{array} \right\}. \tag{7.41}$$

Here $\mathbb{J}_l$ and $\mathbb{H}_l$ are the Riccati-Bessel and the first kind Riccati-Hankel functions of order l, respectively [52], and "'" denotes differentiation with respect to the wave number k_j.

3.4.1   Spectral properties of the MFIE

The MFIE operator in (7.30) comprises terms proportional to $\left(\mathcal{K}_1 + \mathcal{I}/2\right)\left(\mathcal{K}_2 + \mathcal{I}/2\right)$ and $\mathcal{T}_1\mathcal{T}_2$. Operating the former on $\boldsymbol{X}_l^m$ and $\boldsymbol{U}_l^m$ yields

$$\left(\mathcal{K}_1+\frac{\mathcal{I}}{2}\right)\left(\mathcal{K}_2+\frac{\mathcal{I}}{2}\right)\begin{bmatrix} \boldsymbol{X}_l^m \\ \boldsymbol{U}_l^m \end{bmatrix} = \left(\mathcal{K}_1+\frac{\mathcal{I}}{2}\right)\begin{bmatrix} i\,\mathbb{J}'_l(k_2a)\mathbb{H}_l(k_2a)\boldsymbol{X}_l^m \\ -i\,\mathbb{J}_l(k_2a)\mathbb{H}'_l(k_2a)\boldsymbol{U}_l^m \end{bmatrix}$$

$$= \begin{Bmatrix} -\left(\mathbb{J}'_l(k_1a)\mathbb{H}_l(k_1a)\right)\left(\mathbb{J}'_l(k_2a)\mathbb{H}_l(k_2a)\right)\boldsymbol{X}_l^m \\ -\left(\mathbb{J}_l(k_1a)\mathbb{H}'_l(k_1a)\right)\left(\mathbb{J}_l(k_2a)\mathbb{H}'_l(k_2a)\right)\boldsymbol{U}_l^m \end{Bmatrix}. \tag{7.42}$$

Similarly, applying $\mathcal{T}_1\mathcal{T}_2$ to these same functions yields

$$\mathcal{T}_1\mathcal{T}_2\begin{bmatrix} \boldsymbol{X}_l^m \\ \boldsymbol{U}_l^m \end{bmatrix} = \mathcal{T}_1\begin{bmatrix} -\mathbb{J}_l(k_2a)\mathbb{H}_l(k_2a)\boldsymbol{U}_l^m \\ \mathbb{J}'_l(k_2a)\mathbb{H}'_l(k_2a)\boldsymbol{X}_l^m \end{bmatrix}$$

$$= \begin{Bmatrix} -\left(\mathbb{J}'_l(k_1a)\mathbb{H}'_l(k_1a)\right)\left(\mathbb{J}_l(k_2a)\mathbb{H}_l(k_2a)\right)\boldsymbol{X}_l^m \\ -\left(\mathbb{J}_l(k_1a)\mathbb{H}_l(k_1a)\right)\left(\mathbb{J}'_l(k_2a)\mathbb{H}'_l(k_2a)\right)\boldsymbol{U}_l^m \end{Bmatrix}. \tag{7.43}$$

Combining (7.42) and (7.43) to obtain the MFIE operator yields an eigensystem

$$\left\{\frac{\eta_1}{\eta_2}\left(\mathcal{K}_1+\frac{\mathcal{I}}{2}\right)\left(\mathcal{K}_2+\frac{\mathcal{I}}{2}\right)-\mathcal{T}_1\mathcal{T}_2\right\}\begin{bmatrix} \boldsymbol{X}_l^m \\ \boldsymbol{U}_l^m \end{bmatrix} = \begin{Bmatrix} \lambda_l^I\boldsymbol{X}_l^m \\ \lambda_l^{II}\boldsymbol{U}_l^m \end{Bmatrix} \tag{7.44}$$

where the functions $\lambda_l^I = \lambda_l^I(k_1,k_2,\eta_1,\eta_2)$ and $\lambda_l^{II} = \lambda_l^{II}(k_1,k_2,\eta_1,\eta_2)$ are

$$\lambda_l^I \equiv \mathbb{J}'_l(k_1a)\mathbb{H}_l(k_2a)\left[\mathbb{H}'_l(k_1a)\mathbb{J}_l(k_2a)-\frac{\eta_1}{\eta_2}\mathbb{H}_l(k_1a)\mathbb{J}'_l(k_2)\right], \tag{7.45}$$

$$\lambda_l^{II} \equiv \mathbb{J}_l(k_1a)\mathbb{H}'_l(k_2a)\left[\mathbb{H}_l(k_1a)\mathbb{J}'_l(k_2a)-\frac{\eta_1}{\eta_2}\mathbb{H}'_l(k_1a)\mathbb{J}_l(k_2a)\right].. \tag{7.46}$$

Note that $\boldsymbol{X}_l^m$ and $\boldsymbol{U}_l^m$ are the eigenfunctions of the MFIE operator with eigenvalues λ_l^I and λ_l^{II}. The

resonances in the MFIE occur at the zeros of λ_l^I and λ_l^{II} for the $\boldsymbol{X}_l^m$ and $\boldsymbol{U}_l^m$ modes, respectively. As

shown in the Appendix, if $(\eta_1/\eta_2)^2 \neq 1$ then the expressions in brackets in (7.45) and (7.46) have no real

zeroes for all positive values of k_1, k_2 and $l \geq 0$. Therefore, the real zeroes of the functions λ_l^I and λ_l^{II} are

those of $\mathbb{J}'_l(k_1a)$ and $\mathbb{J}_l(k_1a)$, respectively.

The stability of the MFIE operator can be verified by observing the asymptotic behavior of its eigenvalues as the order l grows. Making use of the asymptotic forms of the Bessel and Hankel functions [52] as $l \rightarrow \infty$, it is easily shown that

$$\lim_{l\to\infty} \lambda_l^I(k_1,k_2,\eta_1,\eta_2) = \frac{\eta_1 k_1 + \eta_2 k_2}{4\eta_2 k_1}, \tag{7.47}$$

$$\lim_{l\to\infty} \lambda_l^{II}(k_1,k_2,\eta_1,\eta_2) = \frac{\eta_2 k_1 + \eta_1 k_2}{4\eta_2 k_2}. \tag{7.48}$$

3.4.2 Spectral properties of the CP-EFIE

The CP-FIE operator in (7.32) comprises terms proportional to $\mathcal{T}_0 \mathcal{T}_1 (\mathcal{K}_2 + \mathcal{I}/2)$ and $\mathcal{T}_0 (\mathcal{K}_1 + \mathcal{I}/2) \mathcal{T}_2$.

Operating the former on $\boldsymbol{X}_l^m$ and $\boldsymbol{U}_l^m$ yields

$$
\begin{aligned}
\mathcal{T}_0 \mathcal{T}_1 \left(\mathcal{K}_2 + \frac{\mathcal{I}}{2} \right) \begin{bmatrix} \boldsymbol{X}_l^m \\ \boldsymbol{U}_l^m \end{bmatrix} &= \mathcal{T}_0 \mathcal{T}_1 \begin{bmatrix} i\, \mathbb{J}_l'(k_2 a)\mathbb{H}_l(k_2 a)\boldsymbol{X}_l^m \\ -i\, \mathbb{J}_l(k_2 a)\mathbb{H}_l'(k_2 a)\boldsymbol{U}_l^m \end{bmatrix} \\
&= \mathcal{T}_0 \begin{bmatrix} -i\left(\mathbb{J}_l(k_1 a)\mathbb{H}_l(k_1 a) \right)\left(\mathbb{J}_l'(k_2 a)\mathbb{H}_l(k_2 a) \right)\boldsymbol{U}_l^m \\ -i\left(\mathbb{J}_l'(k_1 a)\mathbb{H}_l'(k_1 a) \right)\left(\mathbb{J}_l(k_2 a)\mathbb{H}_l'(k_2 a) \right)\boldsymbol{X}_l^m \end{bmatrix} \\
&= \left\{ \begin{array}{l} -i\left(\mathbb{J}_l'(ik_1 a)\mathbb{H}_l'(ik_1 a) \right)\left(\mathbb{J}_l(k_1 a)\mathbb{H}_l(k_1 a) \right)\left(\mathbb{J}_l'(k_2 a)\mathbb{H}_l(k_2 a) \right)\boldsymbol{X}_l^m \\ i\left(\mathbb{J}_l(ik_1 a)\mathbb{H}_l(ik_1 a) \right)\left(\mathbb{J}_l'(k_1 a)\mathbb{H}_l'(k_1 a) \right)\left(\mathbb{J}_l(k_2 a)\mathbb{H}_l'(k_2 a) \right)\boldsymbol{U}_l^m \end{array} \right\}
\end{aligned} \tag{7.49}
$$

Similarly, applying $\mathcal{T}_0 (\mathcal{K}_1 + \mathcal{I}/2) \mathcal{T}_2$ to these same functions yields

$$
\begin{aligned}
\mathcal{T}_0 \left(\mathcal{K}_1 + \frac{\mathcal{I}}{2} \right) \mathcal{T}_2 \begin{bmatrix} \boldsymbol{X}_l^m \\ \boldsymbol{U}_l^m \end{bmatrix} &= \mathcal{T}_0 \left(\mathcal{K}_1 + \frac{\mathcal{I}}{2} \right) \begin{bmatrix} -\mathbb{J}_l(k_2 a)\mathbb{H}_l(k_2 a)\boldsymbol{U}_l^m \\ \mathbb{J}_l'(k_2 a)\mathbb{H}_l'(k_2 a)\boldsymbol{X}_l^m \end{bmatrix} \\
&= \mathcal{T}_0 \begin{bmatrix} i\left(\mathbb{J}_l(k_1 a)\mathbb{H}_l'(k_1 a) \right)\left(\mathbb{J}_l(k_2 a)\mathbb{H}_l(k_2 a) \right)\boldsymbol{U}_l^m \\ i\left(\mathbb{J}_l'(k_1 a)\mathbb{H}_l(k_1 a) \right)\left(\mathbb{J}_l'(k_2 a)\mathbb{H}_l'(k_2 a) \right)\boldsymbol{X}_l^m \end{bmatrix} \\
&= \left\{ \begin{array}{l} i\left(\mathbb{J}_l'(ik_1 a)\mathbb{H}_l'(ik_1 a) \right)\left(\mathbb{J}_l(k_1 a)\mathbb{H}_l'(k_1 a) \right)\left(\mathbb{J}_l(k_2 a)\mathbb{H}_l(k_2 a) \right)\boldsymbol{X}_l^m \\ -i\left(\mathbb{J}_l(ik_1 a)\mathbb{H}_l(ik_1 a) \right)\left(\mathbb{J}_l'(k_1 a)\mathbb{H}_l(k_1 a) \right)\left(\mathbb{J}_l'(k_2 a)\mathbb{H}_l'(k_2 a) \right)\boldsymbol{U}_l^m \end{array} \right\}
\end{aligned} \tag{7.50}
$$

Combining (7.49) and (7.50) to obtain the CP-EFIE operator, yields an eigensystem

58

$$\left\{\frac{\eta_1}{\eta_2}\mathcal{T}_0\mathcal{T}_1\left(\mathcal{K}_2+\frac{\mathcal{I}}{2}\right)+\mathcal{T}_0\left(\mathcal{K}_1+\frac{\mathcal{I}}{2}\right)\mathcal{T}_2\right\}\begin{bmatrix} \boldsymbol{X}_l^m \\ \boldsymbol{U}_l^m \end{bmatrix}=\left\{\begin{array}{c} \gamma_l^I\boldsymbol{X}_l^m \\ \gamma_l^{II}\boldsymbol{U}_l^m \end{array}\right\}\tag{7.51}$$

where the functions $\gamma_l^I=\gamma_l^I(k_1,k_2,\eta_1,\eta_2)$ and $\gamma_l^{II}=\gamma_l^{II}(k_1,k_2,\eta_1,\eta_2)$ are

$$\gamma_l^I\equiv i\,\mathbb{H}_l(k_2a)\times\left[\mathbb{J}_l'(ik_1a)\mathbb{H}_l'(ik_1a)\mathbb{J}_l(k_1a)\right]\left[\mathbb{H}_l'(k_1a)\mathbb{J}_l(k_2a)-\frac{\eta_1}{\eta_2}\mathbb{H}_l(k_1a)\mathbb{J}_l'(k_2a)\right],\tag{7.52}$$

$$\gamma_l^{II}\equiv -i\,\mathbb{H}_l'(k_2a)\times\left[\mathbb{J}_l(ik_1a)\mathbb{H}_l(ik_1a)\mathbb{J}_l'(k_1a)\right]\left[\mathbb{H}_l(k_1a)\mathbb{J}_l'(k_2a)-\frac{\eta_1}{\eta_2}\mathbb{H}_l'(k_1a)\mathbb{J}_l(k_2a)\right].\tag{7.53}$$

Just like for the MFIE operator, $\boldsymbol{X}_l^m$ and $\boldsymbol{U}_l^m$ are eigenfunctions of the CP-EFIE operator with eigenvalues γ_l^I and γ_l^{II}. The resonances of the CP-EFIE occur at the zeros of $\mathbb{J}_l(k_1a)$ and $\mathbb{J}_l'(k_1a)$ for the $\boldsymbol{X}_l^m$ and $\boldsymbol{U}_l^m$ modes, respectively. The CP-EFIE operator has a bounded spectrum, as can be verified by observing the asymptotic behavior of its eigenvalues as $l\to\infty$:

$$\lim_{l\to\infty}\gamma_l^I(k_1,k_2,\eta_1,\eta_2)=i\left(\frac{\eta_1k_1+\eta_2k_2}{8\eta_2k_1}\right),\tag{7.54}$$

$$\lim_{l\to\infty}\gamma_l^{II}(k_1,k_2,\eta_1,\eta_2)=-i\left(\frac{\eta_2k_1+\eta_1k_2}{8\eta_2k_2}\right).\tag{7.55}$$

3.4.3 Spectral properties of the CP-CFIE

To avoid the resonances exhibited by the single source CP-EFIE or MFIE, the linear combination CP-CFIE = CP-EFIE + α MFIE is used instead. In the case of the sphere, the operator present in the CP-CFIE gives rise to the following eigensystem:

$$\left\{\text{CP-EFIE}+\alpha\,\text{MFIE}\right\}\begin{bmatrix} \boldsymbol{X}_l^m \\ \boldsymbol{U}_l^m \end{bmatrix}=\left\{\begin{array}{c} \xi_l^I\boldsymbol{X}_l^m \\ \xi_l^{II}\boldsymbol{U}_l^m \end{array}\right\}\tag{7.56}$$

where the eigenvalues $\xi_l^I=\gamma_l^I+\alpha\lambda_l^I$ and $\xi_l^{II}=\gamma_l^{II}+\alpha\lambda_l^{II}$ are

$$\xi_l^I = \gamma_l^I + \alpha\lambda_l^I$$
$$= \mathbb{H}_l(k_2a)\left[\alpha\mathbb{J}_l'(k_1a) + i\,\mathbb{J}_l'(ik_1a)\mathbb{H}_l'(ik_1a)\mathbb{J}_l(k_1a)\right]$$

$$\times\left[\mathbb{J}_l(k_2a)\mathbb{H}_l'(k_1a) - \frac{\eta_1}{\eta_2}\mathbb{J}_l'(k_2a)\mathbb{H}_l(k_1a)\right]$$

(7.57)

$$\xi_l^{II} = \gamma_l^{II} + \alpha\lambda_l^{II}$$
$$= \mathbb{H}_l'(k_2a)\left[\alpha\mathbb{J}_l(k_1a) - i\,\mathbb{J}_l(ik_1a)\mathbb{H}_l(ik_1a)\mathbb{J}_l'(k_1a)\right].$$

$$\times\left[\mathbb{J}_l'(k_2a)\mathbb{H}_l(k_1a) - \frac{\eta_1}{\eta_2}\mathbb{J}_l(k_2a)\mathbb{H}_l'(k_1a)\right]$$

(7.58)

ξ_l^I and ξ_l^{II} have no zeros for all real and positive values of k_1 and k_2, and for any order $l \geq 0$, as long as $(\eta_1/\eta_2)^2 \neq 1$ and α is a real positive number (see Section 3.4.4). As expected, the CP-CFIE operator has a bounded spectrum, which can be verified from the asymptotic behavior of ξ_l^I and ξ_l^{II}:

$$\lim_{l\to\infty}\xi_l^I(k_1,k_2,\eta_1,\eta_2) = \left(\alpha + \frac{i}{2}\right)\left(\frac{\eta_1 k_1 + \eta_2 k_2}{4\eta_2 k_1}\right),$$

(7.59)

$$\lim_{l\to\infty}\xi_l^{II}(k_1,k_2,\eta_1,\eta_2) = \left(\alpha - \frac{i}{2}\right)\left(\frac{\eta_1 k_1 + \eta_2 k_2}{4\eta_2 k_1}\right).$$

(7.60)

3.4.4   Proof of the resonance-free of CP-CFIE

Proving that the CP-CFIE formulation is resonant free for the case of a sphere, is equivalent to proving that the eigenvalues ξ_l^I and ξ_l^{II} (defined in eqns. (7.57) and (7.58), respectively) are non-zero for all positive values of the real wavenumbers k_1 and k_2; and for every order $l \geq 0$. Instead of proving it separately for each eigenvalue, a proof for both can be accomplished by showing that the product $\xi_l^I \overline{\xi}_l^{II}$ is non-zero. Here and in what follows, for any complex number z, $\overline{z}$ denotes its complex conjugate. For the sake of clarity, the following notation is established:

$$\xi_l^I = \mathbb{H}(k_2a)\,x_l^I y_l^I,$$

(7.61)

$$\xi_l^{II} = \mathbb{H}'(k_2a)\,x_l^{II} y_l^{II},$$

(7.62)

where

$$x_l^I = \mathbb{J}_l(k_2 a) \mathbb{H}_l'(k_1 a) - \frac{\eta_1}{\eta_2} \mathbb{J}_l'(k_2 a) \mathbb{H}_l(k_1 a) , \tag{7.63}$$

$$x_l^{II} = \mathbb{J}_l'(k_2 a) \mathbb{H}_l(k_1 a) - \frac{\eta_1}{\eta_2} \mathbb{J}_l(k_2 a) \mathbb{H}_l'(k_1 a) , \tag{7.64}$$

$$y_l^I = \alpha \mathbb{J}_l'(k_1 a) + i \mathbb{J}_l'(ik_1 a) \mathbb{H}_l'(ik_1 a) \mathbb{J}_l(k_1 a) , \tag{7.65}$$

and

$$y_l^{II} = \alpha \mathbb{J}_l(k_1 a) - i \mathbb{J}_l(ik_1 a) \mathbb{H}_l(ik_1 a) \mathbb{J}_l'(k_1 a) . \tag{7.66}$$

With this notation, the product $\xi_l^I \overline{\xi}_l^{II}$ can be decomposed into

$$\xi_l^I \overline{\xi}_l^{II} = \mathbb{H}_l(k_2 a) \overline{\mathbb{H}}_l'(k_2 a) \left[x_l^I \overline{x}_l^{II} \right] \left[y_l^I \overline{y}_l^{II} \right] . \tag{7.67}$$

For $\xi_l^I \overline{\xi}_l^{II}$ to be non-zero, all the partial products in (7.67) have to be non-zero, i.e.,

$\mathbb{H}_l(k_2 a) \overline{\mathbb{H}}_l'(k_2 a) \neq 0$, $x_l^I \overline{x}_l^{II} \neq 0$, and $y_l^I \overline{y}_l^{II} \neq 0$. In what follows, each of these three products is shown to

have no zeros.

(i.) The product $\mathbb{H}_l(k_2 a) \overline{\mathbb{H}}_l'(k_2 a)$ is non-zero for all positive values of k_2 and for $l \geq 0$:

$$\begin{aligned} \mathbb{H}_l(k_2 a) \overline{\mathbb{H}}_l'(k_2 a) &= \left(\mathbb{J}_l(k_2 a) + i \mathbb{Y}_l(k_2 a) \right) \left(\mathbb{J}_l'(k_2 a) - i \mathbb{Y}_l'(k_2 a) \right) \\ &= \mathbb{J}_l'(k_2 a) \mathbb{J}_l(k_2 a) + \mathbb{Y}_l'(k_2 a) \mathbb{Y}_l(k_2 a) \\ &\quad - i \left(\mathbb{J}_l(k_2 a) \mathbb{Y}_l'(k_2 a) - \mathbb{J}_l'(k_2 a) \mathbb{Y}_l(k_2 a) \right) \end{aligned} \tag{7.68}$$

Note that $\mathbb{J}_l(k_2 a) \mathbb{Y}_l'(k_2 a) - \mathbb{J}_l'(k_2 a) \mathbb{Y}_l(k_2 a)$ is nothing but the Wronskian between $\mathbb{J}_l(k_2 a)$ and $\mathbb{Y}_l(k_2 a)$

[49], which is equal to one. Thus, above equation renders into

$$\mathbb{H}_l(k_2 a) \overline{\mathbb{H}}_l'(k_2 a) = \mathbb{J}_l'(k_2 a) \mathbb{J}_l(k_2 a) + \mathbb{Y}_l'(k_2 a) \mathbb{Y}_l(k_2 a) - i . \tag{7.69}$$

It follows that the imaginary part of the product $\mathbb{H}_l(k_2 a) \overline{\mathbb{H}}_l'(k_2 a)$ is equal to -1, regardless of the value of

k_2 or l.

(ii.) If $(\eta_1 / \eta_2)^2 \neq 1$, the product $x_l^I \overline{x}_l^{II}$ is non-zero for all positive values of k_1, k_2, and for $l \geq 0$:

61

$$x_l^I \overline{x}_l^{II} = \left[\mathbb{J}_l(k_2 a) \mathbb{H}_l'(k_1 a) - \frac{\eta_1}{\eta_2} \mathbb{J}_l'(k_2 a) \mathbb{H}_l(k_1 a) \right] \left[\mathbb{J}_l'(k_2 a) \overline{\mathbb{H}}_l(k_1 a) - \frac{\eta_1}{\eta_2} \mathbb{J}_l(k_2 a) \overline{\mathbb{H}}_l'(k_1 a) \right]$$

$$= \mathbb{J}_l(k_2 a) \mathbb{J}_l'(k_2 a) \left[\mathbb{H}_l'(k_1 a) \overline{\mathbb{H}}_l(k_1 a) + \left(\frac{\eta_1}{\eta_2} \right)^2 \mathbb{H}_l(k_1 a) \overline{\mathbb{H}}_l'(k_1 a) \right] \tag{7.70}$$

$$- \frac{\eta_1}{\eta_2} \left[\left| \mathbb{J}_l(k_2 a) \right|^2 \left| \mathbb{H}_l'(k_1 a) \right|^2 + \left| \mathbb{J}_l'(k_2 a) \right|^2 \left| \mathbb{H}_l(k_1 a) \right|^2 \right].$$

The product $\mathbb{H}_l'(k_1 a) \overline{\mathbb{H}}_l(k_1 a)$ can be expanded into

$$\mathbb{H}_l'(k_1 a) \overline{\mathbb{H}}_l(k_1 a) = \left(\mathbb{J}_l'(k_1 a) + i \, \mathbb{Y}_l'(k_1 a) \right) \left(\mathbb{J}_l(k_1 a) - i \, \mathbb{Y}_l(k_1 a) \right)$$

$$= \mathbb{J}_l'(k_1 a) \mathbb{J}_l(k_1 a) + \mathbb{Y}_l'(k_1 a) \mathbb{Y}_l(k_1 a) + i \left(\mathbb{J}_l(k_1 a) \mathbb{Y}_l'(k_1 a) - \mathbb{J}_l'(k_1 a) \mathbb{Y}_l(k_1 a) \right). \tag{7.71}$$

Now, using the Wronskian between $\mathbb{J}_l(k_1 a)$ and $\mathbb{Y}_l(k_1 a)$ the above equation renders into

$$\mathbb{H}_l'(k_1 a) \overline{\mathbb{H}}_l(k_1 a) = \mathbb{J}_l'(k_1 a) \mathbb{J}_l(k_1 a) + \mathbb{Y}_l'(k_1 a) \mathbb{Y}_l(k_1 a) + i \tag{7.72}$$

Similarly, the product $\mathbb{H}_l(k_1 a) \overline{\mathbb{H}}_l'(k_1 a)$ is found to be

$$\mathbb{H}_l(k_1 a) \overline{\mathbb{H}}_l'(k_1 a) = \mathbb{J}_l'(k_1 a) \mathbb{J}_l(k_1 a) + \mathbb{Y}_l'(k_1 a) \mathbb{Y}_l(k_1 a) - i \tag{7.73}$$

Thus, equation (7.70) is reduced to

$$x_l^I \overline{x}_l^{II} = \mathbb{J}_l(k_2 a) \mathbb{J}_l'(k_2 a) \left[\mathbb{J}_l'(k_1 a) \mathbb{J}_l(k_1 a) + \mathbb{Y}_l'(k_1 a) \mathbb{Y}_l(k_1 a) \right] \left[1 + \left(\frac{\eta_1}{\eta_2} \right)^2 \right]$$

$$- \frac{\eta_1}{\eta_2} \left[\left| \mathbb{J}_l(k_2 a) \right|^2 \left| \mathbb{H}_l'(k_1 a) \right|^2 + \left| \mathbb{J}_l'(k_2 a) \right|^2 \left| \mathbb{H}_l(k_1 a) \right|^2 \right] + i \, \mathbb{J}_l(k_2 a) \mathbb{J}_l'(k_2 a) \left[1 - \left(\frac{\eta_1}{\eta_2} \right)^2 \right]. \tag{7.74}$$

As can be seen in (7.74), the imaginary part of $x_l^I \overline{x}_l^{II}$ vanishes either at the zeros of $\mathbb{J}_l(k_2 a)$ or at the zeros of $\mathbb{J}_l'(k_2 a)$, as long as $(\eta_1 / \eta_2)^2 \neq 1$. On the one hand, at a zero of $\mathbb{J}_l(k_2 a)$, the real part of $x_l^I \overline{x}_l^{II}$ equals $-(\eta_1 / \eta_2) \left| \mathbb{J}_l'(k_2 a) \right|^2 \left| \mathbb{H}_l(k_1 a) \right|^2 \neq 0$. On the other hand, at a zero of $\mathbb{J}_l'(k_2 a)$, the real part of $x_l^I \overline{x}_l^{II}$ equals $-(\eta_1 / \eta_2) \left| \mathbb{J}_l(k_2 a) \right|^2 \left| \mathbb{H}_l'(k_1 a) \right|^2 \neq 0$. It follows that real and imaginary parts of $x_l^I \overline{x}_l^{II}$ do not vanish simultaneously, i.e., it has no zeros.

(iii.) For α real and positive, the product $y_l^I \overline{y}_l^{II}$ is non-zero for all positive values of k_1 and for $l \geq 0$:

$$
\begin{aligned}
y_l^I \overline{y}_l^{II} &= \left[\alpha \mathbb{J}_l'(k_1 a) + i\, \mathbb{J}_l'(ik_1 a)\mathbb{H}_l'(ik_1 a)\mathbb{J}_l(k_1 a) \right] \\
&\quad \times \left[\alpha \mathbb{J}_l(k_1 a) + i\, \overline{\mathbb{J}}_l(ik_1 a)\overline{\mathbb{H}}_l(ik_1 a)\mathbb{J}_l'(k_1 a) \right] \\
&= \mathbb{J}_l(k_1 a)\mathbb{J}_l'(k_1 a)\left[\alpha^2 - \overline{\mathbb{J}}_l(ik_1 a)\overline{\mathbb{H}}_l(ik_1 a)\mathbb{J}_l'(ik_1 a)\mathbb{H}_l'(ik_1 a) \right] \\
&\quad + i\left[\alpha \left| \mathbb{J}_l'(k_1 a) \right|^2 \overline{\mathbb{J}}_l(ik_1 a)\overline{\mathbb{H}}_l(ik_1 a) + \left| \mathbb{J}_l(k_1 a) \right|^2 \mathbb{J}_l'(ik_1 a)\mathbb{H}_l'(ik_1 a) \right].
\end{aligned}
\tag{7.75}
$$

It is straightforward to show [49] that for real values of k_1,

$$
\mathbb{J}_l(ik_1 a) = i^{l+1}\sqrt{\frac{\pi k_1 a}{2}}\, I_{l+1/2}(k_1 a) ,
\tag{7.76}
$$

and

$$
\mathbb{H}_l(ik_1 a) = \frac{-i^{l+1}}{(-1)^l}\sqrt{\frac{2k_1 a}{\pi}}\, K_{l+1/2}(k_1 a) .
\tag{7.77}
$$

Here, the functions $I_\nu(z)$ and $K_\nu(z)$ are the modified Bessel functions of first and second kind, respectively. These functions are real and positive for real positive values of ν and z. Unlike ordinary Bessel functions, which are oscillating functions of a real argument z, $I_\nu(z)$ and $K_\nu(z)$ are exponentially growing and decaying functions, respectively; therefore, they have no zeros except (maybe) for the origin [49]. With (7.76) and (7.77) the product $\overline{\mathbb{H}}_l(ik_1 a)\overline{\mathbb{J}}_l(ik_1 a)$ is given by

$$
\overline{\mathbb{H}}_l(ik_1 a)\overline{\mathbb{J}}_l(ik_1 a) = (k_1 a)I_{l+1/2}(k_1 a)K_{l+1/2}(k_1 a) ,
\tag{7.78}
$$

which is real and positive for all positive values of k_1, and for every non-negative order l. Similar arguments apply to the product $\mathbb{H}_l'(ik_1 a)\mathbb{J}_l'(ik_1 a)$, which is also real and positive for all positive values of k_1, and for every non-negative order l. With the above results, it is clear that the imaginary part of $y_l^I \overline{y}_l^{II}$,

$$
\mathrm{Im}\left\{ y_l^I \overline{y}_l^{II} \right\} = \alpha \left| \mathbb{J}_l'(k_1 a) \right|^2 \overline{\mathbb{J}}_l(ik_1 a)\overline{\mathbb{H}}_l(ik_1 a) + \left| \mathbb{J}_l(k_1 a) \right|^2 \mathbb{J}_l'(ik_1 a)\mathbb{H}_l'(ik_1 a)
\tag{7.79}
$$

is non-zero for all $k_1 > 0$, as long as α is a real positive number.

3.5 Discretization of the CP-CFIE

The Galerkin discretization of standard dual source integral equations for analyzing scattering from dielectric objects calls for the discretization of $\mathcal{T}_j$ and $\mathcal{K}_j$. Typically, $\mathcal{T}_j$ is discretized using div-conforming basis functions $\boldsymbol{f}_n^{Q}(\boldsymbol{r}), n = 1,...,N$ and curl-conforming test functions $\hat{\boldsymbol{n}}_r \times \boldsymbol{f}_n^{Q}$, yielding the $N \times N$ matrix $\mathbf{T}_j^{nQ;Q}$ with entries

$$(\mathbf{T}_j^{nQ;Q})_{m,n} = \left\langle \hat{\boldsymbol{n}}_r \times \boldsymbol{f}_m^{Q}, \mathcal{T}_j[\boldsymbol{f}_n^{Q}] \right\rangle. \tag{7.80}$$

Note that eqn. (7.80) is essentially (6.8), but with a notation that allows for more flexibility in the exposition of the topics discussed in this chapter. The superscript Q indicates the type of functions $\boldsymbol{f}_n^{Q}$ used, and nQ refers to functions $\hat{\boldsymbol{n}}_r \times \boldsymbol{f}_n^{Q}$. The choice Q = GWP($p$) is particularly popular. The operator $\mathcal{K}_j$ often is discretized using div-conforming basis functions and either div- or curl-conforming test functions (depending on the role $\mathcal{K}_j$ plays in the equation), yielding the matrices $\mathbf{K}_j^{Q';Q}$ and $\mathbf{K}_j^{nQ';Q}$ with entries

$$(\mathbf{K}_j^{Q';Q})_{m,n} = \left\langle \boldsymbol{f}_m^{Q'}, \mathcal{K}_j[\boldsymbol{f}_n^{Q}] \right\rangle, \tag{7.81}$$

$$(\mathbf{K}_j^{nQ';Q})_{m,n} = \left\langle \hat{\boldsymbol{n}}_r \times \boldsymbol{f}_m^{Q'}, \mathcal{K}_j[\boldsymbol{f}_n^{Q}] \right\rangle. \tag{7.82}$$

In (7.81)-(7.82), it is not necessary that Q = Q'.

Unfortunately, discretization schemes applicable to standalone operators do not immediately apply to the double or triple operator products. In this section, a discretization scheme for products of two operators is presented first. The scheme is trivially extended to products of three or more operators. The product of any two operators $\mathcal{A}$ and $\mathcal{B}$ is discretized as

$$\left(\mathcal{A}\mathcal{B}\right)_{dis} = \mathbf{A}^{Q;Q'}\,\mathbf{G}_{Q'';Q'}^{-1}\,\mathbf{B}^{Q'';Q'''}\,, \tag{7.83}$$

where $\mathbf{A}^{Q;Q'}$ and $\mathbf{B}^{Q'';Q'''}$ are matrices obtained by discretizing the standalone operators $\mathcal{A}$ and $\mathcal{B}$ by means two sets of suitable basis and testing functions $\{Q;Q'\}$ and $\{Q'';Q'''\}$, and $\mathbf{G}_{Q'';Q'}$ is the mixed Gram matrix between the functions Q'' (that test $\mathcal{B}$) and Q' (that source $\mathcal{A}$):

$$(\mathbf{G}_{Q'';Q'})_{m,n} = \left\langle \boldsymbol{f}_m^{Q''}, \boldsymbol{f}_n^{Q'} \right\rangle. \tag{7.84}$$

The inverse of this Gram matrix accounts for the possible lack of (bi-)orthogonality between the sets Q' and Q''. For example, using this scheme, the operator product $\mathcal{T}_1\mathcal{K}_2$ in (7.29) could be discretized as

$$\left(\mathcal{T}_1\mathcal{K}_2 \right)_{dis} = \mathbf{T}_1^{nGWP;GWP} \mathbf{G}_{GWP;GWP}^{-1} \mathbf{K}_2^{GWP;GWP}. \tag{7.85}$$

Note that in (7.85) and in the remainder of this chapter, the set GWP(p) is denoted by GWP. The Gram matrix $\mathbf{G}_{GWP;GWP}$ is known to be well-conditioned; as a result its inverse can be applied to a vector by using just a few iterations of an iterative solver.

A different situation is encountered when this discretization scheme is used for operator products of the form $\mathcal{T}_i\mathcal{T}_j$ present in (7.30) and (7.32). As explained in Section 2.1.2, if Q = GWP is used to discretize both $\mathcal{T}_i$ and $\mathcal{T}_j$, the mixed Gram matrix $\mathbf{G}_{nGWP;GWP}$ is singular and therefore the action of its inverse cannot be evaluated. Here, the CMP idea exposed in the previous chapter is used to discretize $\mathcal{T}_i\mathcal{T}_j$ as

$$\left(\mathcal{T}_i\mathcal{T}_j \right)_{dis} = \mathbf{T}_i^{nDQCC;DQCC} \mathbf{G}_{nGWP;DQCC}^{-1} \mathbf{T}_j^{nGWP;GWP}, \tag{7.86}$$

where GWP and DQCC functions are used to discretize $\mathcal{T}_j$ and $\mathcal{T}_i$, respectively.

With the above discretization scheme, the single source MFIE (7.30) can be discretized as

$$\frac{\eta_1}{\eta_2}\left(\frac{\mathbf{K}_1^{nDQCC;GWP}}{2} + \mathbf{K}_1^{nDQCC;GWP} \mathbf{G}_{GWP;GWP}^{-1} \mathbf{K}_2^{GWP;GWP} + \frac{\mathbf{K}_2^{nDQCC;GWP}}{2} + \frac{\mathbf{G}_{nDQCC;GWP}}{4} \right)\mathbf{I}$$
$$- \left(\mathbf{T}_1^{nDQCC;DQCC} \mathbf{G}_{nGWP;DQCC}^{-1} \mathbf{T}_2^{nGWP;GWP} \right)\mathbf{I} = -\eta_1\mathbf{V}_M, \tag{7.87}$$

where the elements of the vector $\mathbf{V}_M$ are

$$(\mathbf{V}_M)_m = \left\langle \hat{\boldsymbol{n}}_r \times \boldsymbol{f}_m^{\mathrm{DQCC}}, \hat{\boldsymbol{n}}_r \times \boldsymbol{H}^{inc} \right\rangle \tag{7.88}$$

and the elements of $(\mathbf{I})_n = I_n$ are the expansion coefficients of $\boldsymbol{J}_2$ in terms of GWP basis functions:

$$\boldsymbol{J}_2(\boldsymbol{r}) = \sum_{n=1}^{N} I_n \boldsymbol{f}_n^{\mathrm{GWP}}(\boldsymbol{r}) . \tag{7.89}$$

The matrix $\mathbf{G}_{\mathrm{nDQCC;GWP}}$, which discretizes the identity operator $\mathcal{I}$, is nothing but the Gram matrix between curl-conforming DQCC and div-conforming GWP basis functions.

As the discretization scheme for operator products presented here allows for the independent discretization of each standalone operator (and also provides us with a well-conditioned mapping between bases), the extension to the product of three (or even more) operators is straightforward. Using the same ideas described above, the CP-EFIE can be discretized as

$$
\begin{aligned}
&\left(\frac{\eta_1}{\eta_2} \frac{\mathbf{T}_0^{\mathrm{nDQCC;DQCC}} \, \mathbf{G}_{\mathrm{nGWP;DQCC}}^{-1} \, \mathbf{T}_1^{\mathrm{nGWP;GWP}}}{2} + \frac{\eta_1}{\eta_2} \mathbf{T}_0^{\mathrm{nDQCC;DQCC}} \, \mathbf{G}_{\mathrm{nGWP;DQCC}}^{-1} \, \mathbf{T}_1^{\mathrm{nGWP;GWP}} \, \mathbf{G}_{\mathrm{GWP;GWP}}^{-1} \, \mathbf{K}_2^{\mathrm{GWP;GWP}} \right. \\
&\left. + \mathbf{T}_0^{\mathrm{nDQCC;DQCC}} \, \mathbf{G}_{\mathrm{nGWP;DQCC}}^{-1} \, \mathbf{K}_1^{\mathrm{nGWP;DQCC}} \, \mathbf{G}_{\mathrm{nGWP;DQCC}}^{-1} \, \mathbf{T}_2^{\mathrm{nGWP;GWP}} + \frac{\mathbf{T}_0^{\mathrm{nDQCC;DQCC}} \, \mathbf{G}_{\mathrm{nGWP;DQCC}}^{-1} \, \mathbf{T}_2^{\mathrm{nGWP;GWP}}}{2} \right) \mathbf{I} \quad (7.90) \\
&= \mathbf{T}_0^{\mathrm{nDQCC;DQCC}} \, \mathbf{G}_{\mathrm{nGWP;DQCC}}^{-1} \, \mathbf{V}_E,
\end{aligned}
$$

where the elements of the vector $\mathbf{V}_E$ are

$$(\mathbf{V}_E)_m = \left\langle \hat{\boldsymbol{n}}_r \times \boldsymbol{f}_m^{\mathrm{GWP}}, \hat{\boldsymbol{n}}_r \times \boldsymbol{E}^{inc} \right\rangle. \tag{7.91}$$

Of course, the discretized CP-CFIE is obtained by linearly combining (7.87) and (7.90).

Using the transformation matrices $\mathbf{P}$ and $\mathbf{R}$ defined in Section 2.4, the matrices $\mathbf{K}_j^{\mathrm{nDQCC;GWP}}$, $\mathbf{K}_j^{\mathrm{GWP;GWP}}$, $\mathbf{K}_j^{\mathrm{nGWP;DQCC}}$, $\mathbf{T}_j^{\mathrm{nDQCC;DQCC}}$, and $\mathbf{T}_j^{\mathrm{nGWP;GWP}}$ can be expressed as

$$
\begin{aligned}
\mathbf{K}_j^{\mathrm{nDQCC;GWP}} &= \mathbf{P}^{\mathrm{T}} \, \bar{\mathbf{K}}_j^{\mathrm{nGWP;GWP}} \, \mathbf{R}, \\
\mathbf{K}_j^{\mathrm{GWP;GWP}} &= \mathbf{R}^{\mathrm{T}} \, \bar{\mathbf{K}}_j^{\mathrm{GWP;GWP}} \, \mathbf{R}, \\
\mathbf{K}_j^{\mathrm{nGWP;DQCC}} &= \mathbf{R}^{\mathrm{T}} \, \bar{\mathbf{K}}_j^{\mathrm{nGWP;GWP}} \, \mathbf{P},
\end{aligned} \tag{7.92}
$$

$$\mathbf{T}_j^{\text{nDQCC;DQCC}} = \mathbf{P}^{\text{T}} \, \overline{\mathbf{T}}_j^{\text{nGWP;GWP}} \, \mathbf{P},$$
$$\mathbf{T}_j^{\text{nGWP;GWP}} = \mathbf{R}^{\text{T}} \, \overline{\mathbf{T}}_j^{\text{nGWP;GWP}} \, \mathbf{R},$$

$$(7.93)$$

where the matrices $\overline{\mathbf{K}}_j^{\text{nGWP;GWP}}$, $\overline{\mathbf{K}}_j^{\text{GWP;GWP}}$, and $\overline{\mathbf{T}}_j^{\text{nGWP;GWP}}$ are obtained through a standard discretization of

the operators $\mathcal{T}_j$ and $\mathcal{K}_j$ on $\overline{S}_\delta$.

In conclusion, the iterative solution of the proposed CP-CFIE only requires the multiplication of

$\overline{\mathbf{K}}_j^{\text{nGWP;GWP}}$, $\overline{\mathbf{K}}_j^{\text{GWP;GWP}}$ ($j = 1,2$) and $\overline{\mathbf{T}}_j^{\text{nGWP;GWP}}$ ($j = 0,1,2$) by vectors. A careful analysis reveals that only 9

multiplications are required. Of course, all of these matrices can be computed (and compressed) using

standard MoM codes provided with $\overline{S}_\delta$, instead of S_δ. The transformation matrices $\mathbf{P}$ and $\mathbf{R}$ are highly

sparse and can be multiplied by a vector in $O(N)$ operations.

3.6 Numerical Results

This section presents several examples that demonstrate the effectiveness of the proposed CP-CFIE and

the discretization scheme used for discretizing it. The results especially focus on the two most relevant

features of the CP-CFIE: its immunity to resonance frequencies and dense-mesh breakdown. All results

shown here were obtained using $\alpha = 0.5$.

3.6.1 Resonant frequencies of single source formulations

The first examples show that the CP-CFIE is resonance free for spherical and cubical scatterers. The

first example involves a dielectric sphere of radius 1 m and permittivity $\epsilon_2 = 2\epsilon_1$, with

$\epsilon_1 = \epsilon_0 = 8.854187 \times 10^{-12}$ F/m. The condition number of the impedance matrices obtained by discretizing

four single source equations (EFIE, MFIE, CFIE, and CP-CFIE) is plotted versus frequency in Fig. III.2.

As expected, the matrices obtained by discretizing the EFIE and MFIE become ill-conditioned in the

vicinity of the resonant frequencies of a spherical PEC cavity of radius 1 m. On the other hand, those

obtained by discretizing the CFIE and CP-CFIE are free from these resonances.
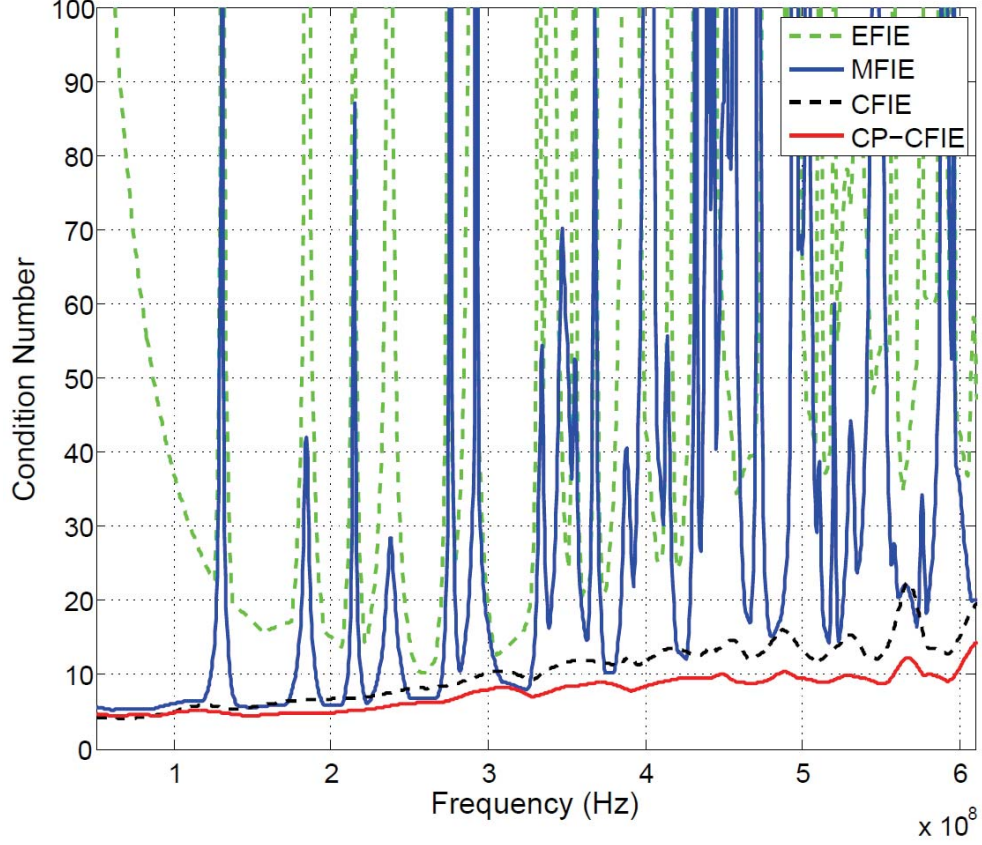
Fig. III.2. Condition number versus frequency for the sphere example of the impedance matrices obtained for four different formulations: EFIE, MFIE, CFIE, and CP-CFIE.

Although the analytical results presented here are limited to the case of a dielectric sphere, numerical experiments show that these results also hold true for other (more complex) geometries. The second example involves a dielectric cube of side 1 m and permittivity $\epsilon_2 = 2\epsilon_1$ with $\epsilon_1 = \epsilon_0$. This geometry, like most targets of practical interest, involves edges. The condition numbers of the system matrices derived from for the various formulations are plotted in Fig. III.3. These results suggest that for a cube, the four single source formulations behave in the same way they do when used for a sphere. In particular, the CP-CFIE remains resonant free.
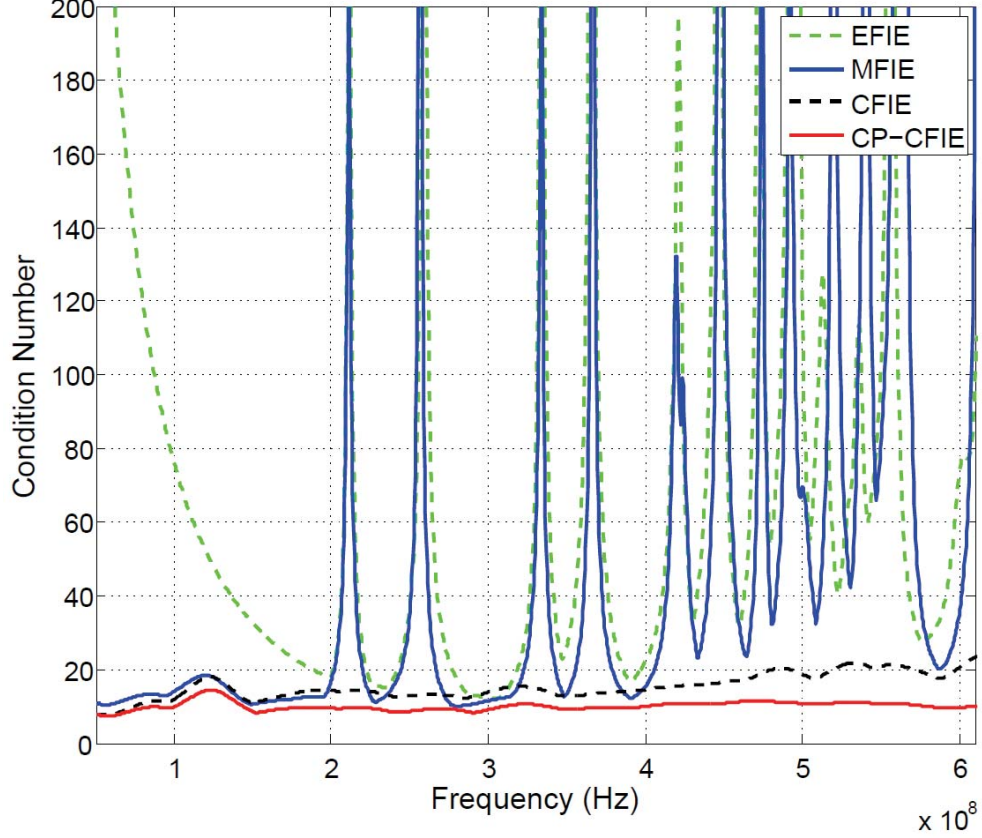
Fig. III.3. Condition number versus frequency for the cube example of the impedance matrices obtained for four different formulations: EFIE, MFIE, CFIE, and CP-CFIE.

3.6.2 Dense-mesh breakdown in CFIEs

Although both the CFIE and CP-CFIE are resonant free, the latter does not suffer from dense-mesh breakdown, while the former does. This advantage of the CP-CFIE over the CFIE becomes significant when the penetrable object has sub-wavelength geometric features. Consider a dielectric sphere of radius $R = \lambda / 20$ and permittivity $\epsilon_2 = 2\epsilon_1$ with $\epsilon_1 = \epsilon_0$. The sphere is illuminated by an x-polarized plane wave propagating in the z direction. Fig. III.4 shows the residual error versus iteration count achieved by a TFQMR solver [53] during the iterative solution of the matrix systems obtained by discretizing CFIE and CP-CFIE. The simulation is repeated for five discretizations with minimum edge size ranging from $\delta = \lambda / 400$ to $\delta = \lambda / 2000$. The number of unknowns ranges from $N = 153$ to $N = 1080$, respectively. For the CFIE, the convergence rate deteriorates as $\delta \to 0$, and the number of iterations needed to reach a

relative residual error of 10^{-5} increases. The CP-CFIE exhibits a convergence rate that is independent of the discretization and a low number of iterations.
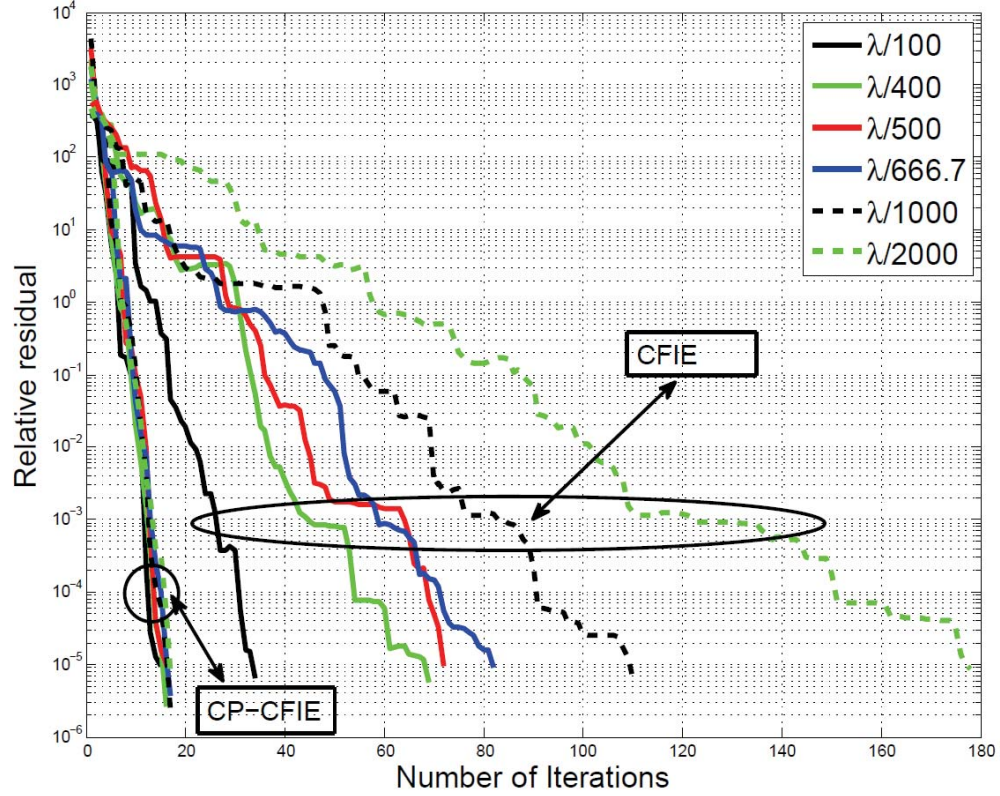
Fig. III.4. Residual history of CFIE and CP-CFIE for different discretizations of the surface of a sphere of radius 1 m.

3.6.3   Broadband T-shaped dielectric resonator antenna

The final example involves the T-shaped dielectric resonator antenna (DRA) shown in Fig. III.5(a)-(d) [50]. The DRA has an equilateral-triangular shape, and is placed on a square ground plane of side $L_3 = 260$ mm. The permittivity of the DRA is $\epsilon_2 = 9.2\epsilon_1$ with $\epsilon_1 = \epsilon_0$. The two equilateral triangle cross sections have heights $h_1 = 12.0$ mm and $h_2 = 18.0$ mm, and side lengths of $L_1 = 25.0$ mm and $L_2 = 64.0$ mm. The antenna is fed by a z-directed coaxial probe located at the center of both triangles. The probe's length is $h = 11.0$ mm and its radius is 0.38 mm. Note that the formulation presented here is not suitable for different penetrable objects touching a PEC or each other. Thus, in this example, an artificial gap of 0.5 mm. was introduced between the DRA and the PEC surfaces.

For an excitation frequency $f = 1.6$ GHz, the equivalent electric current density $\boldsymbol{J}_1$ is shown in Fig. III.6(a)-(b). Similarly, the equivalent magnetic current density $\boldsymbol{M}_1$ is shown in Fig. III.7(a)-(b). Fig. III.8(a)-(c) show the antenna's normalized radiation patterns in the three principal planes, also for an excitation frequency of $f = 1.6$ GHz. Fig. III.9(a)-(c) show the normalized radiation patterns for an excitation frequency of $f = 3.1$ GHz. For this example, the CP-CFIE was used for the dielectric surface, and the CMP-EFIE for the PEC surface. The matrix system obtained after discretizing both equations was solved (iteratively) using a TFQMR solver. For the mesh in Fig. III.5(c-d), the total number of unknowns is approximately 15000, and the minimum edge length of 0.23 mm. The results obtained with a coupled surface-volume integral equation solver [51][52] are also displayed for both frequencies.
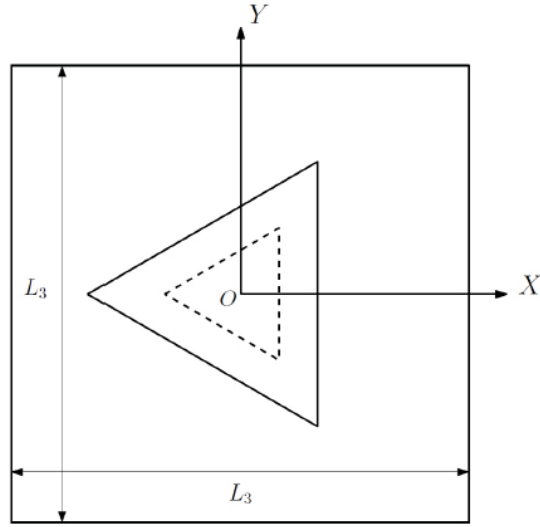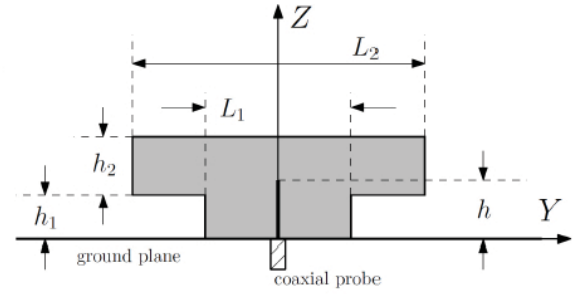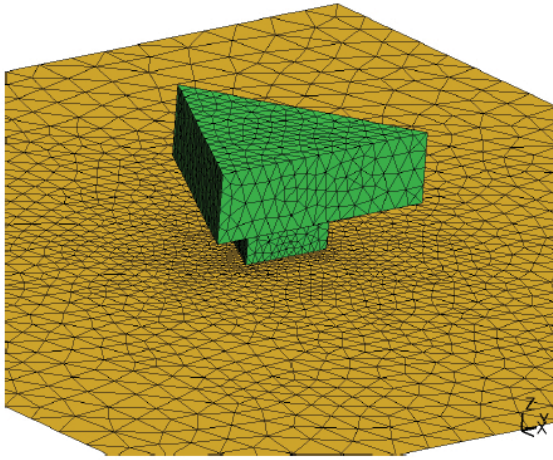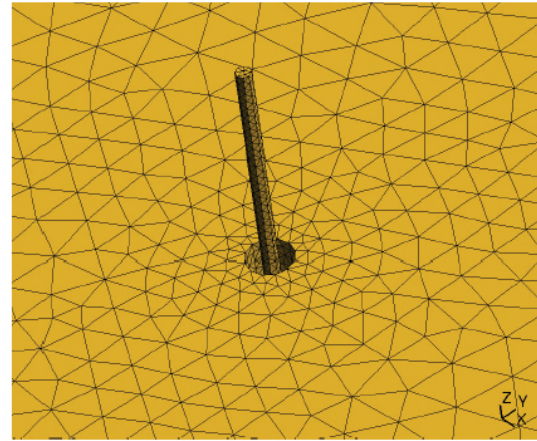
Fig. III.5. Broadband T-shaped DRA with equilateral-triangle cross sections. (a) Top view of schematic diagram. (b) Side view of schematic diagram. (c) Perspective view of the mesh used for the simulations. (d) Detailed view of the coaxial probe feed. A gap of 0.5 mm. exists between the dielectric and PEC surfaces.
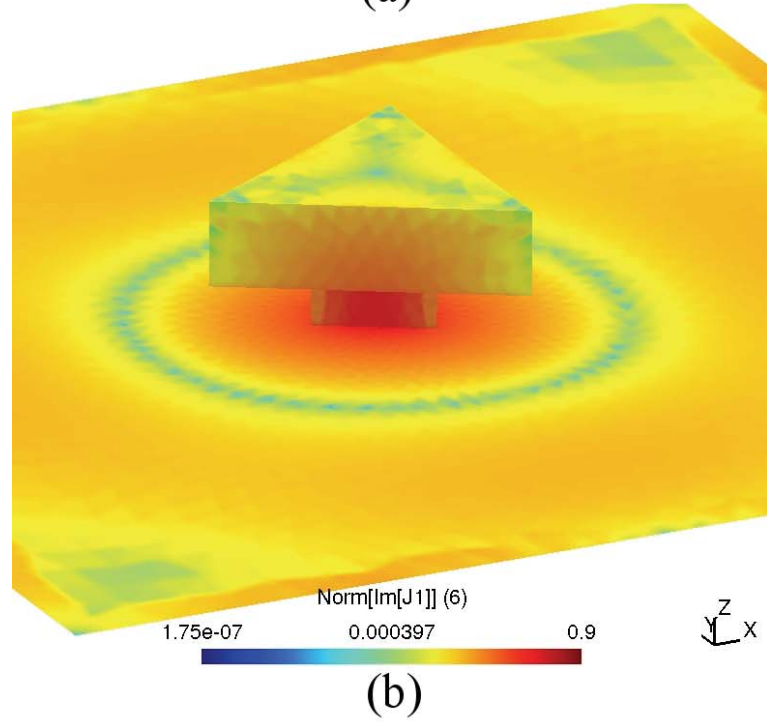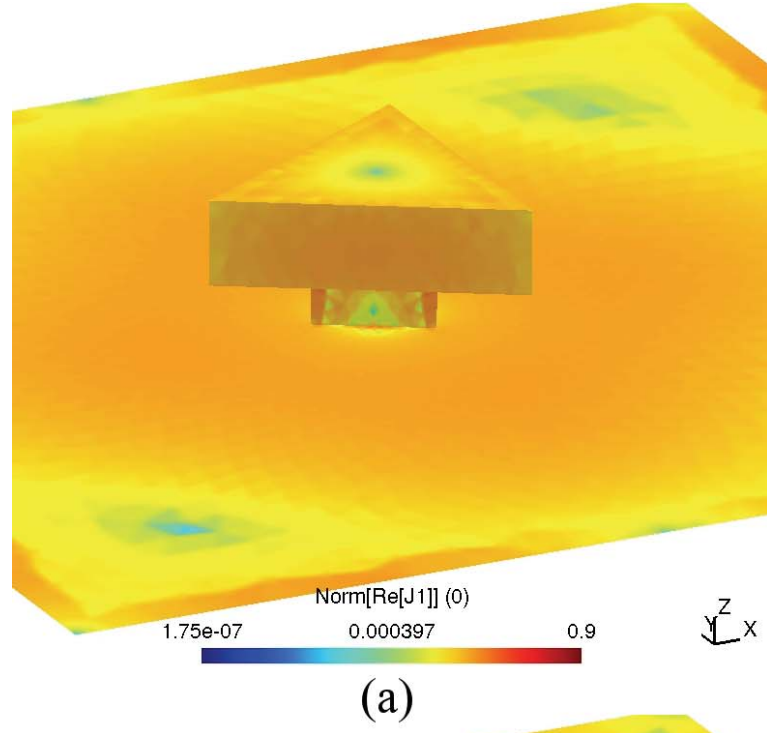
Fig. III.6. Equivalent electric current density J_1 for the example of Broadband T-shaped DRA with equilateral-triangle cross sections operating at 1.6 GHz. (a) Norm of the real part of J_1. (b) Norm of the imaginary part of J_1. Plots are in logarithmic scale.
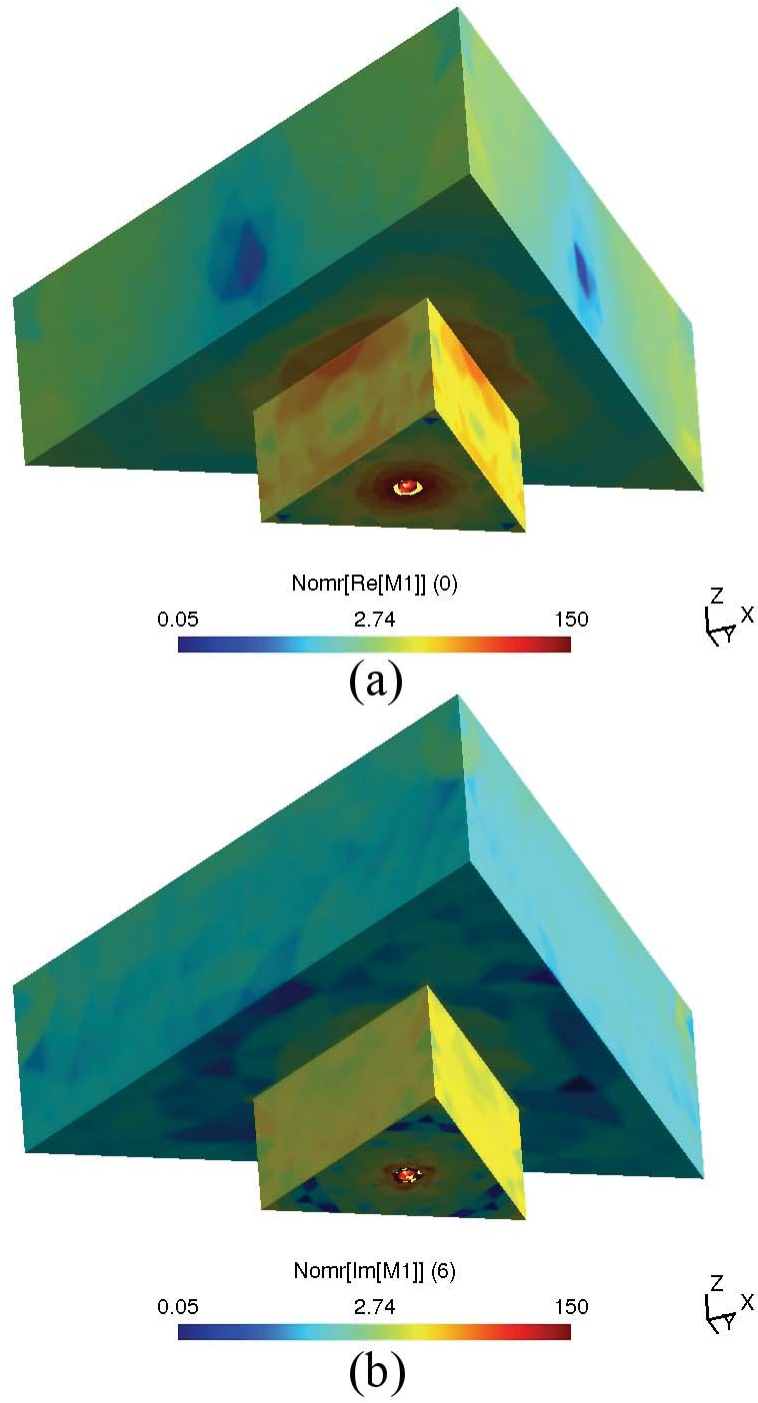
Fig. III.7. Equivalent magnetic current density M_1 for the example of Broadband T-shaped DRA with equilateral-triangle cross sections operating at 1.6 GHz. (a) Norm of the real part of M_1. (b) Norm of the imaginary part of M_1. Plots are in logarithmic scale.
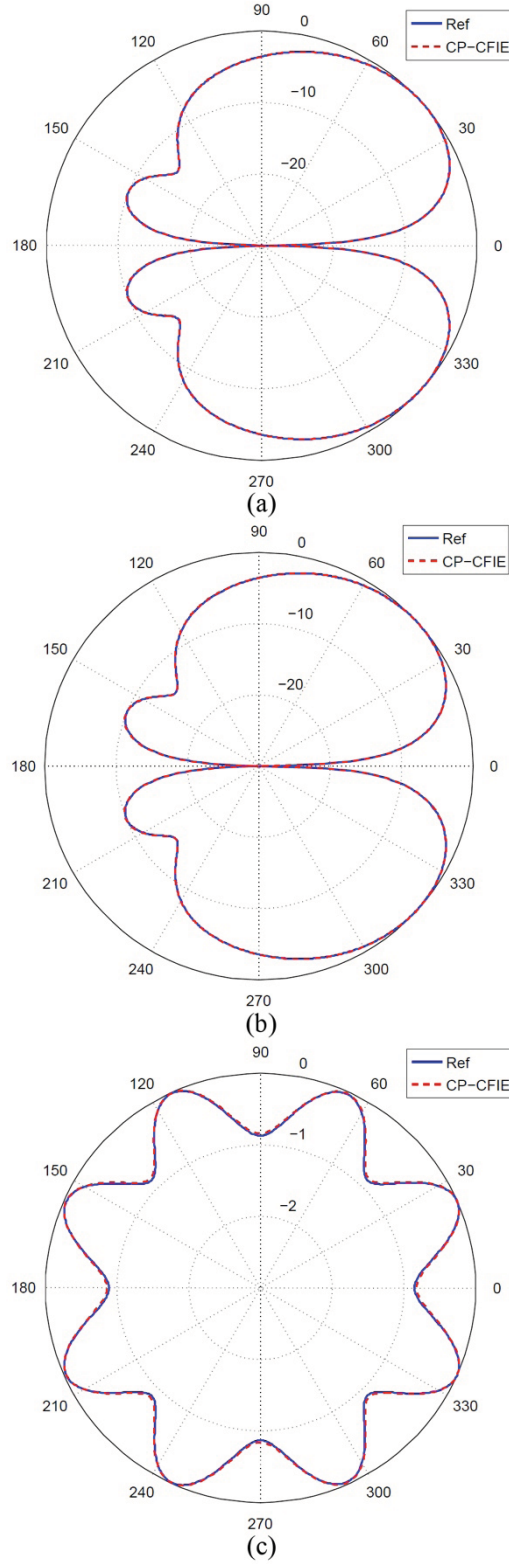
Fig. III.8. Normalized radiation pattern of the DRA operating at 1.6 GHz. Result obtained with the CP-CFIE is compared to the one obtained with a coupled surface-volume integral equation solver (labeled as "Ref"). (a) Radiation pattern in the XZ plane. (b) Radiation pattern in the YZ plane. (c) Radiation pattern in the XY plane.
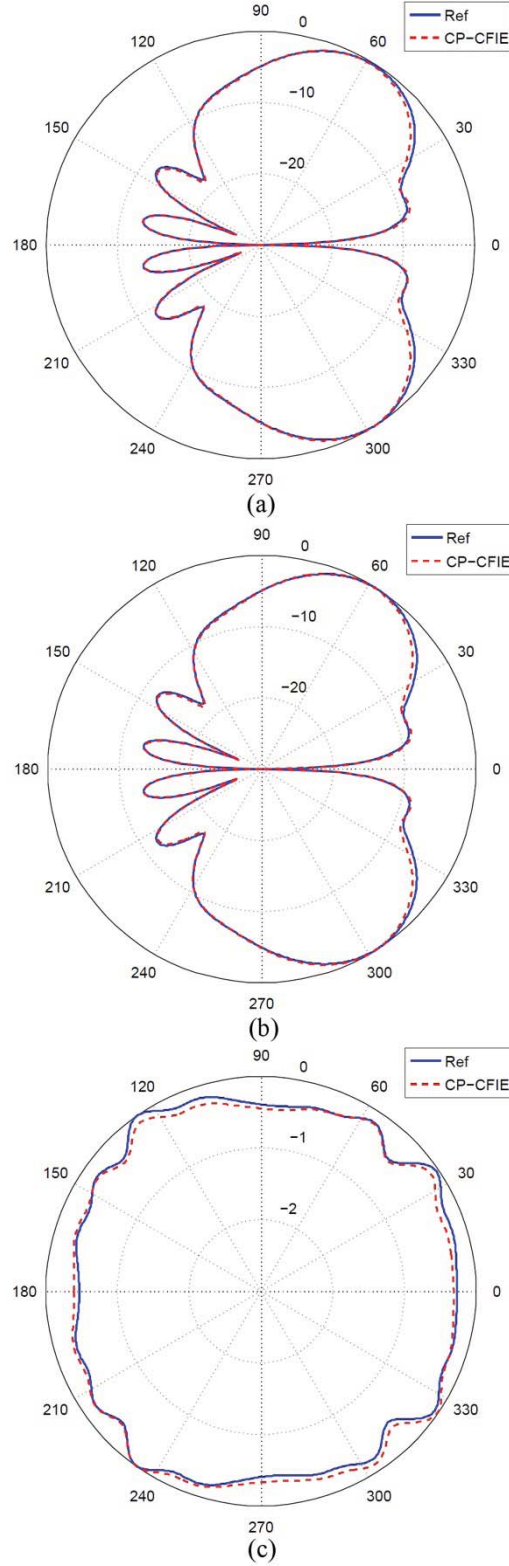
Fig. III.9. Normalized radiation pattern of the DRA operating at 3.1 GHz. Result obtained with the CP-CFIE is compared to the one obtained with a coupled surface-volume integral equation solver (labeled as "Ref"). (a) Radiation pattern in the XZ plane. (b) Radiation pattern in the YZ plane. (c) Radiation pattern in the XY plane.

76

High-Order Dot-Trick and Calderón Multiplicative Preconditioner for Time Domain Electric Field Integral Equations

4.1 Time Domain Electric Field Integral Equation and its Discretization

Consider a closed, simply connected PEC surface S residing in a homogeneous medium with permittivity ϵ and permeability μ. The incident electric field $\boldsymbol{E}^{inc}(\boldsymbol{r},t)$, which is zero for all $t < 0$ and temporally bandlimited to maximum frequency f_{max} induces the current density $\boldsymbol{J}(\boldsymbol{r},t)$ on S. The scattered field $\boldsymbol{E}^s(\boldsymbol{r},t)$ radiated by $\boldsymbol{J}(\boldsymbol{r},t)$ satisfies the TDEFIE

$$
\begin{aligned}
\boldsymbol{0} &= \hat{\boldsymbol{n}}_r \times \boldsymbol{E}^{inc}(\boldsymbol{r},t) + \hat{\boldsymbol{n}}_r \times \boldsymbol{E}^s(\boldsymbol{r},t) \\
&= \hat{\boldsymbol{n}}_r \times \boldsymbol{E}^{inc}(\boldsymbol{r},t) + \eta \mathcal{T}[\boldsymbol{J}](\boldsymbol{r},t)
\end{aligned}
\tag{8.1}
$$

where

$$
\mathcal{T}[\boldsymbol{J}] = \mathcal{T}_s[\boldsymbol{J}] + \mathcal{T}_h[\boldsymbol{J}]
\tag{8.2}
$$

with

$$
\mathcal{T}_s[\boldsymbol{J}](\boldsymbol{r},t) = -\frac{1}{4\pi c}\hat{\boldsymbol{n}}_r \times \int_S \frac{\dot{\boldsymbol{J}}(\boldsymbol{r}',t-R/c)}{R}\,ds'
\tag{8.3}
$$

and

$$
\mathcal{T}_h[\boldsymbol{J}](\boldsymbol{r},t) = \frac{c}{4\pi}\hat{\boldsymbol{n}}_r \times \nabla \int_S \frac{\int_0^{t-R/c} \nabla'_s \boldsymbol{J}(\boldsymbol{r}',t')\,dt'}{R}\,ds'.
\tag{8.4}
$$

Here $\hat{\boldsymbol{n}}_r$ is the outward pointing unit vector normal to S at $\boldsymbol{r}$, $\eta = \sqrt{\mu/\varepsilon}$ and $c = 1/\sqrt{\varepsilon\mu}$ are the background medium's impedance and speed of light respectively, and $R = |\boldsymbol{r} - \boldsymbol{r'}|$ is the distance between observation $\boldsymbol{r}$ and source $\boldsymbol{r'}$ points. The "dot" on top of a symbol denotes the action of a temporal derivative. The subscripts "s" and "h" stand for "singular" (vector potential) and "hyper-singular" (scalar potential), respectively. To numerically solve (8.1) $\boldsymbol{J}(\boldsymbol{r},t)$ is approximated as

$$\boldsymbol{J}(\boldsymbol{r},t) \approx \sum_{j=1}^{N_T} \sum_{n=1}^{N_S} I_{j,n} g_j(t) \boldsymbol{f}_n(\boldsymbol{r}) . \tag{8.5}$$

where $I_{j,n}$, $j = 1,\ldots,N_T$, $n = 1,\ldots,N_S$ are expansion coefficients of $\boldsymbol{J}(\boldsymbol{r},t)$ in terms of N_T scalar temporal basis functions $g_j(t)$ and N_S vector spatial basis functions $\boldsymbol{f}_n(\boldsymbol{r})$.

Throughout this chapter it is assumed that S is approximated by a mesh $S_{\Delta s}$ comprising N_P planar or curvilinear triangular patches, N_V vertices and N_E edges. The minimum edge size in $S_{\Delta s}$ is denoted by Δs.

The set of spatial basis functions $F = \{\boldsymbol{f}_n, n = 1,\ldots,N_S\}$ is, unless otherwise stated, assumed to be the set of (div-conforming) p^{th}-order interpolatory Graglia-Wilton-Peterson functions, i.e. $F = \text{GWP}(p)$ [5]. Unless $p = 0$ (in which case $\text{GWP}(p) = \text{RWG}$), $p \geq 1$ is assumed and suppressed.

The temporal basis functions $g_j(t) = g^{LAG}(t - j\Delta t)$, $j = 1,\ldots,N_T$ are shifted piecewise polynomial Lagrange interpolants of degree $q > 1$ defined as [26]

$$g^{LAG}(t) = \left(\prod_{i=1}^{k} \frac{i\Delta t - t}{i\Delta t} \right) \left(\prod_{i=1}^{q-k} \frac{i\Delta t + t}{i\Delta t} \right) \tag{8.6}$$

for $t \in [(k-1)\Delta t, k\Delta t]$ and $k = 0,\ldots,q$, with $\Delta t = 1/(\chi f_{max})$ the time step; χ is an over-sampling factor typically chosen in the range $10 \leq \chi \leq 20$.

Substitution of expansion (8.5) into (8.1), and testing the resulting equation with curl-conforming

functions in $nF = \{\hat{\boldsymbol{n}}_r \times \boldsymbol{f}_m(\boldsymbol{r}), m = 1,\ldots,N_S \mid \boldsymbol{f}_m(\boldsymbol{r}) \in F\}$ at $t = j\Delta t$, $j = 1,\ldots,N_T$ yields the following

marching on time (MOT) TDEFIE system

$$\mathbf{T}_F^{(0)}\mathbf{I}^{(j)} = \mathbf{V}_F^{(j)} - \sum_{k=1}^{\min\{j-1,k_{max}\}} \mathbf{T}_F^{(k)}\mathbf{I}^{(j-k)} \tag{8.7}$$

for $j = 1,\ldots,N_T$. In (8.7), the elements of the vectors $\mathbf{I}^{(j)}$ and $\mathbf{V}_F^{(j)}$ are given by

$$\left(\mathbf{I}^{(j)}\right)_n = I_{j,n} \tag{8.8}$$

$$\begin{aligned}
\left(\mathbf{V}_F^{(j)}\right)_m &= \left\langle \delta(t - j\Delta t)\hat{\boldsymbol{n}}_r \times \boldsymbol{f}_m(\boldsymbol{r}), \frac{1}{\eta}\hat{\boldsymbol{n}}_r \times \boldsymbol{E}^{inc}(\boldsymbol{r},t) \right\rangle \\
&= \frac{1}{\eta}\int_S \boldsymbol{f}_m(\boldsymbol{r})\, \boldsymbol{E}^{inc}(\boldsymbol{r}, j\Delta t)\, ds
\end{aligned} \tag{8.9}$$

and the elements of the matrices $\mathbf{T}_F^{(k)}$ can be written as

$$\begin{aligned}
\left(\mathbf{T}_F^{(k)}\right)_{m,n} &= \left\langle \delta(t - j\Delta t)\hat{\boldsymbol{n}}_r \times \boldsymbol{f}_m(\boldsymbol{r}), \mathcal{T}[g_{j-k}(t)\boldsymbol{f}_n(\boldsymbol{r})] \right\rangle \\
&= -\frac{1}{4\pi c}\iint_{S\times S} \boldsymbol{f}_m(\boldsymbol{r})\, \boldsymbol{f}_n(\boldsymbol{r}')\frac{\dot{g}^{LAG}(k\Delta t - R/c)}{R}ds'\,ds \\
&\quad - \frac{c}{4\pi}\iint_{S\times S} \nabla_s \boldsymbol{f}_m(\boldsymbol{r})\nabla'_s \boldsymbol{f}_n(\boldsymbol{r}')\frac{\int_0^{k\Delta t - R/c} g^{LAG}(t')dt'}{R}ds'\,ds
\end{aligned} \tag{8.10}$$

Note the subscript in $\mathbf{T}_F^{(k)}$ and $\mathbf{V}_F^{(j)}$, specifying the set of spatial basis functions used. Since

$g^{LAG}(t) = 0, \forall t < -\Delta t$, all matrices $\mathbf{T}_F^{(k)}$ are identically zero for $k < 0$. The number k_{max} of nonzero

interaction matrices $\mathbf{T}_F^{(k)}$ is of the order of $D/(c\Delta t)$, where D is the diameter of the smallest sphere

circumscribing S. Equation (8.7) is solved for the current coefficients vector $\mathbf{I}^{(j)}$ after the current

coefficients vectors $\mathbf{I}^{(i)}$, $i = 1,\ldots,j-1$ have been computed. This recursive procedure is termed MOT and it

can be written as the linear system of equations

$$
\begin{pmatrix}
\mathbf{T}_F^{(0)} & & & \\
\mathbf{T}_F^{(1)} & \mathbf{T}_F^{(0)} & & \\
\mathbf{T}_F^{(2)} & \mathbf{T}_F^{(1)} & \mathbf{T}_F^{(0)} & \\
\vdots & \vdots & \vdots & \ddots
\end{pmatrix}
\begin{pmatrix}
\mathbf{I}^{(1)} \\
\mathbf{I}^{(2)} \\
\mathbf{I}^{(3)} \\
\vdots
\end{pmatrix}
=
\begin{pmatrix}
\mathbf{V}^{(1)} \\
\mathbf{V}^{(2)} \\
\mathbf{V}^{(3)} \\
\vdots
\end{pmatrix}
\tag{8.11}
$$

or

$$
\mathbf{T}_F \mathbf{I} = \mathbf{V}_F . \tag{8.12}
$$

Successively solving (8.7) for time steps $j = 1, \ldots, N_T$ is equivalent to solve (8.12) by forward substitution.

The evaluation of the matrix elements in (8.10) requires the evaluation of a temporal integral, which is computationally expensive. For this reason, most TDIE schemes solve the time-differentiated TDEFIE

$$
\eta \dot{\mathcal{T}}[\boldsymbol{J}](\boldsymbol{r},t) = -\hat{\boldsymbol{n}}_r \times \dot{\boldsymbol{E}}^{inc}(\boldsymbol{r},t) \tag{8.13}
$$

with

$$
\dot{\mathcal{T}}[\boldsymbol{J}] = \dot{\mathcal{T}}_s[\boldsymbol{J}] + \dot{\mathcal{T}}_h[\boldsymbol{J}] \tag{8.14}
$$

$$
\dot{\mathcal{T}}_s[\boldsymbol{J}](\boldsymbol{r},t) = -\frac{1}{4\pi c} \hat{\boldsymbol{n}}_r \times \int_S \frac{\ddot{\boldsymbol{J}}(\boldsymbol{r}',t-R/c)}{R} ds' \tag{8.15}
$$

$$
\dot{\mathcal{T}}_h[\boldsymbol{J}](\boldsymbol{r},t) = \frac{c}{4\pi} \hat{\boldsymbol{n}}_r \times \nabla \int_S \frac{\nabla_s' \, \boldsymbol{J}(\boldsymbol{r}',t-R/c)}{R} ds' . \tag{8.16}
$$

The differentiated TDEFIE (8.13) can be solved via the same MOT scheme already used to solve (8.1). In particular, (8.7) remains valid provided that $\mathbf{T}_F^{(k)}$ and $\mathbf{V}_F^{(j)}$ are replaced by $\dot{\mathbf{T}}_F^{(k)}$ and $\dot{\mathbf{V}}_F^{(j)}$, defined by

$$
\begin{aligned}
\left(\dot{\mathbf{T}}_F^{(k)} \right)_{m,n} &= \left\langle \delta(t - j\Delta t)\hat{\boldsymbol{n}}_r \times \boldsymbol{f}_m(\boldsymbol{r}), \dot{\mathcal{T}}[g_{j-k}(t)\boldsymbol{f}_n(\boldsymbol{r})] \right\rangle \\
&= -\frac{1}{4\pi c} \iint_{S \times S} \boldsymbol{f}_m(\boldsymbol{r}) \boldsymbol{f}_n(\boldsymbol{r}') \frac{\ddot{g}^{LAG}(k\Delta t - R/c)}{R} ds' ds \\
&\quad - \frac{c}{4\pi} \iint_{S \times S} \nabla_s \boldsymbol{f}_m(\boldsymbol{r}) \nabla_s' \, \boldsymbol{f}_n(\boldsymbol{r}') \frac{g^{LAG}(k\Delta t - R/c)}{R} ds' ds
\end{aligned}
\tag{8.17}
$$

$$\left(\dot{\mathbf{V}}_F^{(j)}\right)_m = \left\langle \delta(t - j\Delta t)\hat{\boldsymbol{n}}_r \times \boldsymbol{f}_m(\boldsymbol{r}), -\frac{1}{\eta}\hat{\boldsymbol{n}}_r \times \dot{\boldsymbol{E}}^{inc}(\boldsymbol{r},t)\right\rangle$$

$$= -\frac{1}{\eta}\int_S \boldsymbol{f}_m(\boldsymbol{r})\,\dot{\boldsymbol{E}}^{inc}(\boldsymbol{r}, j\Delta t)\,ds \tag{8.18}$$

When analyzing electromagnetic phenomena involving electrically large and/or complex structures, i.e., when N_S is large, (8.7) cannot be solved directly and iterative solvers are called for. At each time step, the computational cost of solving (8.7) iteratively is proportional to the cost of multiplying the impedance matrix $\mathbf{T}_F^{(0)}$ by a trial solution vector and the number of iterations N_{iter} required to reach a desired residual error; N_{iter} typically is proportional to $\mathbf{T}_F^{(0)}$'s condition number, viz. the ratio of $\mathbf{T}_F^{(0)}$'s largest and smallest singular values. Unfortunately, the singular values of the operator $\mathcal{T}$ comprise two branches, one accumulating at zero, and the other at infinity (see Chapter II). Thus the condition number of $\mathbf{T}_F^{(0)}$ grows without bound as the spatial dependence of $\boldsymbol{J}$ is increasingly well-approximated, i.e. as $\Delta s \to 0$ and/or $p \to \infty$. When this happens the number of iterations required for convergence often is prohibitively high. Similar observations apply to the time-differentiated TDEFIE.

4.2 Calderón Preconditioned and DC Stable TDEFIEs

A well-conditioned TDEFIE can be obtained by leveraging $\mathcal{T}$'s self-regularizing property expressed by the time-domain Calderón identity [12],

$$\mathcal{T}^2[\boldsymbol{J}](\boldsymbol{r},t) = -\frac{\ddot{\boldsymbol{J}}(\boldsymbol{r},t)}{4} + \mathcal{K}^2[\boldsymbol{J}](\boldsymbol{r},t) \tag{8.19}$$

with

$$\mathcal{K}[\boldsymbol{J}](\boldsymbol{r},t) = -\hat{\boldsymbol{n}}_r \times \frac{1}{4\pi}\int_S \nabla\frac{\boldsymbol{J}(\boldsymbol{r}',t - R/c)}{R}\,ds'. \tag{8.20}$$

Operators $\mathcal{K}$ and $\mathcal{K}^2$ in time-domain have the same properties that their frequency-domain counterparts have. Eqn. (8.19) implies that the Calderón-preconditioned TDEFIE

$$\eta\mathcal{T}^2[\boldsymbol{J}](\boldsymbol{r},t) = -\mathcal{T}[\hat{\boldsymbol{n}}_r \times \boldsymbol{E}^{inc}](\boldsymbol{r},t) \tag{8.21}$$

and its time-differentiated version

$$\eta \dot{\mathcal{T}}^2[\boldsymbol{J}](\boldsymbol{r},t) = -\dot{\mathcal{T}}[\hat{\boldsymbol{n}}_r \times \dot{\boldsymbol{E}}^{inc}](\boldsymbol{r},t) \tag{8.22}$$

may be amenable to well-conditioned systems, regardless of the mesh density or the order of the spatial basis functions. In general, eqn. (8.22) is preferred over (8.21) to avoid evaluating the time integral present in $\mathcal{T}_h$. Calderón-preconditioned TDEFIEs (8.21) and (8.22) suffer from DC instabilities as the operators $\mathcal{T}^2$ and $\dot{\mathcal{T}}^2$ have the same null space $\mathcal{T}$ and $\dot{\mathcal{T}}$ have, respectively. To construct an equation that is DC stable, we define the operators

$$\widehat{\mathcal{T}}_s[\boldsymbol{X}](\boldsymbol{r},t) = -\frac{1}{4\pi c}\hat{\boldsymbol{n}}_r \times \int_S \frac{\boldsymbol{X}(\boldsymbol{r}',t-R/c)}{R}ds' , \tag{8.23}$$

$$\widehat{\mathcal{T}}_h[\boldsymbol{X}](\boldsymbol{r},t) = \frac{c}{4\pi}\hat{\boldsymbol{n}}_r \times \nabla \int_S \frac{\nabla'_s \boldsymbol{X}(\boldsymbol{r}',t-R/c)}{R}ds' . \tag{8.24}$$

Since spatial integrations and temporal differentiations in (8.3) and (8.4) commute, the following equations hold:

$$\mathcal{T}_s\mathcal{T}_h = \widehat{\mathcal{T}}_s\widehat{\mathcal{T}}_h \tag{8.25}$$

$$\mathcal{T}_h\mathcal{T}_s = \widehat{\mathcal{T}}_h\widehat{\mathcal{T}}_s . \tag{8.26}$$

Using (8.25) and (8.26), and since $\mathcal{T}_h^2 = 0$, $\mathcal{T}^2$ can be expressed as

$$\mathcal{T}^2 = \mathcal{T}_s^2 + \mathcal{T}_s\mathcal{T}_h + \mathcal{T}_h\mathcal{T}_s = \mathcal{T}_s^2 + \widehat{\mathcal{T}}_s\widehat{\mathcal{T}}_h + \widehat{\mathcal{T}}_h\widehat{\mathcal{T}}_s . \tag{8.27}$$

As demonstrated in [13] the static and linear-in-time functions in the null space of $\mathcal{T}$ and $\dot{\mathcal{T}}$ are not present in $(\mathcal{T}_s^2 + \widehat{\mathcal{T}}_s\widehat{\mathcal{T}}_h + \widehat{\mathcal{T}}_h\widehat{\mathcal{T}}_s)$. Thus, the "Dottrick-TDEFIE" defined as

$$\eta\left(\mathcal{T}_s^2 + \widehat{\mathcal{T}}_s\widehat{\mathcal{T}}_h + \widehat{\mathcal{T}}_h\widehat{\mathcal{T}}_s\right)[\boldsymbol{J}](\boldsymbol{r},t) = -\mathcal{T}[\hat{\boldsymbol{n}}_r \times \boldsymbol{E}^{inc}](\boldsymbol{r},t) \tag{8.28}$$

is immune to DC instabilities.

82

Unfortunately, the discretization of either (8.22) or (8.28) is by no means trivial. Here the sets $F = \mathrm{GWP}(p)$ and $\tilde{F} = \mathrm{DQCC}(p)$ (see Chapter II) are used to discretize $\mathcal{T}^2$ either directly or in its "Dottrick" form. The operator $\mathcal{T}^2[J]$ is discretized as the product of two impedance matrices $\mathbf{T}_{\tilde{F}}$ and $\mathbf{T}_F$, separated by a Gram matrix that accounts for the possible lack of (bi-)orthogonality between the functions in $\tilde{F}$ and nF. In particular, the discretization of (8.22) reads

$$\left(\dot{\mathbf{T}}_{\tilde{F}} \, \mathbf{G}_S^{-1} \right) \dot{\mathbf{T}}_F \mathbf{I} = \left(\dot{\mathbf{T}}_{\tilde{F}} \, \mathbf{G}_S^{-1} \right) \dot{\mathbf{V}}_F \tag{8.29}$$

or

$$\begin{pmatrix} \dot{\mathbf{T}}_{\tilde{F}}^{(0)} & & & \\ \dot{\mathbf{T}}_{\tilde{F}}^{(1)} & \dot{\mathbf{T}}_{\tilde{F}}^{(0)} & & \\ \dot{\mathbf{T}}_{\tilde{F}}^{(2)} & \dot{\mathbf{T}}_{\tilde{F}}^{(1)} & \dot{\mathbf{T}}_{\tilde{F}}^{(0)} & \\ \vdots & \vdots & \vdots & \ddots \end{pmatrix} \mathbf{G}_S^{-1} \left\{ \begin{pmatrix} \dot{\mathbf{T}}_F^{(0)} & & & \\ \dot{\mathbf{T}}_F^{(1)} & \dot{\mathbf{T}}_F^{(0)} & & \\ \dot{\mathbf{T}}_F^{(2)} & \dot{\mathbf{T}}_F^{(1)} & \dot{\mathbf{T}}_F^{(0)} & \\ \vdots & \vdots & \vdots & \ddots \end{pmatrix} \begin{pmatrix} \mathbf{I}^{(1)} \\ \mathbf{I}^{(2)} \\ \mathbf{I}^{(3)} \\ \vdots \end{pmatrix} - \begin{pmatrix} \dot{\mathbf{V}}^{(1)} \\ \dot{\mathbf{V}}^{(2)} \\ \dot{\mathbf{V}}^{(3)} \\ \vdots \end{pmatrix} \right\} = \begin{pmatrix} \mathbf{0} \\ \mathbf{0} \\ \mathbf{0} \\ \vdots \end{pmatrix} \tag{8.30}$$

with $\mathbf{G}_S$ a block-diagonal spatial Gram matrix given by

$$\mathbf{G}_S = \begin{pmatrix} \mathbf{G}_{nF;\tilde{F}} & & \\ & \mathbf{G}_{nF;\tilde{F}} & \\ & & \ddots \end{pmatrix} \tag{8.31}$$

where

$$(\mathbf{G}_{nF;\tilde{F}})_{m,n} = \left\langle \hat{\boldsymbol{n}}_r \times \boldsymbol{f}_m, \tilde{\boldsymbol{f}}_n \right\rangle \tag{8.32}$$

is the matrix of overlap integrals of functions in $\tilde{F}$ and nF. Eqn. (8.29) does not require the decomposition of matrix elements in $\mathbf{T}_{\tilde{F}}$ and $\mathbf{T}_F$ into their singular (vector potential) and hypersingular (scalar potential) components, simplifying its implementation.

Similarly to (8.11), the linear system in (8.30) can be solved by forward substitution as

$$\left(\dot{\mathbf{T}}_{\tilde{F}}^{(0)} \, \mathbf{G}_{nF;\tilde{F}}^{-1} \, \dot{\mathbf{T}}_F^{(0)} \right) \mathbf{I}^{(j)} = \dot{\mathbf{T}}_{\tilde{F}}^{(0)} \, \mathbf{G}_{nF;\tilde{F}}^{-1} \left(\dot{\mathbf{V}}^{(j)} - \sum_{k=1}^{\min\{j-1,k_{max}\}} \dot{\mathbf{T}}_F^{(k)} \, \mathbf{I}^{(j-k)} \right)$$
$$+ \sum_{l=1}^{\min\{j-1,k_{max}\}} \dot{\mathbf{T}}_{\tilde{F}}^{(l)} \, \mathbf{G}_{nF;\tilde{F}}^{-1} \left(\dot{\mathbf{V}}^{(j-l)} - \sum_{k=0}^{\min\{j-l-1,k_{max}\}} \dot{\mathbf{T}}_F^{(k)} \, \mathbf{I}^{(j-l-k)} \right) \tag{8.33}$$

for $j = 1, \ldots, N_T$. The expression in parenthesis, in the second term of the right hand side of (8.33) can be rearranged by splitting the sum into $\dot{\mathbf{T}}_F^{(0)} \mathbf{I}^{(j)}$ and all other terms with $1 \le k \le \min\{j - l - 1, k_{max}\}$. Considering the MOT system in (8.7) for time step $j - l$ it follows that

$$\left(\dot{\mathbf{V}}^{(j-l)} - \sum_{k=0}^{\min\{j-l-1,k_{max}\}} \dot{\mathbf{T}}_F^{(k)} \mathbf{I}^{(j-l-k)} \right) = \dot{\mathbf{V}}^{(j-l)} - \dot{\mathbf{T}}_F^{(0)} \mathbf{I}^{(j-l)} - \sum_{k=1}^{\min\{j-l-1,k_{max}\}} \dot{\mathbf{T}}_F^{(k)} \mathbf{I}^{(j-l-k)} = 0 \,. \tag{8.34}$$

Thus, the CMP-TDEFIE system in (8.33) is simplified into

$$\left(\dot{\mathbf{T}}_{\tilde{F}}^{(0)} \, \mathbf{G}_{nF;\tilde{F}}^{-1} \, \dot{\mathbf{T}}_F^{(0)} \right) \mathbf{I}^{(j)} = \dot{\mathbf{T}}_{\tilde{F}}^{(0)} \, \mathbf{G}_{nF;\tilde{F}}^{-1} \left(\dot{\mathbf{V}}^{(j)} - \sum_{k=1}^{\min\{j-1,k_{max}\}} \dot{\mathbf{T}}_F^{(k)} \mathbf{I}^{(j-k)} \right). \tag{8.35}$$

The system matrix $\dot{\mathbf{T}}_{\tilde{F}}^{(0)} \mathbf{G}_{nF;\tilde{F}}^{-1} \dot{\mathbf{T}}_F^{(0)}$ in (8.35) is well conditioned only if conditions C1 through C3 (see Chapter II) are satisfied by the functions in F and $\tilde{F}$. As explained in section 2.3, the above criteria is satisfied by the sets $F = \text{GWP}(p)$ and $\tilde{F} = \text{DQCC}(p)$.

To discretize the Dottrick-TDEFIE in (8.28), each term in the Dottrick operator is handled separately using the same sets of functions used for CMP:

$$\left(\mathbf{T}_{s,\tilde{F}} \, \mathbf{G}_s^{-1} \, \mathbf{T}_{s,F} + \widehat{\mathbf{T}}_{s,\tilde{F}} \, \mathbf{G}_s^{-1} \, \widehat{\mathbf{T}}_{h,F} + \widehat{\mathbf{T}}_{h,\tilde{F}} \, \mathbf{G}_s^{-1} \, \widehat{\mathbf{T}}_{s,F} \right) \mathbf{I} = \mathbf{T}_{\tilde{F}} \, \mathbf{G}_s^{-1} \, \mathbf{V}_F \,. \tag{8.36}$$

The matrices $\mathbf{T}_{s,Q}$, $\widehat{\mathbf{T}}_{s,Q}$, and $\widehat{\mathbf{T}}_{h,Q}$, with $Q = F, \tilde{F}$, are given by

$$\mathbf{T}_{s,Q} = \begin{pmatrix} \mathbf{T}_{s,Q}^{(0)} & & & \\ \mathbf{T}_{s,Q}^{(1)} & \mathbf{T}_{s,Q}^{(0)} & & \\ \mathbf{T}_{s,Q}^{(2)} & \mathbf{T}_{s,Q}^{(1)} & \mathbf{T}_{s,Q}^{(0)} & \\ \vdots & \vdots & \vdots & \ddots \end{pmatrix}, \tag{8.37}$$

$$\widehat{\mathbf{T}}_{s,Q} = \begin{pmatrix} \widehat{\mathbf{T}}_{s,Q}^{(0)} & & & \\ \widehat{\mathbf{T}}_{s,Q}^{(1)} & \widehat{\mathbf{T}}_{s,Q}^{(0)} & & \\ \widehat{\mathbf{T}}_{s,Q}^{(2)} & \widehat{\mathbf{T}}_{s,Q}^{(1)} & \widehat{\mathbf{T}}_{s,Q}^{(0)} & \\ \vdots & \vdots & \vdots & \ddots \end{pmatrix}, \tag{8.38}$$

84

$$
\widehat{\mathbf{T}}_{h,Q} = \begin{pmatrix}
\widehat{\mathbf{T}}_{h,Q}^{(0)} & & & \\
\widehat{\mathbf{T}}_{h,Q}^{(1)} & \widehat{\mathbf{T}}_{h,Q}^{(0)} & & \\
\widehat{\mathbf{T}}_{h,Q}^{(2)} & \widehat{\mathbf{T}}_{h,Q}^{(1)} & \widehat{\mathbf{T}}_{h,Q}^{(0)} & \\
\vdots & \vdots & \vdots & \ddots
\end{pmatrix},
\tag{8.39}
$$

with

$$
\begin{aligned}
\left(\mathbf{T}_{s,F}^{(k)} \right)_{m,n} &= \left\langle \delta(t-j\Delta t)\hat{\boldsymbol{n}}_r \times \boldsymbol{f}_m(\boldsymbol{r}), \mathcal{T}_s[g_{j-k}(t)\boldsymbol{f}_n(\boldsymbol{r})] \right\rangle \\
&= -\frac{1}{4\pi c} \iint_{S\times S} \boldsymbol{f}_m(\boldsymbol{r})\,\boldsymbol{f}_n(\boldsymbol{r}')\frac{\dot{g}^{LAG}(k\Delta t - R/c)}{R} ds' ds
\end{aligned},
\tag{8.40}
$$

$$
\begin{aligned}
\left(\widehat{\mathbf{T}}_{s,F}^{(k)} \right)_{m,n} &= \left\langle \delta(t-j\Delta t)\hat{\boldsymbol{n}}_r \times \boldsymbol{f}_m(\boldsymbol{r}), \widehat{\mathcal{T}}_s[g_{j-k}(t)\boldsymbol{f}_n(\boldsymbol{r})] \right\rangle \\
&= -\frac{1}{4\pi c} \iint_{S\times S} \boldsymbol{f}_m(\boldsymbol{r})\,\boldsymbol{f}_n(\boldsymbol{r}')\frac{g^{LAG}(k\Delta t - R/c)}{R} ds' ds
\end{aligned},
\tag{8.41}
$$

$$
\begin{aligned}
\left(\widehat{\mathbf{T}}_{h,F}^{(k)} \right)_{m,n} &= \left\langle \delta(t-j\Delta t)\hat{\boldsymbol{n}}_r \times \boldsymbol{f}_m(\boldsymbol{r}), \widehat{\mathcal{T}}_h[g_{j-k}(t)\boldsymbol{f}_n(\boldsymbol{r})] \right\rangle \\
&= -\frac{c}{4\pi} \iint_{S\times S} \nabla_s \boldsymbol{f}_m(\boldsymbol{r})\nabla'_s \boldsymbol{f}_n(\boldsymbol{r}')\frac{g^{LAG}(k\Delta t - R/c)}{R} ds' ds
\end{aligned}.
\tag{8.42}
$$

Matrices $\mathbf{T}_{s,\tilde{F}}^{(k)}$, $\widehat{\mathbf{T}}_{s,\tilde{F}}^{(k)}$, and $\widehat{\mathbf{T}}_{h,\tilde{F}}^{(k)}$ are obtained as in (8.40), (8.41), and (8.42) respectively, but with functions in $\tilde{F}$ instead of F.

As in a standard MOT scheme, the linear system in (8.36) can be solved by forward substitution, which is equivalent to solve

$$
\begin{aligned}
\left(\mathbf{T}_{s,\tilde{F}}^{(0)}\, \mathbf{G}_s^{-1}\, \mathbf{T}_{s,F}^{(0)} + \widehat{\mathbf{T}}_{s,\tilde{F}}^{(0)}\, \mathbf{G}_s^{-1}\, \widehat{\mathbf{T}}_{h,F}^{(0)} + \widehat{\mathbf{T}}_{h,\tilde{F}}^{(0)}\, \mathbf{G}_s^{-1}\, \widehat{\mathbf{T}}_{s,F}^{(0)} \right)\mathbf{I}^{(j)} &= \sum_{l=0}^{\min\{j-1,k_{max}\}} \mathbf{T}_{\tilde{F}}^{(l)}\, \mathbf{G}_s^{-1}\, \mathbf{V}_F^{(j-l)} \\
- \sum_{l=1}^{\min\{j-1,k_{max}\}} \left(\mathbf{T}_{s,\tilde{F}}^{(l)}\, \mathbf{G}_s^{-1}\, \mathbf{T}_{s,F}^{(0)} \right)\mathbf{I}^{(j-l)} &- \sum_{l=0}^{\min\{j-1,k_{max}\}} \mathbf{T}_{s,\tilde{F}}^{(l)}\, \mathbf{G}_s^{-1}\left(\sum_{k=1}^{\min\{j-l-1,k_{max}\}} \mathbf{T}_{s,F}^{(k)}\, \mathbf{I}^{(j-l-k)} \right) \\
- \sum_{l=1}^{\min\{j-1,k_{max}\}} \left(\widehat{\mathbf{T}}_{s,\tilde{F}}^{(l)}\, \mathbf{G}_s^{-1}\, \widehat{\mathbf{T}}_{h,F}^{(0)} \right)\mathbf{I}^{(j-l)} &- \sum_{l=0}^{\min\{j-1,k_{max}\}} \widehat{\mathbf{T}}_{s,\tilde{F}}^{(l)}\, \mathbf{G}_s^{-1}\left(\sum_{k=1}^{\min\{j-l-1,k_{max}\}} \widehat{\mathbf{T}}_{h,F}^{(k)}\, \mathbf{I}^{(j-l-k)} \right) \\
- \sum_{l=1}^{\min\{j-1,k_{max}\}} \left(\widehat{\mathbf{T}}_{h,\tilde{F}}^{(l)}\, \mathbf{G}_s^{-1}\, \widehat{\mathbf{T}}_{s,F}^{(0)} \right)\mathbf{I}^{(j-l)} &- \sum_{l=0}^{\min\{j-1,k_{max}\}} \widehat{\mathbf{T}}_{h,\tilde{F}}^{(l)}\, \mathbf{G}_s^{-1}\left(\sum_{k=1}^{\min\{j-l-1,k_{max}\}} \widehat{\mathbf{T}}_{s,F}^{(k)}\, \mathbf{I}^{(j-l-k)} \right)
\end{aligned}
\tag{8.43}
$$

for every time step $j = 1,2,\ldots,N_T$.

The implementation of equations (8.35) and (8.43) follows exactly the same procedure described earlier for frequency domain solvers. In particular, using the transformation matrices $\mathbf{P}$ and $\mathbf{R}$ (defined in section 2.4), matrices $\dot{\mathbf{T}}_{\tilde{F}}^{(0)}$ and $\dot{\mathbf{T}}_{F}^{(0)}$ in (8.35) can be evaluated as

$$\dot{\mathbf{T}}_{\tilde{F}}^{(0)} = \mathbf{P}^{\mathrm{T}} \, \mathbf{H}_{\tilde{F}}^{\mathrm{T}} \, \dot{\mathbf{T}}_{\mathrm{GWP}}^{(0)} \, \mathbf{H}_{\tilde{F}} \, \mathbf{P} \tag{8.44}$$

and

$$\dot{\mathbf{T}}_{F}^{(0)} = \mathbf{H}_{F}^{\mathrm{T}} \, \dot{\mathbf{T}}_{\mathrm{GWP}}^{(0)} \, \mathbf{H}_{F} \, . \tag{8.45}$$

Evaluation of matrices $\widehat{\mathbf{T}}_{s,F}^{(k)}$, $\widehat{\mathbf{T}}_{h,F}^{(k)}$, $\widehat{\mathbf{T}}_{s,\tilde{F}}^{(k)}$, and $\widehat{\mathbf{T}}_{h,\tilde{F}}^{(k)}$ is performed in a similar fashion:

$$\widehat{\mathbf{T}}_{s,F}^{(k)} = \mathbf{H}_{F}^{\mathrm{T}} \, \widehat{\mathbf{T}}_{s,\mathrm{GWP}}^{(k)} \, \mathbf{H}_{F} \, , \tag{8.46}$$

$$\widehat{\mathbf{T}}_{h,F}^{(k)} = \mathbf{H}_{F}^{\mathrm{T}} \, \widehat{\mathbf{T}}_{h,\mathrm{GWP}}^{(k)} \, \mathbf{H}_{F} \, , \tag{8.47}$$

$$\widehat{\mathbf{T}}_{s,\tilde{F}}^{(k)} = \mathbf{P}^{\mathrm{T}} \, \mathbf{H}_{\tilde{F}}^{\mathrm{T}} \, \widehat{\mathbf{T}}_{s,\mathrm{GWP}}^{(k)} \, \mathbf{H}_{\tilde{F}} \, \mathbf{P} \, , \tag{8.48}$$

$$\widehat{\mathbf{T}}_{h,\tilde{F}}^{(k)} = \mathbf{P}^{\mathrm{T}} \, \mathbf{H}_{\tilde{F}}^{\mathrm{T}} \, \widehat{\mathbf{T}}_{h,\mathrm{GWP}}^{(k)} \, \mathbf{H}_{\tilde{F}} \, \mathbf{P} \, . \tag{8.49}$$

4.3 Numerical Results

This section presents several examples that demonstrate the effectiveness of the basis functions presented in Chapter II and its performance in the high-order CMP-TDEFIE and the high-order Dottrick-TDEFIE. The results presented here are obtained using a time-domain solver which implements all three MOT schemes presented in this chapter, i.e., the differentiated TDEFIE in (8.7), the CMP-TDEFIE in (8.35), and the Dottrick-TDEFIE in (8.43). In either case, a generalized minimal residual (GMRES)-based iterative method [39] is used to solve the linear systems in each time step.

In all numerical experiments the excitation is considered to be a modulated Gaussian plane wave of the form

$$E^{inc}(r,t) = \hat{p} e^{-\left[(\tau - t_p)/\sqrt{2}\sigma\right]^2} \cos(2\pi f_0 \tau) \, . \tag{8.50}$$

In (8.50) f_0 is the center frequency, $\tau = t - \hat{r}\,\hat{k}\,/\,c$, $\hat{k}$ denotes the direction of propagation and $\hat{p}$ denotes the polarization of the incident wave. The temporal standard deviation σ is related to the nominal bandwidth f_{BW} by $\sigma = 6\,/\,(2\pi f_{BW})$. The delay time of the wave relative to the origin is denoted by t_p.

The performance of the CMP-TDEFIE is studied here with three different structures: a sphere, an Airbus A380, and a model of an avionics bay. Specific parameters used for each structure are summarized in Table IV.A.

Table IV.A.
Parameters used in the excitation for the different geometries

Mesh	$\hat{p}$	$\hat{k}$	f_0	f_{BW}	t_p
Sphere	$\hat{x}$	$\hat{z}$	50 MHz	10 MHz	1 µs
Airbus A380	$\hat{z}$	$\hat{x}$	70 MHz	20 MHz	360 ns
Avionics bay	$\hat{y}$	$\hat{x}$	50 MHz	10 MHz	760 ns

4.3.1   Sphere

The first example demonstrates the convergence of the RCS as the order of the basis functions in the high-order CMP-TDEFIE is increased. The target geometry is a sphere of radius 1 m, which is discretized with 32 curvilinear patches. Each patch is obtained by means of an exact mapping from a reference patch onto the surface of the sphere. The simulation is run with a time step $\Delta t = 250$ ps and $N_T = 8192$ time steps. All frequency-domain results attributed to the proposed solver are obtained by (discrete) Fourier transforming time-domain data while accounting for the spectral content of the incident field.

To demonstrate the effect of the spatial basis functions, Fig. IV.1(a) shows the bistatic RCS of the PEC sphere when computed with time basis functions of order $q = 4$ and spatial basis functions of orders $p = 0,1,2$. Fig. IV.1(b) shows the relative error of the computed RCS with respect to Mie series solution. To demonstrate the effect of temporal basis order, Fig. IV.2(a) show the bistatic RCS of the sphere when computed with spatial basis functions of order $p = 2$ and temporal basis functions of orders $q = 2, 3, 4$. Fig. IV.2(b) shows the relative error with respect to Mie series solution. All RCS are computed at a frequency

of 50 MHz. As expected, increasing the order of time and/or spatial basis functions improves the accuracy of the results.

Fig. IV.3(a-c) show the residual error versus iteration count achieved by a GMRES solver during the iterative solution of the MOT matrix systems obtained by discretizing the diagonally-preconditioned TDEFIE and CMP-TDEFIE with basis functions of orders $p = 0, 1, 2$. As dictated by the condition number of $(\dot{\mathbf{T}}_{\tilde{F}}^{(0)} \mathbf{G}_{nF;\tilde{F}}^{-1} \dot{\mathbf{T}}_{F}^{(0)})$ the number of iterations required for the CMP-TDEFIE to reach the prescribed accuracy does not grow as the discretization density is increased. In contrast, the diagonally-preconditioned TDEFIE requires an increasing number of iterations as the mesh becomes denser. Moreover, this behavior worsens as the order p of the basis functions is increased, severely penalizing the efficiency and accuracy of high-order basis functions.
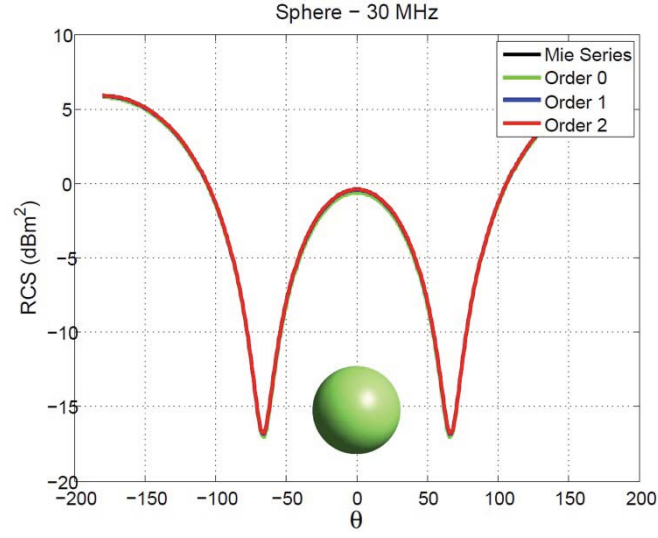
(a)
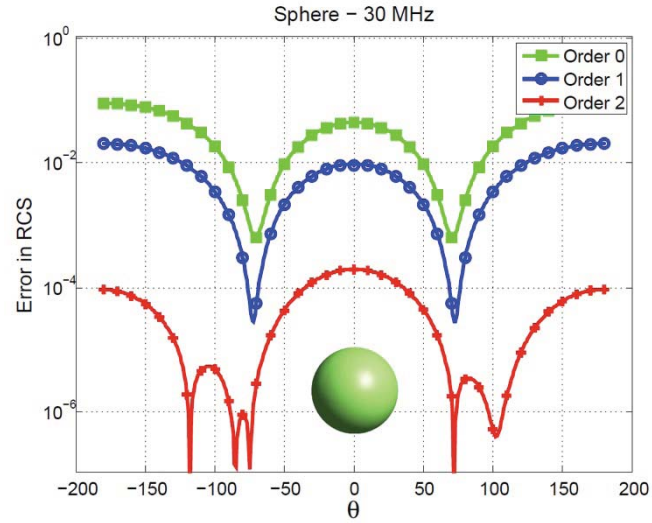
(b)

Fig. IV.1. Bistatic RCS of a PEC sphere of radius 1 m. computed at 30 MHz from the current density obtained with the CMP-TDEFIE. The surface of the sphere is modeled with 32 curvilinear patches. The current density is modeled with spatial basis functions of orders $p = 0,1,2$ and temporal basis functions of order $q = 4$. (a) Bistatic RCS in the x-z plane. (b) Relative error in the RCS with respect to Mie series solution.
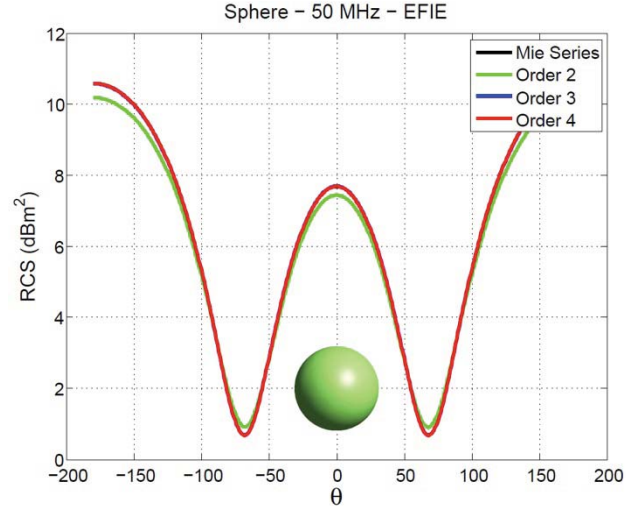
(a)
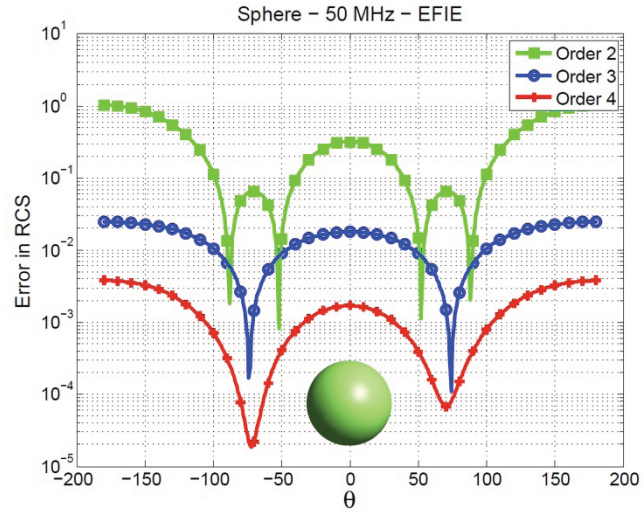
(b)

Fig. IV.2. Bistatic RCS of a PEC sphere of radius 1 m. computed at 50 MHz from the current density obtained with the CMP-TDEFIE. The surface of the sphere is modeled with 32 curvilinear patches. The current density is modeled with spatial basis functions of order $p = 2$ and temporal basis functions of degrees $q = 2, 3, 4$. (a) Bistatic RCS in the x-z plane. (b) Relative error in the RCS with respect to Mie series solution.
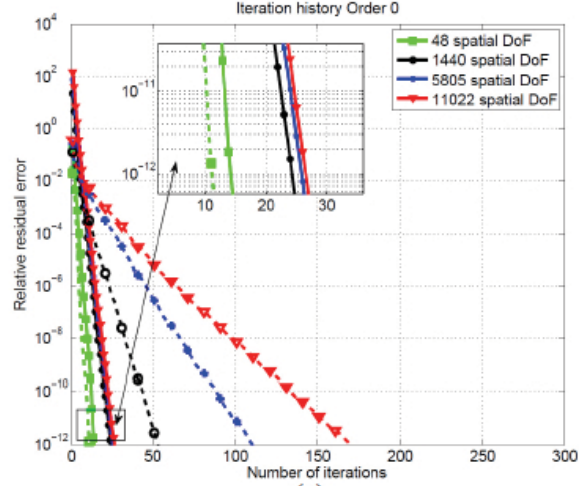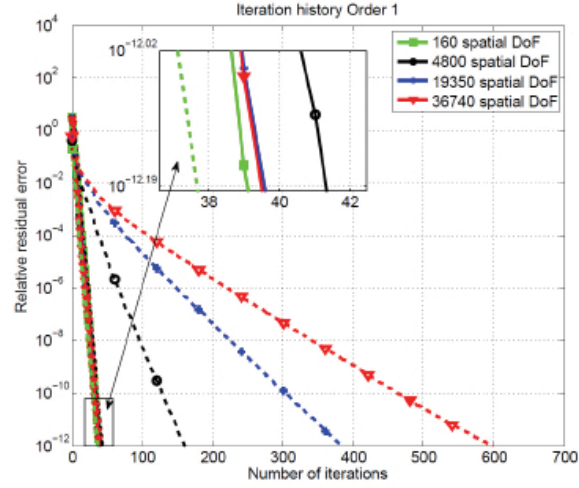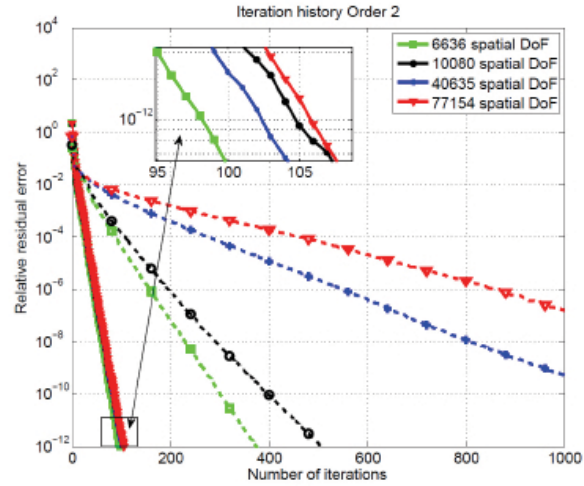
Fig. IV.3. Residual history of diagonally-preconditioned TDEFIE (dashed lines) and CMP-TDEFIE (solid lines) when solving for a single time step. The illuminated target is a PEC sphere of radius 1 m. Four different discretizations are used, ranging from 32 to 7000 curvilinear elements. Results are shown for several orders of the spatial basis functions: (a) order 0; (b) order 1; (c) order 2.

The next example involves an open cavity in the fuselage of an Airbus A380, as shown in Fig. IV.4(a-c). The cavity penetrates 40.0 cm along the $\hat{y}$ axis and into the aircraft. The aperture of the cavity is a rectangular slot of dimensions 20.0 x 1.0 cm, and oriented along the $\hat{x}$ axis. Note that the airplane is illuminated by a $\hat{z}$-polarized plane wave traveling in the $\hat{x}$ direction, thus the polarization is orthogonal to the orientation of the slot. Fig. IV.5(a-d) show snapshots of the transient current density at different instances of time. Fig. IV.5(f) shows the transient current observed at three different locations (probes) on the surface of the aircraft (see Fig. IV.5(e)): the tip of the nose, inside the cavity, and the tip of the vertical stabilized. The results shown in these figures are obtained with the CMP-TDEFIE using time basis functions of order $q = 4$ (and a time step of $\Delta t = 80$ ps) and spatial basis functions of order $p = 2$.
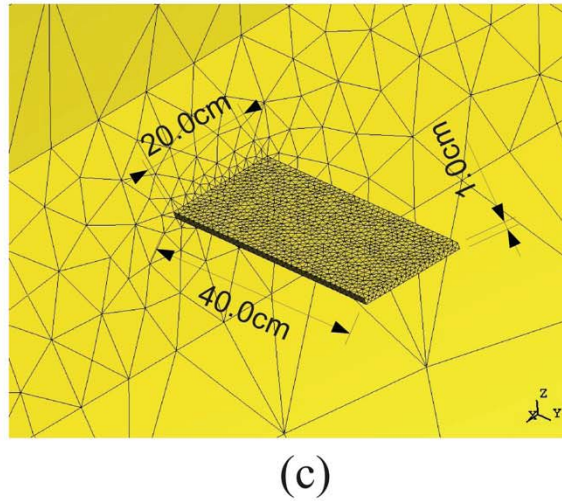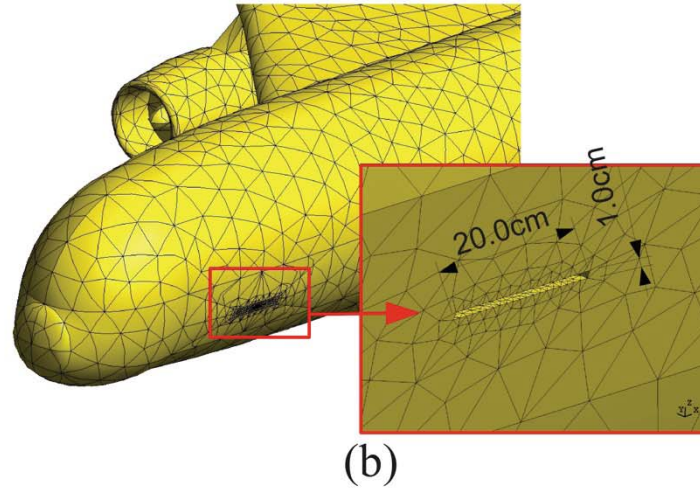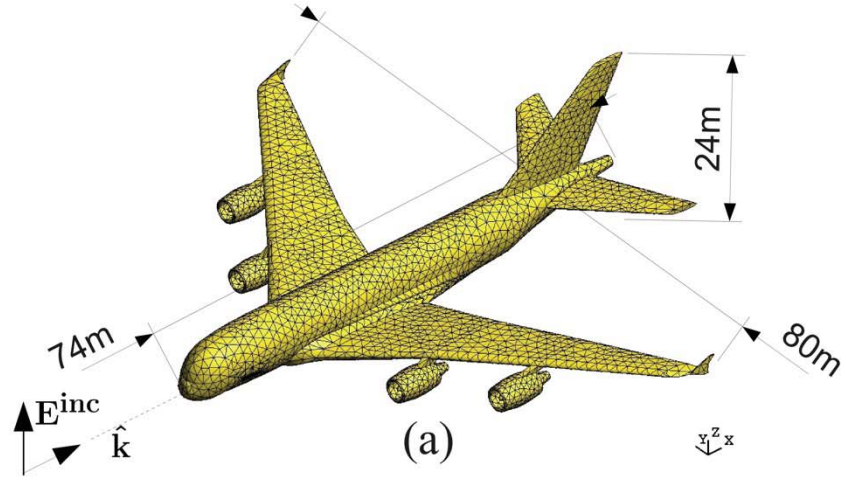
Fig. IV.4. Airbus A380 model illuminated by a $\hat{z}$-polarized plane wave traveling in the $\hat{x}$ direction. (a) Mesh and main dimensions of the aircraft; second order curvilinear patches are used to discretize the surface. (b) Detail of the slot in the aircraft's fuselage. (c) Cavity seeing from inside.
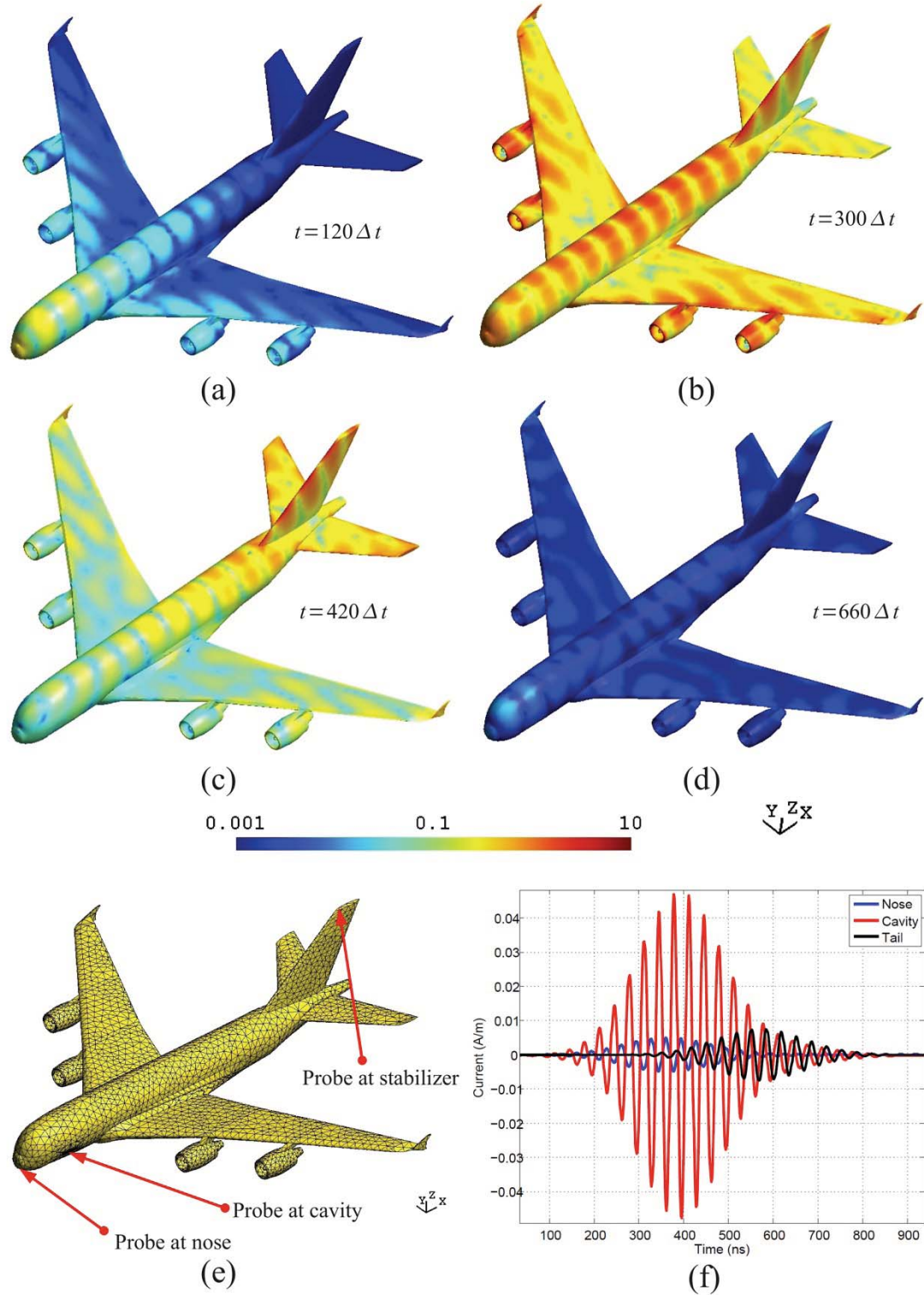
Fig. IV.5. Current distribution on the surface of the Airbus A380 of Fig. IV.4 at (a) $t = 120\Delta t$, (b) $t = 300\Delta t$, (c) $t = 420\Delta t$, and (d) $t = 660\Delta t$. (e) Location of the three probes; one is located at the tip of the nose, one inside the small cavity, and one at the tip of the vertical stabilizer. (f) Transient currents observed at the three probes.

4.3.3 Avionics bay

The last example involves a model of an avionics bay, with compartments and equipment (PCs) inside. As shown in Fig. IV.6(a-c), the geometry comprises an almost rectangular box with six compartments inside. The box is closed, except for three 7 cm diameter holes in the back of the bay. Inside the box there are four vertical divisions and a horizontal one. Vertical divisions have 3 cm –diameter holes (not shown). The bay stores two rectangular boxes (PCs) of dimensions 20 x 10 x 35 cm. Fig. IV.6(b) shows the dimensions of the compartments. Fig. IV.6(c) shows the bay with its cover, as well as its main dimensions.

Fig. IV.7(a-d) show snapshots of the transient current density at different instances of time. Fig. IV.7(f) shows the transient current observed at each PC inside the bay (see Fig. IV.7(e)). The results shown in these figures are obtained with the high-order CMP-TDEFIE using time basis functions of order $q = 4$ (and a time step of $\Delta t = 1500$ ps) and spatial basis functions of order $p = 2$.
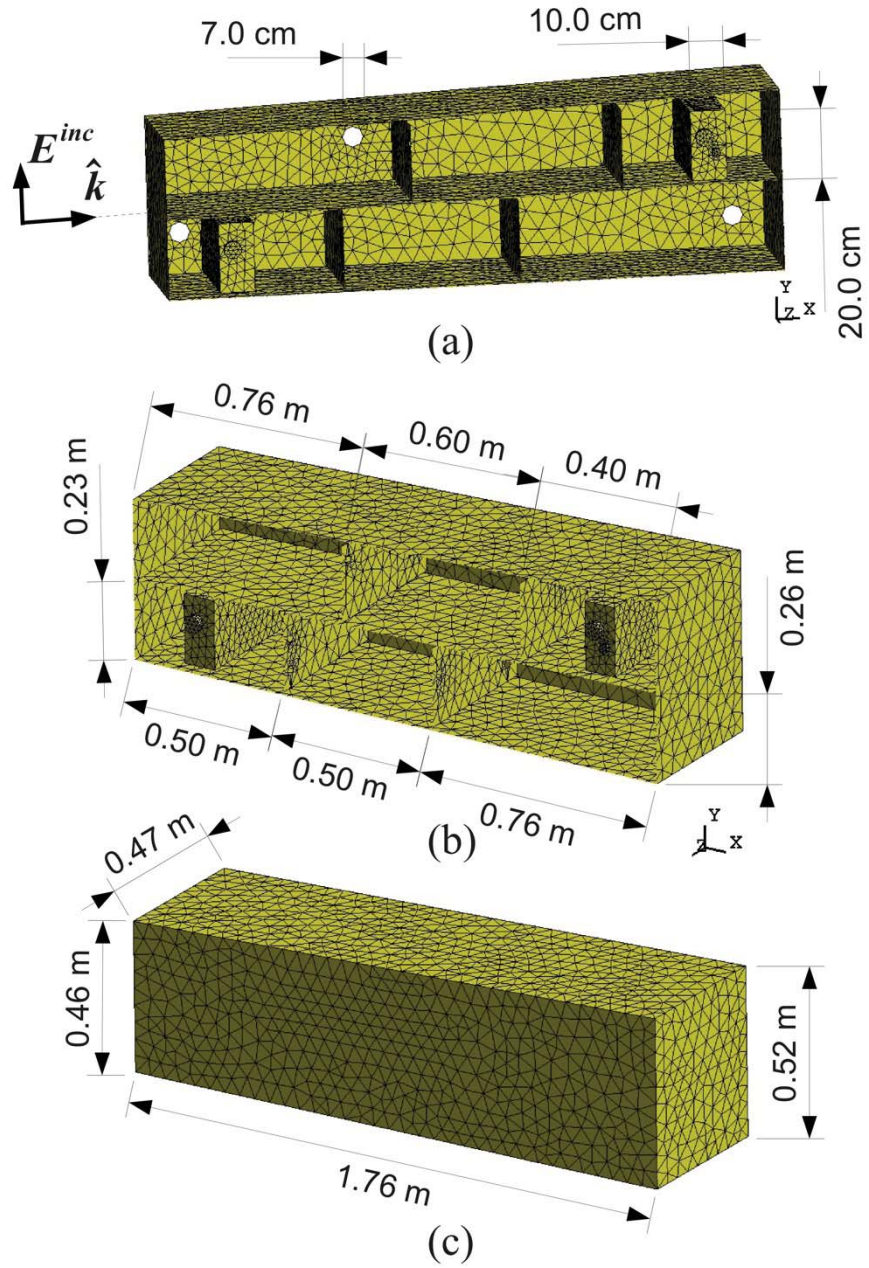
Fig. IV.6. Avionics bay illuminated by a $\hat{y}$-polarized plane wave traveling in the $\hat{x}$ direction. (a) Bay without its cover, with six compartments and two PCs inside. (b) Dimensions of the compartments. (c) Main dimensions of the bay.
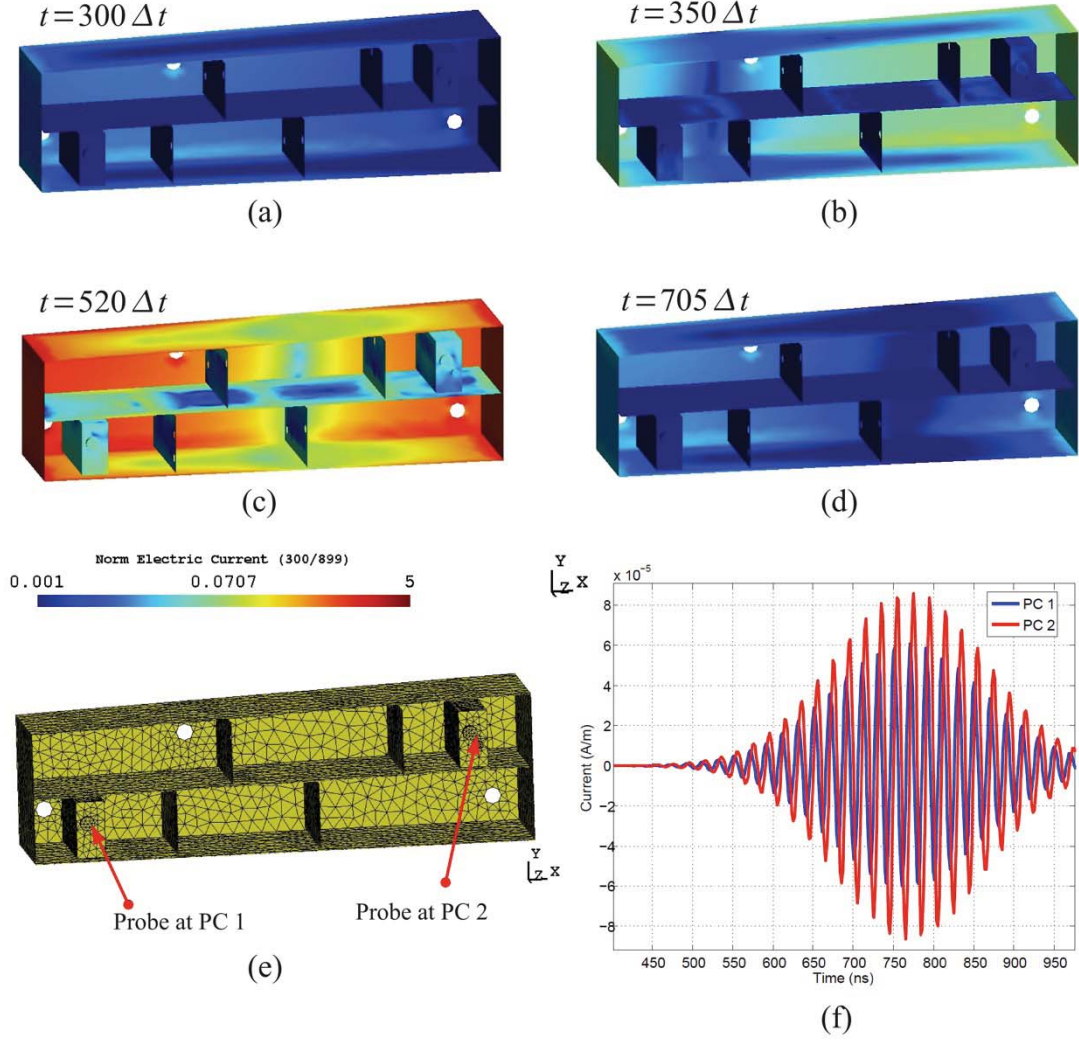
Fig. IV.7. Current distribution on the surface of the avionics bay of Fig. IV.6 at (a) $t = 300\Delta t$, (b) $t = 350\Delta t$, (c) $t = 520\Delta t$, and (d) $t = 705\Delta t$. (e) Location of the two probes; one on each PC. (f) Transient currents observed at the two probes.

In the remainder of this section, the high-order implementation of the Dottrick-TDEFIE is studied. To demonstrate that the scheme in (8.43) is free from DC instabilities, consider the companion matrix $\mathbf{T}_C$ [13]

$$\mathbf{T}_C = \begin{pmatrix} -(\dot{\mathbf{T}}^{(0)})^{-1}\dot{\mathbf{T}}^{(1)} & -(\dot{\mathbf{T}}^{(0)})^{-1}\dot{\mathbf{T}}^{(2)} & -(\dot{\mathbf{T}}^{(0)})^{-1}\dot{\mathbf{T}}^{(3)} & \cdots & -(\dot{\mathbf{T}}^{(0)})^{-1}\dot{\mathbf{T}}^{(k_{max})} \\ \mathbf{I} & & & & \\ & \mathbf{I} & & & \\ & & \mathbf{I} & & \\ & & & \ddots & \end{pmatrix} \tag{8.51}$$

4.3.4   High-Order Dottrick-TDEFIE Applied to a Sphere

The first example considered is a PEC sphere of radius 1 m. The surface of the sphere is discretized with 32 curvilinear patches. Each patch is obtained by means of an exact mapping from a reference patch onto the surface of the sphere. The incident field is described by (8.50), with $f_0 = 30$ KHz, $f_{BW} = 20$ KHz, $\hat{k} = \hat{x}$, $\hat{p} = \hat{z}$, and $t_p = 500\,\mu s$. The simulation is run with a time step $\Delta t = 1\,\mu s$ and a total of $N_T = 2000$ time steps. Results shown in this section are obtained using temporal basis functions of order $q = 3$ and spatial basis functions of order $p = 0, 1, 2, 3$.

The polynomial eigenvalues of the differentiated TDEFIE and the Dottrick-TDEFIE (both discretized with spatial basis functions of order $p = 0$) are plotted in Fig. IV.8(a) and Fig. IV.8(b), respectively. As detailed in Fig. IV.8(a), the polynomial eigenvalues of the differentiated TDEFIE contains a cluster of poles in the vicinity of $1 + 0i$. These poles are responsible of the DC instability of the differentiated TDEFIE. As expected, this cluster is not present in the polynomial eigenvalues of the Dottrick-TDEFIE. Similar results are obtained using spatial basis functions of order $p = 1$ (Fig. IV.8(c-d)), $p = 2$ (Fig. IV.9 (a-b)), and $p = 3$ (Fig. IV.9(c-d)). Note that as the order of the spatial basis functions is increased, the cluster around $1 + 0i$ becomes denser, with poles situated further away from the unit circle.

The current obtained with the Dottrick-TDEFIE (using spatial basis functions of order $p = 0, 1, 2, 3$) is plotted in Fig. IV.10(a-d) and compared to the one obtained with the differentiated TDEFIE and the CMP-TDEFIE. Irrespective of the order of the spatial basis functions, the DC instabilities are not present in the Dottrick-TDEFIE. In contrast, and as expected, DC instabilities are more outspoken for the differentiated TDEFIE and the CMP-TDEFIE as the order of the spatial basis functions is increased.

It is worth noting that in the MOT process for solving the differentiated TDEFIE for spatial basis functions of order $p = 2, 3$, the GMRES solver could not reach a relative residual error smaller than 10^{-1} at any time step, even after 30,000 iterations. For this reason, the solution obtained with this scheme does not resemble at all with the one obtained with the Dottrick-TDEFIE. The solution obtained with the CMP-

TDEFIE (in this case, the GMRES solver could reach the specified error of 10^{-8} in a few iterations) does resemble the one obtained with the Dottrick-TDEFIE, yet it still suffers from DC instabilities.

To demonstrate the effect of the spatial basis functions in the accuracy of the Dottrick-TDEFIE, Fig. IV.11(a) shows the bistatic radar cross-section (RCS) calculated for $\phi = 0°$ and $-180° \leq \theta \leq 180°$ for a frequency of 30 KHz. RCS is computed from the current obtained from solving the Dottrick-TDEFIE using temporal basis functions of order $q = 4$ and spatial basis functions of orders $p = 0,1,2$. Fig. IV.11(b) shows the error of the computed RCS with respect to Mie series solution.
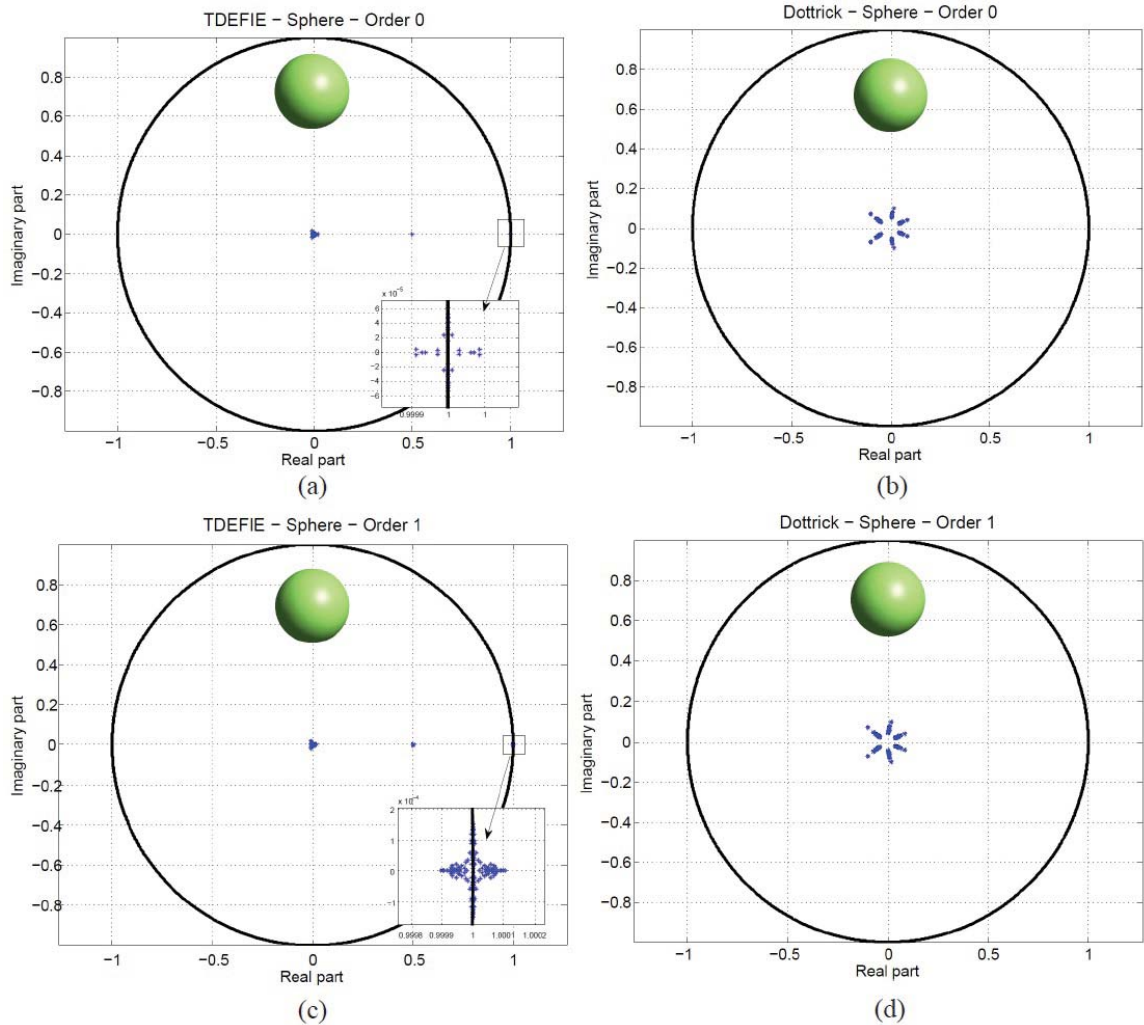
Fig. IV.8. Polynomial eigenvalues of differentiated TDEFIE and Dottrick-TDEFIE applied to a 1 m radius PEC sphere. (a) Differentiated TDEFIE with spatial basis functions of order $p = 0$. (b) Dottrick-TDEFIE with spatial basis functions of order $p = 0$. (c) Differentiated TDEFIE with spatial basis functions of order $p = 1$. (d) Dottrick-TDEFIE with spatial basis functions of order $p = 1$.
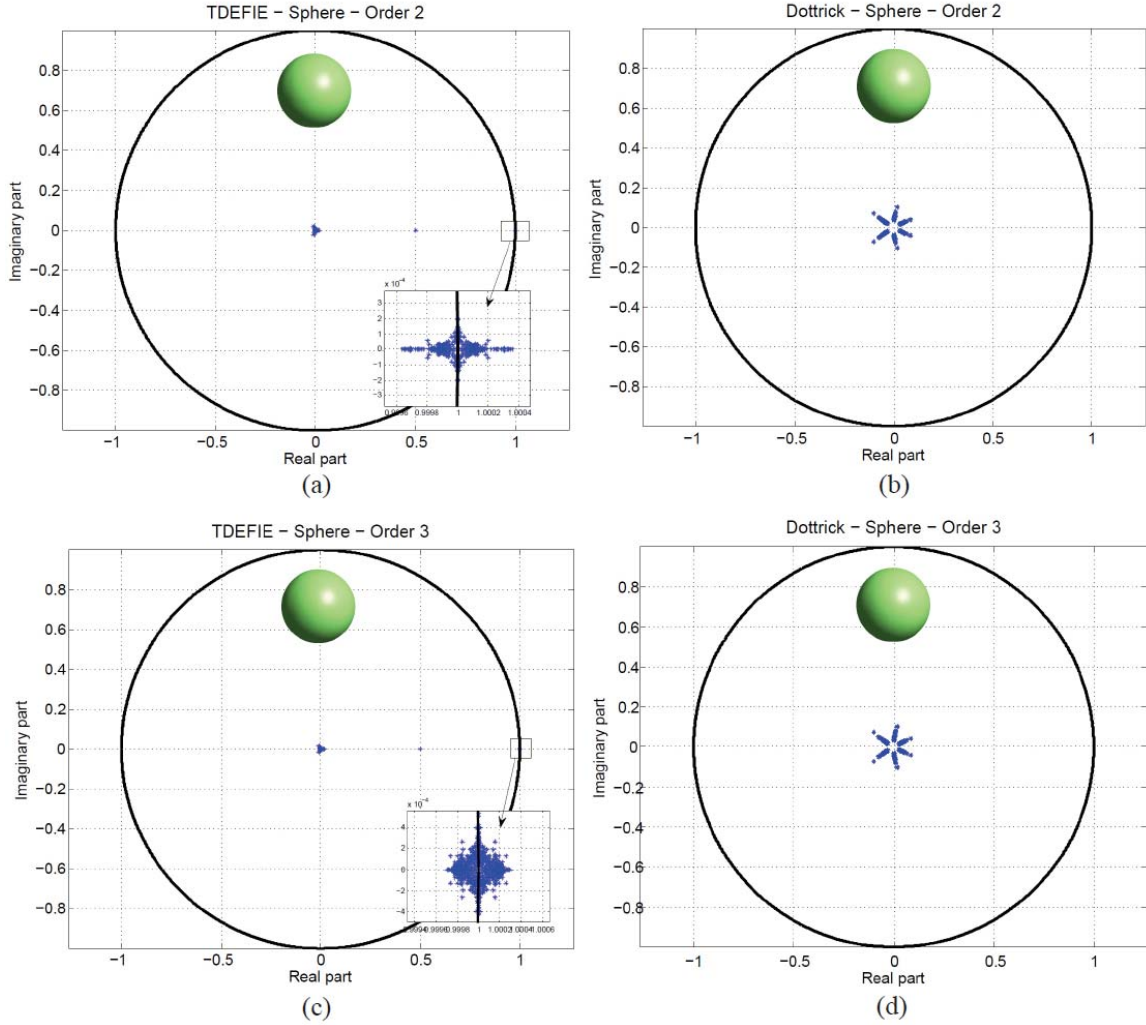
Fig. IV.9. Polynomial eigenvalues of differentiated TDEFIE and Dottrick-TDEFIE applied to a 1 m radius PEC sphere. (a) Differentiated TDEFIE with spatial basis functions of order $p = 2$. (b) Dottrick-TDEFIE with spatial basis functions of order $p = 2$. (c) Differentiated TDEFIE with spatial basis functions of order $p = 3$. (d) Dottrick-TDEFIE with spatial basis functions of order $p = 3$.
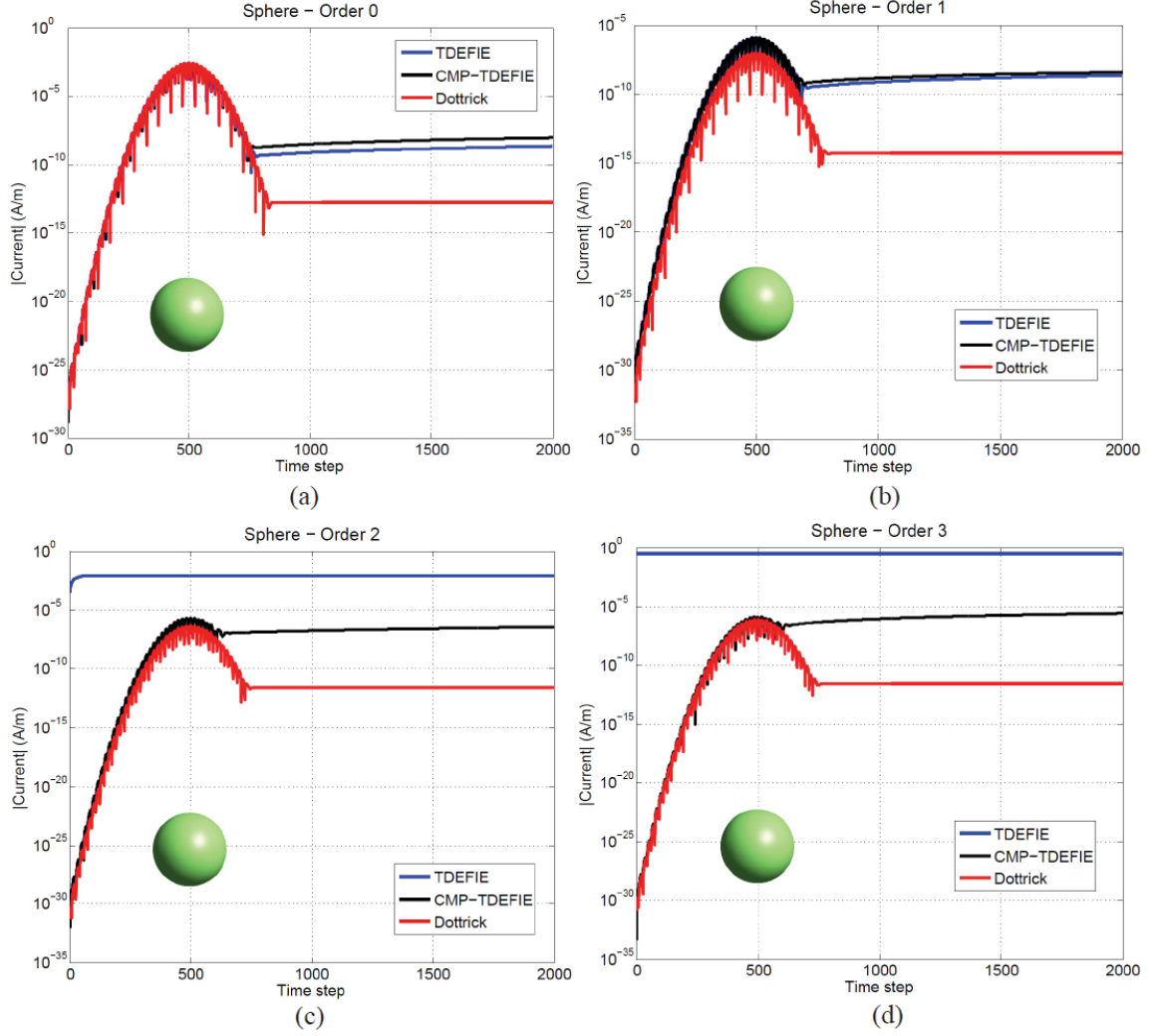
Fig. IV.10. Electric current density obtained after solving the differentiated TDEFIE, CMP-TDEFIE, and Dottrick-TDEFIE. The target is a 1 m radius PEC sphere, illuminated by a Gaussian pulse with center frequency $f_0 = 30$ KHz and bandwidth $f_{BW} = 20$ KHz traveling along $\hat{k} = \hat{z}$ and with polarization $\hat{p} = \hat{x}$. All equations are discretized using temporal basis functions of order $q = 3$ and spatial basis functions of order (a) $p = 0$, (b) $p = 1$, (c) $p = 2$, and (d) $p = 3$.
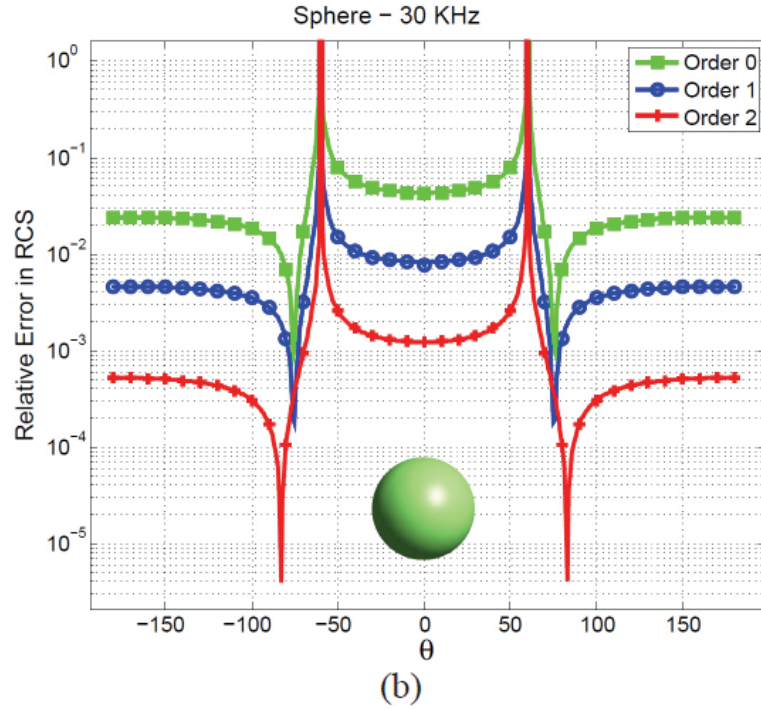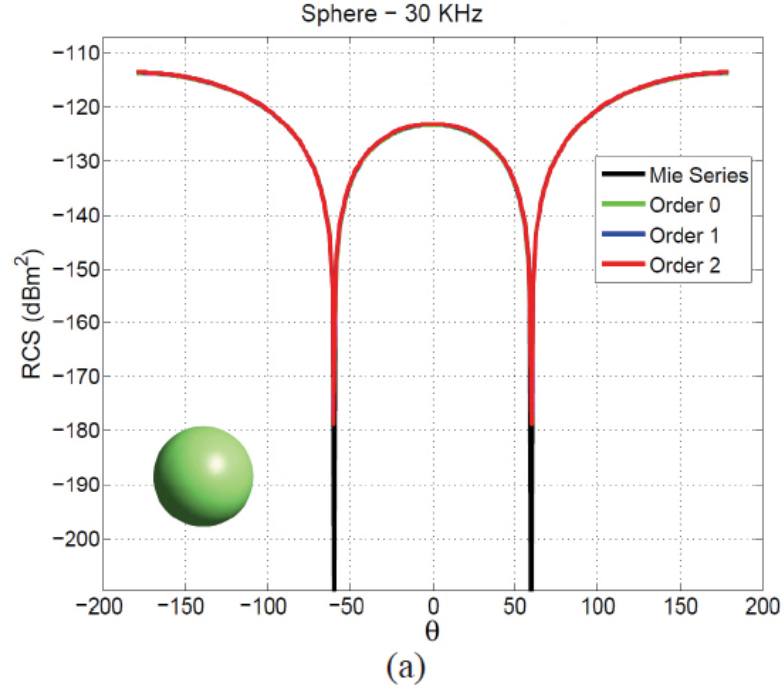
Fig. IV.11. Bistatic RCS at a frequency of 30 KHz obtained after solving the Dottrick-TDEFIE for a 1 m radius PEC sphere, illuminated by a Gaussian pulse with center frequency $f_0 = 30\,\text{KHz}$ and bandwidth $f_{BW} = 20\,\text{KHz}$, traveling along $\hat{\boldsymbol{k}} = \hat{\boldsymbol{z}}$ and with polarization $\hat{\boldsymbol{p}} = \hat{\boldsymbol{x}}$. The surface of the sphere is modeled with 32 curvilinear patches. The current density is modeled with temporal basis functions of order $q = 4$ and spatial basis functions of orders $p = 0,1,2$. The number of spatial unknowns ranges from 48 ($p = 0$) to 336 ($p = 2$). (a) Bistatic RCS in the x-z plane. (b) Error in RCS with respect to Mie series solution.

4.3.5 *High-Order Dottrick-TDEFIE Applied to a Cube*

The same experiments shown for the sphere are now performed for a cube of 1 m side length. In this case the incident field is described by (8.50), with $f_0 = 30$ KHz, $f_{BW} = 20$ KHz, $\hat{k} = \hat{x}$, $\hat{p} = \hat{z}$, and $t_p = 500\ \mu$s. The simulation is run with a time step $\Delta t = 1\ \mu$s and a total of $N_T = 2000$ time steps.

The polynomial eigenvalues of the differentiated TDEFIE and Dottrick-TDEFIE are shown in Fig. IV.12(a-b), Fig. IV.12(c-d), Fig. IV.13(a-b), and Fig. IV.13(c-d), for spatial basis functions of order $p = 0,1,2,3$, respectively. The current obtained with the Dottrick-TDEFIE (using spatial basis functions of order $p = 0,1,2,3$) is plotted in Fig. IV.14(a-d) and compared to the one obtained with the differentiated TDEFIE and the CMP-TDEFIE. As expected, the results obtained here with the differentiated TDEFIE, CMP-TDEFIE, and Dottrick-TDEFIE are consistent to those obtained for the sphere.
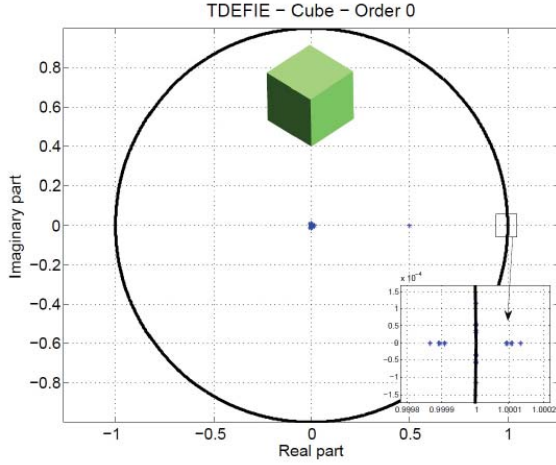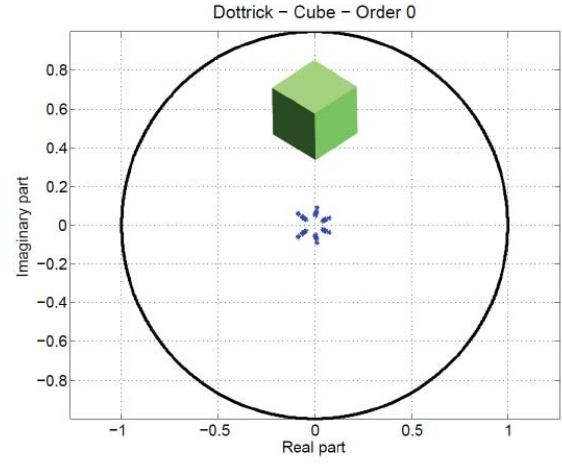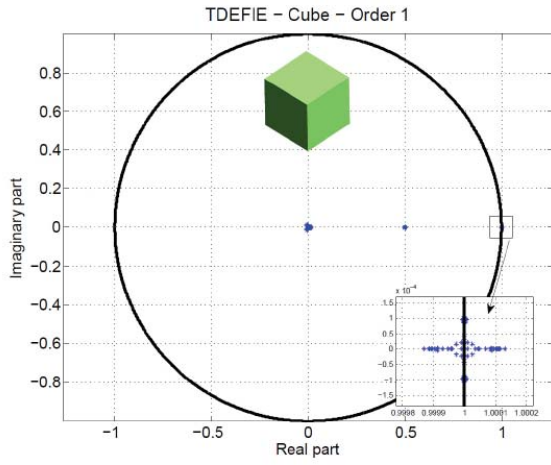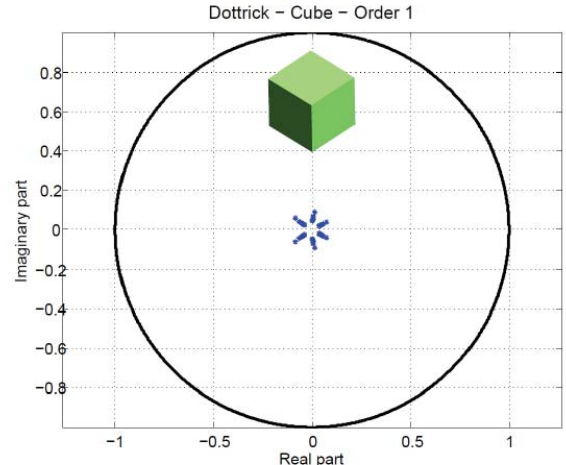
Fig. IV.12. Polynomial eigenvalues of differentiated TDEFIE and Dottrick-TDEFIE applied to a PEC cube with side length of 1 m. (a) Differentiated TDEFIE with spatial basis functions of order $p = 0$. (b) Dottrick-TDEFIE with spatial basis functions of order $p = 0$. (c) Differentiated TDEFIE with spatial basis functions of order $p = 1$. (d) Dottrick-TDEFIE with spatial basis functions of order $p = 1$.
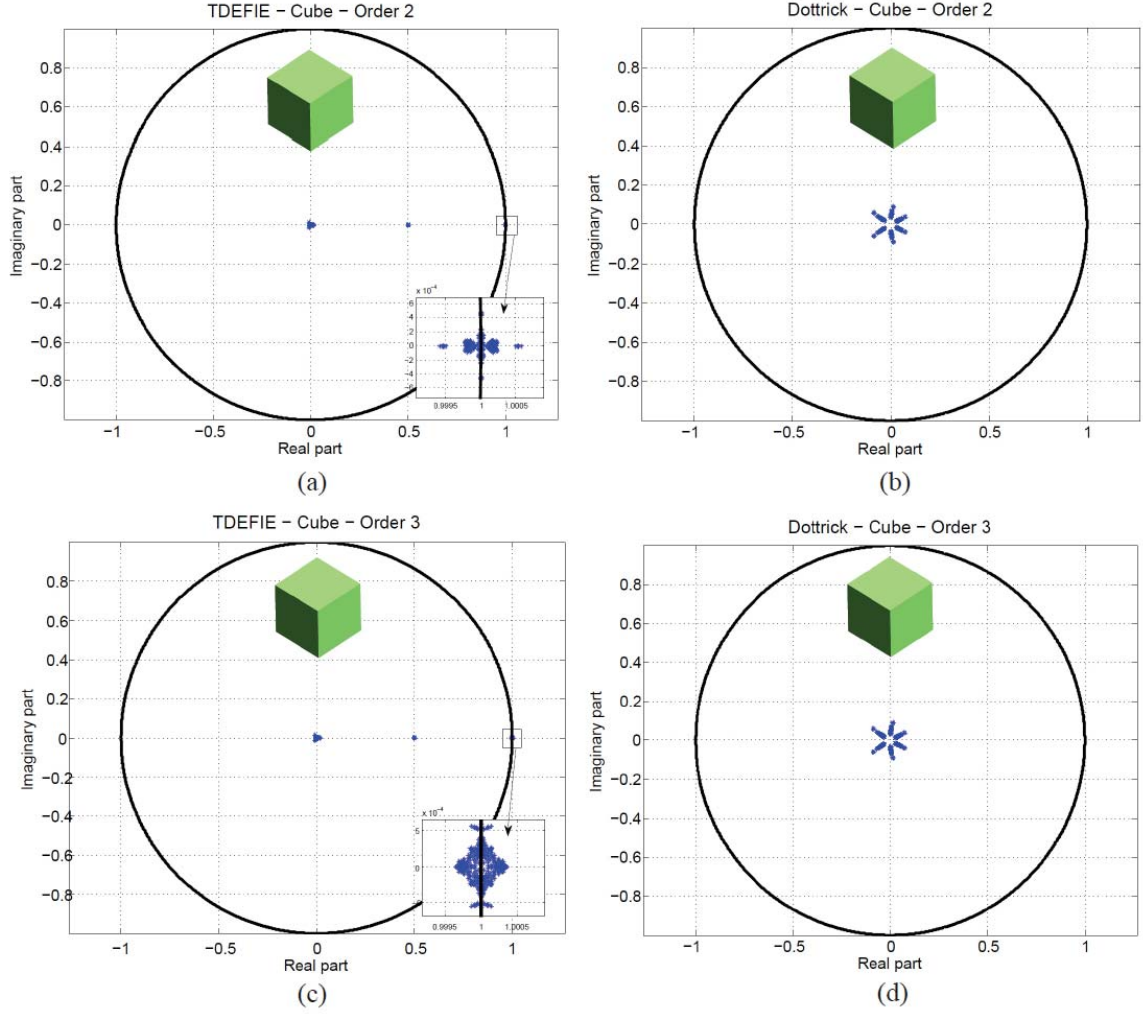
Fig. IV.13. Polynomial eigenvalues of differentiated TDEFIE and Dottrick-TDEFIE applied to a PEC cube with side length of 1 m. (a) Differentiated TDEFIE with spatial basis functions of order $p = 1$. (b) Dottrick-TDEFIE with spatial basis functions of order $p = 1$. (c) Differentiated TDEFIE with spatial basis functions of order $p = 2$. (d) Dottrick-TDEFIE with spatial basis functions of order $p = 2$.
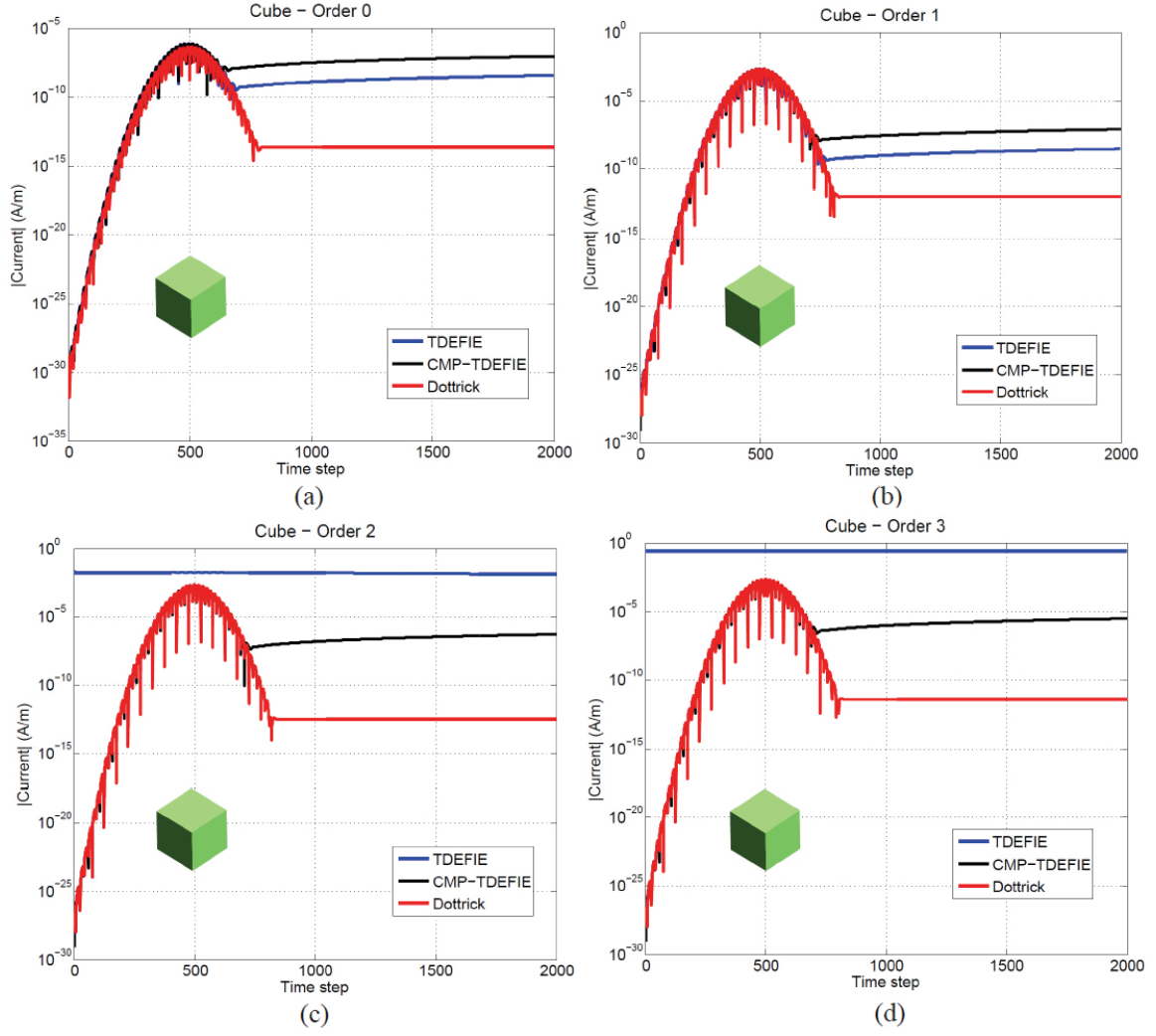
Fig. IV.14. Electric current density obtained by solving the differentiated TDEFIE, CMP-TDEFIE, and Dottrick-TDEFIE. The target is a 1 m radius PEC sphere illuminated by a Gaussian pulse with center frequency $f_0 = 30$ KHz and $f_{BW} = 20$ KHz traveling along $\hat{k} = \hat{z}$ and polarization $\hat{p} = \hat{x}$. All equations are discretized using temporal basis functions of order $q = 3$ and spatial basis functions of order (a) $p = 0$, (b) $p = 1$, (c) $p = 2$, and (d) $p = 3$.

Time Domain Single Source Integral Equations for Analyzing Scattering from Homogeneous Penetrable Objects

5.1 Time-Domain Single Source Equations

Consider a homogeneous penetrable object with surface S and outward pointing unit normal vector $\hat{\boldsymbol{n}}_r$, which is immersed in a homogeneous background medium (Fig. III.1(a)). The object is illuminated by electric and magnetic fields $\{\boldsymbol{E}^{inc}(\boldsymbol{r},t), \boldsymbol{H}^{inc}(\boldsymbol{r},t)\}$ that are zero for all $t < 0$ and temporally band-limited to maximum frequency f_{max}. Let ϵ_j, μ_j, η_j, and c_j denote the permittivity, permeability, impedance, and propagation speed of medium j, respectively. The background and the object are labeled by $j = 1$ and $j = 2$, respectively. We wish to find the total electric and magnetic fields $\{\boldsymbol{E}_j(\boldsymbol{r},t), \boldsymbol{H}_j(\boldsymbol{r},t)\}$ in regions $j = 1,2$.

For any vector field $\boldsymbol{X}$ tangential to S, the identity operator is denoted by $\mathcal{I}$; single and double layer operators pertinent to medium j are defined as

$$\mathcal{T}_j[\boldsymbol{X}](\boldsymbol{r},t) = -\frac{1}{4\pi c_j}\hat{\boldsymbol{n}}_r \times \int_S \frac{\dot{\boldsymbol{X}}(\boldsymbol{r}',t-R/c_j)}{R}ds' + \frac{c_j}{4\pi}\hat{\boldsymbol{n}}_r \times \nabla \int_S \frac{\int_0^{t-R/c_j}\nabla_s'\boldsymbol{X}(\boldsymbol{r}',t')dt'}{R}ds' \tag{5.1}$$

and

$$\mathcal{K}_j[\boldsymbol{X}](\boldsymbol{r},t) = -\hat{\boldsymbol{n}}_r \times \frac{1}{4\pi}\int_S \nabla \frac{\boldsymbol{X}(\boldsymbol{r}',t-R/c_j)}{R}ds' \tag{5.2}$$

respectively. Here R is the distance between observation $\boldsymbol{r}$ and source $\boldsymbol{r}'$ points., i.e. $R = |\boldsymbol{R}|$, where $\boldsymbol{R} = \boldsymbol{r} - \boldsymbol{r}'$. The derivation of time-domain single source equations follows closely the one illustrated in

Section 3.1. Therefore time domain single source EFIE and MFIE are presented here without formal derivation. Time-domain single source EFIE and MFIE read:

$$\frac{\eta_1}{\eta_2}\frac{\mathcal{T}_1}{2}[\boldsymbol{J}_2](\boldsymbol{r},t) + \frac{\eta_1}{\eta_2}\mathcal{T}_1\mathcal{K}_2[\boldsymbol{J}_2](\boldsymbol{r},t) + \mathcal{K}_1\mathcal{T}_2[\boldsymbol{J}_2](\boldsymbol{r},t) + \frac{\mathcal{T}_2}{2}[\boldsymbol{J}_2](\boldsymbol{r},t) = \hat{\boldsymbol{n}}_r \times \boldsymbol{E}^{inc}(\boldsymbol{r},t) \,, \tag{5.3}$$

$$\frac{\eta_1}{\eta_2}\left(\frac{\mathcal{K}_1}{2} + \mathcal{K}_1\mathcal{K}_2 + \frac{\mathcal{K}_2}{2} + \frac{\mathcal{I}}{4}\right)[\boldsymbol{J}_2](\boldsymbol{r},t) - \mathcal{T}_1\mathcal{T}_2[\boldsymbol{J}_2](\boldsymbol{r},t) = -\eta_1\hat{\boldsymbol{n}}_r \times \boldsymbol{H}^{inc}(\boldsymbol{r},t) \,. \tag{5.4}$$

Equivalent external current densities $\{\boldsymbol{J}_1(\boldsymbol{r},t), \boldsymbol{M}_1(\boldsymbol{r},t)\}$ can be expressed in terms of $\boldsymbol{J}_2$ as

$$\boldsymbol{J}_1(\boldsymbol{r},t) = \frac{\eta_1}{\eta_2}\mathcal{K}_2[\boldsymbol{J}_2](\boldsymbol{r},t) \tag{5.5}$$

$$\boldsymbol{M}_2(\boldsymbol{r},t) = -\mathcal{T}_2[\boldsymbol{J}_2](\boldsymbol{r},t) \tag{5.6}$$

5.2   Marching on Time Single Source Equations

To numerically solve either dual or the single source IEs, equivalent currents and fields are discretized in time and space. Using the same notation established in Chapter IV, it is assumed that S is approximated by a mesh $S_{\Delta s}$ comprising N_P planar or curvilinear patches (triangles), N_V vertices and N_E edges. The minimum edge size in $S_{\Delta s}$ is denoted by Δs. In addition, it is assumed that time is discretized into N_T time steps of duration $\Delta t = 1/(\chi f_{max})$, where χ is an over-sampling factor typically chosen in the range $10 \leq \chi \leq 20$. Under these assumptions, a current distribution $\boldsymbol{X}(\boldsymbol{r},t)$ on $S_{\Delta s}$ is approximated as

$$\boldsymbol{X}(\boldsymbol{r},t) \approx \sum_{i=1}^{N_T}\sum_{n=1}^{N_S} I_{i,n} g_i(t) \boldsymbol{f}_n^Q(\boldsymbol{r}) \tag{5.7}$$

where $I_{i,n}$, $i = 1,\ldots,N_T$, $n = 1,\ldots,N_S$ are expansion coefficients of $\boldsymbol{X}(\boldsymbol{r},t)$ in terms of N_T scalar temporal basis functions $g_i(t)$ and N_S vector spatial div-conforming basis functions $\boldsymbol{f}_n^Q(\boldsymbol{r})$.

The set of spatial basis functions $Q = \{\boldsymbol{f}_n^Q(\boldsymbol{r}), n = 1,\ldots,N_S\}$ is, unless otherwise stated, assumed to be the set of (div-conforming) p^{th}-order interpolatory Graglia-Wilton-Peterson functions, i.e. $Q = \text{GWP}(p)$.

The temporal basis functions $g_i(t) = g^{LAG}(t - i\Delta t)$, $i = 1, \ldots, N_T$ are shifted piecewise polynomial Lagrange interpolants of degree $q > 1$ defined as [26]

$$g^{LAG}(t) = \left(\prod_{i=1}^{k} \frac{i\Delta t - t}{i\Delta t} \right) \left(\prod_{i=1}^{q-k} \frac{i\Delta t + t}{i\Delta t} \right) \tag{5.8}$$

for $t \in [(k-1)\Delta t, k\Delta t]$ and $k = 0, \ldots, q$. Note that $g^{LAG}(t)$ is non-zero only in the interval $(-\Delta t, q\Delta t)$.

The discretization of standard dual source integral equations for analyzing scattering from dielectric objects calls for the discretization of standalone operators $\mathcal{T}_j$ and $\mathcal{K}_j$. Typically, $\mathcal{T}_j$ is discretized using div-conforming basis functions $f_n^Q(r)$ and curl-conforming test functions $\hat{n}_r \times f_n^Q(r)$, yielding the $N_S N_T \times N_S N_T$ lower triangular block matrix

$$\mathbf{T}_j^{nQ;Q} = \begin{bmatrix} \mathbf{T}_j^{nQ;Q}(0) & & & \\ \mathbf{T}_j^{nQ;Q}(1) & \mathbf{T}_j^{nQ;Q}(0) & & \\ \mathbf{T}_j^{nQ;Q}(2) & \mathbf{T}_j^{nQ;Q}(1) & \mathbf{T}_j^{nQ;Q}(0) & \\ \vdots & \vdots & \vdots & \ddots \end{bmatrix} \tag{5.9}$$

with matrices $\mathbf{T}_j^{nQ;Q}(k)$, $k = 0, 1, \ldots, k_{max}$, given by

$$\begin{aligned} \left(\mathbf{T}_j^{nQ;Q}(k) \right)_{m,n} &= \left\langle \hat{n}_r \times f_m^Q(r), \mathcal{T}_j[g_{-k} f_n^Q](r,t) \right\rangle \\ &= -\frac{1}{4\pi c} \iint_{S \times S} f_m^Q(r) \cdot f_n^Q(r') \frac{\dot{g}^{LAG}(k\Delta t - R/c_j)}{R} ds' ds \\ &\quad -\frac{c_j}{4\pi} \iint_{S \times S} \nabla_s \cdot f_m^Q(r) \nabla_s' \cdot f_n^Q(r') \frac{\int_0^{k\Delta t - R/c_j} g^{LAG}(t') dt'}{R} ds' ds \end{aligned} \tag{5.10}$$

The superscript " $nQ;Q$ " indicates that functions in Q and nQ are used as basis and test (space) functions, respectively. At any position $r \in S_{\Delta s}$ and for any time $t > 0$, $\mathcal{T}_j[g_{-k} f_n^Q](r,t)$ accounts for the electric field originated by electric current f_n^Q , k time steps ago i.e., at time $t - k\Delta t$. The number of non-zero interaction matrices is given by

$$k_{max} = \frac{D}{c_j \Delta t} + q,$$
(5.11)

where D is the diameter of the smallest sphere circumscribing $S_{\Delta s}$.

The operator $\mathcal{W}_j \equiv \left(\mathcal{K}_j + \mathcal{I}/2 \right)$ often is discretized using div-conforming basis functions and either div- or curl-conforming test functions (depending on the role $\mathcal{K}_j$ plays in the equation), yielding the matrices $\mathbf{W}_j^{Q':Q}(k)$ and $\mathbf{W}_j^{nQ':Q}(k)$, $k = 0,1,\ldots,k_{max}$, with entries

$$\left(\mathbf{W}_j^{Q':Q}(k) \right)_{m,n} = \left\langle \boldsymbol{f}_m^{Q'}(\boldsymbol{r}), \mathcal{K}_j [g_{-k} \boldsymbol{f}_n^{Q}](\boldsymbol{r},t) \right\rangle + \frac{1}{2} \left\langle \boldsymbol{f}_m^{Q'}(\boldsymbol{r}), g_{-k}(t) \boldsymbol{f}_n^{Q}(\boldsymbol{r}) \right\rangle$$

$$= \frac{1}{4\pi} \iint_{S \times S} \boldsymbol{f}_m^{Q'}(\boldsymbol{r}) \cdot \left(\hat{\boldsymbol{n}}_r \times \frac{\boldsymbol{f}_n^{Q}(\boldsymbol{r}') \times \boldsymbol{R}}{R^2} \right)$$

$$\times \left[\frac{1}{c_j} \dot{g}^{LAG}(k\Delta t - R/c_j) + \frac{1}{R} g^{LAG}(k\Delta t - R/c_j) \right] ds' ds$$
(5.12)

$$+ \frac{1}{2} g^{LAG}(k\Delta t) \int_S \boldsymbol{f}_m^{Q'}(\boldsymbol{r}) \cdot \boldsymbol{f}_n^{Q}(\boldsymbol{r}) ds$$

and

$$\left(\mathbf{W}_j^{nQ':Q}(k) \right)_{m,n} = \left\langle \hat{\boldsymbol{n}}_r \times \boldsymbol{f}_m^{Q'}(\boldsymbol{r}), \mathcal{K}_j [g_{-k} \boldsymbol{f}_n^{Q}](\boldsymbol{r},t) \right\rangle + \frac{1}{2} \left\langle \hat{\boldsymbol{n}}_r \times \boldsymbol{f}_m^{Q'}(\boldsymbol{r}), g_{-k}(t) \boldsymbol{f}_n^{Q}(\boldsymbol{r}) \right\rangle$$

$$= \frac{1}{4\pi} \iint_{S \times S} \left(\hat{\boldsymbol{n}}_r \times \boldsymbol{f}_m^{Q'}(\boldsymbol{r}) \right) \cdot \left(\frac{\boldsymbol{f}_n^{Q}(\boldsymbol{r}') \times \boldsymbol{R}}{R^2} \right)$$

$$\times \left[\frac{1}{c_j} \dot{g}^{LAG}(k\Delta t - R/c_j) + \frac{1}{R} g^{LAG}(k\Delta t - R/c_j) \right] ds' ds$$
(5.13)

$$+ \frac{1}{2} g^{LAG}(k\Delta t) \int_S \hat{\boldsymbol{n}}_r \times \boldsymbol{f}_m^{Q'}(\boldsymbol{r}) \cdot \boldsymbol{f}_n^{Q}(\boldsymbol{r}) ds$$

In (5.12) and (5.13), it is not necessary that $Q = Q'$.

Unfortunately, discretization schemes applicable to standalone operators do not immediately apply to operator products like those appearing in (5.3) and (5.4). A discretization scheme for products of two or more operators has been previously presented in the context of single source equations in frequency domain [21]. This scheme is used and extended here for time domain equations. The product of any two operators $\mathcal{A}$ and $\mathcal{B}$ is discretized as

$$
\left(\mathcal{AB}\right)_{dis} = \mathbf{A}^{Q;Q'}\ \mathbf{G}^{-1}_{Q'';Q'}\ \mathbf{B}^{Q'';Q'''}
$$

$$
= \begin{bmatrix} \mathbf{A}^{Q;Q'}(0) & & & \\ \mathbf{A}^{Q;Q'}(1) & \mathbf{A}^{Q;Q'}(0) & & \\ \mathbf{A}^{Q;Q'}(2) & \mathbf{A}^{Q;Q'}(1) & \mathbf{A}^{Q;Q'}(0) & \\ \vdots & \vdots & \vdots & \ddots \end{bmatrix}
$$

$$
\times \begin{bmatrix} \mathbf{G}^{-1}_{Q'';Q'} & & & \\ & \mathbf{G}^{-1}_{Q'';Q'} & & \\ & & \ddots & \\ & & & \mathbf{G}^{-1}_{Q'';Q'} \end{bmatrix} \begin{bmatrix} \mathbf{B}^{Q'';Q'''}(0) & & & \\ \mathbf{B}^{Q'';Q'''}(1) & \mathbf{B}^{Q'';Q'''}(0) & & \\ \mathbf{B}^{Q'';Q'''}(2) & \mathbf{B}^{Q'';Q'''}(1) & \mathbf{B}^{Q'';Q'''}(0) & \\ \vdots & \vdots & \vdots & \ddots \end{bmatrix}
$$

(5.14)

where $\mathbf{A}^{Q;Q'}(k)$ and $\mathbf{B}^{Q'';Q'''}(k)$, $k = 0,1,\ldots,k_{max}$, are matrices obtained by discretizing the standalone operators $\mathcal{A}$ and $\mathcal{B}$ by means two sets of suitable basis and testing functions $\{Q;Q'\}$ and $\{Q'';Q'''\}$, and $\mathbf{G}^{-1}_{Q'';Q'}$ (we slightly abuse of the notation here) is the mixed Gram matrix between the functions Q'' (that test $\mathcal{B}$) and Q' (that source $\mathcal{A}$):

$$
\left(\mathbf{G}_{Q'';Q'}\right)_{m,n} = \left\langle \boldsymbol{f}^{Q''}_m, \boldsymbol{f}^{Q'}_n \right\rangle.
$$

(5.15)

The inverse of this Gram matrix accounts for the possible lack of (bi-)orthogonality between the sets Q' and Q''. For example, using this scheme, the operator product $\mathcal{T}_1\mathcal{W}_2$ in (5.3) could be discretized as

$$
\left(\mathcal{T}_1\mathcal{W}_2\right)_{dis} = \mathbf{T}^{nGWP;GWP}_1\ \mathbf{G}^{-1}_{GWP;GWP}\ \mathbf{W}^{GWP;GWP}_2.
$$

(5.16)

The Gram matrix $\mathbf{G}_{GWP;GWP}$ is known to be well-conditioned; as a result its inverse can be applied to a vector by using just a few iterations of an iterative solver.

A different situation is encountered when this discretization scheme is used for the operator product present in (5.4). In this case, if $Q = $ GWP is used to discretize both $\mathcal{T}_1$ and $\mathcal{T}_2$, the mixed Gram matrix $\mathbf{G}_{nGWP;GWP}$ is singular (see Chapter II) and therefore the action of its inverse cannot be evaluated. Here, a high-order discretization is achieved using GWP and DQCC functions:

$$
\left(\mathcal{T}_1\mathcal{T}_2\right)_{dis} = \mathbf{T}^{nDQCC;DQCC}_1\ \mathbf{G}^{-1}_{nGWP;DQCC}\ \mathbf{T}^{nGWP;GWP}_2.
$$

(5.17)

With the discretization scheme described above, the time-domain single source EFIE (5.3) can be discretized as

$$\left(\frac{\eta_1}{\eta_2} \mathbf{T}_1^{\text{nGWP;GWP}} \ \mathbf{G}_{\text{GWP;GWP}}^{-1} \ \mathbf{W}_2^{\text{GWP;GWP}} + \mathbf{W}_1^{\text{nGWP;DQCC}} \ \mathbf{G}_{\text{nGWP;DQCC}}^{-1} \ \mathbf{T}_2^{\text{nGWP;GWP}} \right) \mathbf{I} = \mathbf{V}_E, \qquad (5.18)$$

where $\mathbf{V}_E$ contains the (tested) incident field at consecutive time steps, i.e.

$$\mathbf{V}_E = \begin{pmatrix} \mathbf{V}_E^{(1)} \\ \mathbf{V}_E^{(2)} \\ \mathbf{V}_E^{(3)} \\ \vdots \end{pmatrix}, \qquad (5.19)$$

with

$$\left(\mathbf{V}_E^{(i)} \right)_m = \left\langle \hat{\boldsymbol{n}}_r \times \boldsymbol{f}_m^{\text{GWP}}(\boldsymbol{r}), \hat{\boldsymbol{n}}_r \times \boldsymbol{E}^{inc}(\boldsymbol{r}, i\Delta t) \right\rangle. \qquad (5.20)$$

The vector $\mathbf{I}$ contains the expansion coefficients of $\boldsymbol{J}_2$ as described in (5.7),

$$\mathbf{I} = \begin{pmatrix} \mathbf{I}^{(1)} \\ \mathbf{I}^{(2)} \\ \mathbf{I}^{(3)} \\ \vdots \end{pmatrix}, \qquad (5.21)$$

with $\left(\mathbf{I}^{(i)} \right)_n = I_{i,n}$.

Similarly, time-domain single source MFIE (5.4) is discretized as

$$\left(\frac{\eta_1}{\eta_2} \mathbf{W}_1^{\text{nDQCC;GWP}} \ \mathbf{G}_{\text{GWP;GWP}}^{-1} \ \mathbf{W}_2^{\text{GWP;GWP}} - \mathbf{T}_1^{\text{nDQCC;DQCC}} \ \mathbf{G}_{\text{nGWP;DQCC}}^{-1} \ \mathbf{T}_2^{\text{nGWP;GWP}} \right) \mathbf{I} = -\eta_1 \mathbf{V}_M, \qquad (5.22)$$

with

$$\mathbf{V}_M = \begin{pmatrix} \mathbf{V}_M^{(1)} \\ \mathbf{V}_M^{(2)} \\ \mathbf{V}_M^{(3)} \\ \vdots \end{pmatrix}, \qquad (5.23)$$

and

$$\left(\mathbf{V}_M^{(i)}\right)_m = \left\langle \hat{\boldsymbol{n}}_r \times \boldsymbol{f}_m^{\mathrm{DQCC}}(\boldsymbol{r}), \hat{\boldsymbol{n}}_r \times \boldsymbol{H}^{inc}(\boldsymbol{r}, i\Delta t) \right\rangle. \tag{5.24}$$

As in any standard MOT scheme, the linear systems in (5.18) and (5.22) can be solved by forward substitution, which is equivalent to solve the systems

$$\begin{aligned}
&\left(\frac{\eta_1}{\eta_2} \mathbf{T}_1^{\mathrm{nGWP;GWP}}(0)\, \mathbf{G}_{\mathrm{GWP;GWP}}^{-1}\, \mathbf{W}_2^{\mathrm{GWP;GWP}}(0) + \mathbf{W}_1^{\mathrm{nGWP;DQCC}}(0)\, \mathbf{G}_{\mathrm{nGWP;DQCC}}^{-1}\, \mathbf{T}_2^{\mathrm{nGWP;GWP}}(0) \right) \mathbf{I}^{(i)} \\
&= \mathbf{V}_E^{(i)} - \frac{\eta_1}{\eta_2} \sum_{l=1}^{\min\{i-1,k_{max}\}} \left(\mathbf{T}_1^{\mathrm{nGWP;GWP}}(l)\, \mathbf{G}_{\mathrm{GWP;GWP}}^{-1}\, \mathbf{W}_2^{\mathrm{GWP;GWP}}(0) \right) \mathbf{I}^{(i-l)} \\
&\quad - \frac{\eta_1}{\eta_2} \sum_{l=0}^{\min\{i-1,k_{max}\}} \mathbf{T}_1^{\mathrm{nGWP;GWP}}(l)\, \mathbf{G}_{\mathrm{GWP;GWP}}^{-1} \left(\sum_{k=1}^{\min\{i-l-1,k_{max}\}} \mathbf{W}_2^{\mathrm{GWP;GWP}}(k)\, \mathbf{I}^{(i-l-k)} \right) \\
&\quad - \sum_{l=1}^{\min\{i-1,k_{max}\}} \left(\mathbf{W}_1^{\mathrm{nGWP;DQCC}}(l)\, \mathbf{G}_{\mathrm{nGWP;DQCC}}^{-1}\, \mathbf{T}_2^{\mathrm{nGWP;GWP}}(0) \right) \mathbf{I}^{(i-l)} \\
&\quad - \sum_{l=0}^{\min\{i-1,k_{max}\}} \mathbf{W}_1^{\mathrm{nGWP;DQCC}}(l)\, \mathbf{G}_{\mathrm{nGWP;DQCC}}^{-1} \left(\sum_{k=1}^{\min\{i-l-1,k_{max}\}} \mathbf{T}_2^{\mathrm{nGWP;GWP}}(k)\, \mathbf{I}^{(i-l-k)} \right)
\end{aligned} \tag{5.25}$$

and

$$\begin{aligned}
&\left(\frac{\eta_1}{\eta_2} \mathbf{W}_1^{\mathrm{nDQCC;GWP}}(0)\, \mathbf{G}_{\mathrm{GWP;GWP}}^{-1}\, \mathbf{W}_2^{\mathrm{GWP;GWP}}(0) - \mathbf{T}_1^{\mathrm{nDQCC;DQCC}}(0)\, \mathbf{G}_{\mathrm{nGWP;DQCC}}^{-1}\, \mathbf{T}_2^{\mathrm{nGWP;GWP}}(0) \right) \mathbf{I}^{(i)} \\
&= -\eta_1 \mathbf{V}_M^{(i)} - \frac{\eta_1}{\eta_2} \sum_{l=1}^{\min\{i-1,k_{max}\}} \left(\mathbf{W}_1^{\mathrm{nDQCC;GWP}}(l)\, \mathbf{G}_{\mathrm{GWP;GWP}}^{-1}\, \mathbf{W}_2^{\mathrm{GWP;GWP}}(0) \right) \mathbf{I}^{(i-l)} \\
&\quad - \frac{\eta_1}{\eta_2} \sum_{l=1}^{\min\{i-1,k_{max}\}} \mathbf{W}_1^{\mathrm{nDQCC;GWP}}(l)\, \mathbf{G}_{\mathrm{GWP;GWP}}^{-1} \left(\sum_{k=1}^{\min\{i-l-1,k_{max}\}} \mathbf{W}_2^{\mathrm{GWP;GWP}}(k)\, \mathbf{I}^{(i-l-k)} \right) \\
&\quad + \sum_{l=1}^{\min\{i-1,k_{max}\}} \left(\mathbf{T}_1^{\mathrm{nDQCC;DQCC}}(l)\, \mathbf{G}_{\mathrm{nGWP;DQCC}}^{-1}\, \mathbf{T}_2^{\mathrm{nGWP;GWP}}(0) \right) \mathbf{I}^{(i-l)} \\
&\quad + \sum_{l=0}^{\min\{i-1,k_{max}\}} \mathbf{T}_1^{\mathrm{nDQCC;DQCC}}(l)\, \mathbf{G}_{\mathrm{nGWP;DQCC}}^{-1} \left(\sum_{k=1}^{\min\{i-l-1,k_{max}\}} \mathbf{T}_2^{\mathrm{nGWP;GWP}}(k)\, \mathbf{I}^{(i-l-k)} \right)
\end{aligned} \tag{5.26}$$

for every time step $i = 1, 2, \ldots, N_T$.

Using the transformation matrices $\mathbf{P}$ and $\mathbf{R}$ (see Section 2.4), the matrices $\mathbf{T}_j^{\mathrm{nGWP;GWP}}(k)$, $\mathbf{W}_j^{\mathrm{GWP;GWP}}(k)$, $\mathbf{W}_j^{\mathrm{nGWP;DQCC}}(k)$, $\mathbf{W}_j^{\mathrm{nDQCC;GWP}}(k)$, and $\mathbf{T}_j^{\mathrm{nDQCC;DQCC}}(k)$ can be expressed as

$$\mathbf{T}_j^{\mathrm{nGWP;GWP}}(k) = \mathbf{R}^{\mathrm{T}}\, \bar{\mathbf{T}}_j^{\mathrm{nGWP;GWP}}(k)\, \mathbf{R} , \tag{5.27}$$

$$\mathbf{W}_j^{\mathrm{GWP;GWP}}(k) = \mathbf{R}^{\mathrm{T}} \, \bar{\mathbf{W}}_j^{\mathrm{GWP;GWP}}(k) \, \mathbf{R} \,, \tag{5.28}$$

$$\mathbf{W}_j^{\mathrm{nGWP;DQCC}}(k) = \mathbf{R}^{\mathrm{T}} \, \bar{\mathbf{W}}_j^{\mathrm{nGWP;GWP}}(k) \, \mathbf{P} \,, \tag{5.29}$$

$$\mathbf{W}_j^{\mathrm{nDQCC;GWP}}(k) = \mathbf{P}^{\mathrm{T}} \, \bar{\mathbf{W}}_j^{\mathrm{GWP;GWP}}(k) \, \mathbf{R} \,, \tag{5.30}$$

$$\mathbf{T}_j^{\mathrm{nDQCC;DQCC}}(k) = \mathbf{P}^{\mathrm{T}} \, \bar{\mathbf{T}}_j^{\mathrm{GWP;GWP}}(k) \, \mathbf{P} \,, \tag{5.31}$$

where the matrices $\bar{\mathbf{T}}_j^{\mathrm{nGWP;GWP}}(k)$, $\bar{\mathbf{W}}_j^{\mathrm{GWP;GWP}}(k)$, and $\bar{\mathbf{W}}_j^{\mathrm{nGWP;GWP}}(k)$ are obtained through standard discretization of the operators $\mathcal{T}_j$ and $\mathcal{W}_j$ on $\bar{S}_{\Delta s}$.

5.3   Numerical Results

This section presents several examples that demonstrate the effectiveness of the time-domain single source equations and of the discretization scheme presented in this chapter. The results shown here are obtained using a parallel MOT single source TDIE solver which implements both EFIE and MFIE discussed in the previous sections. This solver uses a generalized minimal residual (GMRES)-based iterative method [39] to solve the linear systems on each time step. In all examples considered here, objects are illuminated by a Gaussian plane wave given by

$$\boldsymbol{E}^{inc}(\boldsymbol{r},t) = \hat{\boldsymbol{p}} e^{-[(\tau - t_p)/\sqrt{2}\sigma]^2} \cos(2\pi f_0 \tau) \,, \tag{5.32}$$

where f_0 is the center frequency, $\tau = t - \hat{\boldsymbol{r}} \cdot \hat{\boldsymbol{k}}/c$, $\hat{\boldsymbol{k}}$ denotes the direction of propagation and $\hat{\boldsymbol{p}}$ denotes the polarization of the incident wave. The temporal standard deviation σ is related to the nominal bandwidth f_{BW} by $\sigma = 6/(2\pi f_{BW})$. The delay time of the wave relative to the origin is denoted by t_p. All frequency-domain results attributed to the proposed solver are obtained by (discrete) Fourier transforming time-domain data while accounting for the spectral content of the incident field. Whenever pertinent, results obtained with time-domain single source EFIE/MFIE are compared to those obtained with frequency-domain single source EFIE/MFIE, using the same spatial discretization and integration rules.

5.3.1 MOT Analysis of Scattering from a Sphere

The first example considered is a sphere of radius 1 m with permittivity $\epsilon_2 = 2\epsilon_1$ and permeability $\mu_2 = \mu_1$ ($\epsilon_1 = \epsilon_0 = 8.854187 \times 10^{-12}$ F/m, $\mu_1 = \mu_0 = 4\pi \times 10^{-7}$ H/m). The incident field is described by (5.32), with $f_0 = 50$ MHz, $f_{BW} = 50$ MHz, $\hat{k} = \hat{x}$, $\hat{p} = \hat{z}$, and $t_p = 150$ ns. The surface of the sphere is discretized with 32 curvilinear patches. Each patch is obtained by means of an exact mapping from a reference patch onto the surface of the sphere. The simulation is run with a time step $\Delta t = 250$ ps and a total of $N_T = 2000$ time steps. Fig. V.1 to V.3 show plots of the transient equivalent currents $J_1(r,t)$ and $M_1(r,t)$ obtained by solving single source EFIE and MFIE using temporal basis functions of order $q = 4$ and spatial basis functions of order $p = 0,1,2$. Fig. V.1(a-b) show the equivalent currents at a position $r = (-0.816, 0.408, 0.408)$ m along the direction (-0.577, -0.577, -0.577) obtained using spatial basis functions of order $p = 0$. The number of spatial unknowns is $N_S = 48$. Fig. V.2(a-b) show the equivalent currents at a position $r = (-0.534, -0.801, 0.267)$ m along the direction (0.577, -0.577, -0.577) obtained using spatial basis functions of order $p = 1$. The number of spatial unknowns is $N_S = 160$. Fig. V.3(a-b) show the equivalent currents at a position $r = (0.0, -0.187, 0.982)$ m along the direction (-1.0, 0.0, 0.0) obtained using spatial basis functions of order $p = 2$. The number of spatial unknowns is $N_S = 336$.

The consistency between results obtained from time- and frequency-domain single source EFIE and MFIE is studied in Fig. V.4 to V.6. Fig. V.4(a) shows the bistatic RCS calculated for $\phi = 0°$ and $-180° \le \theta \le 180°$ for frequencies of 30, 50 and 70 MHz. RCS is computed from the equivalent currents J_1 and M_1 obtained from solving the single source EFIE in time- and frequency-domain separately. Currents are obtained using spatial basis functions of order $p = 0$, and (for time-domain) temporal basis functions of order $q = 4$. The relative error in RCS between time- and frequency-domain solutions is shown in Fig. V.4(c). Results obtained from solving the single source MFIE are shown in Fig. V.4(b,d). Similar to the data illustrated in Fig. V.4(a-d), Fig. V.5(a-d) show results obtained using spatial basis functions of order $p = 1$. Finally, Fig. V.14(a-d) show results obtained using $p = 2$.

To demonstrate the effect of the spatial basis functions, Fig. V.7(a,c,e) show the bistatic radar cross-section (RCS) calculated for $\phi = 0°$ and $-180° \leq \theta \leq 180°$ for frequencies of 30, 50 and 70 MHz respectively. RCS is computed from the equivalent currents $\mathbf{J}_1$ and $\mathbf{M}_1$ obtained from solving the single source EFIE using temporal basis functions of order $q = 4$ and spatial basis functions of orders $p = 0,1,2,3$. Fig. V.7(b,d,f) show the error of the computed RCS with respect to Mie series solution. Similarly, to demonstrate the effect of temporal basis functions, Fig. V.8(a,c,e) show the bistatic RCS when computed with spatial basis functions of order $p = 2$ and time basis functions of orders $q = 2,3,4$. Fig. V.8(b,d,f) show the relative error with respect to Mie series solution.
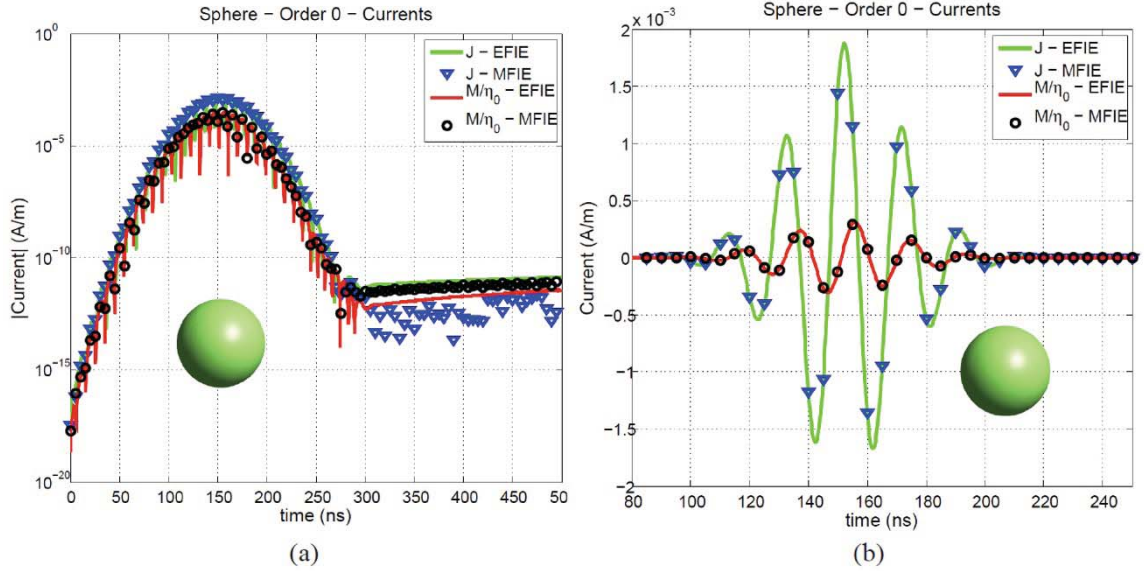
Fig. V.1. Electric and (scaled) Magnetic equivalent current densities obtained after solving time-domain single source EFIE and MFIE using temporal basis functions of order $q = 4$ and spatial basis functions of order $p = 0$. The target is a 1 m radius sphere with permittivity $\epsilon_2 = 2\epsilon_0$ illuminated by a Gaussian pulse with center frequency $f_0 = 50$ MHz and bandwidth $f_{BW} = 50$ MHz traveling along $\hat{k} = \hat{z}$ and with polarization $\hat{p} = \hat{x}$. Currents are observed at point (-0.816, 0.408, 0.408) m and along the direction (-0.577, -0.577, -0.577) (a) Absolute value of the currents for $0 \leq t \leq 500$ ns. (b) Currents for $80 \leq t \leq 250$ ns.
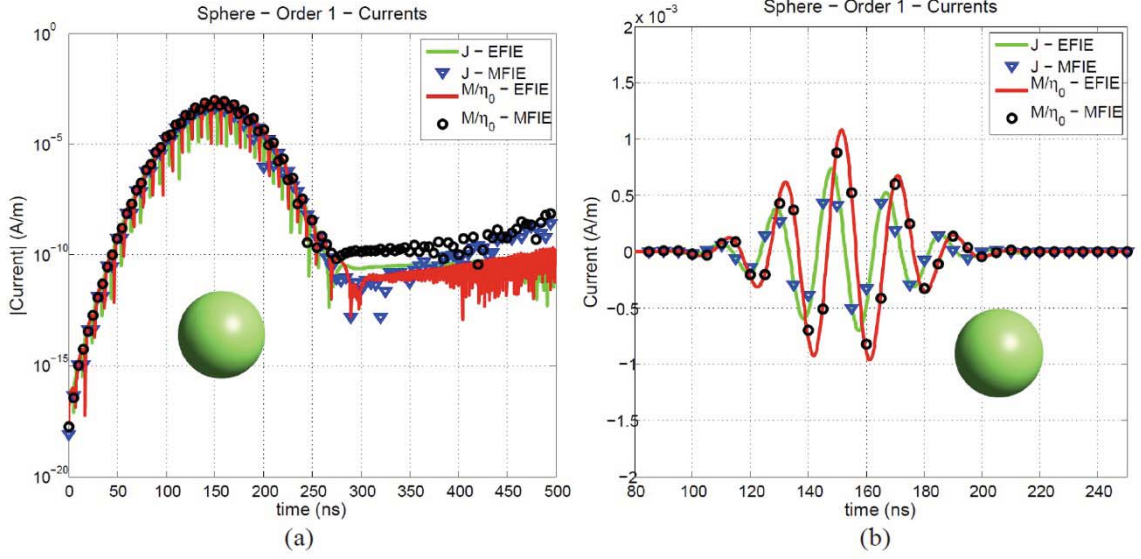
Fig. V.2. Electric and (scaled) Magnetic equivalent current densities obtained after solving time-domain single source EFIE and MFIE using temporal basis functions of order $q = 4$ and spatial basis functions of order $p = 1$. The target is a 1 m radius sphere with permittivity $\epsilon_2 = 2\epsilon_0$ illuminated by a Gaussian pulse with center frequency $f_0 = 50$ MHz and bandwidth $f_{BW} = 50$ MHz traveling along $\hat{k} = \hat{z}$ and with polarization $\hat{p} = \hat{x}$. Currents are observed at point (-0.534, -0.801, 0.267) m and along the direction (0.577, -0.577, -0.577) (a) Absolute value of the currents for $0 \le t \le 500$ ns. (b) Currents for $80 \le t \le 250$ ns.
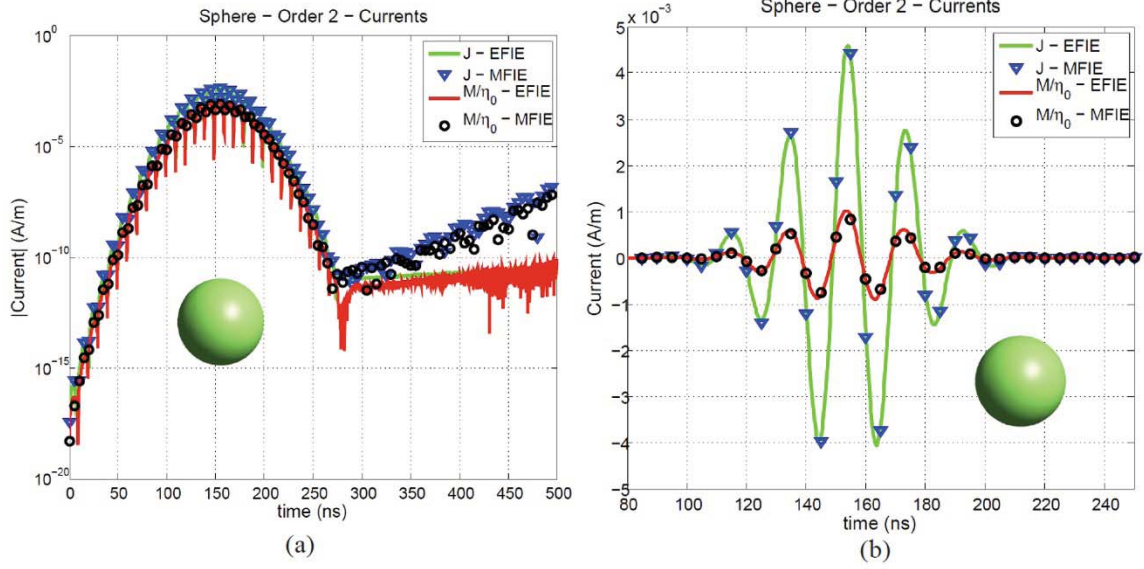
Fig. V.3. Electric and (scaled) Magnetic equivalent current densities obtained after solving time-domain single source EFIE and MFIE using temporal basis functions of order $q = 4$ and spatial basis functions of order $p = 2$. The target is a 1 m radius sphere with permittivity $\epsilon_2 = 2\epsilon_0$ illuminated by a Gaussian pulse with center frequency $f_0 = 50$ MHz and bandwidth $f_{BW} = 50$ MHz traveling along $\hat{k} = \hat{z}$ and with polarization $\hat{p} = \hat{x}$. Currents are observed at point (0.0, -0.187, 0.982) m and along the direction (-1.0, 0.0, 0.0) (a) Absolute value of the currents for $0 \leq t \leq 500$ ns. (b) Currents for $80 \leq t \leq 250$ ns.

Fig. V.4. Comparison of bistatic RCS at frequencies 30 MHz, 50 MHz, and 70 MHz obtained after solving time-domain and frequency-domain single source EFIE and MFIE using spatial basis functions of order $p=0$ for a 1 m radius sphere with $\epsilon_2 = 2\epsilon_0$. (a) RCS obtained from single source EFIE. (b) RCS obtained from singe source MFIE. (c) Relative error in RCS between time- and frequency-domain EFIE. (d) Relative error in RCS between time- and frequency-domain MFIE.

Fig. V.5. Comparison of bistatic RCS at frequencies 30 MHz, 50 MHz, and 70 MHz obtained after solving time-domain and frequency-domain single source EFIE and MFIE using spatial basis functions of order $p = 1$ for a 1 m radius sphere with $\epsilon_2 = 2\epsilon_0$. (a) RCS obtained from single source EFIE. (b) RCS obtained from singe source MFIE. (c) Relative error in RCS between time- and frequency-domain EFIE. (d) Relative error in RCS between time- and frequency-domain MFIE.
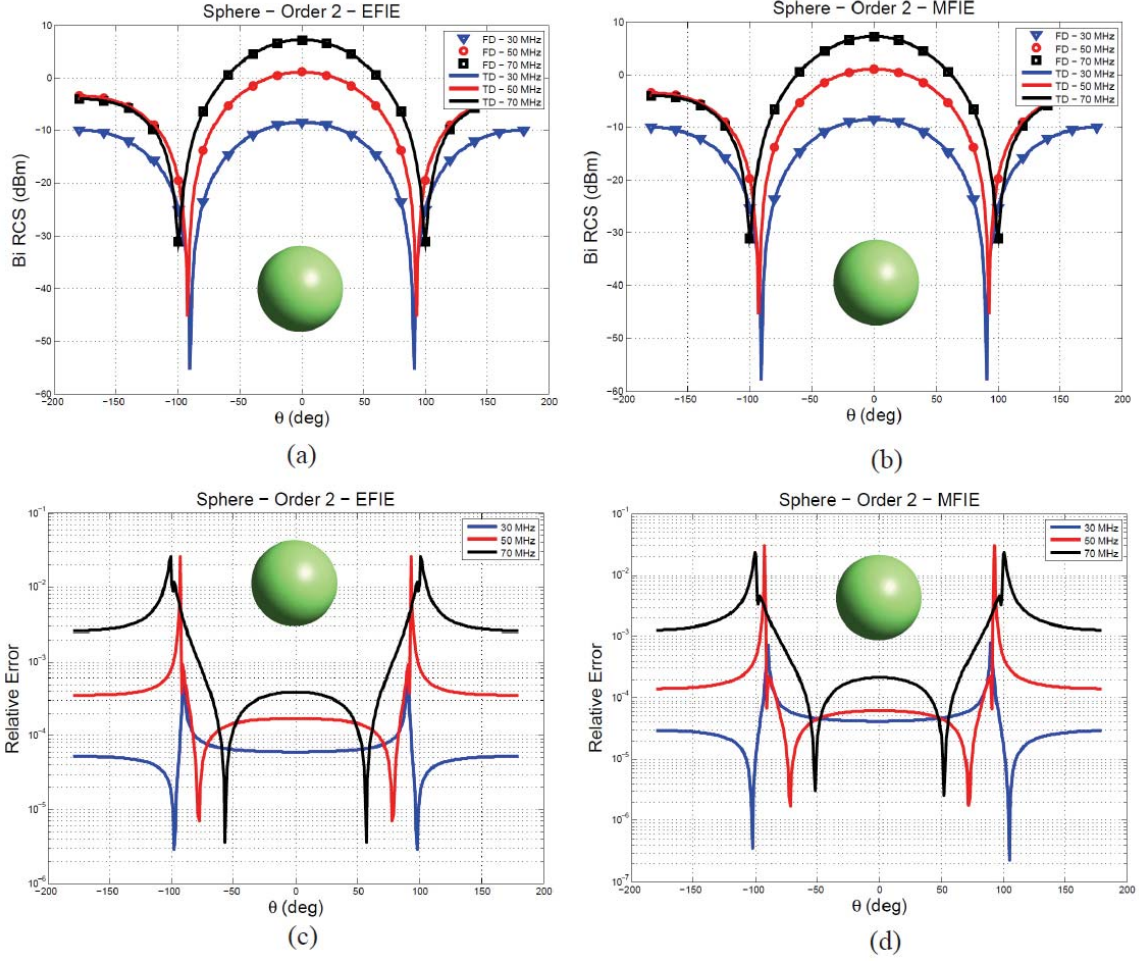
Fig. V.6. Comparison of bistatic RCS at frequencies 30 MHz, 50 MHz, and 70 MHz obtained after solving time-domain and frequency-domain single source EFIE and MFIE using spatial basis functions of order $p = 2$ for a 1 m radius sphere with $\epsilon_2 = 2\epsilon_0$. (a) RCS obtained from single source EFIE. (b) RCS obtained from singe source MFIE. (c) Relative error in RCS between time- and frequency-domain EFIE. (d) Relative error in RCS between time- and frequency-domain MFIE.

Fig. V.7. Bistatic RCS at frequencies 30 MHz, 50 MHz, and 70 MHz obtained after solving time-domain single source EFIE for a 1 m radius sphere with $\epsilon_2 = 2\epsilon_0$ illuminated by a Gaussian pulse with center frequency $f_0 = 50$ MHz and bandwidth $f_{BW} = 50$ MHz traveling along $\hat{\boldsymbol{k}} = \hat{\boldsymbol{z}}$ and with polarization $\hat{\boldsymbol{p}} = \hat{\boldsymbol{x}}$. The surface of the sphere is modeled with 32 curvilinear patches. The current density is modeled with temporal basis functions of order $q = 4$ and spatial basis functions of orders $p = 0,1,2,3$. The number of spatial unknowns ranges from 48 ($p = 0$) to 576 ($p = 3$). (a) Bistatic RCS in the x-z plane at 30 MHz. (b) Error in RCS at 30 MHz with respect to Mie series solution. (c) Bistatic RCS in the x-z plane at 50 MHz. (d) Error in RCS at 50 MHz with respect to Mie series solution. (e) Bistatic RCS in the x-z plane at 70 MHz. (f) Error in RCS at 70 MHz with respect to Mie series solution.
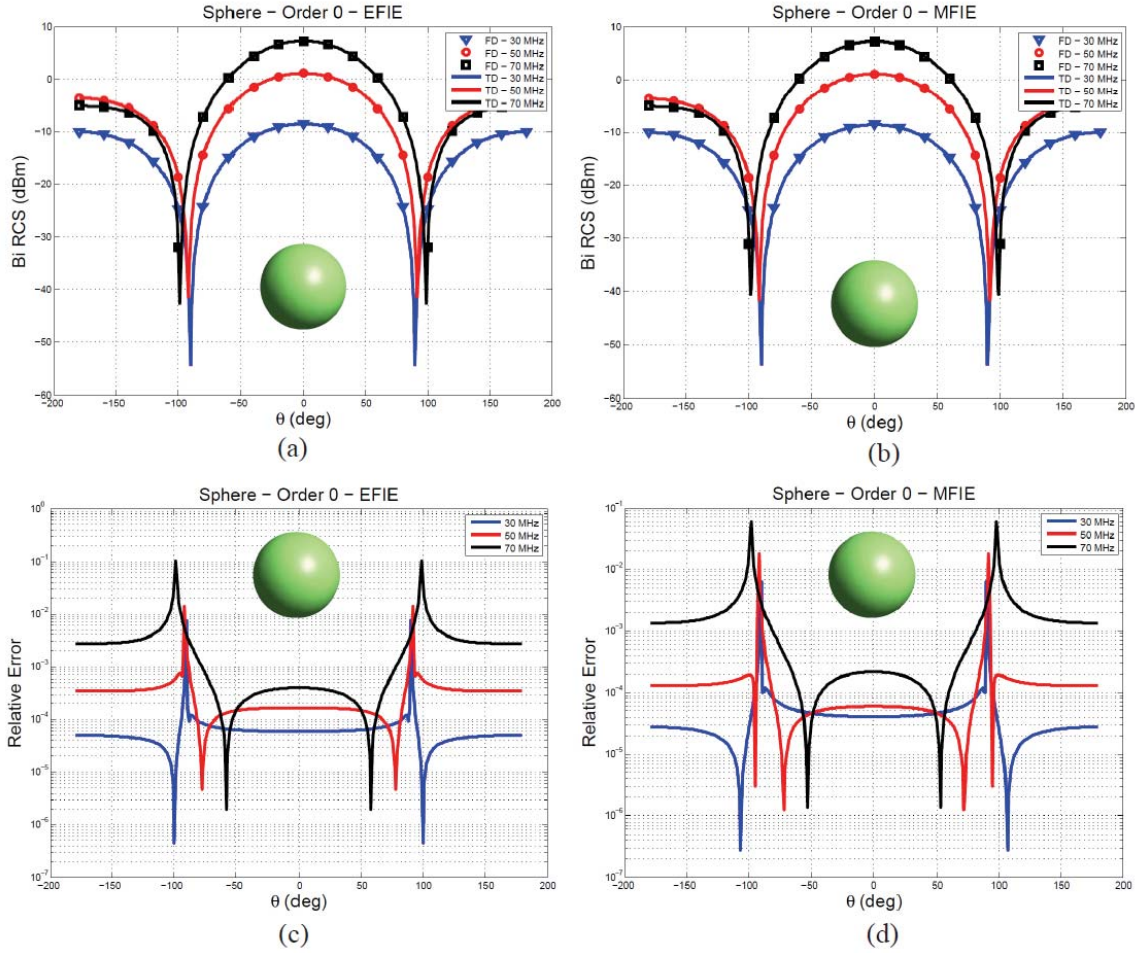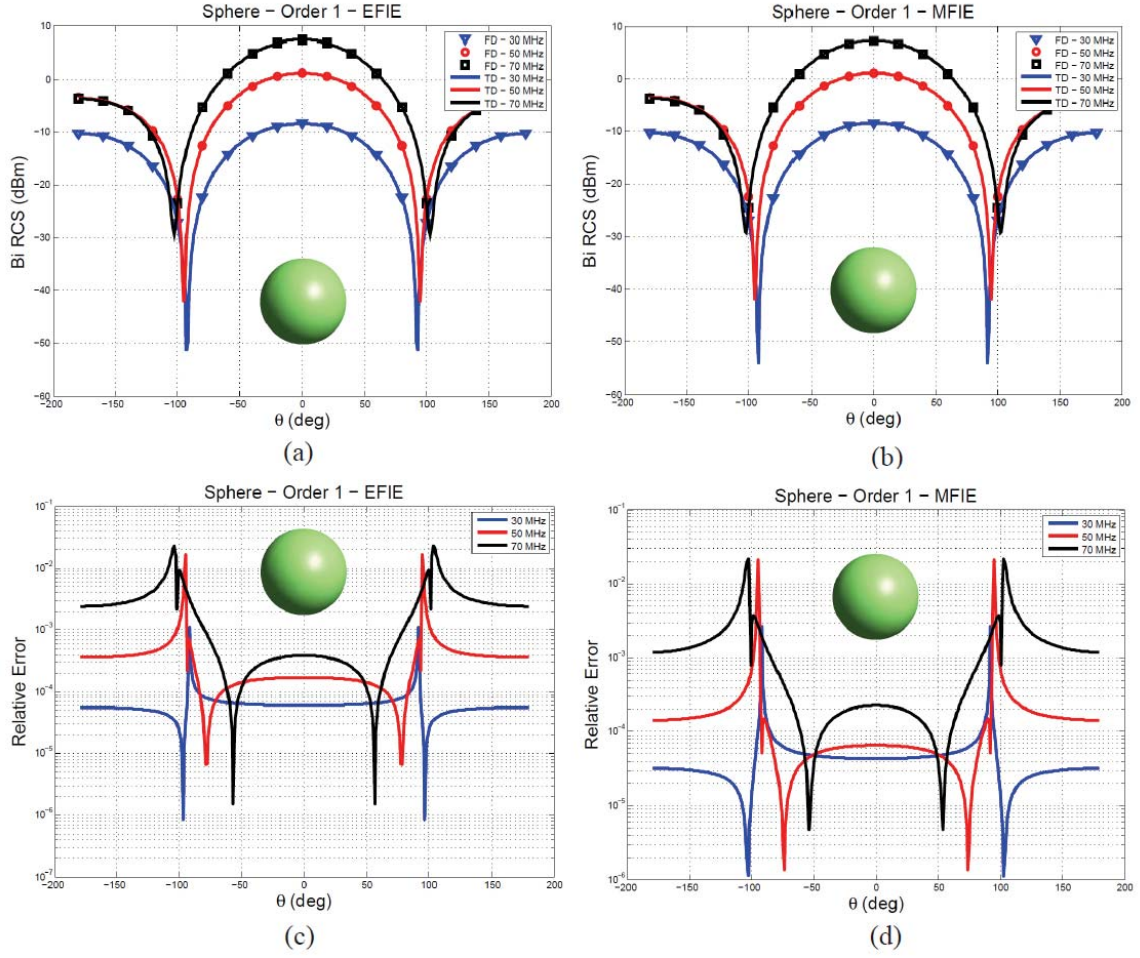
Fig. V.8. Bistatic RCS at frequencies 30 MHz, 50 MHz, and 70 MHz obtained after solving time-domain single source EFIE for a 1 m radius sphere with $\epsilon_2 = 2\epsilon_0$ illuminated by a Gaussian pulse with center frequency $f_0 = 50\,\text{MHz}$ and bandwidth $f_{BW} = 50\,\text{MHz}$ traveling along $\hat{\boldsymbol{k}} = \hat{\boldsymbol{z}}$ and with polarization $\hat{\boldsymbol{p}} = \hat{\boldsymbol{x}}$. The surface of the sphere is modeled with 32 curvilinear patches. The current density is modeled with spatial basis functions of order $p = 3$ and temporal basis functions of orders $q = 2,3,4$. (a) Bistatic RCS in the x-z plane at 30 MHz. (b) Error in RCS at 30 MHz with respect to Mie series solution. (c) Bistatic RCS in the x-z plane at 50 MHz. (d) Error in RCS at 50 MHz with respect to Mie series solution. (e) Bistatic RCS in the x-z plane at 70 MHz. (f) Error in RCS at 70 MHz with respect to Mie series solution.

123

5.3.2   MOT Analysis of Scattering from a Smooth Star-shaped object

The next example considered is a smooth star-shaped object with permittivity $\epsilon_2 = 5\epsilon_1$ and permeability $\mu_2 = 2\mu_1$ ($\epsilon_1 = \epsilon_0$, $\mu_1 = \mu_0$) and whose surface is described as

$$r(\theta,\phi) = \left(2 + \cos^2(2.5\theta) + 1.5\sin^2(\theta)\cos^2(2\phi)\right)/4 \tag{5.33}$$

The incident field is described by (5.32), with $f_0 = 50$ MHz, $f_{BW} = 50$ MHz, $\hat{k} = \hat{x}$, $\hat{p} = \hat{z}$, and $t_p = 150$ ns. The surface of the star-shaped 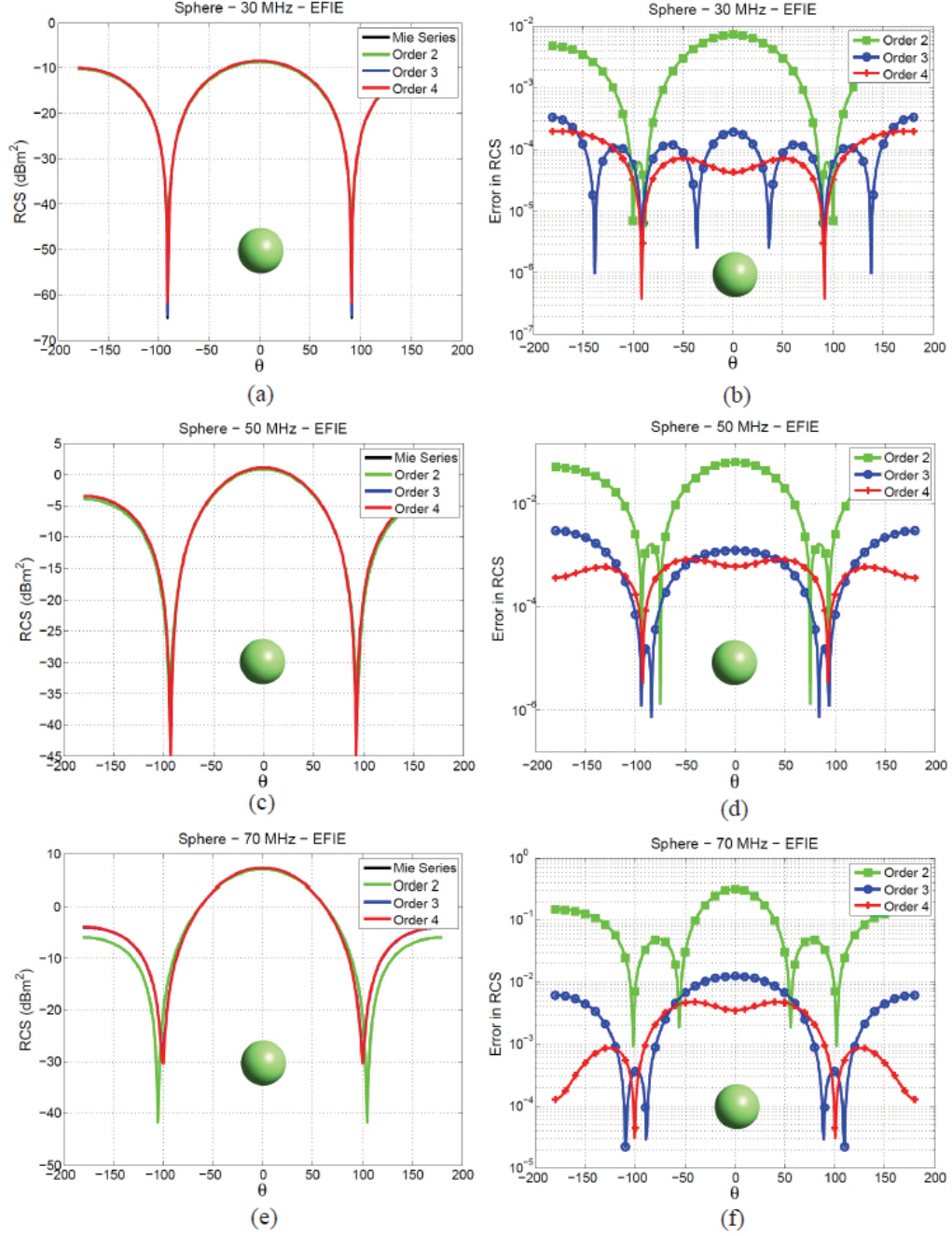object is discretized with 32 curvilinear patches. Each patch is obtained by means of an exact mapping from a reference patch onto the surface described in (5.33). The simulation is run with a time step $\Delta t = 250$ ps and a total of $N_T = 2000$ time steps. Fig. V.9 to V.11 show plots of the transient equivalent currents $J_1(r,t)$ and $M_1(r,t)$ obtained by solving single source EFIE and MFIE using temporal basis functions of order $q = 4$ and spatial basis functions of order $p = 0,1,2$. Fig. V.9(a-b) show the equivalent currents at a position $r = (-0.690, 0.345, 0.345)$ m along the direction (-0.973, -0.102, -0.205) obtained using spatial basis functions of order $p = 0$. The number of spatial unknowns is $N_S = 48$. Fig. V.10(a-b) show the equivalent currents at a position $r = (-0.690, 0.345, 0.345)$ m along the direction (0.264, -0.774, -0.574) obtained using spatial basis functions of order $p = 1$. The number of spatial unknowns is $N_S = 160$. Fig. V.11(a-b) show the equivalent currents at a position $r = (0.0, -0.133, 0.699)$ m along the direction (-1.0, 0.0, 0.0) obtained using spatial basis functions of order $p = 2$. The number of spatial unknowns is $N_S = 336$.

The consistency between results obtained from time- and frequency-domain single source EFIE and MFIE is studied in Fig. V.12 to V.14. Fig. V.12(a) shows the bistatic radar cross section (RCS) calculated for $\phi = 0°$ and $-180° \le \theta \le 180°$ for frequencies of 30, 50 and 70 MHz. RCS is computed from the equivalent currents J_1 and M_1 obtained from solving the single source EFIE in time- and frequency-domain separately. Currents are obtained using spatial basis functions of order $p = 0$, and (for time-domain) temporal basis functions of order $q = 4$. The relative error in RCS between time- and frequency-

domain solutions is shown in Fig. V.12(c). Results obtained from solving the single source MFIE are shown in Fig. V.12(b,d). Similar to the data illustrated in Fig. V.12(a-d), Fig. V.13(a-d) show results obtained using spatial basis functions of order $p = 1$ and Fig. V.14(a-d) show results obtained using $p = 2$.

To demonstrate the effect of the spatial basis functions, Fig. V.15(a,c,e) show the bistatic radar cross-section (RCS) calculated for $\phi = 0°$ and $-180° \leq \theta \leq 180°$ for frequencies of 30, 50 and 70 MHz respectively. RCS is computed from the equivalent currents $\boldsymbol{J}_1$ and $\boldsymbol{M}_1$ obtained from solving the single source MFIE using temporal basis functions of order $q = 4$ and spatial basis functions of orders $p = 0,1,2,3$. Fig. V.15(b,d,f) show the error of the computed RCS with respect to the solution obtained using spatial basis functions of order $p = 4$.

Fig. V.9. Electric and (scaled) Magnetic equivalent current densities obtained after solving time-domain single source EFIE and MFIE using temporal basis functions of order $q = 4$ and spatial basis functions of order $p = 0$. The target is the "smooth star" described in (5.33) with permittivity $\epsilon_2 = 5\epsilon_0$ and permeability $\mu_2 = 2\mu_0$, illuminated by a Gaussian pulse with center frequency $f_0 = 50\,\text{MHz}$ and bandwidth $f_{BW} = 50\,\text{MHz}$ traveling along $\hat{\boldsymbol{k}} = \hat{\boldsymbol{z}}$ and with polarization $\hat{\boldsymbol{p}} = \hat{\boldsymbol{x}}$. Currents are observed at point (-0.690, 0.345, 0.345) m and along the direction (-0.973, -0.102, -0.205). (a) Absolute value of the currents for $0 \leq t \leq 500\,\text{ns}$. (b) Currents for $80 \leq t \leq 250\,\text{ns}$.
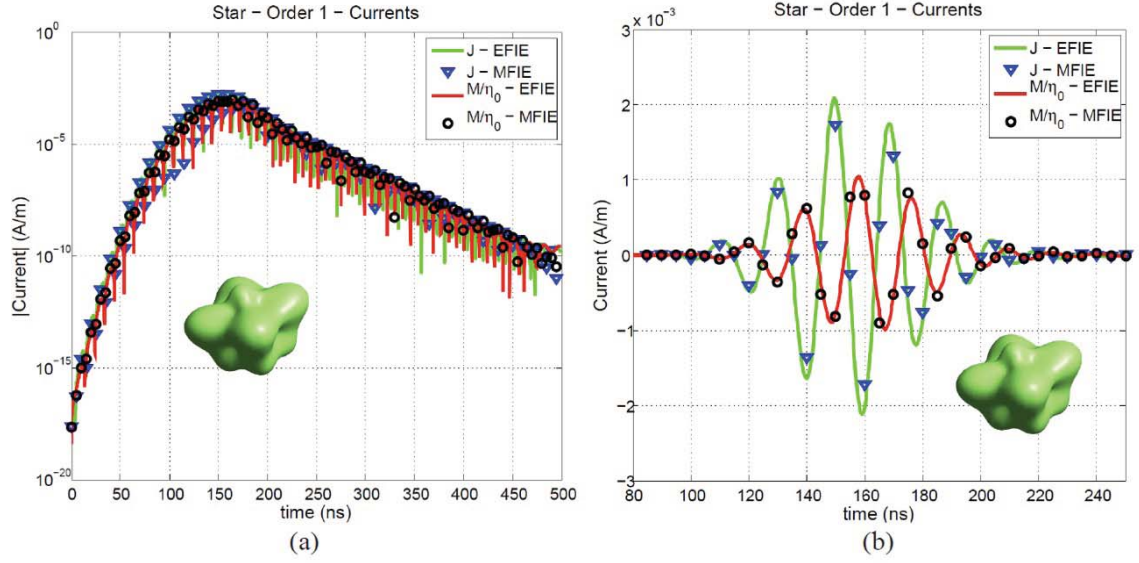
Fig. V.10. Electric and (scaled) Magnetic equivalent current densities obtained after solving time-domain single source EFIE and MFIE using temporal basis functions of order $q = 4$ and spatial basis functions of order $p = 1$. The target is the "smooth star" described in (5.33) with permittivity $\epsilon_2 = 5\epsilon_0$ and permeability $\mu_2 = 2\mu_0$, illuminated by a Gaussian pulse with center frequency $f_0 = 50$ MHz and bandwidth $f_{BW} = 50$ MHz traveling along $\hat{k} = \hat{z}$ and with polarization $\hat{p} = \hat{x}$. Currents are observed at point (-0.426, -0.640, 0.213) m and along the direction (0.264, -0.774, -0.574). (a) Absolute value of the currents for $0 \le t \le 500$ ns. (b) Currents for $80 \le t \le 250$ ns.
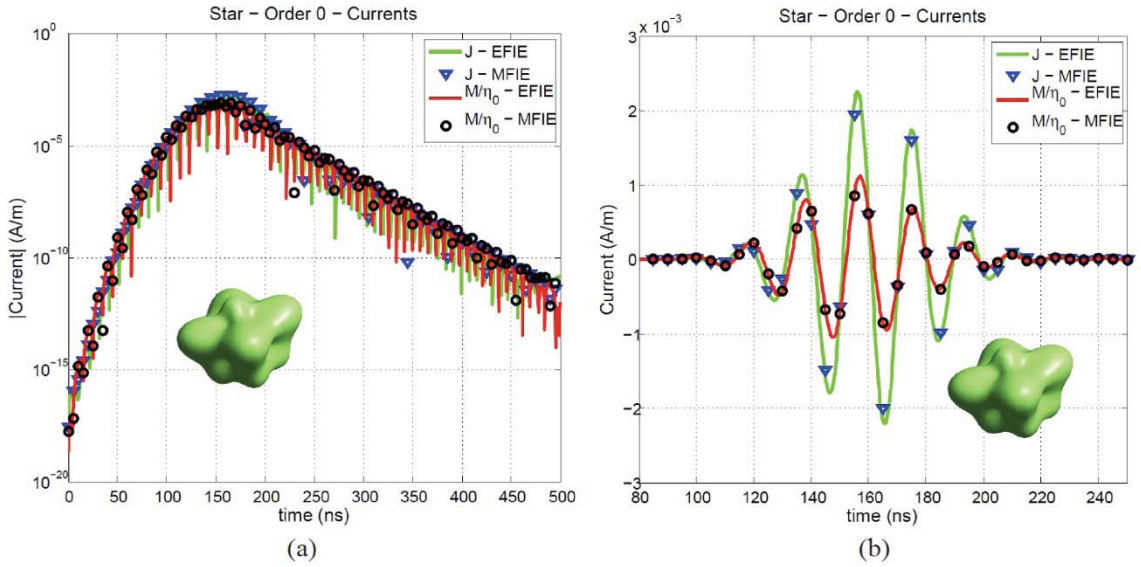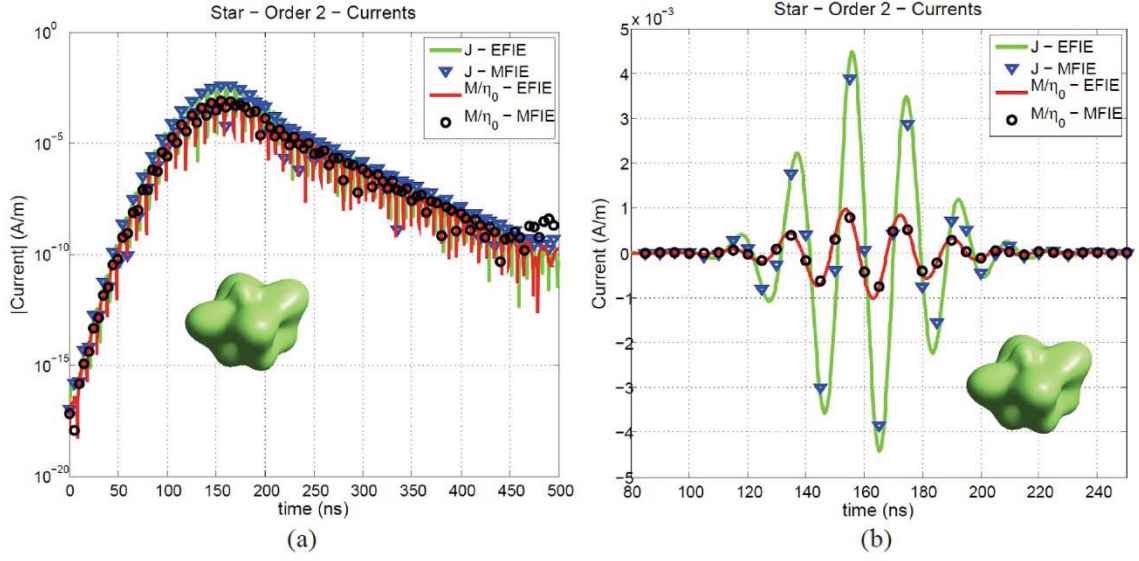
Fig. V.11. Electric and (scaled) Magnetic equivalent current densities obtained after solving time-domain single source EFIE and MFIE using temporal basis functions of order $q = 4$ and spatial basis functions of order $p = 2$. The target is the "smooth star" described in (5.33) with permittivity $\epsilon_2 = 5\epsilon_0$ and permeability $\mu_2 = 2\mu_0$, illuminated by a Gaussian pulse with center frequency $f_0 = 50$ MHz and bandwidth $f_{BW} = 50$ MHz traveling along $\hat{k} = \hat{z}$ and with polarization $\hat{p} = \hat{x}$. Currents are observed at point (0.0, -0.133, 0.699) m and along the direction (-1.0, 0.0, 0.0). (a) Absolute value of the currents for $0 \leq t \leq 500$ ns . (b) Currents for $80 \leq t \leq 250$ ns .

Fig. V.12. Comparison of bistatic RCS at frequencies 30 MHz, 50 MHz, and 70 MHz obtained after solving time-domain and frequency-domain single source EFIE and MFIE using spatial basis functions of order $p = 0$ for the "smooth star" described in (5.33), with $\epsilon_2 = 5\epsilon_0$ and $\mu_2 = 2\mu_0$. (a) RCS obtained from single source EFIE. (b) RCS obtained from singe source MFIE. (c) Relative error in RCS between time- and frequency-domain EFIE. (d) Relative error in RCS between time- and frequency-domain MFIE.

Fig. V.13. Comparison of bistatic RCS at frequencies 30 MHz, 50 MHz, and 70 MHz obtained after solving time-domain and frequency-domain single source EFIE and MFIE using spatial basis functions of order $p = 1$ for the "smooth star" described in (5.33), with $\epsilon_2 = 5\epsilon_0$ and $\mu_2 = 2\mu_0$. (a) RCS obtained from single source EFIE. (b) RCS obtained from singe source MFIE. (c) Relative error in RCS between time- and frequency-domain EFIE. (d) Relative error in RCS between time- and frequency-domain MFIE.

129
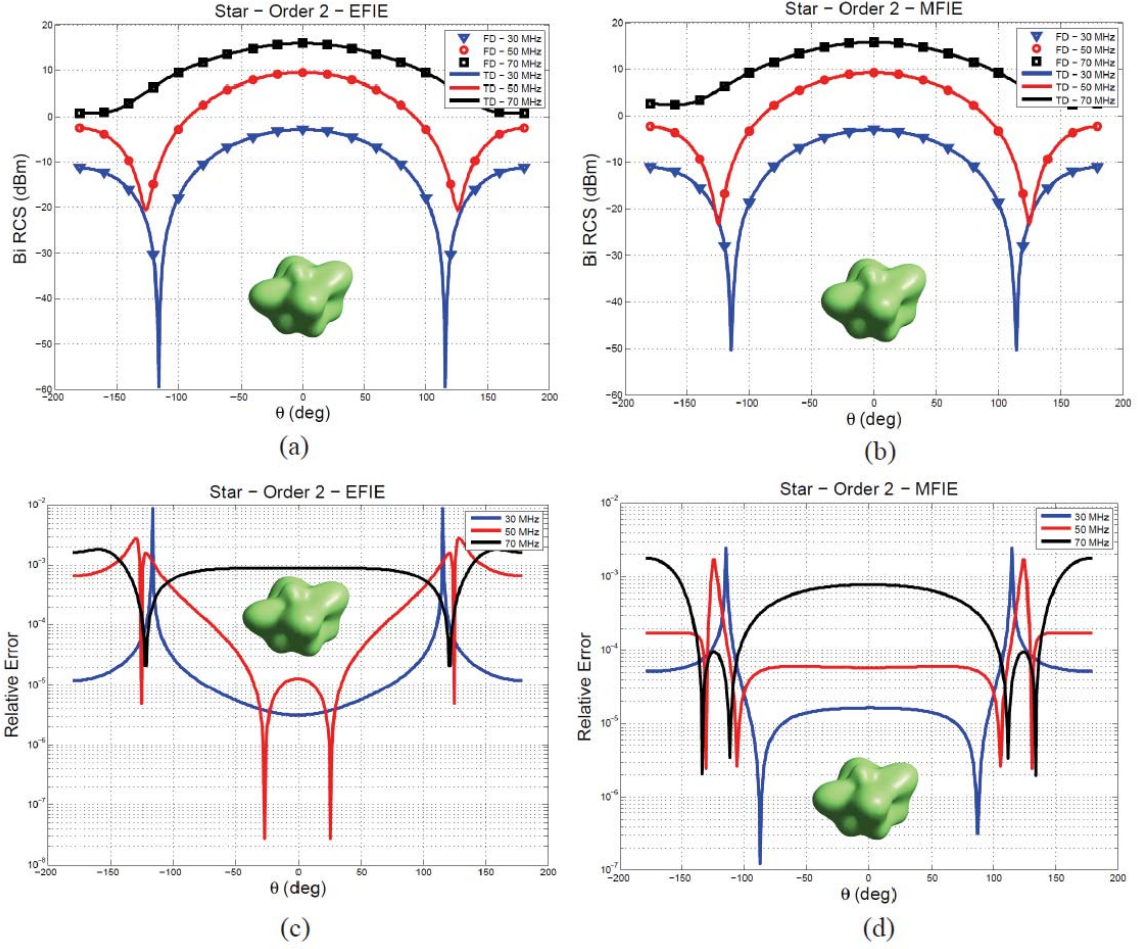
Fig. V.14. Comparison of bistatic RCS at frequencies 30 MHz, 50 MHz, and 70 MHz obtained after solving time-domain and frequency-domain single source EFIE and MFIE using spatial basis functions of order $p = 2$ for the "smooth star" described in (5.33), with $\epsilon_2 = 5\epsilon_0$ and $\mu_2 = 2\mu_0$. (a) RCS obtained from single source EFIE. (b) RCS obtained from singe source MFIE. (c) Relative error in RCS between time- and frequency-domain EFIE. (d) Relative error in RCS between time- and frequency-domain MFIE.
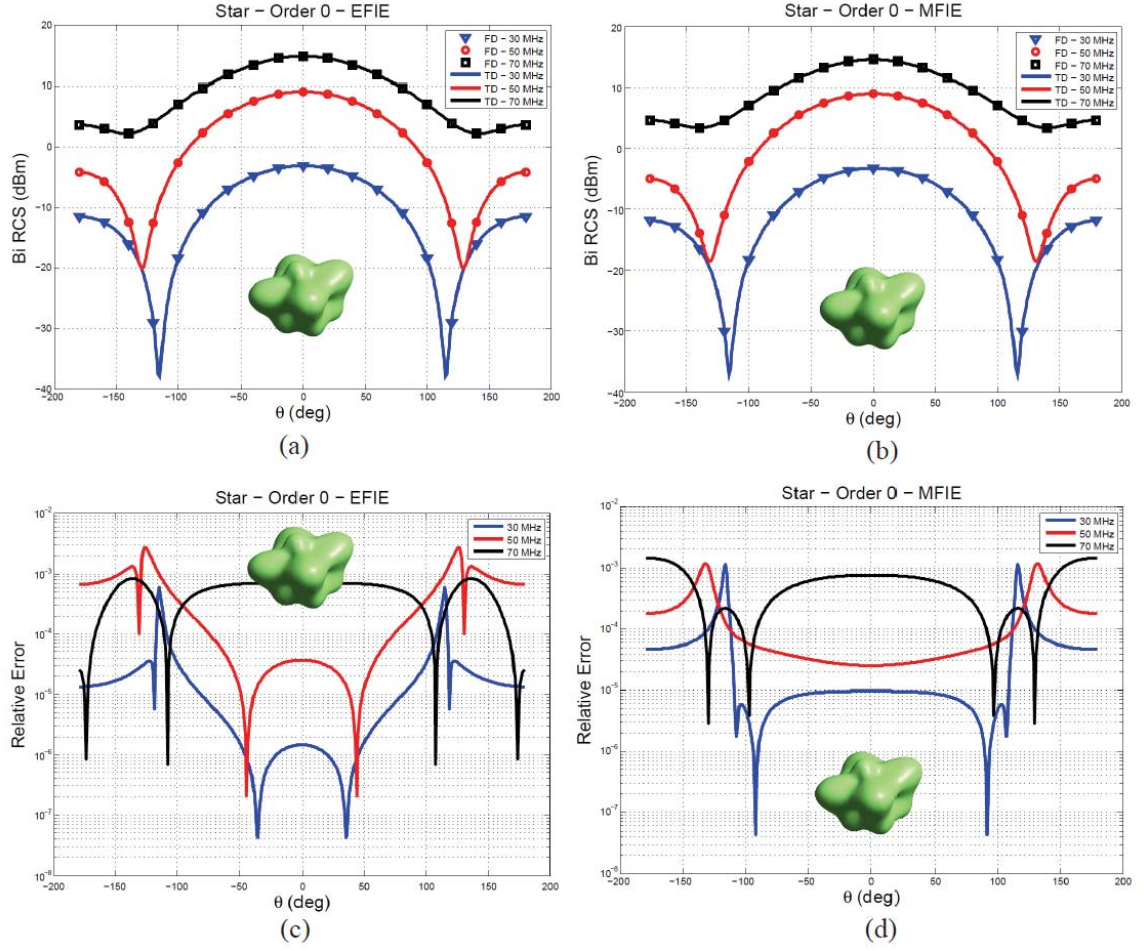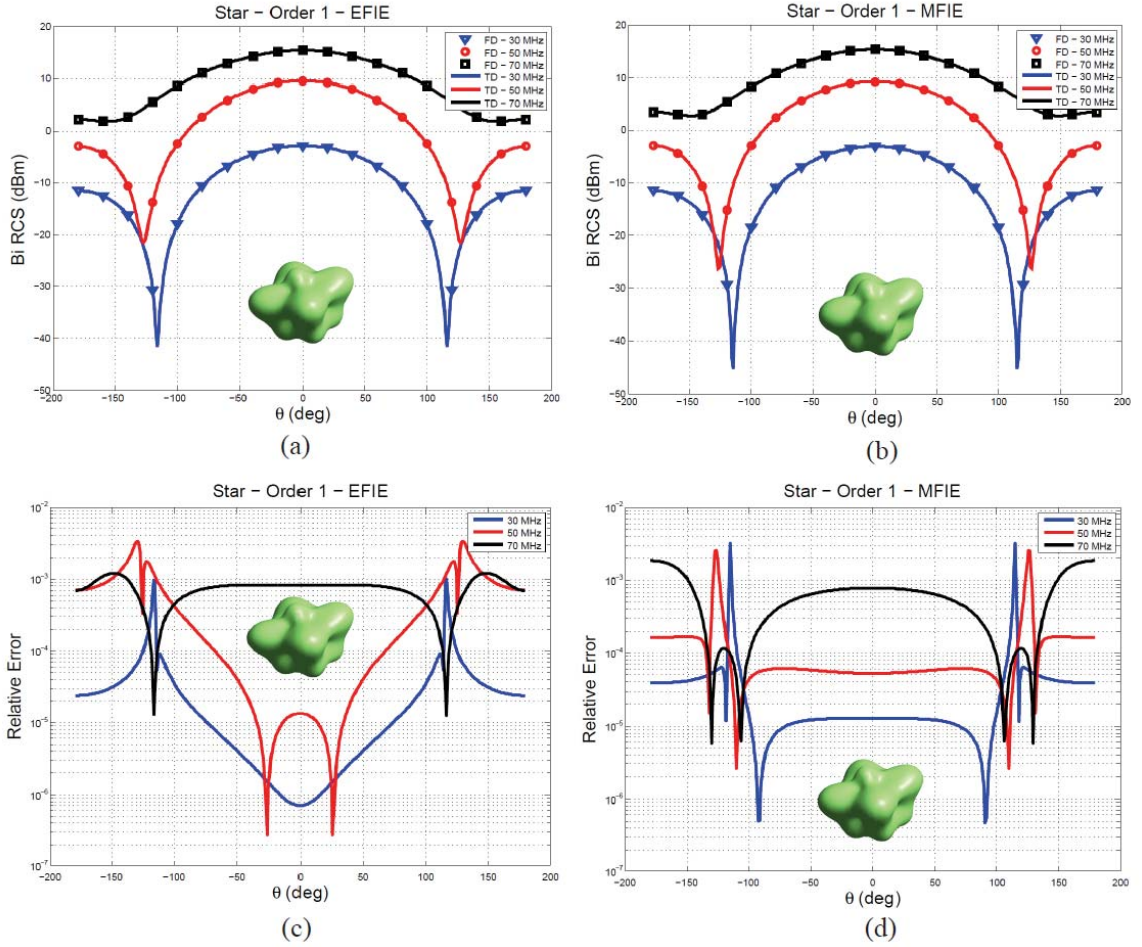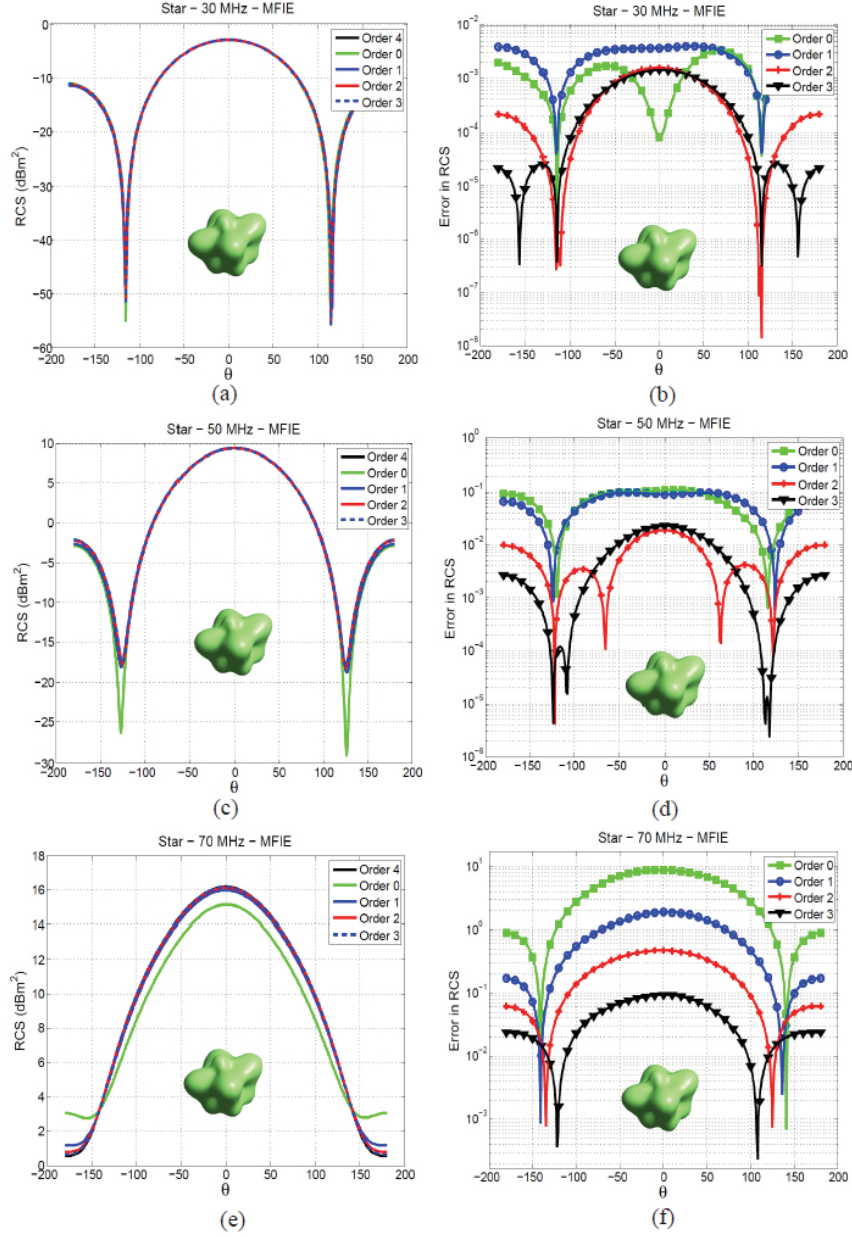
Fig. V.15. Bistatic RCS at frequencies 30 MHz, 50 MHz, and 70 MHz obtained after solving time-domain single source MFIE for the "smooth star" described in (5.33), with $\epsilon_2 = 5\epsilon_0$ and $\mu_2 = 2\mu_0$, illuminated by a Gaussian pulse with center frequency $f_0 = 50$ MHz and bandwidth $f_{BW} = 50$ MHz traveling along $\hat{\boldsymbol{k}} = \hat{\boldsymbol{z}}$ and with polarization $\hat{\boldsymbol{p}} = \hat{\boldsymbol{x}}$. The surface is modeled with 102 curvilinear patches. The current density is modeled with temporal basis functions of order $q = 4$ and spatial basis functions of orders $p = 0,1,2,3$. The number of spatial unknowns ranges from 153 ($p = 0$) to 1836 ($p = 3$). All solutions here are compared to the solution obtained using spatial basis functions of order $p = 4$ ($N_S = 2805$). (a) Bistatic RCS in the x-z plane at 30 MHz. (b) Error in RCS at 30 MHz with respect to solution obtained with spatial basis functions of order $p = 4$. (c) Bistatic RCS in the x-z plane at 50 MHz. (d) Error in RCS at 50 MHz with respect solution obtained with spatial basis functions of order $p = 4$. (e) Bistatic RCS in the x-z plane at 70 MHz. (f) Error in RCS at 70 MHz with respect solution obtained with spatial basis functions of order $p = 4$.

5.3.3   MOT Analysis of Scattering from a Cube

In this subsection, scattering from a dielectric cube with $\epsilon_2 = 5\epsilon_1$ and $\mu_2 = 2\mu_1$ ($\epsilon_1 = \epsilon_0$, $\mu_1 = \mu_0$) is analyzed. The cube has a side length of 1 m, is centered at the origin and two of its faces are parallel to the x-y plane. The incident field is described by (5.32), with $f_0 = 50$ MHz, $f_{BW} = 50$ MHz, $\hat{k} = \hat{z}$, $\hat{p} = \hat{x}$, and $t_p = 150$ ns. The surface of the cube is discretized with 24 flat triangular patches. The simulation is run with a time step $\Delta t = 250$ ps and a total of $N_T = 2000$ time steps. Fig. V.16 to V.18 show plots of the transient equivalent currents $J_1(r,t)$ and $M_1(r,t)$ obtained by solving single source EFIE and MFIE using temporal basis functions of order $q = 4$ and spatial basis functions of order $p = 0,1,2$. Fig. V.16(a-b) show the equivalent currents at a position $r = (0.5, -0.25, 0.25)$ m along the direction (0.0, -0.707, -0.707) obtained using spatial basis functions of order $p = 0$. The number of spatial unknowns is $N_S = 36$. Fig. V.17(a-b) show the equivalent currents at a position $r = (0.333, 0.5, 0.166)$ m along the direction (0.0, -0.707, -0.707) obtained using spatial basis functions of order $p = 1$. The number of spatial unknowns is $N_S = 120$. Fig. V.18(a-b) show the equivalent currents at a position $r = (0.5, 0.25, -0.25)$ m along the direction (0.0, 0.707, 0.707) obtained using spatial basis functions of order $p = 2$. The number of spatial unknowns is $N_S = 252$.

The consistency between results obtained from time- and frequency-domain single source EFIE and MFIE is studied in Fig. V.19 to V.21. Fig. V.19(a) shows the bistatic radar cross section (RCS) calculated for $\phi = 0°$ and $-180° \leq \theta \leq 180°$ for frequencies of 30, 50 and 70 MHz. RCS is computed from the equivalent currents J_1 and M_1 obtained from solving the single source EFIE in time- and frequency-domain separately. Currents are obtained using spatial basis functions of order $p = 0$, and (for time-domain) temporal basis functions of order $q = 4$. The relative error in RCS between time- and frequency-domain solutions is shown in Fig. V.19(c). Results obtained from solving the single source MFIE are shown in Fig. V.19(b,d). Similar to the data illustrated in Fig. V.19(a-d), Fig. V.20(a-d) show results obtained using spatial basis functions of order $p = 1$ and Fig. V.21(a-d) show results obtained using $p = 2$.

132

Fig. V.16. Electric and (scaled) Magnetic equivalent current densities obtained after solving time-domain single source EFIE and MFIE using temporal basis functions of order $q = 4$ and spatial basis functions of order $p = 0$. The target is a cube with 1 m side length with permittivity $\epsilon_2 = 5\epsilon_0$ and permeability $\mu_2 = 2\mu_0$, illuminated by a Gaussian pulse with center frequency $f_0 = 50$ MHz and bandwidth $f_{bw} = 50$ MHz traveling along $\hat{k} = \hat{z}$ and with polarization $\hat{p} = \hat{x}$. Currents are observed at point (0.5, -0.25, 0.25) m and along the direction (0.0, -0.707, -0.707). (a) Absolute value of the currents for $0 \leq t \leq 500$ ns. (b) Currents for $80 \leq t \leq 250$ ns.

133

Fig. V.17. Electric and (scaled) Magnetic equivalent current densities obtained after solving time-domain single source EFIE and MFIE using temporal basis functions of order $q = 4$ and spatial basis functions of order $p = 1$. The target is a cube with 1 m side length with permittivity $\epsilon_2 = 5\epsilon_0$ and permeability $\mu_2 = 2\mu_0$, illuminated by a Gaussian pulse with center frequency $f_0 = 50$ MHz and bandwidth $f_{bw} = 50$ MHz traveling along $\hat{k} = \hat{z}$ and with polarization $\hat{p} = \hat{x}$. Currents are observed at point (0.333, 0.5, 0.166) m and along the direction (0.0, -0.707, -0.707). (a) Absolute value of the currents for $0 \leq t \leq 500$ ns. (b) Currents for $80 \leq t \leq 250$ ns.
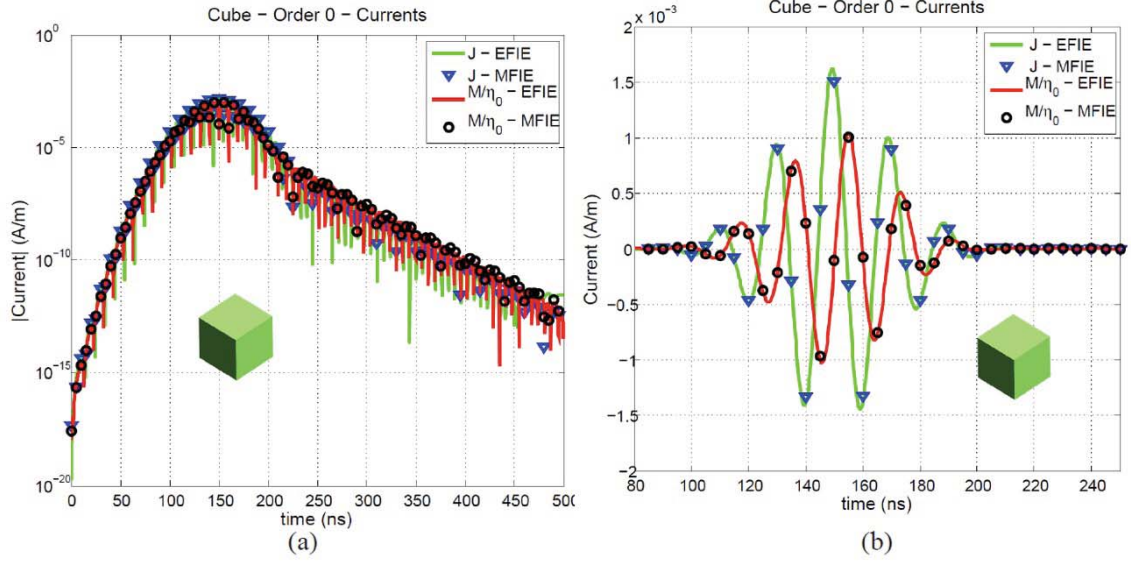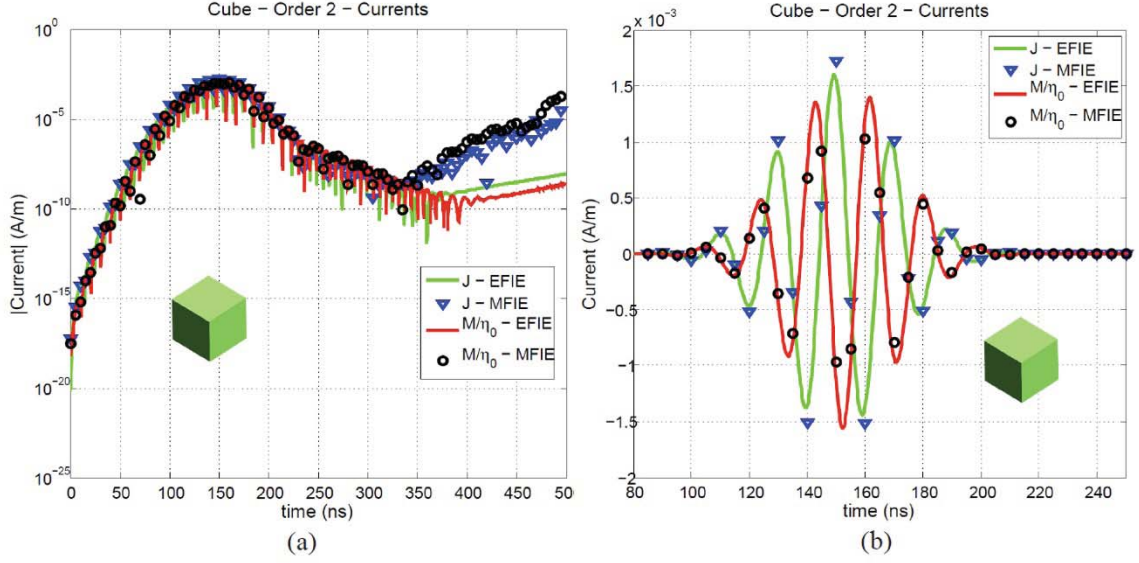
Fig. V.18. Electric and (scaled) Magnetic equivalent current densities obtained after solving time-domain single source EFIE and MFIE using temporal basis functions of order $q = 4$ and spatial basis functions of order $p = 2$. The target is a cube with 1 m side length with permittivity $\epsilon_2 = 5\epsilon_0$ and permeability $\mu_2 = 2\mu_0$, illuminated by a Gaussian pulse with center frequency $f_0 = 50$ MHz and bandwidth $f_{bw} = 50$ MHz traveling along $\hat{k} = \hat{z}$ and with polarization $\hat{p} = \hat{x}$. Currents are observed at point (0.5, 0.25, -0.25) m and along the direction (0.0, 0.707, 0.707). (a) Absolute value of the currents for $0 \le t \le 500$ ns. (b) Currents for $80 \le t \le 250$ ns.

Fig. V.19. Comparison of bistatic RCS at frequencies 30 MHz, 50 MHz, and 70 MHz obtained after solving time-domain and frequency-domain single source EFIE and MFIE using spatial basis functions of order $p = 0$ for a 1 m side cube with $\epsilon_2 = 5\epsilon_0$ and $\mu_2 = 2\mu_0$. (a) RCS obtained from single source EFIE. (b) RCS obtained from singe source MFIE. (c) Relative error in RCS between time- and frequency-domain EFIE. (d) Relative error in RCS between time- and frequency-domain MFIE.
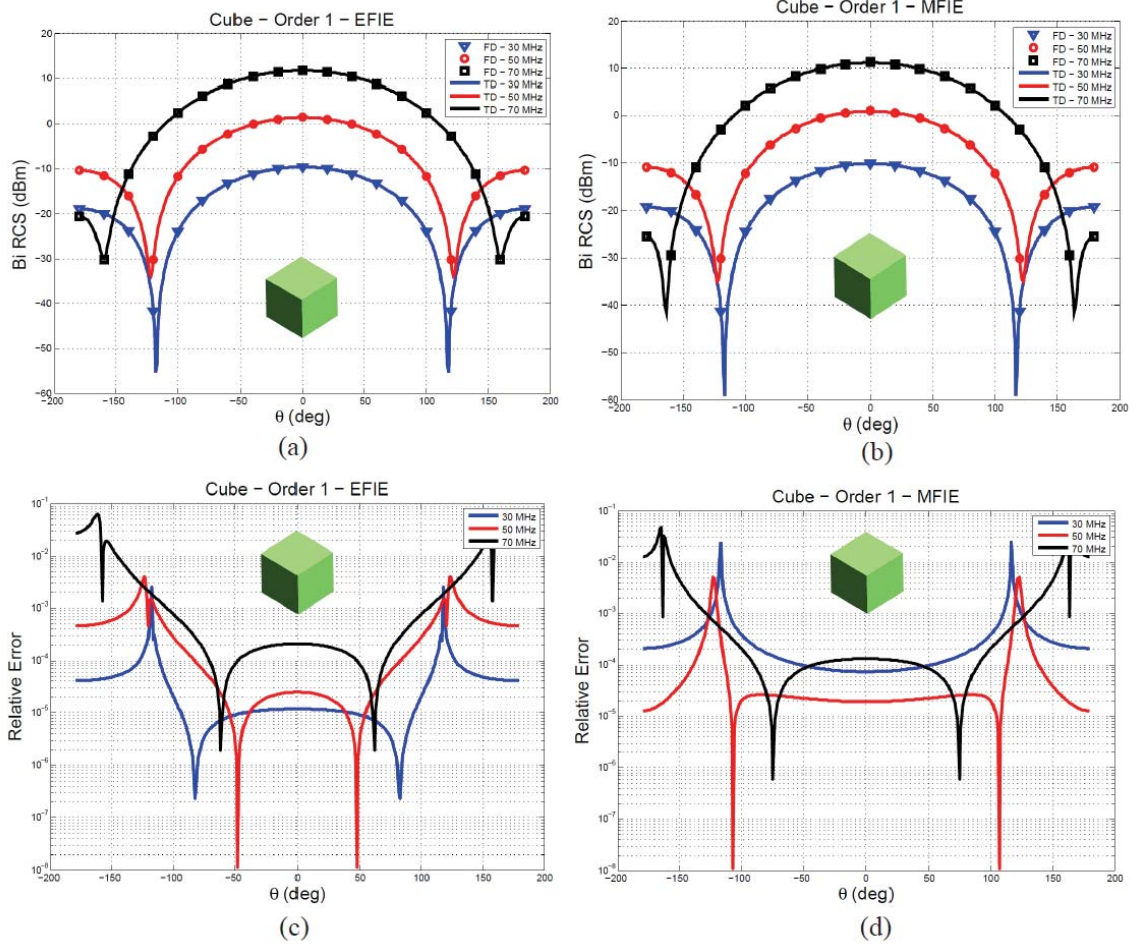
Fig. V.20. Comparison of bistatic RCS at frequencies 30 MHz, 50 MHz, and 70 MHz obtained after solving time-domain and frequency-domain single source EFIE and MFIE using spatial basis functions of order $p = 1$ for a 1 m side cube with $\epsilon_2 = 5\epsilon_0$ and $\mu_2 = 2\mu_0$. (a) RCS obtained from single source EFIE. (b) RCS obtained from singe source MFIE. (c) Relative error in RCS between time- and frequency-domain EFIE. (d) Relative error in RCS between time- and frequency-domain MFIE.
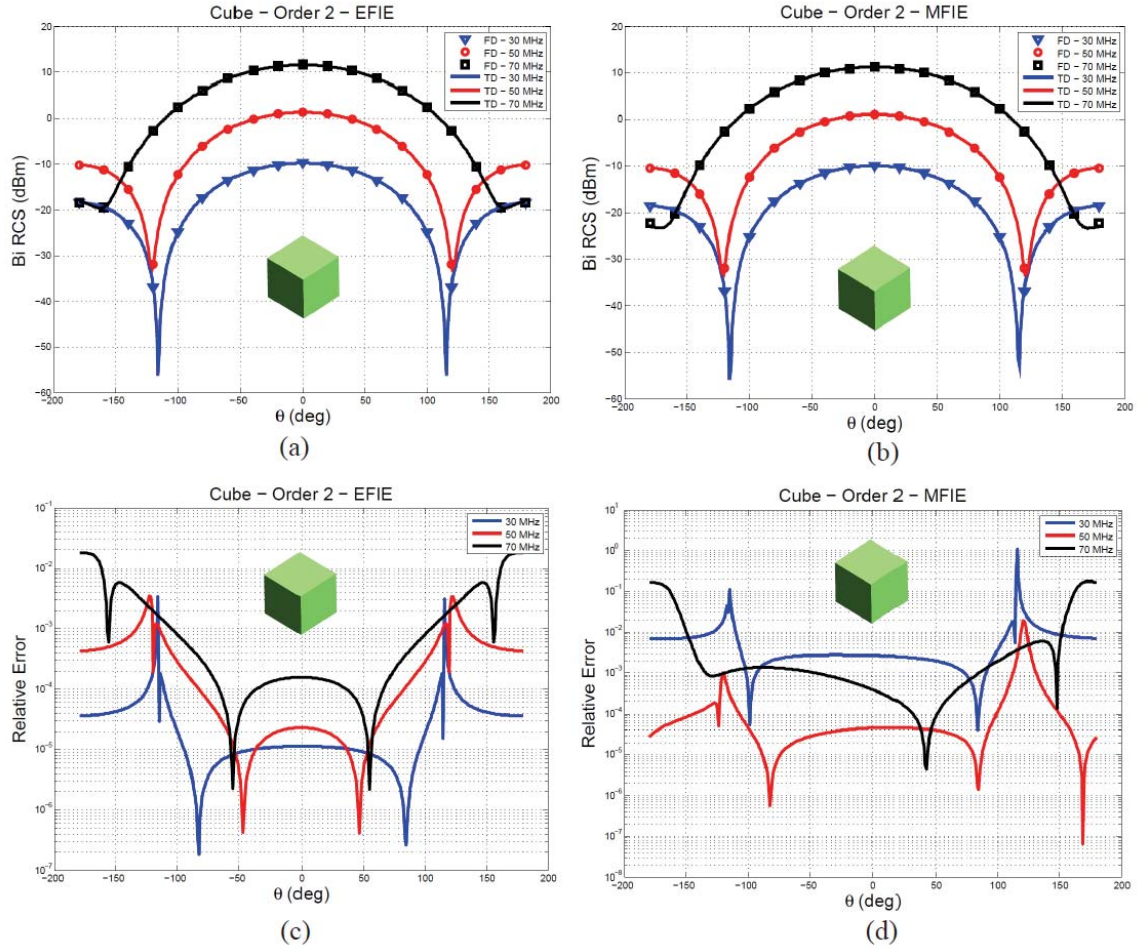
Fig. V.21. Comparison of bistatic RCS at frequencies 30 MHz, 50 MHz, and 70 MHz obtained after solving time-domain and frequency-domain single source EFIE and MFIE using spatial basis functions of order $p = 2$ for a 1 m side cube with $\epsilon_2 = 5\epsilon_0$ and $\mu_2 = 2\mu_0$. (a) RCS obtained from single source EFIE. (b) RCS obtained from singe source MFIE. (c) Relative error in RCS between time- and frequency-domain EFIE. (d) Relative error in RCS between time- and frequency-domain MFIE.

CHAPTER VI

Conclusions and Future Work

This thesis improved existing CMP techniques for the analysis of scattering from PEC objects, and presented new equations for the analysis of scattering from homogeneous penetrable objects. All these contributions were explored and extensively tested in frequency- and time-domain.

6.1 Summary

A new set of high-order div- and quasi curl-conforming basis functions ($\mathrm{DQCC}(p)$) was presented in Chapter II. This set was used alongside $\mathrm{GWP}(p)$ basis functions in a high-order implementation of the Calderon-preconditioned EFIE in frequency-domain. The numerical results presented in this chapter demonstrate fast convergence rates of the HO-CMP, regardless of the mesh density and the order of the basis functions used. The set $\mathrm{DQCC}(p)$ has also been used to extend the existing implementations of Calderon-preconditioned equations in time-domain. In particular, Chapter IV presented high-order CMP-TDEFIE and Dottrick-TDEFIE. Numerical results in this chapter demonstrate the stability and accuracy of both time-domain equations. They also demonstrate fast convergence rates as observed in the frequency-domain case.

A Calderón-preconditioned single source combined field integral equation for analyzing scattering from homogeneous penetrable objects was presented in Chapter III. The number of unknowns in this equation is half that in standard dual source equations. The proposed equation is not susceptible to dense-mesh or low-frequency breakdown. The regularization of the equation was achieved by leveraging the self-regularizing property of the EFIE operator. The spectrum of the CP-CFIE operator was analyzed for the case of a dielectric sphere, for which the equation was proven to be resonant free. Numerical results indicate that the resonant free character of the equation is maintained for non-spherical structures as well. In close

connection to Chapter III, time-domain single source EFIE and MFIE are presented in Chapter V. Both equations are discretized appropriately into a MOT scheme. The discretization technique presented here makes use of GWP(p) and the DQCC(p) basis functions presented in Chapter II. Since this is the first time these equations are presented in the CEM community, an extensive set of numerical results that demonstrate the stability and accuracy of both equations is provided.

6.2   Future Work

The work presented in this thesis is subject to improvements and/or extension in their applicability, especially if they are to be deployed as part of commercial software. In the current stage, only triangular surface patches (planar and curvilinear) are supported. In this context, further extensions may include the use of quadrilateral patches, wire, elements and junctions among them. The stability (w.r.t. the order p) of the DQCC(p) basis functions (and therefore also the stability of the high-order CMP) is closely related to the stability of the Helmholtz decomposition in the standard basis functions. Any improvement in the way this Helmholtz decomposition is achieved will have a direct impact on the stability and efficiency of the preconditioner.

The single source CP-CFIE presented in Chapter III is also susceptible to further study and development. Recently, Calderón-preconditioned dual source integral equation solvers have been developed. It is of great interest to compare the accuracy and efficiency of the single source CP-CFIE with respect to its dual source counterpart. In addition, the single source CP-CFIE can be modified to allow for different penetrable objects touching one another and/or PEC surfaces. In the time-domain front, future work will be aimed in the development of a time-domain single source combined field integral equation, which is free from resonances and immune to dense-mesh breakdown.

6.3 Contributions

This thesis resulted in the following contributions:

Journal Papers

1. Valdés, F.; Andriulli, F.P.; Cools, K.; Michielssen, E., "High-order Div- and Quasi Curl-Conforming Basis Functions for Calderón Multiplicative Preconditioning of the EFIE," *IEEE Transactions on Antennas and Propagation*, vol.59, no.4, pp.1321-1337, April 2011.

2. Valdes, F.; Andriulli, F.P.; Bagci, H.; Michielssen, E., "A Calderón-Preconditioned Single Source Combined Field Integral Equation for Analyzing Scattering From Homogeneous Penetrable Objects," *IEEE Transactions on Antennas and Propagation*, vol.59, no.6, pp.2315-2328, June 2011.

3. Valdes, F.; Andriulli, F.P.; Michielssen, E., "Time Domain Single Source Integral Equations for Analyzing Scattering from Homogeneous Penetrable Objects," *to be Submitted to IEEE Transactions on Antennas and Propagation,* 2012.

4. Valdes, F.; Ghaffari-Miab, M.; Andriulli, F.P.; Cools, K.; Kotulski, J.D.; Michielssen, E., "High-Order Dot-Trick and Calderón Multiplicative Preconditioner for Time Domain Electric Field Integral Equations," *to be Submitted to IEEE Transactions on Antennas and Propagation,* 2012.

Conference Papers

5. Valdes, F.; Andriulli, F.P.; Bagci, H.; Michielssen, E., "On the discretization of single source integral equations for analyzing scattering from homogeneous penetrable objects," *Antennas and Propagation Society International Symposium, 2008. AP-S 2008. IEEE* , vol., no., pp.1-4, 5-11 July 2008.

6. Valdés, F.; Andriulli, F.P.; Bagci, H.; Michielssen, E., "On the regularization of single source combined integral equations for analyzing scattering from homogeneous penetrable objects," *Antennas and Propagation Society International Symposium, 2009. APSURSI '09. IEEE* , vol., no., pp.1-4, 1-5 June 2009.

7. Valdes, F.; Andriulli, F.P.; Cools, K.; Michielssen, E., "High-order quasi-curl conforming functions for multiplicative Calderón preconditioning of the EFIE," *Antennas and Propagation Society International Symposium, 2009. APSURSI '09. IEEE* , vol., no., pp.1-4, 1-5 June 2009.

8. Valdes, F.; Andriulli, F.P.; Cools, K.; Kotulski, J.D.; Michielssen, E.;, "Fully localized high-order div- and quasi-curl-conforming basis functions for multiplicative Calderón preconditioning of the EFIE," *Antennas and Propagation Society International Symposium (APSURSI), 2010 IEEE* , vol., no., pp.1-4, 11-17 July 2010.

9. Valdes, F.; Ghaffari-Miab, M.; Andriulli, F.P.; Cools, K.; Kotulski, J.D.; Michielssen, E., "High-order Calderón multiplicative preconditioner for time domain electric field integral equations," *Antennas and Propagation (APSURSI), 2011 IEEE International Symposium*, vol., no., pp.2362, 3-8 July 2011.

BIBLIOGRAPHY

[1] A. J. Poggio, and E. K. Miller, "Integral equation solutions of three-dimensional scattering problems," in *Computer Techniques for Electromagnetics*, R. Mittra, Ed. New York: Pergamon, 1973.

[2] W. C. Chew, J. M. Jin, C. C. Lu, E. Michielssen, and J. M. Song, "Fast solution methods in electromagnetics," *IEEE Trans. Antennas Propagat.*, vol. 45, no. 3, pp. 533-543, Mar. 1997.

[3] J. M. Song, C. C. Lu, and W. C. Chew, "Multilevel fast-multipole algorithm for solving electromagnetic scattering by large complex objects," *IEEE Trans. Antennas Propagat.*, vol. 45, no. 10, pp. 1488-1493, Oct. 1997.

[4] E. Bleszynski, M. Bleszynski, and T. Jaroszewic, "AIM: Adaptive integral method for solving large-scale electromagnetic scattering and radiation problems," *Radio Sci.* 31 (1996), pp. 1225–1151.

[5] A. Dutt and V. Rokhlin, "Fast Fourier transforms for nonequispaced data," SIAM J. *Sci. Comput.* 14 (1993), pp. 1368–1393.

[6] Bagci, H.; Yilmaz, A.E.; Michielssen, E.; , "An FFT-Accelerated Time-Domain Multiconductor Transmission Line Simulator," *Electromagnetic Compatibility, IEEE Transactions on* , vol.52, no.1, pp.199-214, Feb. 2010.

[7] Shanker, B.; Ergin, A.A.; Mingyu Lu; Michielssen, E.; , "Fast analysis of transient electromagnetic scattering phenomena using the multilevel plane wave time domain algorithm," *Antennas and Propagation, IEEE Transactions on* , vol.51, no.3, pp. 628- 641, March 2003.

[8] J.-C. Nedéléc, *Acoustic and Electromagnetic Equations*. New York: Springer-Verlag, 2000.

[9] H. Contopanagos, B. Dembart, M. Epton, J.J. Ottusch, V. Rokhlin, J.L. Visher, and S.M. Wandzura, "Well-conditioned boundary integral equations for three-dimensional electromagnetic scattering," *IEEE Trans. Antennas Propagat.*, vol.50, no.12, pp. 1824-1830, Dec 2002.

[10] R. J. Adams, and N.J. Champagne, "A numerical implementation of a modified form of the electric field Integral equation," *IEEE Trans. Antennas Propagat.*, vol.52, no.9, pp. 2262-2266, Sept. 2004.

[11] F. P. Andriulli, K. Cools, H. Bagci, F. Olyslager, A. Buffa, S. Christiansen, and E. Michielssen, "A Multiplicative Calderón Preconditioner for the Electric Field Integral Equation," *IEEE Trans. Antennas Propagat.*, vol.56, no.8, pp.2398-2412, Aug. 2008.

[12] K. Cools, F.P. Andriulli, F. Olyslager, and E. Michielssen, "Time-Domain Calderón Identities and their Application to the Integral Equations analysis of Scattering by PEC objects Part I: Preconditioning," *IEEE Trans. Antennas Propagat.*, vol. 57, pp. 2352-2364, Aug 2009.

[13] Andriulli, F.P.; Cools, K.; Olyslager, F.; Michielssen, E.; , "Time Domain CalderÓn Identities and Their Application to the Integral Equation Analysis of Scattering by PEC Objects Part II: Stability," *Antennas and Propagation, IEEE Transactions on* , vol.57, no.8, pp.2365-2375, Aug. 2009

[14] F. P. Andriulli, and E. Michielssen, "A Regularized Combined Field Integral Equation for Scattering from 2-D Perfect Electrically Conducting Objects," *IEEE Trans. Antennas Propagat.*, vol. 55, pp. 2522-2529, Sept. 2007.

[15] H. Bagci, F. P. Andriulli, K. Cools, F. Olyslager, and E. Michielssen, "A Calderón Multiplicative Preconditioner for the Combined Field Integral Equation," *IEEE Trans. Antennas Propagat.*, vol. 57, pp. 3387-3392, Oct. 2009.

[16] S. M. Rao, D. R. Wilton, and A W. Glisson, "Electromagnetic scattering by surfaces of arbitrary shape," *IEEE Trans. Antennas Propagat.*, vol. AP-30, pp. 409-418, May 1982.

[17] A. Buffa and S. Christiansen, "A dual finite element complex on the barycentric refinement," *Math. Comp.*, vol. 76, pp. 1743-1769, 2007.

[18] Q. Chen and D. R. Wilton, "Electromagnetic scattering by three-dimensional arbitrary complex material/conducting bodies," in *Proc. IEEE AP-S Symp.*, vol. 2, 1990, pp. 590-593.

[19] R.D. Graglia, D.R. Wilton, and A.F. Peterson, "Higher order interpolatory vector bases for computational electromagnetics," *IEEE Trans. Antennas Propagat.*, vol.45, no.3, pp.329-342, Mar 1997.

[20] K. C. Donepudi, J. M. Jin, S. Velamoarambil, J. M. Song, and W. C. Chew, "A higher-order parallelized multilevel fast multipole algorithm for 3D scattering," *IEEE Trans. Antennas Propagat.*, vol. 49, pp. 1078-1078, July 2001.

[21] F. Valdés, F.P. Andriulli, H. Bagci, and E. Michielssen, "On the discretization of single source integral equations for analyzing scattering from homogeneous penetrable objects," Antennas and Propagation Society International Symposium, 2008. AP-S 2008. IEEE , vol., no., pp.1-4, 5-11 July 2008.

[22] M. B. Stephanson, and Jin-Fa Lee, "Preconditioned Electric Field Integral Equation Using Calderón Identities and Dual Loop/Star Basis Functions," *IEEE Trans. Antennas Propagat.*, vol. 57, pp. 1274-1279, Apr. 2009.

[23] S. Yan, J-M. Jin, and Z. Nie, "Implementation of the Calderón Multiplicative Preconditioner for the EFIE Solution with Curvilinear Triangular Patches," presented in Antennas and Propagation Society International Symposium, 2009. AP-S 2009. IEEE , June 2009.

[24] C. Müller, *Foundations of the Mathematical Theory of Electromagnetic Waves*. Berlin: Springer-Verlag, 1969.

[25] E. Marx, "Integral equation for scattering by a dielectric," *IEEE Trans. Antennas Propagat.*, vol. AP-32, pp. 166-172, Feb. 1984.

[26] A. W. Glisson, "An integral equation for electromagnetic scattering from homogeneous dielectric bodies," *IEEE Trans. Antennas Propagat.*, vol. AP-32, pp. 173-175, Feb. 1984.

[27] H. Contopanagos, B. Dembart, M. Epton, J. J. Ottusch, V. Rokhlin, J. L. Visher, and S. M. Wandzura, "Well-conditioned boundary integral equations for three-dimensional electromagnetic scattering," *IEEE Trans. Antennas and Propagat.*, vol.50, no.12, pp. 1824-1830, Dec 2002.

[28] J. S. Zhao, and W. C. Chew, "Integral equation solution of Maxwell's equations from zero frequency to microwave frequencies," *IEEE Trans. Antennas and Propagat.*, vol. 48, pp. 1635-1645, 2000.

[29] A. Colliander and P. Ylä-Oijala, "Electromagnetic scattering from rough surface using single integral equation and adaptive integral method", *IEEE Trans. Antennas Propagat.*, vol. 55, pp. 3639-3646, 2007.

[30] M. S. Yeung, "Single integral equation for electromagnetic scattering by three-dimensional homogeneous dielectric objects," *IEEE Trans. Antennas Propagat.*, vol. 47, pp. 1615-1622, 1999.

[31] J. R. Mautz, "A Stable Integral Equation for Electromagnetic Scattering from Homogenous Dielectric Bodies," *IEEE Trans. Antennas Propagat.*, vol. 37, no 8, pp. 1070-1071, August 1989.

[32] G. C. Hsiao and R. E. Kleinman, "Mathematical foundations for error estimation in numerical solutions of integral equations in electromagnetics," *IEEE Trans. Antennas Propagat.*, vol. 53, pp. 3316-3323, Oct. 2005.

[33] R. Kress, *Linear Integral Equations*, 2nd edition, Springer, New York, 1999.

[34] J.S. Zhao, and W.C. Chew, "Integral equation solution of Maxwell's equations from zero frequency to microwave frequencies," *IEEE Trans. Antennas Propagat.*, vol. 48, pp. 1635-1645, 2000.

[35] W. Wu, A.W. Glisson, and D. Kajfez, "A study of two numerical solutions procedures for the electric field integral equation at low frequency," *Appl. Comput. Electromagn. Soc. J.*, vol. 10, pp. 69-80, 1995.

[36] F. Valdés, F.P. Andriulli, K. Cools, and E. Michielssen, "High-order Div- and Quasi Curl-Conforming Basis Functions for Calderón Multiplicative Preconditioning of the EFIE," IEEE Transactions on Antennas and Propagation, vol.59, no.4, pp.1321-1337, April 2011.

[37] R.A. Wildman, and D.S. Weile, "An accurate broad-band method of moments using higher order basis functions and tree-loop decomposition," *IEEE Trans. Antennas Propagat.*, vol.52, no.11, pp. 3005-3011, Nov. 2004.

[38] F. Valdes, F.P. Andriulli, K. Cools, J.D. Kotulski, and E. Michielssen, "Fully localized high-order div- and quasi-curl-conforming basis functions for multiplicative Calderón preconditioning of the EFIE," Antennas and Propagation Society International Symposium (APSURSI), 2010 IEEE , vol., no., pp.1-4, 11-17 July 2010.

[39] Y. Saad, and M.H. Schultz, "GMRES: A generalized minimal residual algorithm for solving non-symmetric linear systems," *SIAM J. Sci. Stat. Comput.*, 3, vol. 7, 1986, 856-869.

[40] R. W. Freund, "A transpose-free quiasi-minimal residual algorithm for non-Hermitian linear systems," *SIAM J. Sci. Comput*. Volume 14, Issue 2, pp. 470-482, 1993.

[41] M. A. Antoniades, and G. V. Eleftheriades, "A Broadband Dual-Mode Monopole Antenna Using NRI-TL Metamaterial Loading," *IEEE Antennas and Wireless Propagation Letters*., vol.8, pp. 258-261, May 2009.

[42] R. F. Harrington, *Time-Harmonic Electromagnetic Fields*, IEEE Press, 2001.

[43] R. J. Adams, and N. J. Champagne, "A numerical implementation of a modified form of the electric field Integral equation," *IEEE Trans. Antennas Propagat.*, vol. 52, no. 9, pp. 2262-2266, Sept. 2004.

[44] P. Ylä-Oijala and M. Taskinen, "Well-Conditioned Müller Formulation for electromagnetic Scattering by Dielectric Objects," *IEEE Trans. Antennas Propagat.*, vol. 45, pp. 316-328, Mar. 1997.

[45] A. F. Peterson, "The 'interior resonance' problem associated with surface integral equations of electromagnetics: Numerical consequences and a survey of remedies," *Electromagn*., no. 10, pp. 293-312, 1990.

[46] F. Valdés, F. P. Andriulli, H. Bagci, and E. Michielssen, "On the regularization of single source combined integral equations for analyzing scattering from homogeneous penetrable objects," Antennas and Propagation Society International Symposium, 2009. APSURSI '09. IEEE , vol., no., pp.1-4, 1-5 June 2009.

[47] D. Colton and R. Kress, *Integral Equation Methods in Scattering Theory*. Willey, New York, 1983.

[48] G. W. Hanson and A. B. Yakovlev, *Operator Theory for Electromagnetics*. New York: Springer-Verlag, 2001.

[49] G. Abramowitz and L. A. Stegun, *Handbook of Mathematical Functions with Formulas, Graphs, and Mathematical Tables*., National Bureau of Standards, 1964.

[50] Q. Rao, T. A. Denidni, and A. R. Sebak, "Broadband Compact Stacked T-Shaped DRA with Equilateral-Triangle Cross Sections," *IEEE Microvawe and Wireless Components Leters*., vol. 16, pp. 7-9, Jan. 2006.

[51] H. Bagci, F. P. Andriulli, K. Cools, F. Olyslager, and E. Michielssen, "A multiplicative Calderón-based preconditioner for the coupled surface and volume electric field integral equations," accepted for publication, *IEEE Trans. Antennas Propagat*., Feb. 2010.

[52] H. Bagci, F. P. Andriulli, K. Cools, F. Olyslager, and E. Michielssen, "CMP-based discretization of the coupled surface and volume electric field integral equations," in *Proc. IEEE Int. Symp. Antennas Propagat*., 2009.

146